Modulated magnetic structures for vortex pinning in high temperature superconductors

Traian Petrisor

Nancy-Université
Université Henri Poincaré

U. F. R. Sciences et Techniques de la Matière et des Procédés
Ecole doctorale EMMA
D. F. D. Physique et Chimie de la Matière et des Matériaux

UNIVERSITATEA TEHNICĂ DIN CLUJ-NAPOCA

Thèse

présentée pour obtenir le titre de

Docteur de l'Université Henri Poincaré Nancy-Université

en Physique et Chimie de la Matière et des Matériaux

par **Traian PETRIŞOR**

Structures magnétiques modulées pour le pinning magnétique dans les supraconducteurs à haute température

Composition du jury:

Rapporteurs:	Nathalie Viart	Prof. Université Louis Pasteur, Strasbourg
	Viorel Sandu	Prof. National Institute of Materials Physics, Bucharest
Examinateurs:	Michel Hehn	Prof. Institut Jean-Lamour, Nancy Université, Nancy
	Ioan Vida-Simiti	Prof. Université Technique de Cluj-Napoca
	Adelina Carmen Ianculescu	Prof. Université "Politehnica", Bucharest
	Gilles Gaudin	CR CNRS, Laboratoire "Spintec", Grenoble
Directeurs de thèse:	Coriolan Tiuşan	CR CNRS, Institut Jean-Lamour, Nancy Université, Nancy
	Ionel Chicinaş	Prof. Université Technique de Cluj-Napoca

Thèse en cotutelle préparée au :
Institut Jean-Lamour, CNRS-Nancy Université, Nancy, France
Laboratoire de Sciences des Matériaux, Université Technique de Cluj-Napoca, Roumanie

Mme. Nathalie Viart	professeur Institut de Physique et Chimie des Matériaux de Strasbourg Université Louis Pasteur, Strasbourg, France
M. Viorel Sandu	professeur National Institute of Materials Physics, Bucharest, Romania
M. Michel Hehn	professeur Institut Jean-Lamour Nancy Université, Nancy, France
M. Ioan Vida-Simiti	professeur Doyen de la Faculté des Sciences et Ingénierie des Matériaux Université Technique de Cluj-Napoca, Roumanie
M. Adelina Carmen Ianculescu	professeur Faculté de Chimie Industrielle Département des Sciences et Ingénierie des Matériaux Oxydiques Université "Politehnica", Bucharest, Roumanie
M. Gilles Gaudin	chargé de recherches au CNRS Laboratoire "Spintec" CNRS-CEA, UAR 2512, Grenoble, France
M. Coriolan Tiuşan	chargé de recherches au CNRS habilitation à diriger des recherches Institut Jean-Lamour Nancy Université, Nancy, France
M. Ionel Chicinaş	professeur Faculté des Sciences et Ingénierie des Matériaux Université Technique de Cluj-Napoca, Roumanie

Overview

Large scale application of superconductivity, such as energy transport, superconducting magnets, engines, generators, etc., require superconducting materials with a critical current density, J_c, greater than 1 MA/cm^2 and a high irreversibility line. In order to fulfill these requirements, the only way is to avoid the vortex motion, which is responsible for energy dissipation in a type II superconductor (SC). Up to date the method used to block the vortex movement is their pinning on normal impurities present in a superconductor, the so-called conventional pinning. This type of pinning relies on the tendency of the vortex normal core to attach itself to regions in the superconductor where superconductivity is suppressed, in an attempt to minimize the overall system energy. For this reason, normal zones within the superconductor are artificially created in different ways, such as ion implantation, surface decoration or artificially introduced nanoparticles. In the past decade numerous research groups have addressed the problem of magnetic pinning in superconductors. The relevance of this subject lies in the possibility of attaining large, temperature independent pinning forces of vortices in type II superconductors, through the interaction between the vortex flux and the magnetization of magnetic structures, *i.e.* ferromagnetic films or ferromagnetic micro-, and nanostructures (FM), situated in the proximity of the former. In the present thesis we focus on the study of several magnetic systems for magnetic pinning applications in $YBa_2Cu_3O_7$ (YBCO) thin films. The choice of the YBCO superconductor for our studies was motivated by the fact that currently a consistent part of the high field applications use this material for its high critical temperature, 92 K, which makes it economically viable for technological applications.

The present thesis is structured as follows. In **Chapter 1** an overview of current literature reports in the field of magnetic pinning is given. The focus of this review was magnetic systems that are similar to the ones that we study throughout the thesis. The particularity of the up-to-date literature is that most of the studies of magnetic pinning concern low-temperature superconductors. Our approach, to use high temperature superconductors, *i.e.* YBCO, present an interest both from a theoretical and a practical point of view. Such experiments open the possibility to investigate the role of magnetic pinning on the thermally activated flux flow and related phenomena. On the other hand, the control of the superconducting properties by magnetic modulations could represent a step towards new

magneto-superconducting devices.

The experimental techniques that were used in the framework of the thesis are presented in **Chapter 2**. A description of the deposition methods, pulsed laser deposition and dc magnetron sputtering is given, together with the structural, morphological and magnetic characterization techniques. Special attention has been devoted to the description of the X-ray diffraction methods as they play an important role throughout the thesis.

In our choice of ferromagnetic materials for pinning applications we have chosen two classes materials. The first is the doped rare earth manganite $La_{0.66}Sr_{0.33}MnO_3$ (LSMO), while the second is represented by Co and Permalloy ($Ni_{80}Fe_{20}$, Py). Our studies of epitaxial LSMO thin films are presented in **Chapter 3**. They consist of a study regarding the optimization of the film growth process and a detailed study of oxygen incorporation effects in epitaxial LSMO layers. With respect to the overall goal of the thesis, we have shown that by controlling the growth mode of LSMO, highly regular LSMO nano-islands on $SrTiO_3$ (STO) substrates may be produced. Thermal treatment in oxygen atmosphere of the STO substrates induces the formation of atomic terraces. The steps represent nucleation centers for the LSMO film, so that after the deposition, the film consists of regular nano-islands arranged along the substrate step edges. Upon the deposition of the superconducting YBCO on top, two effects are to be expected with respect to flux pinning: the first consists in the creation of dislocations in the YBCO film at the sites were the LSMO nano-islands are present, while the second is the creation of a modulated stray magnetic field of the structures having the same spatial periodicity as that of the islands.

Divalent ion doped rare earth manganites are known for their strong connection between their structural, magnetic and electric properties. Behind this relation lies the *double exchange* interaction between Mn ions in the Mn^{3+}-O-Mn^{4+} bond, mediated by the simultaneous transfer of an e_g electron from Mn^{3+} to an O^{2-} ion and from O^{2-} to Mn^{4+}. In this picture oxygen plays an important role, as it is directly involved in the double exchange mechanism. Also, it has been show that if oxygen in found in excess in the LSMO lattice it produces additional hole doping, *i.e.* produces additional Mn^{4+} valence ions, as well as cationic (La, Sr, Mn) vacancies. From the above considerations, it can be seen that oxygen content plays a crucial role in determining the physical properties of LSMO thin films. In order to evaluate these effects, we have performed a systematic oxygen incorporation study by annealing LSMO thin films in different mixtures of Ar:O_2 flowing gas. High resolution x-ray diffraction measurements were used to quantify the effects of oxygen incorporation on the crystalline structure of the films. Also using a numerical model we have simulated the ω-scan diffraction data in order to describe the effect of vacancies on the structure of the LSMO film. This last point represents an original approach in the study of excess oxygen incorporation effects. In order to support our assumptions based on the diffraction data, as well as to depict a more accurate physical picture of the processes involved, we have also

performed the magnetic characterization of the samples, by means of SQUID measurements. From the chemical composition point of view, XPS analyses were employed to trace the evolution of the Mn and O ion concentration in the different annealing gas mixtures. Electrical measurements were performed using the four probe method and the results were interpreted using the variable range hopping regime.

The study of magnetic stripe modulated films for flux pinning is presented in **Chapter 4**. We have fabricated metallic thin films, Co and Py, exhibiting parallel *weak stripe* domains. The films were deposited on Si (111) single crystal substrates at room temperature. In order to stabilize the stripe domain pattern, we performed a study of the films with varying thickness. It is known that perpendicular magnetic anisotropy, the cause behind the stripe domain formation, stabilizes only for thicknesses exceeding a critical value. An interesting aspect of the films is that as the thickness increases so does the periodicity of the magnetic stripes. This is an important result as it allows for the study of the influence of the superconducting properties on the YBCO layer as a function of the field modulation periodicity. Films with weak stripe domain structures also present the so-called *rotatable anisotropy*. This type of anisotropy refers to the fact that if an external field is applied in any in-plane direction, the in-plane component of the magnetization will align itself in the direction of the applied field, and will remain as such even after the field is removed. This phenomena allows for the study of the magnetic flux pinning as a function of the stray magnetic field having different orientations with respect to the current direction in the superconducting layers. The magnetic studies on the films were performed by magnetic force microscopy, MFM and vibrating sample magnetometry, VSM. An interesting case of ferromagnetic film with true perpendicular anisotropy is the case of epitaxial Co thin film grown on $Al_2O_3(0001)$ substrates. A short study was dedicated to this structure, but due challenges related to the epitaxial Co film growth on YBCO layers, this subject was analyzed only as a proof of concept. A further step in magnetic modulation consists in the micro and nanostructuration of magnetic structures. Optical lithography and ion beam etching were used for the fabrication of magnetic objects on the micron scale. An important part of the work in this field was devoted to the technical aspects of the above techniques and to the optimization of the overall microfabrication process. As the dimensionality of the magnetic objects is decreased, border effects, *i.e.* closure domains, begin to play the leading role in determining the domain configuration. We studied the evolution of the domain structure with decreasing the object lateral size. As far as nanostructuturation process is concerned, we have employed an alternative lithographic process, with respect to the "classic" techniques such as e-beam lithography. This consisted in the use of self-assembled polystyrene beads, with diameters of hundreds of nanometers, as a lithographic mask for nanofabrication. After the deposition of the magnetic film and removal of the spheres, triangular magnetic features of a few hundreds of nanometers were defined on the substrate. Depending on their thickness we were able to

stabilize a magnetic dipole type structure of these objects, as well as vortex-like configuration of the magnetization. This method may prove itself to be valuable if large scale applications of magnetic pinning are envisioned.

The last chapter of the thesis, **Chapter 5** is concerned with the actual integration of the FM structures presented in the previous chapters in bi-layered structures with YBCO superconducting films. A brief account is given on the preparation of epitaxial YBCO films deposited by pulsed layer deposition on STO(001) substrates. Two categories of structures are analyzed. First, we present the LSMO/YBCO structures, were the ferromagnetic film represents the bottom layer while YBCO is epitaxially grown on top of it. High resolution x-ray diffraction measurements were performed in order to establish the influence of the modulated LSMO surface on the structural properties of the superconducting films. The morphological evaluation of the samples was performed by means of AFM. The superconducting properties of the structures were analyzed using VSM measurements at low temperatures. Our studies reveal that a two component pinning mechanism is present in the YBCO films: a classic mechanism, due to the defects created in the superconducting film by the particular morphology of the LSMO layers, and a magnetic pinning component arising from the stray field gradients produced by the LSMO nano-islands. As far as the metallic films are concerned, Py layers were deposited on top of the YBCO films. Because of the fact that the electric transport properties were determined performing $I-V$ measurements at different temperatures, lithography was employed in order to define structures having a precise geometry. The results of the $I-V$ characteristics and critical current density, J_c , measurements for different magnetic configurations are given. A 20% increase in J_c was recorded for the parallel configuration of the magnetic stripes to the current in the superconductor, with respect to the perpendicular configuration, confirming thus the pinning potential of weak stripe domains for magnetic SC vortex pinning.

Contents

Chapter 1

Magnetic flux pinning in superconductors

In the past decade numerous research groups have addressed the problem of magnetic pinning in superconductors. The relevance of this subject lies in the possibility of attaining large pinning forces of vortices in type II superconductors, that are temperature independent, through the interaction between the vortex flux and the magnetization of a magnetic structure, *i.e.* ferromagnetic films, ferromagnetic micro-, or nanostructures.

Large scale application of superconductivity, such as energy transport, superconducting magnets, engines, generators, etc., require superconducting materials with a critical current density, J_c, greater than 1 MA/cm^2 and a high irreversibility line. In order to fulfill these requirements, the only way is to avoid the vortex motion, which is responsible for energy dissipation in a type II superconductor. Up to date the method used to block the vortex movement is their pinning on normal impurities present in a superconductor, the so-called conventional pinning. This type of pinning relies on the tendency of the vortex normal core to attach itself to regions in the superconductor where superconductivity is suppressed, in an attempt to minimize the overall system energy. For this reason, normal zones within the superconductor are artificially created in different ways. These zones coexist with the natural occurring normal regions arising from inherent growth defects, such as grain boundaries, dislocations and the presence of secondary phases. Several ways of externally inducing normal regions in superconductors have been demonstrated. They include: irradiation by swift heavy ions, artificially introduced regular arrays of holes, artificially introduced nanoparticles that create columnar defect in superconducting films, or surface decoration of the substrate upon which the superconducting film is grown. Examples of artificially induced pinning centers are given in Figure 1.1.

Bulaevskii *et al.* [24] argued that the maximal energy/unit length of the vortex, available for non-magnetic, "classic" pinning is the condensation energy of the Cooper pairs in the

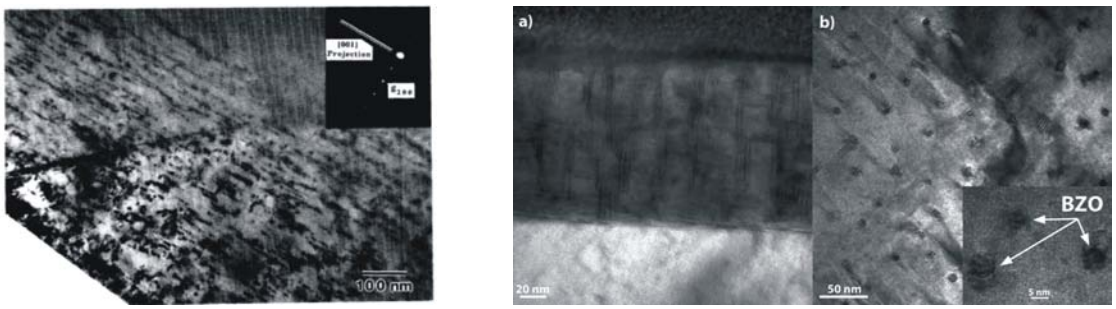

(a) **(b)**

Figure 1.1: (a) Electron micrographs of Sn^{30+} irradiated YBCO single crystal. The tracks are seen to consist of discontinuous columns of highly damaged or amorphous regions (Taken from [3]); (b)Scanning transmission electron microscope (STEM) dark field micrograph of cross section and planar view for a YBCO-BZO (5 mol %) film (Taken from [4]).

volume of the vortex core, that is

$$U_{cp} = \left(\frac{H_c^2}{8\pi}\right)\pi\xi^2 = \left(\frac{\Phi_0}{8\pi\lambda_L}\right)^2, \tag{1.1}$$

where H_c is the thermodynamic critical field, ξ is the radius of the vortex normal core, *i.e.* the superconducting coherence length, Φ_0 the elementary flux quanta, $h/2e$, while λ_L is the London penetration length. Considering that the penetration length varies with temperature as

$$\lambda_L \sim \frac{1}{\sqrt{T_c - T}}, \tag{1.2}$$

with T_c being the superconducting critical temperature, one can observe that the pinning potential, U_{cp}, decreases linearly with T, reaching zero at T_c. In the case of HTS (high critical temperature superconductors), where one would like to take advantage of the high T_c, and set the operating temperature as close as possible to this limiting value, typically at the nitrogen boiling point, 77 K, thermal fluctuations tend to destroy pinning at a rate proportional to $\exp(U_p/k_BT)$. From the above considerations it can thus be observed that classic non-magnetic pinning becomes ineffective at high temperatures making it difficult to imagine practical applications of HTS materials.

In this context, magnetic pinning may be a valid alternative for effective vortex pinning applications, as the pinning potential created by a magnetic structure, in this case displaying a stripe domain structure varying along the x axis, is expressed as [24]:

$$U_{mp} = \Phi_0 M(x) d_s, \tag{1.3}$$

d_s being the superconducting layer thickness and $M(x)$ the magnetization value, which, neglecting the domain wall contributions, takes the values of $\pm M_0$. Even though the above

expression of the pinning potential is calculated for a particular case of magnetic configuration, the point it stands for may be generalized to any magnetic distribution, and it is that magnetic pinning potential is independent of temperature. Of course, the Curie temperature of the ferromagnet has to be high enough so that there is no significant variation of the magnetization with temperature, in the superconducting regime. This fact makes this type of pinning as the ideal case of superconducting vortex pinning, suitable for high temperature superconductors.

In the present chapter we set out to give an overview of the literature data on the the ferromagnetic/superconducting (FM/SC) hybrid structures. Even though the focus of the present thesis is the study of magnetic pinning in YBCO/FM structures, the overview is not limited strictly to these systems, as the majority of the studies performed so far are dealing with low temperature superconductors, Nb, Pb, Al, etc... Two major classes of systems will be covered: the first is represented by SC/FM structures in which the ferromagnet is a continuous layer, displaying different magnetic configurations, stripe domains and bubble domains. The second is represented by structures in which the FM layer is laterally structured in arrays of micronic and submicronic arrays of particles. Due to the reduced lateral size the magnetic state of the particles may be tuned to be a single domain or exhibit a magnetic vortex configuration. A systematic classification of the different FM/SC structures published so far in the literature can be found in Ref. [13]. Also, in the next Section of the Chapter a brief account is given on the relation between the vortex flux flow regime and energy dissipation within type II superconductors. This section was included in order to emphasize the importance of flux pinning in superconductors. A more detailed account of the vortex state and dynamics is given in Appendix A.

1.1 Flux flow and energy dissipation

It is known that in type II superconductors the external magnetic field penetrates in the superconductor in form of elementary flux quanta, Φ_0. The flux quanta is carried by a co-called vortex, theoretically predicted by Abrikosov [1]. The vortex is comprised of a normal core, having the width of the order of the superconducting coherence length, ξ, and is surrounded by superconducting region in which a supercurrent, $\mathbf{J}(\mathbf{r})$, generates the magnetic field of the flux quanta. The radius of the superconducting region, the superconducting tube, is of the order of the penetration length, λ. A schematic representation of the Abrikosov vortex is given in Figure 1.2a. Because of the repulsion force that exists between vortices, they arrange themselves in a triangular lattice, called the vortex lattice. The vortex lattice is in equilibrium until the only circulating currents in the superconductor are vortex currents. If in the superconductor a current, $\mathbf{J}$, is injected by external sources, each vortex is subjected to a Lorentz force per unit length $\mathbf{f}_L = \mathbf{J} \times \Phi_0 \mathbf{i}_z$, as it is shown Figure 1.2b. The Lorentz

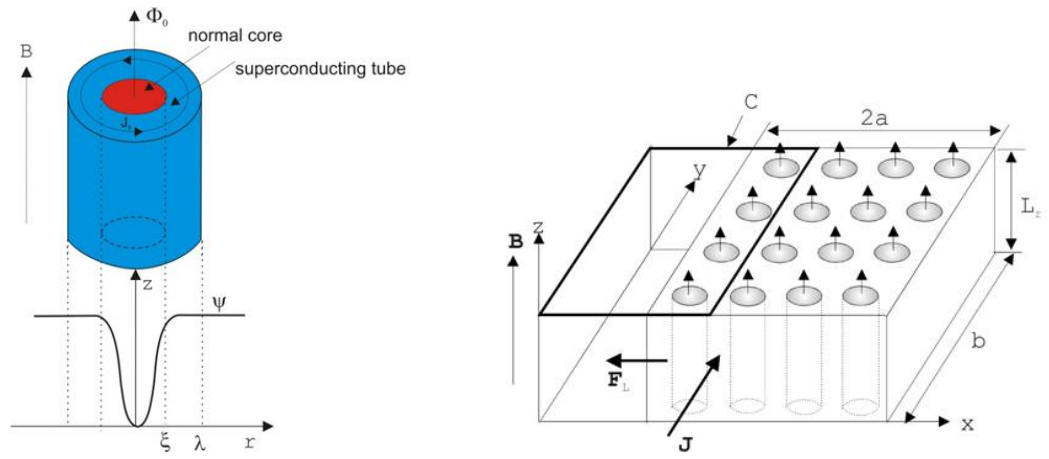

(a) **(b)**

Figure 1.2: (a) The model of an Abrikosov vortex; (b)The contour (C) of integration for Farady's law.

force due to the current **J** will cause the vortices to move with a velocity u_x in the x-direction (perpendicular to the current). The variation of the flux in the contour C is the total number of vortices which enter in the contour in a time Δt multiplied by Φ_0:

$$\Delta\Phi = \Phi_0 n_v u_x b \Delta t \tag{1.4}$$

where n_v is the vortex density. According to Faraday's law, the voltage across the contour will be:

$$U = \frac{d\Phi}{dt} = \Phi_0 n_v u_x b. \tag{1.5}$$

It is important to be noted that the induced electric field $\mathbf{E} = \mathbf{B} \times \mathbf{v}$ is parallel with the current density **J**. Because the current is in the same direction as the voltage difference, there must be power dissipated equal to UI,

$$P = UI = I\Phi_0 n_v u_x b \tag{1.6}$$

Since the flux line motion dissipates energy, it can be described in terms of a viscosity. The vortex motion is assumed to be damped by a force proportional to the velocity, $f_\eta = \eta u_x$, where η is the viscosity. The drift velocity of the vortex line can be obtained by equating the Lorentz force to the friction force, $f_L = f_\eta$, resulting

$$u_x = \frac{J\varphi_0}{\eta}. \tag{1.7}$$

Combining the equations 1.5, 1.7 and taking into account that $E = U/b$, results in a linear relation between the electric field and the current density, similar to the Ohm's law:

$$E = \rho_{ff} J, \tag{1.8}$$

where,

$$\rho_{ff} = \frac{B\Phi_0}{\eta} \tag{1.9}$$

is called *flux flow* resistivity. The microscopic calculation of the viscosity gives the value [3]

$$\eta = \frac{\Phi_0^2 \sigma_n}{2\pi\xi^2}, \tag{1.10}$$

σ_n is the electrical conductivity in the normal state. Using this relation, the flux flow resistivity can also be written as

$$\rho_{ff} = \frac{B}{B_{c2}}\rho_0 \tag{1.11}$$

1.2 Magnetic flux pinning in hybrid SC/FM bi-layer structures

As mentioned in the Introduction of the present chapter, Bulaevskii *et al.* [24] showed that in the case of SC/FM structures, with the FM layer exhibiting stripe domain structures, effective magnetic vortex pinning potential is generated by the domain stripes. The stripe domain structure consists of alternating magnetic domains in which the magnetization, perpendicular to the film surface, points upwards and downwards. Thus, for strong perpendicular anisotropy magnetic films, such as Co-Pt, Tb-Fe or hexagonal Co films, within each domain the magnetization has its saturation value, $\pm M_0$, in the case in which the external applied magnetization field is less than the coercive field, H_{coer}. Equating the magnetic pinning force, calculated from the pinning potential 1.3, as U_{mp}/l, with l as the domain width, to the Lorentz force acting on the vortex line, stemming from the transport current in the SC layer, $J\Phi_0 d_s/c$, gives a rough estimate of the critical current

$$J_c \sim cM_0/l. \tag{1.12}$$

It can be seen that within the model proposed, the critical current density, J_c, increases as the perpendicular component of the magnetization, M_0 increases, justifying the use in magnetic pinning experiments of FM structures that exhibit strong or weak perpendicular anisotropy. Using 1.12 one finds an estimate of 10^7A/cm^2 for J_c in the case of M_0=50 emu,

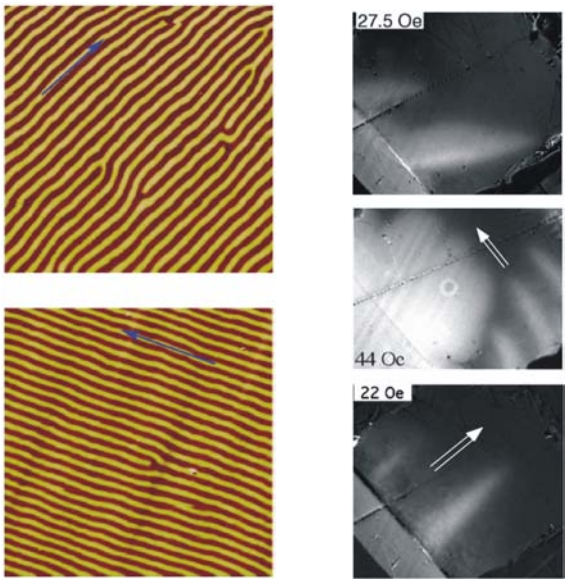

Figure 1.3: (a) 20 × 20 mm^2 MFM images of stripe domains in permalloy (Py) film after applying and turning off an H=1 kOe parallel magnetic field along the directions indicated by the arrows; (b) Magneto-optical images of flux entry for a $NbSe_2$ single crystal, see details in text, with the Py stripe domains oriented at 45deg (top), parallel (middle) and perpendicular (bottom) to a surface edge. The double-line arrow shows the preferential flux entry direction coinciding with the direction of the stripe domains in the Py. Taken from [5].

and for fields inferior to H_{coer}, with H applied perpendicularly to the film plane.

Vlasko-Vlasov *et al.* [5] studied the vortex entrance and exit patterns in a 20 μm thick $NbSe_2$ single crystal, having T_c=7.2 K, upon which a 0.8 μm thick permalloy, $Ni_{80}Fe_{20}$ (Py), was grown. The MFM images of the Py top layer, Figure 1.3a, show magnetic domains that are formed by parallel stripes with an alternating out-of-plane component of the magnetization. The particularity of thick Py films that exhibit stripe domain patterns is the so-called *rotatable anisotropy*, which means that the in-plane orientation of the stripes can be easily modified with the help of a relatively low magnetic field, in the order of hundreds of Oe, without affecting the parallel character of the domains. In order to study the influence of presence of the magnetic domains and their orientation on the entrance and exit patterns of vortices in the SC, three different stripe configurations were prepared. They included a parallel, perpendicular and 45° orientations with respect to the sample edge. An external magnetic field, perpendicular to the sample surface, H_z, for vortex generation was also applied. Three main results are shown in Figure 1.3b. The bright contrast corresponds to the normal induction, B_z, associated with the local vortex density. As it can be seen, in all three cases the bright stripes are oriented preferentially along the direction of the stripes, denoted by the white arrow. The lower left dark line represents a scratch oriented perpendicular to the reference surface edge. This result was interpreted as a consequence of the pinning

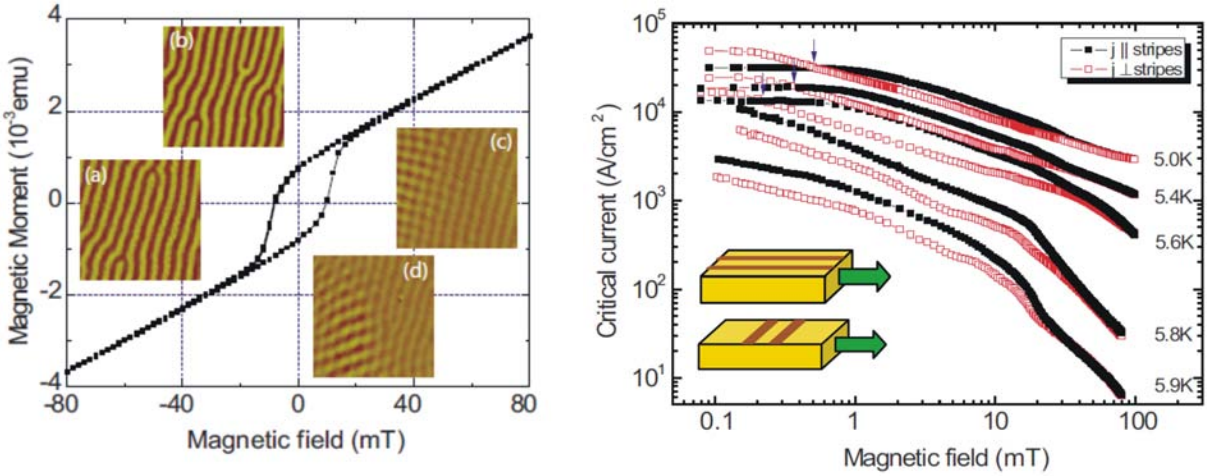

(a) **(b)**

Figure 1.4: (a)Magnetization curve of the 2 μm-thick Permalloy film as a function of magnetic field applied perpendicular to the film surface. The insets show the MFM images of the same film in (a) H=0 mT, (b) 10 mT, (c) 40 mT, and (d) 300 mT perpendicular magnetic field at room temperature; (b) Magnetic field dependence of the critical current density for several temperatures. Taken from [7].

provided by the stripe domain walls. Vortices parallel to the stripes, without being impeded by the presence of domain walls, *i.e.* variations of the magnetization, which leads to the additional pinning force, are able to move "freely" and hence the parallel direction becomes preferential for vortex motion.

Belkin *et al.* [7] studied the influence of the relative orientation of the Py stripe domains on the the superconducting properties of a 80 nm thick MoGe superconducting film having the T_c=6.2 K. The entire structure consisted of the MoGe film a 30 nm SiO_2 capping layer and, on top, a 2 μm Py film. The role of the SiO_2 spacer layer was to prevent any proximity effects between the FM and SC layer and to isolate only the *magnetic coupling* between the two. Generally speaking, magnetic coupling between a FM and SC layer is considered to consist of the interaction of the magnetic stray field with the SC layer. MFM studies of the top Py layer, Figure 1.4a, revealed the fact that at higher values of the external magnetic field a "bubble" type domain structure is stabilized. The critical current densities, J_c, were determined for two configurations of the stripe domains at different fields for different temperatures, Figure 1.4b. The two cases consisted of two different orientations of the stripe domains with respect to the current passing through the superconductor. One corresponded to the case in which the stripes were aligned parallel to the current, while the second consisted of a perpendicular configuration of the two. If we consider the two cases at 5.9 K, we can clearly see that in the case in which the current, j, flows parallel to the magnetic stripes (black squares) the critical current is considerably larger, note the logarithmic scale in Figure 1.4b,

than the critical current evaluated when j flows perpendicular to the stripes, in the low field part of the evaluation. This situation can be understood if we consider the findings presented before, [5], namely that the superconducting vortices may move without any opposition from the magnetic stray field created by a strip domain structure, if this displacement is performed along the stripe direction. This is so because of the absence of any stray field gradient along the displacement direction of the vortices, that would give rise to a force and, hence, to flux pinning. When the j is directed along the domain stripes, the Lorentz force acting on the vortices is directed perpendicular to the stripes and so the vortices will tend to move accordingly in this direction with respect to the magnetic domains. This situation will correspond to one in which the pinning force will be large as the vortices will be trapped by the stray field variation produced by the domain walls, corresponding thus to a high J_c value. On the contrary, when the current flows perpendicular to the domains, the Lorentz force will act parallel to them so that the motion of the vortices will not be obstructed by the presence of the magnetic pinning potential. As a consequence the critical current density will be lower in this case (empty red squares). An interesting situation occurs at perpendicular field values situated above 30 mT. As it can be observed in this field range, the critical current densities, corresponding to the two different stripe orientations, tend towards the same values. This fact is attributed to the nucleation of the bubble domain structure and to its isotropic nature, which in turn leads to an isotropic pinning potential. Because from the magnetic pinning potential point of view all directions are equivalent, there is no difference between the values obtained for J_c in the two cases.

Another magnetic system that has been studied in relation to its influence on superconducting films, is the Co/Pt multilayered system. It is known that these structures exhibit an out-of-plane magnetic anisotropy. Lange *et al.* [27] studied hybrid structures that contained 14 nm of alternating Co/Pt $[\mathrm{Co}(0.4\ \mathrm{nm})/\mathrm{Pt}(1.0\ \mathrm{nm})]_{10}$ layers and a 60 nm Pb film, T_c=7.23 K separated by a 10 nm Ge spacer, used as an insulating layer to prevent proximity effects. The main results obtained in this study are summarized in Figure 1.5. The authors introduced a parameter, s, that is defined as the fraction of magnetic moments that are pointing upwards, $m > 0$, relative to the total number of magnetic moments, in order to describe different remanent states of the Co/Pt system. The critical current density evaluation was done by performing $M(H)$ measurements on the superconductor, taking into account that the amplitude of the $M(H)$ signal is directly proportional to J_c, as shown in the Bean critical state model. This model will be dealt with in more detail in the final chapter of the present thesis, in which results on magnetic pinning in YBCO thin films are discussed. Figure 1.5 (a) and (d) show the MFM image of the demagnetized state and the corresponding $M(H)$ curves for this state and for the $s = 0$ state, *i.e.* for the FM film fully magnetized in the opposite direction. The results show a higher critical current in the case of the $s = 0$ state than for the demagnetized one. This somewhat surprising effect is explained as a conse-

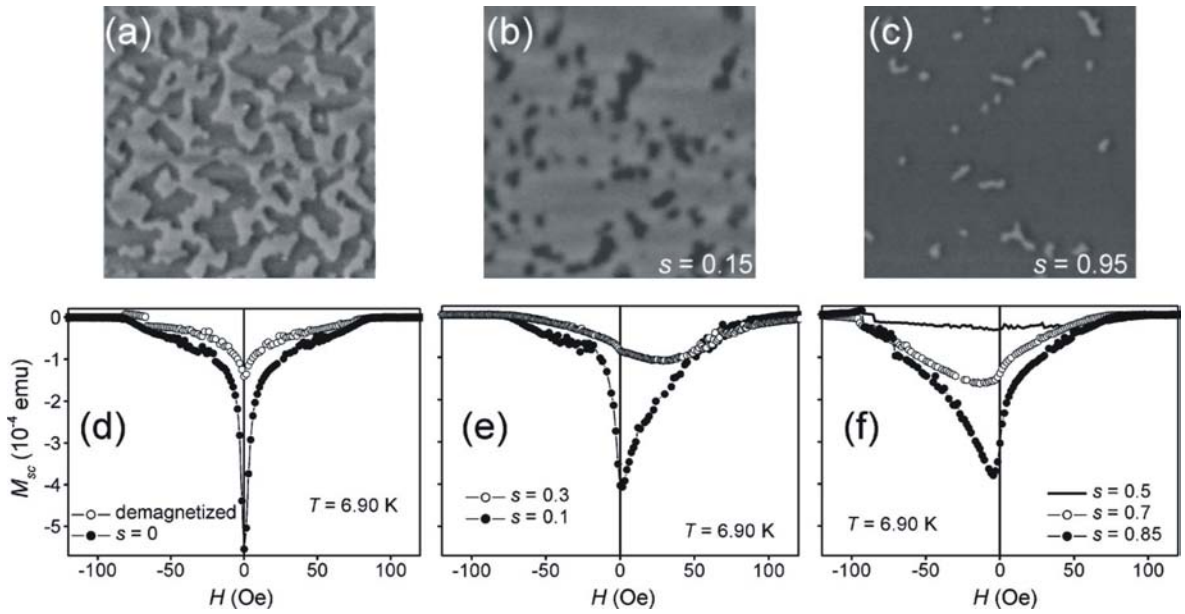

Figure 1.5: (a)(c) MFM images (5×5 μm^2) at room temperature and H=0 of the Co/Pt multilayer in different magnetic states: (a) after demagnetization, (b) after magnetizing the sample in a perpendicularly applied field H=-10 kOe→+0.83 kOe→0 (s=0.15), and (c) H=-10 kOe→1.10 kOe→0 (s=0.95); (d)-(f) Magnetization measurements of a type-II superconducting Pb film covering a Co/Pt multilayer. Taken from [27].

quence of the domain structure present in the demagnetized film that creates alternating stray fields above the magnetic domains which in turn suppress the order parameter in the SC and also may lead to the creation of vortex-antivortex pairs connecting the domains with opposite magnetization and result in an overall reduction of J_c. This situation is reflected by the reduction of T_c to 7.04 K in the case of a demagnetized FM. Figures 1.5(e) and (f) show that when $m > 0$ the bubble domains in Figure 1.5(b) provide magnetic pinning of vortices when $H > 0$, resulting in an enhanced amplitude of M for positive values of H. On the contrary, for $m < 0$, Figure 1.5(c), effective pinning is achieved for $H < 0$ as it can be seen from Figure 1.5(f). This asymmetry can be understood if one considers that the interaction energy between the magnetic field of SC vortices B and the magnetic moments, m, in the FM may be of attractive nature if B and m have the same polarity and repulsive in the case for which the two have opposite polarities. Magnetic measurements also point out that effective pinning is achieved for bubble domains that have a smaller size and lower densities. The amplitude of M, in the lower curve of Figure 1.5(f), is increased by a factor 3 when compared to the reference $s = 0$ case and by a factor of 2 with respect to the middle curve, $s = 0.7$. As in the demagnetized state, it is apparent that larger magnetic bubbles having higher densities, associated with a reduced SC order parameter, counteract efficient vortex pinning and lead to low M amplitudes, *i.e.* low J_c values.

The FM domain walls (DWs) interaction with the SC vortices has been studied in detail by Goa *et al.* [9]. The structure that has been studied by this group consisted of a FM

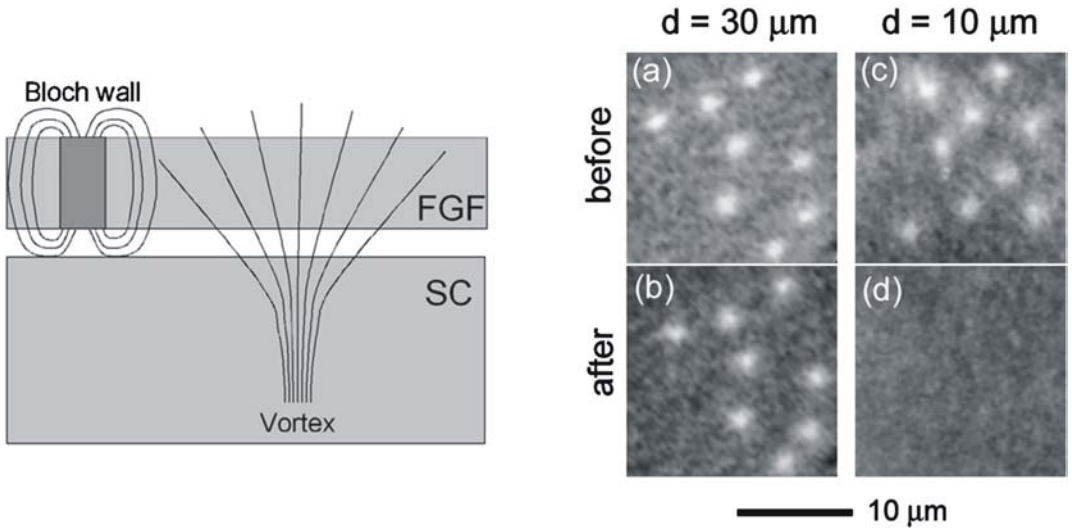

Figure 1.6: (left) Experimental procedure: A magnetic domain wall in a FGF is passed above a vortex in a superconducting sample. The interaction between the two can cause the vortex to move if the interaction force is large enough. (right) Results for two samples with different thicknesses. In the d=30 μm sample, only small changes in the vortex positions are observed from before (a) and after (b) a pass of the domain wall. In the d=10 μm sample, all initial vortices (c) are swept away with one pass of the domain wall (d). Taken from [9].

bismuth doped ferrite garnet film (FGF) 0.14 μm thick, which was brought very close to the surface of a 30 μm and 10 μm thick cleaved $NbSe_2$ single crystal. A movable Bloch domain wall was used to study the interaction with the SC vortices. The displacement field of the DW was B=0.1 mT. Magneto-optical imaging was employed to study the vortex structures present within the SC layer. The principle of the experiment is summarized in Figure 1.6 (left panel). The results of the study are presented in Figure 1.6 (right panel). In the "before" images 1.6(a) and (c) the vortex structure is present within the SC layer. After the DW is displaced above the studied area of the d=30 μm thick SC, only a slight, few microns, displacement of the vortices is noticeable. This means that the force acting between the DW and the SC vortices, f_w, is smaller than the intrinsic vortex pinning force, f_p. Since the total pinning force decreases with the decreasing the sample thickness, a lower f_p is expected for the 10 μm thick SC crystal. As it can be observed from Figures 1.6 (c) and (d) after the DW is passed over the selected area, no vortices are any longer visible. This situation corresponds to $f_w > f_p$. In conclusion this study clearly demonstrates that DW within FM layers can act as effective pinning centers for SC vortices as the DW-vortex interaction force surpasses the intrinsic pinning one.

As far as HTS materials are concerned, the studies that have been performed on FM/SC bi-layer hybrid structures also confirmed the additional pinning force provided by the FM layer. Zhang *et al.* [10] studied a $Pr_{0.67}Sr_{0.33}MnO_3$ (PSMO) and a YBCO heterostructure in order to identify the influence of a FM manganite on the YBCO pinning characteristics. Doped rare earth manganites are a well known class of materials that exhibit, for optimum

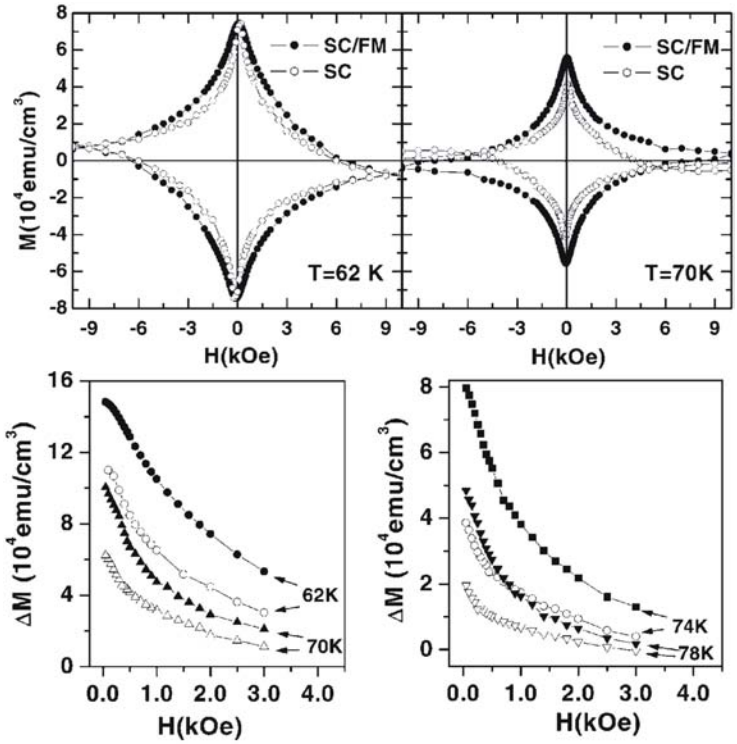

Figure 1.7: (upper panel) Hysteresis loops for both samples obtained at 62K and 70 K, respectively. The applied field is perpendicular to the film plane. (lower panel) Field-dependent ΔM extracted from the hysteresis loops obtained at different temperatures for the YBCO single layer (open symbols) and the YBCO/PSMO bilayer (solid symbols). Taken from [10].

divalent ion (Sr, Ca, Ba) doping regimes $x \approx 0.33$, ferromagnetism and metallic conductivity in the HTS critical temperature range. This fact doubled by an excellent lattice parameter match with YBCO, recommend these materials as ideal candidates for FM/SC studies. As it will be shown in a later Chapter of the present thesis, the magnetic anisotropy of manganites is highly controllable and can be tuned to vary from out-of-plane uniaxial to four-fold in-plane, as a function of the lattice strain. In their choice of the substrate, $SrTiO_3$ (STO), Zhang *et al.* stabilized for the PSMO layer an in-plane anisotropy. In Figure 1.7 (top panel) the $M(H)$ curves of the FM/SC bilayer and of the SC reference layer are shown at 62 K and 70 K. Also in the irreversible magnetization part ΔM is extracted, Figure 1.7 (bottom panel), at different temperatures close to 77 K, in order to give a measure of J_c ($\Delta M \propto J_c$). It can clearly be seen that the presence of the FM layer provides effective pinning of the vortices present in the YBCO layer, as at every temperature studied $\Delta M_{FM/SC} > \Delta M_{FM}$. Since the magnetization of the PSMO layer is confined to an in-plane direction because of the magnetic anisotropy, the question that arises is which component of the magnetization provides magnetic vortex pinning. The authors pointed out that this effect might come from the out-of-plane component of the magnetization present within the domain walls. It is important to notice that magnetic pinning is still effective even at high temperatures where thermal fluctuations are expected to surpass the pinning potential barrier.

In accordance with the predictions made by Bulaevskii *et al.* [24], that a FM film with perpendicular anisotropy produces an important flux pinning in the SC layer, Jan *et al.* [11] fabricated a FM/SC heterostructure in which the FM layer was comprised of 0.9 nm Pt/0.2 nm Co alterantions that were deposited on top of a 180 nm and 500 nm thick YBCO layers grown on (001) $LaAlO_3$ (LAO) single crystal substrates. A 1.5 nm Pt spacer layer was intercalated in the SC/FM sequence. The MFM image of the CoPt multilayer is shown in Figure 1.8(left panel). The typical maze-like pattern with high contrast between domains of opposite polarity is observed, characteristic for films that have an out-of-plane anisotropy.

The out-of-plane coercive field is ∼600 Oe. The middle panel shows the $J_c(B)$ dependence for all the samples studied. The measurements were performed at 86 K. The difference between the J_c for the YBCO films with and without the top CoPt structure at 75 K and 86 K as a function of the perpendicularly applied magnetic field is plotted in Figure 1.8 (right panel). The results on magnetic pinning of the YBCO vortices may be summarized as follows: first, the enhancement of J_c is higher at 86 K than at 75 K, indicating that intrinsic pinning is still dominant over magnetic pinning at lower temperatures. Secondly, the "boost" in J_c is most significant for fields between -600 Oe and 600 Oe, with a maximum at 0 Oe, while it decreases for the higher field range. Taking into account the coercive field value of the FM layer, we see that for larger field values, when some of the domains expand, while others shrink, the domain contribution to magnetic pinning diminishes. Also, a higher J_c value is observed for the thinner 180 nm sample than for the 500 nm thick one. This is explained by a greater penetration of the magnetic field in the thinner films, giving rise to an enhanced magnetic pinning. Lastly, an important observation is that at 86 K the magnitude of the critical current density is ∼10 times lower than the predicted one. The explanation comes from the random DW pattern which facilitates the vortex movement along domain boundaries. From this perspective a highly ordered stripe domain structure, as the one present in Py films, shown in Figure 1.3a, is bound to produce a more effective pinning due to its anisotropic nature.

Alternative FM layers have been considered for magnetic pinning applications of YBCO thin films. One of these consists of $BaFe_{12}O_{19}$(BFO), barium hexaferite. This compound has a hexagonal lattice and, when grown epitaxially, it stabilizes an uniaxial out-of-plane magnetic anisotropy. Also, the lattice is excellently matched to the YBCO lattice and also to ZrO_2-Y_2O_3(YSZ), yttria-stabilized zirconia, a well established buffer layer material for YBCO film growth on different substrates. These two characteristics, crystal lattice match and out-of-plane anisotropy, offer the possibility to use BFO thin films to provide magnetic pinning sites for YBCO layers. Garcia-Santiago *et al.* [12] fabricated a FM/SC heterostructure consisting of a YSZ (001) substrate upon which a BFO/YSZ/YBCO sequence was grown. The BFO layers were 100 nm and 80 nm thick, while for the YBCO layer the thickness was chosen as 100 nm, respectively. From field cooled (FC) and zero field cooled

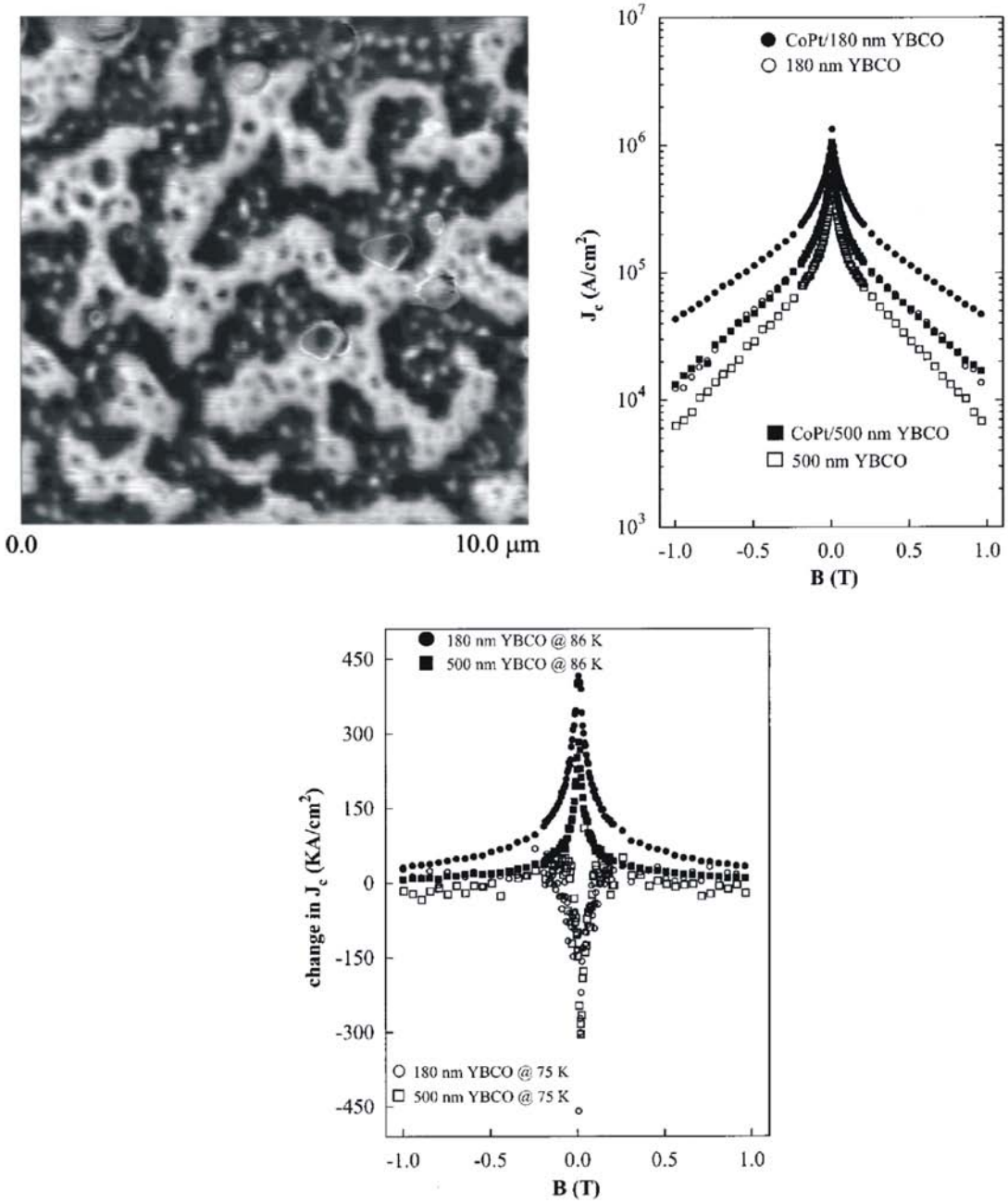

Figure 1.8: (left) MFM image of a multilayer CoPt on YBCO, showing maze-like domain structure with uniaxial perpendicular magnetic anisotropy; (center) J_c vs. $B||c$ transport measurements for 500 and 180 nm YBCO films at 86 K with and without CoPt multilayer applied; (right) Difference of J_c (with and without CoPt layer applied) vs. $B||c$ transport measurements for 500 and 180 nm YBCO films at 75 and 86 K. Taken from [11].

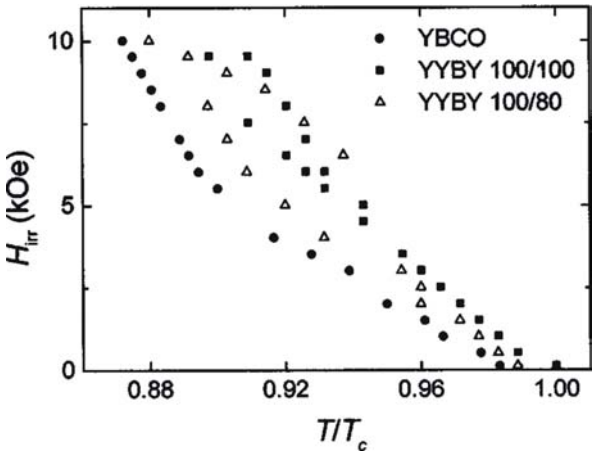

Figure 1.9: Irreversibility lines (in a reduced temperature representation) extracted from ZFCFC data for samples YBCO (solid circles), YYBY 100/100 (solid squares), and YYBY 100/80 (open triangles). Taken from [12].

(ZFC) magnetization curves performed below the superconducting critical temperature, the irreversibility line (IL) of the YBCO layer was deduced. The meaning of the irreversibility line is discussed in the Appendix. The result is presented in Figure 1.9 for the FM/SC structures, as well as for a reference YBCO film. It can be observed that for the bi-layers the ILs are shifted upwards with respect to the reference YBCO film. This is an indication that the the pinning is more intense in the bi-layers. Again, the reason for the additional pinning resides in the presence of the perpendicular magnetic structure with stripe-like domains.

1.3 Magnetic flux pinning in SC/FM structures with periodic arrays of FM micro,- and nanostructures

A particularly relevant topic in the study of SC/FM structures is the case in which the FM component of the system is comprised of regular arrays of micro,- or nanostructures. Besides the practical aspect of magnetic flux pinning, these type of systems offer the possibility to study collective phenomena related to the periodicity of the magnetic arrays, the so called *commensurability* effects, as well as the superconducting *vortex-antivortex* pair generation [13]. Although the wealth of results concerning this topic, both theoretical and experimental are overwhelming, we will limit our discussion to only a few cases that are most important for the main topic of the present thesis, magnetic pinning of superconducting vortices.

In the case of a magnetic dipole-superconducting vortex system, Carneiro [28] expressed the interaction free energy term as being

$$G_{int} = -\frac{1}{2}\mathbf{m}_0 \cdot \mathbf{B}_m(\mathbf{R}_d) - \mathbf{m}_0 \cdot \mathbf{B}_v(\mathbf{R}_d), \tag{1.13}$$

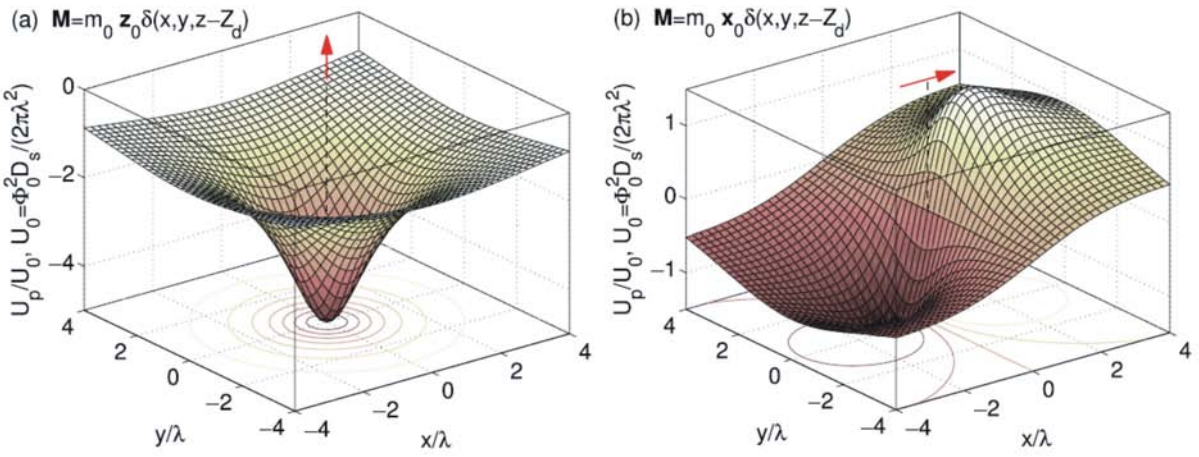

Figure 1.10: The spatial dependence of the energy of a single vortex in a field of point magnetic dipole: (a) vertically magnetized and (b) horizontally magnetized. Taken from [13].

where the first term is the interaction term between the magnetic moment of the dipole, $\mathbf{m}_0$, and the magnetic field at the dipole's site, $\mathbf{R}_d$, produced by the superconducting screening currents, $\mathbf{B}_m$. On the other hand, the second term accounts for the vortex and magnetic dipole interaction, which in turn consists of two terms: one which is due to the interaction between the circulating supercurrents of the vortex and the magnetic moment of the dipole, and the other due to the magnetic stray field of the vortex and the dipole. Both contributions are found to be equal and represent half of the second energy term in 1.13. The first term, due to the Meissner currents induced in the superconductor, is always positive and thus gives rise to a repulsive force between the SC and the FM dipole. This interaction term is responsible for the well known magnetic levitation phenomenon. The other part of the energy represents the actual pinning energy, denoted by the authors as U_p. An expression was calculated by Carneiro [28] for the angular dependence of U_p for two cases: one in which the magnetic moment of a point dipole is considered to be oriented out-of-plane, and another for which the moment was considered to lay in the in-plane direction, with respect to the SC film surface. The results are shown in Figure 1.10. It can be seen that in the case of a perpendicular magnetic moment the interaction with a SC vortex is purely of an attractive nature, while for an in-plane magnetic moment, the interaction is both attractive and repulsive, depending on the position of the vortex. However, it is clear that in both cases magnetic pinning is feasible.

By their own claim, Martin *et al.* [15] were the first to study the pinning interaction between the vortex lattice and a periodic array of submicrometric magnetic dots. Their experimental structure consisted of triangular lattice array of circular ferromagnetic dots (Fe or Ni), having a diameter of 200 nm, and a lattice constant that varied between d= 400 - 600 nm, Figure 1.11a. A thin superconducting Nb film having a thickness of 100 nm was deposited on top of the dots. Resistivity measurements were performed on the this

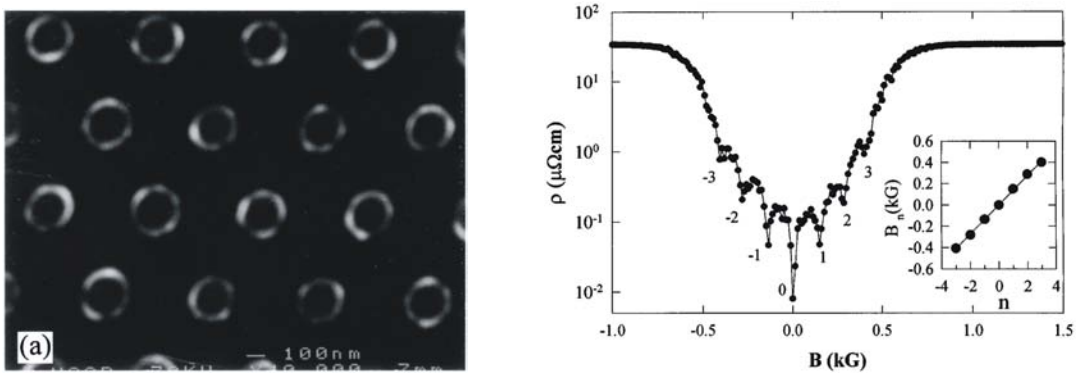

(a) **(b)**

Figure 1.11: (left) SEM image of a triangular array of Fe magnetic dots fabricated by e-beam lithography on a Si substrate. The lattice constant is d=600 nm and the Fe dots have a radius r=100 nm; (right) Field dependence of the resistivity of a Nb thin film with a triangular array of Ni dots (d=410 nm), measured at T=8.2 K and with J=2.5×10^4 A/cm^2. Inset shows the position of the minima B_n versus the index number n. The solid line is a fit to the expression $B_n = n\Delta B_0$ with ΔB_0=141±4 G. Taken from [15].

SC/FM structure at 8.2 K below the critical temperature of the Nb film. The results are shown in Figure 1.11b. It can be observed that the particularity of the $\rho(B)$ measurement, where B is the perpendicular applied field, is the existence of evenly spaced local minima, separated by a constant field spacing ΔB_0. It is well known (see Appendix) that the lattice parameter of the vortex lattice, in the case of a triangular lattice, is $a_0 = \left(\frac{4}{3}\right)^{1/4} (\Phi_0/B)^{1/2}$, where Φ_0 is the elemental flux quanta and B is the applied magnetic field. Upon calculating the vortex lattice spacing, a_0=413 nm±6 nm, the authors found excellent agreement with the lattice parameter of the magnetic dot array, d=410 nm±10 nm. The authors pointed out that this finding implies that the resistivity minima appear when there is an integer number of vortices per unit cell of the array of magnetic dots. When this situation occurs it is referred to as the two lattices (vortex and magnetic dot) being *commensurate*, hence the term *commensurability effects*. As far as the physical interpretation of the resistivity minima is concerned they are attributed to the pinning effect of the magnetic dots on the vortex motion. When the commensurability conditions are met, the pinning strength is maximum, so that vortex motion is impeded, reducing thus energy dissipation within the superconductor and thus an electrical resistivity drop. Within the same study also $\rho(B)$ curves were also recorded for several angles, θ, between the surface normal and the applied field. It was found that the field separation, $\Delta B_0(\theta)$, scales well with a $1/\cos(\theta)$ in the sense that $\Delta B_0(\theta) = \Delta B_0(0)/\cos(\theta)$. This proves that the relevant quantity for flux pinning is the perpendicular component of the field and, as a consequence, only the number of vortices/unit cell of periodic array is important.

Van Bael *et al.* [16] studied the influence of the magnetic configuration of Co rectangular

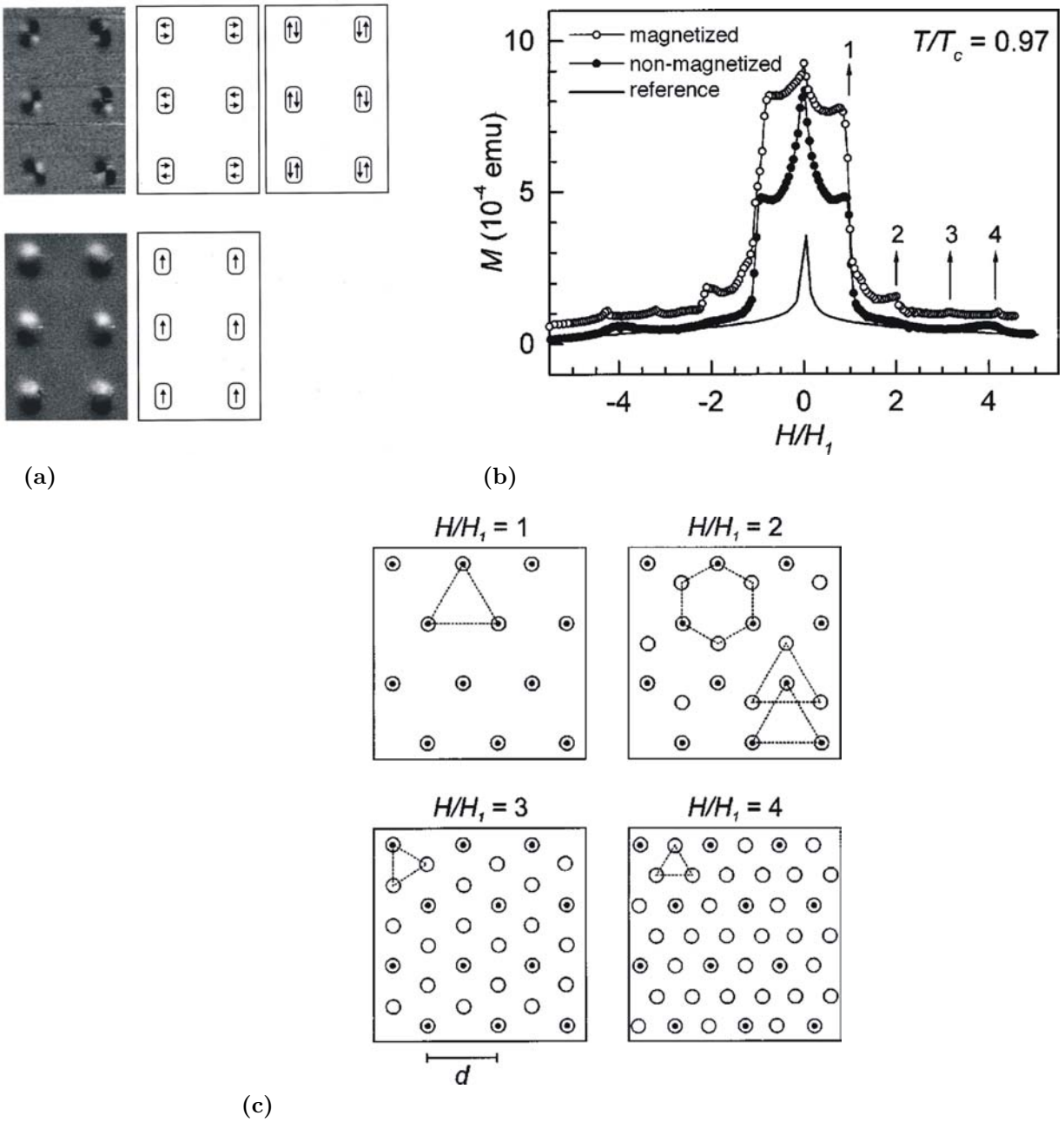

Figure 1.12: (a) (a) and (d) MFM images recorded at room temperature in zero field of a (2.7×4.0) μm^2 area of the island lattice, containing six magnetic islands. (a) shows the magnetic response of the islands before applying a magnetic field. The magnetic image of a similar area of the sample in the remanent state, after magnetic saturation in a magnetic field of 10 kOe pointing upwards, is given in (d). The suggested remanent magnetic domain configurations of the islands before and after magnetization are schematically presented in (b) and (c), and in (e), respectively. (b) Upper half of the magnetization loop M vs. H/H_1 at T/T_c=0.97, for a 500 ÅPb film on a triangular lattice of Au/Co/Au dots (period 1.5 μm) before (filled symbols) and after (open symbols) magnetizing the dots, and for a reference Pb (500 Å) film (line). (c)Schematic presentation of the stable vortex configurations (dots) at integer matching fields for a triangular lattice of pinning centers (open circles). Taken from [16].

nanostructures on the vortex pinning in a thin superconducting Pb film. The whole structure consisted of a Au(7.5 nm)/Co(20 nm)/Au(7.5 nm) sequence on top of which a 60 nm Pb film was deposited. The Co dots consisted of 360 nm × 540 nm rectangles. Their magnetic domain configuration was studied by MFM. Figure 1.12a shows two magnetic configurations that have been prepared for the magnetic pinning study. The first represents a demagnetized state with possible configurations of the magnetic moment schematically shown on the left. The other is the magnetized state in which the magnetic nanostructures are in the mono-domain state, represented on the left. $M(H)$ loops were performed in order to quantify the influence of the different magnetic states on the flux pinning characteristics of the dots on the Pb vortices. As a reminder, the amplitude of M is directly proportional to the critical current density, J_c, and thus to the flux pinning strength. The results are shown in Figure 1.12b and were measured close to $T_c = 7.2K$. In the case of the dipole configuration, the "magnetized" state there is evidence of strong pinning, and also of the afore mentioned commensurability effects. The spikes in the $M(H)$ curve correspond to integer multiples of the *matching field* H_1. The *matching fields* are the external magnetic fields for which the magnetic dot lattice and the vortex lattice are commensurate, Figure 1.12c. H_1 represents the field for which the dots and vortices are perfectly matched. The $M(H)$ measurement for the demagnetized state show a lower pinning strength, but still the commensurate M spikes appear. The difference between the two, besides the net magnetic moment, lies also in the stray field generated by the dots. Thus the difference between the two pinning potentials lies also in the contribution of the magnetic stray field to the overall magnetic flux pinning. The reference single Pb layer exhibits the lowest $M(H)$ signal, demonstrating thus the effectiveness of the magnetic interactions in determining high J_c superconducting films.

Magnetic dot arrays having perpendicular magnetization have also been studied. Van Bael *et al.* [17] prepared 400 nm $[\text{Co}(0.3\text{ nm})/\text{Pt}(1.1\text{ nm})]_{10}$ squares. A 10 nm Ge spacer layer was deposited on top of the FM structure to avoid any proximity effects on a 50 nm Pb (SC) film. Scanning Hall probe microscopy was employed in order to study the magnetic signal generated by the magnetic dots and SC vortices. Their study revealed that if $m > 0$ and $H > 0$, *i.e.* have the same polarity, the SC vortices are positioned at the dot sites. In contrast, if the two point in opposite directions, $m > 0$ and $H < 0$, the vortices are located in the dot interstitial sites. The two vortex configurations lead to different pinning characteristics. While in the case of a parallel configuration strong pinning is expected, in the antiparallel configuration a weaker interaction is expected since the vortices' positions are shifted towards the dot interstices. These assumptions, backed by energetic considerations, were confirmed by $M(H)$ measurements, Figure 1.13. Indeed, when the magnetization points outwards, $m > 0$, a high value of ΔM is registered in the positive H range, while it is rather small for negative H. On the contrary, for $m < 0$, strong pinning is detected for negative values of H, while weaker pinning corresponds to positive values of the external field. Similar

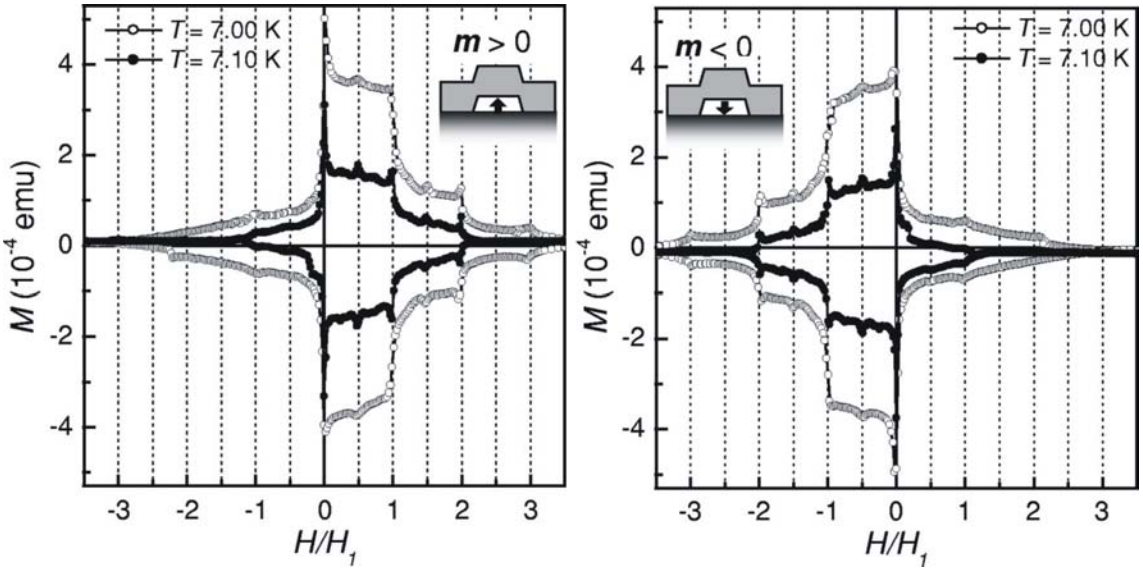

Figure 1.13: $M(H/H_1)$ magnetization curves at different temperatures near T_c (7.00 K open symbols, 7.10 K filled symbols) showing the superconducting response of the Pb layer on top of the Co/Pt dot array with all dots aligned in a positive (left panel) and negative (right panel) sense. H_1=20.68 Oe is the first matching field. Taken from [17].

results were obtained by Lange *et al.* [27] and were presented in the previous Section.

As far as HTS materials are concerned, the results on magnetic pinning using arrays of magnetic dots are not nearly as many or as detailed as in the case of low T_c thin films. Yeh *et al.* [18] performed both numerical calculations as well as experimental studies on arrays of Ni dots deposited on top of YBCO thin films. In their calculations they used material constants of the two. The calculations were also performed under a matching field condition, in the sense that they considered that to each magnetic dot there is a corresponding SC vortex. The interaction force is taken to be the force that acts on the magnetization of a dot, by the magnetic field created by the vortex. The result of the simulation is presented in Figure 1.14a where the interaction, pinning, force is given as a function of the lattice parameter of the triangular lattice of magnetic dots. The results indicate that the interaction force is zero if the vortex lies underneath the center of the magnetic dot, while the attraction, pinning, force is at a maximum when the vortex is placed at the edge of the dot. In the middle point between to magnetic elements, the force is zero, while it becomes repulsive if the mid-point is passed since the vortex is attracted by the adjacent dot. The authors argue that the force curve presented in the top panel is an idealization and that it is subjected to decrease due to factors such as imperfect lithographic process on the dots or modifications on the magnetic material parameters due to lateral structuring. Also, temperature plays an important role as the coherence length within the superconductor increases with increasing temperature. The effect of a higher coherence length is illustrated in Figure 1.14a (bottom panel). As a conclusion of their theoretical approach the authors predict that close to T_c the magnetic

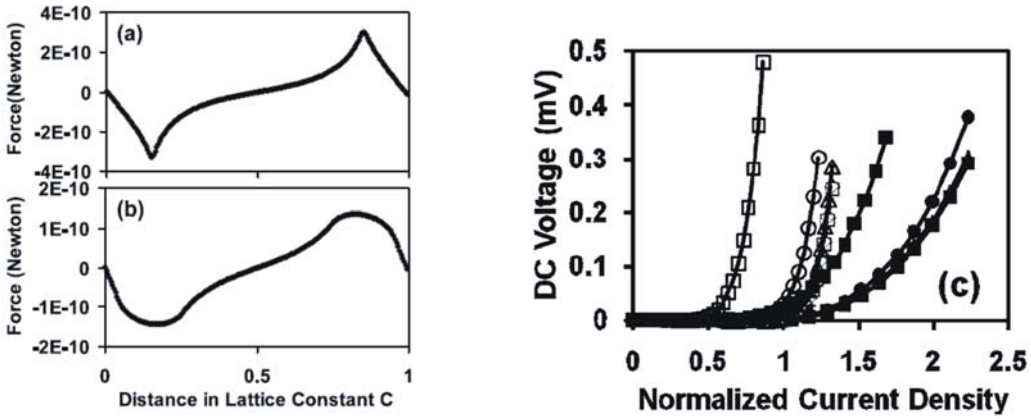

(a) **(b)**

Figure 1.14: (a) Pinning forces calculated for (a) $\xi = 2$ nm and (b) $\xi = 30$ nm. (b) IV curves under various fields for the reference sample (open symbols) and for the sample with magnetic dots grown on top (solid symbols). The measurements were performed at T_c-5.5 K. Taken from [18].

pinning force and the normal, core, pinning force might have the same amplitude.

For the experimental part of the study, a special technique was employed in order to deposit the magnetic nano structures on the thin YBCO SC film. This technique uses a so-called nanochannel glass (NCG), which is a material having hollow cylinders of ≈30 nm in diameter, form a hexagonal lattice with a lattice constant between 400-625 nm, in order to transfer a regular array of dots onto a substrate. In the present case NCG was used to deposit ordered Ni dots on top of the YBCO film. A reference single YBCO film was also grown for comparison. The evaluation of the magnetic pinning strength was performed by tracing $I - V$ curves on the two samples at different temperatures. Since the T_c of the two YBCO films was different, measurements were performed at fixed temperature intervals lower than the respective critical temperatures. Figure 1.14b shows the $I - V$ characteristic of the two samples at 5.5 K below T_c, in order to avoid differences related to th existence of different T_c values, at three different field values. It can be observed that all the curves corresponding to the sample having Ni dots on top (solid symbols) are shifted towards higher values of the current. This situation corresponds to a higher pinning strength exerted by the magnetic dots on the vortices. The shift may be understood as follows: for small currents passing through the SC layer the Lorentz force is low so that no vortices begin to flow, so that the voltage drop is zero. As soon as the current increases to a point in which the Lorentz force is strong enough to depin the vortices, a voltage drop is registered. In consequence, the higher the current for voltage onset the higher the pinning force and the critical current density. With respect to the case at hand, at all temperatures the measurements were performed, improved pinning forces were observed in the sample with FM dots over the simple SC layer. Even though commensurability phenomena have not been observed, the study shows that

even for HTS thin films, periodic arrays of magnetic particles lead to an enhancement of the pinning potential and as a consequence of J_c.

1.4 Résumé de chapitre en français

Le chapitre introduit les phénomènes d'ancrage magnétique des vortex dans les supraconducteurs de type II. Le mouvement des vortex dans ce type de supraconducteurs implique la dissipation de l'énergie. Ainsi, l'ancrage des vortex représente une nécessité impérative en vue des applications potentielles pour le transport d'énergie sans perte. Typiquement, deux types d'ancrage sont utilisés: intrinsèque ou topologique, par des défauts artificiellement introduites dans la structure cristalline du supraconducteur, et plus récemment, extrinsèque via des champs magnétiques localisés générés par des nanostructures magnétiques. Ce deuxième type d'ancrage est particulièrement intéressant car il est indépendant de la température. Cela est possible dans la mesure où l'aimantation, ainsi que l'intensité du champ de fuite généré par un nano-objet constitué d'un matériau avec une température de Curie bien supérieure à la témpérature critique du supraconducteur, resteront quasiment constantes dans l'intervalle de température où le supraconducteur sera utilisé.

Dans la première partie du chapitre on explique la limitation de l'ancrage topologique dont l'efficacité tend vers zéro lorsque la température se rapproche de la témpérature critique Tc du supraconducteur. Par la suite, on explique l'intérêt de l'ancrage magnétique en exemplifiant le cas particulier d'une nanostructure magnétique de type bande perpendiculaire (*perpendicular stripe*), pour laquelle dans une fenêtre en température autour de Tc les propriétés magnétiques et micromagnétiques sont pratiquement constantes.

L'ensemble du chapitre présente une analyse bibliographique à jour (state of the art) dans le domaine de l'ancrage magnétique des vortex dans les supraconducteurs de type II. Deux classes des structures de type système ferromagnétique (FM)/supraconducteur (SC) sont analysés. Dans la première classe, le film ferromagnétique FM est continu et les nanostructures magnétiques sont représentées par des modulations périodiques de l'aimantation sous forme de bandes alternées à aimantation perpendiculaire. La deuxième classe des structures FM/SC implique des nanostructures magnétiques obtenues par la réduction de la taille latérale à partir d'un film magnétique continu, en utilisant des techniques de lithographie.

Le deuxième paragraphe du chapitre introduit les concepts de base nécessaires à la compréhension des phénomènes de dissipation de l'énergie liée au mouvement des vortex dans un supraconducteur. Nous montrons que le mouvement de flux des vortex dans le SC de type II peut être assimilé à une résistivité et ainsi qu'une loi de type Ohm pourra être écrite.

Le paragraphe suivant présente des exemples de la littérature sur l'ancrage des vortex dans des structures bicouche de type SC/FM. La couche FM est continue et elle comporte

des modulations périodiques de l'aimantation par des structures de type bandes magnétiques perpendiculaires (*i.e.* structure de type weak-stripe dans le cas du Permalloy). Les premiers deux exemples présentés sont basés sur des films SC de type II à basse température critique: $NbSe_2$ et MoGe. Par l'analyse électrique de la densité de courant critique ces études démontrent clairement l'efficacité de l'ancrage magnétique. Le courant critique augmente dans une échelle logarithmique lorsque les bandes magnétiques sont orientées parallèlement à la direction du courant électrique dans la bande supraconductrice. Ceci démontre que le mouvement des vortex, sous l'influence d'une force de type Lorenz perpendiculaire à la direction du courant, est bloqué par la modulation périodique de l'aimantation parallèle à la direction du courant. l'ancrage des vortex se réalise par le champ de fuite perpendiculaire à la surface du film généré par les parois de domaine qui séparent deux domaines adjacents d'aimantation *up-down*.

Une autre étude utilise comme système magnétique l'alternance multicouche $(Co/Pt)_n$ et le Pb comme couche supraconductrice. L'analyse du courant critique est faite par des mesures magnétiques de type $M(H)$ en utilisant par la suite le modèle de Bean. L'influence directe des parois des domaines sur les vortex dans le SC a été analysé dans une structure de type ferrite de Bi/NbSe2. En déplaçant par un champ magnétique externe une paroi de type Bloch on observe l'influence directe sur le mouvement des vortex dans les SC. L'analyse bibliographique effectuée et présentée dans ce chapitre montre que relativement peu d'études ont été réalisées sur des systèmes à base de supraconducteurs à haute température. L'un des rares exemples trouvé dans la littérature montre, via une analyse magnétique (cycles d'hystérésis), les effets d'ancrage dans une bicouche $Pr_{0.67}Sr_{0.33}MnO_3$/YBCO. Un autre exemple discute des résultats similaires observés dans des structures de type $(Co/Pt)_n$/YBCO ou l'ancrage magnétique des vortex est démontré par des mesures électriques. Un dernier exemple présenté dans ce paragraphe du chapitre illustre les résultats obtenus pour un système complexe de type ($BaFe_{12}O_{19}$/ZrO_2-Y_2O_3)/YBCO. Par une analyse magnétique de type Field Cooled-Zero Field Cooled (FC-ZFC) les auteurs de l'étude déduisent la ligne d'irréversibilité du supraconducteur et démontrent que l'ancrage des vortex dans les structures bicouches étudiées est bien plus efficace que dans une couche d'YBCO unique. Ils expliquent ces résultats par l'influence directe du champ de fuite perpendiculaire dans les structures magnétiques utilisés (de type perpendicular stripe).

Le quatrième paragraphe du premier chapitre introduit le concept de l'ancrage magnétique dans des structures de type SC/FM constitués par des réseaux d'objets ferromagnétiques micro et nano-structurés. On montre que l'effet d'un dipôle magnétique sur un vortex supraconducteur est double. Une première composante de l'interaction dipôle-vortex est de type répulsif. Ceci explique le phénomène bien connu de la lévitation. Une deuxième composante de l'interaction est de type attractif et d'un point de vue analytique a une forme très similaire à celle qui donne l'interaction entre une pointe MFM (Magnetic Force Microscopy) et

un champ de fuite généré par la nanostructure mesurée. Cette interaction attractive sera responsable de l'ancrage magnétique d'un vortex par le dipôle magnétique.

Après cette analyse phénoménologique, le paragraphe présente des exemples issus de la littérature avec des études concernant l'interaction entre un réseau des vortex SC et un réseau périodique des nanostructures magnétiques (réseau triangulaire de nano-objets circulaires de Fe et Ni). L'intérêt majeur pour ce type de structure réside dans le fait que le paramètre de réseau des vortex SC peut être modulé par le champ magnétique externe. Ainsi, une situation toute particulière apparaît lorsque ce paramètre devient commensurable avec le paramètre de réseau des nanostructures magnétiques. Les mesures de résistivité électrique effectuées dans des systèmes de type Nb/nanostructures Fe et Ni montrent les effets de commensurabilité entre les deux réseaux via des minima locaux de la résistivité en fonction du champ. Lorsque les deux réseaux sont commensurables, l'efficacité de l'ancrage magnétique sera maximale donc la résistivité de flux-flow du SC minimale. Dans la même étude, une analyse angulaire de la résistivité démontre encore une fois clairement que la quantité importante pour l'ancrage magnétique est la composante perpendiculaire du champ de fuite. D'autres analyses similaires présentées dans ce chapitre ont étés effectuées dans des systèmes de type (Au/Co/Au)/Pb, où les effets d'ancrage magnétique ont étés démontrés par une étude corrélée MFM (Magnetic Force Microscopy) - $M(H)$. Par la suite, dans des structures de type $(Co/Pt)_n$/Pb, des mesures de microscopie Hall à balayage ont été utilisées pour extraire les signaux magnétiques générés par les structures magnétiques et les vortex et montrer ainsi leur interaction réciproque et les effets d'ancrage magnétique.

Comme pour les systèmes SC/FM à base de films FM continus, l'analyse bibliographique démontre que le nombre d'études impliquant des supraconducteurs à haute température reste pour l'instant relativement limité. Toutefois, nous présentons quelques exemples trouvés dans la littérature. Un premier exemple comporte des réseaux de Ni sur YBCO. Dans ces systèmes, les mesures expérimentales ont été confrontées avec des calculs micromagnétiques. Même si les effets de commensurabilité du réseau magnétique et celui des vortex SC n'ont pas été démontrés, les résultats de l'analyse démontrent clairement l'augmentation du potentiel d'ancrage par le réseau magnétique périodique.

Bibliography

[1] T. P. Orlando and K. A. Delin, *Foundations of Applied Superconductivity*, Addison-Wesley (1991);

[2] L. N. Bulaevskii, E. M. Chudnovsky and P. M. Maley, *Magnetic pinning in superconductorferromagnet multilayers* Appl. Phys. Lett. **76**, 2594 (2000);

[3] L. Civale, A. D. Marwick, T. K. Worthington, M. A. Kirk, J. R. Thompson, L. Krusin-Elbaum, Y. Sun, J. R. Clem, and F. Holtzberg, *Vortex confinement by columnar defects in $YBa_2Cu_30_7$ crystals: Enhanced pinning at high fields and temperatures* Phys. Rev. Lett. **67**, 648 (1991);

[4] A. Augieri, G. Celentano, V. Galluzzi, A. Mancini, A. Rufoloni, A. Vannozzi, A. Angrisani Armenio, T. Petrisor, L. Ciontea, S. Rubanov, E. Silva and N. Pompeo, *Pinning analyses on epitaxial $YBa_2Cu_3O_{7-\delta}$ films with $BaZrO_3$ inclusions* J. Appl. Phys. **108**, 063906 (2010);

[5] V. Vlasko-Vlasov, U. Welp, G. Karapetrov, V. Novosad, D. Rosenmann, M. Iavarone, A. Belkin and W.-K. Kwok, *Guiding superconducting vortices with magnetic domain walls* Phys. Rev. B **77**, 134518 (2008);

[6] A. Belkin, V. Novosad, M. Iavarone, J. Pearson, and G. Karapetrov, *Superconductor/ferromagnet bilayers: Influence of magnetic domain structure on vortex dynamics* Phys. Rev. B **77**, 180506(R) (2008);

[7] A. Belkin, V. Novosad, M. Iavarone, J. Fedor, J. E. Pearson, A. Petrean-Troncalli, and G. Karapetrov, *Tunable transport in magnetically coupled MoGe/Permalloy hybrids* Appl. Phys. Lett. **93**, 072510 (2008);

[8] M. Lange, M. J. Van Bael, V. V. Moshchalkov, and Y. Bruynseraede, *Magnetic-domain-controlled vortex pinning in a superconductor/ferromagnet bilayer* Appl. Phys. Lett. **81**, 322 (2002);

[9] P. E. Goa, H. Hauglin, Å. A. F. Olsen, D. Shantsev, and T. H. Johansen, *Manipulation of vortices by magnetic domain walls* Appl. Phys. Lett. **82**, 79 (2003);

[10] X. X. Zhang, G. H. Wen, R. K. Zheng, G. C. Xiong, and G. J. Lian, *Enhanced flux pinning in a high-T_c superconducting film by a ferromagnetic buffer layer* Europhys. Lett. **56(1)**, 119 (2001);

[11] D. B. Jan, J. Y. Coulter, M. E. Hawley, L. N. Bulaevskii, M. P. Maley, Q. X. Jia, B. B. Maranville, F. Hellman, and X. Q. Pan, *Flux pinning enhancement in ferromagnetic and superconducting thin-film multilayers* Appl. Phys. Lett **82**, 778 (2003);

[12] A. García-Santiago, F. Sánchez, M. Varela, and J. Tejada, *Enhanced pinning in a magnetic-superconducting bilayer* Appl. Phys. Lett. **77**, 2900 (2000);

[13] A. Yu Aladyshkin, A. V. Silhanek, W. Gillijns, and V. V. Moshchalkov, *Nucleation of superconductivity and vortex matter in superconductorferromagnet hybrids* Supercond. Sci. Technol. **22**, 053001 (2009);

[14] G. Carneiro, *Pinning and creation of vortices in superconducting films by a magnetic dipole* Phys. Rev. B **69**, 214504 (2004);

[15] J. I. Martín, M. Vélez, J. Nogués, and Ivan K. Schuller, Flux Pinning in a Superconductor by an Array of Submicrometer Magnetic Dots Phys. Rev. Lett. **79**, 1929 (1997);

[16] M. J. Van Bael, K. Temst, V. V. Moshchalkov, and Y. Bruynseraede, *Magnetic properties of submicron Co islands and their use as artificial pinning centers* Phys. Rev. B **59**, 14674 (1999);

[17] M. J. Van Bael, M. Lange, S. Raedts, V. V. Moshchalkov, A. N. Grigorenko and S. J. Bending, *Local visualization of asymmetric flux pinning by magnetic dots with perpendicular magnetization* Phys. Rev. B **68**, 014509 (2003);

[18] Bo Cheng, Tony Ragsdale, and W.J. Yeh, *Interaction between the Ferromagnetic Dots and Vortices: Numerical Calculation and Experimental Results* J. Supercond. Nov. Magn. **21**, 289 (2008);

[19] A. A. Abrikosov, *On the Magnetic Properties of Superconductors of the Second Group*, Sov. Phys. JTEP **5**, 1174 (1957).

Chapter 2

Experimental Methods

2.1 Thin Film Deposition

2.1.1 DC Magnetron Sputtering

One of the techniques that were used for thin film deposition was the DC magnetron sputtering technique [1]. The working principle behind this method is the creation of a plasma and the acceleration of the ions in the plasma towards a cathode, called target, made from the material one wishes to be deposited onto the substrate. The accelerated ions transfer their kinetic energy upon impact, to the atoms forming the target, resulting in the phenomena known as sputtering, which consists in the ejection of the target atoms with a certain kinetic energy. This process in not chemically selective, in the sense, for example, thermal evaporation is, as it is a process that does not occur at thermodynamic equilibrium. However, selectivity manifests itself in the different sputtering yields of the different atoms composing the target, i.e. the ratio of the number of target atoms ejected from the target to the number of ions incident on the target. The sputtered atoms are adsorbed on the substrate surface, leading to film growth. In the case of DC sputtering, the plasma is created applying a high voltage in a region in space, called the dark space, in which low pressure gas is present. Typically, the gas pressure is situated in the mTorr range. Because the target is negatively polarized, gas ions, commonly Ar^+, are accelerated towards the target. Besides sputtering, other processes take place at the target surface depending on the ionic energy, such as ionic implantation, secondary electron emission or ion retro-reflection, Figure 2.1b. Secondary electron emission is a phenomenon that is crucial to the plasma formation. Secondary electrons in their path collide with atoms in the gas filling the evaporation chamber. If the electron energy is higher than the ionization energy of the atoms, ions are formed, which will consequently be accelerated towards the target, while the resulting electrons are free to participate in other collision processes. If, on the contrary, the electron energy is lower than the ionization energy, during collision the transferred energy

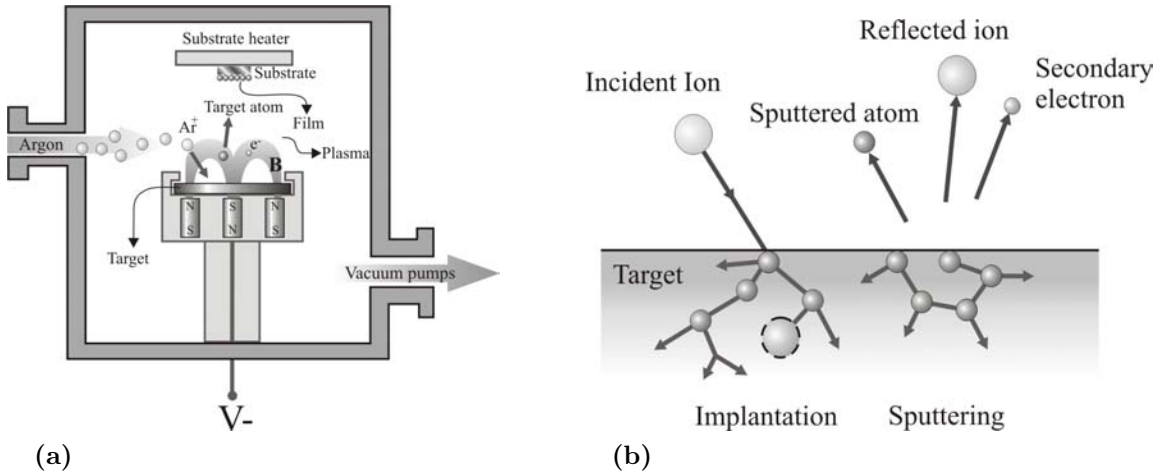

Figure 2.1: (a)Principle of operation of a DC magnetron sputtering deposition system; (b) Processes that occur at the target surface (Taken from [1]).

will cause the electrons in the atom to jump on a high energy level, and then through relaxation go back on the initial state. The latter is usually an optical transition, i.e. the emitted photons have the energies corresponding to frequencies in the visible domain, and is responsible for the characteristic color of the plasma. Because the sputtering yield is very low, film growth rate in a classic DC sputtering set-up is very low. In order to increase the deposition rate, a series of methods were developed in order to increase plasma density and obtain more efficient sputtering. Among these, probably the most used is the magnetron sputtering set-up Figure 2.1a. This method uses electron precession in a magnetic field to increase their path length allowing them to participate in more collision processes and thus producing more Ar^+ ions and a higher density plasma, which will produce higher sputtering yields. The plasma density obtained by magnetron sputtering is of 0.03% as opposed to 0.0001% in a classic configuration. Also, the use of magnetron sputtering, allows for the use of lower gas pressures, between 0.01-1mTorr.

2.1.2 Pulsed Laser Deposition

Pulsed laser deposition (PLD) is a deposition technique that has evolved in close relation with the advances in the domain of oxide thin films growth, in general, and of high temperature superconducting thin film deposition in particular [2]. Pulsed laser deposition consists of directing a pulsed laser towards a target made of the material one wishes to deposit. The result is the ablation of small portions of the target, when appropriate laser energy density is achieved. The central feature of PLD is the so called *plume*. The plume is a result of the laser-target interaction and consists of a mixture of the atomic species ejected from the target. The plasma observed at the target surface is a consequence of laser absorption by the expelled atoms. The thin film deposition process by the PLD technique is summarized

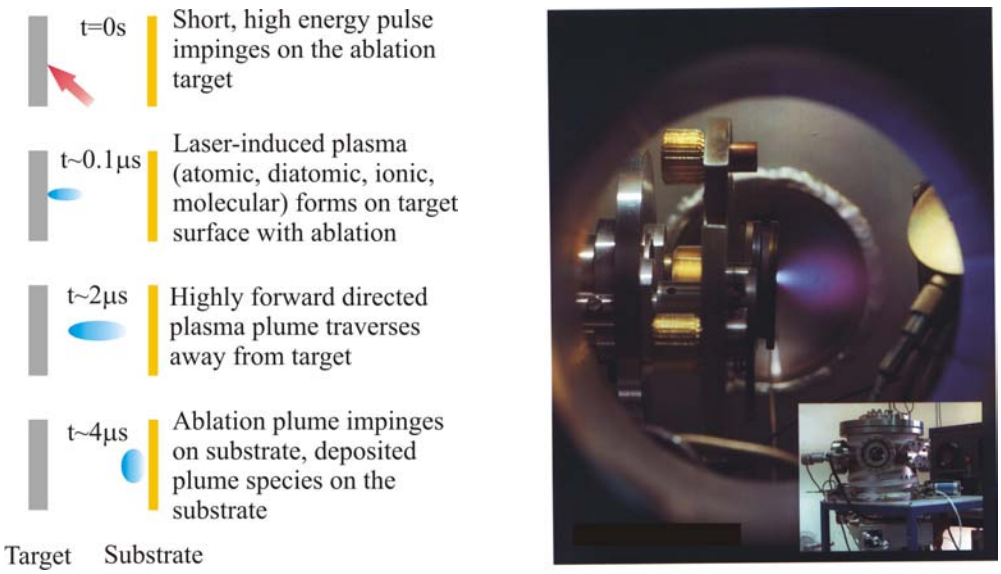

Figure 2.2: (a) Schematic presentation of the pulsed laser deposition technique (Taken from [2]), (b) PLD set-up used to grow the YBCO thin films (ENEA-Frascati).

in Figure 2.2a. The characteristic of this method, which recommends it to be the method of choice in the growth of multi-cationic thin films, is the ability to perform a stoichiometric transfer to the film of the target material. This is achieved by performing a non-equilibrium ablation of the target material. The non-equilibrium nature of the ablation is determined by the *laser fluence*, which is defined as the laser pulse energy/focal spot area. If the laser fluence is high enough as to overcome an ablation threshold, that is the energy of the pulse is higher than that needed for thermal evaporation, non-equilibrium ablation is attained. Also, in this process laser wavelength is important as it determines the absorption of the laser energy by the target.

We have used the PLD deposition method to grow $YBa_2Cu_3O_7$ (YBCO) thin films. The set-up was located at the ENEA-Frascati Laboratories in Italy, Figure 2.2b.

2.2 Photolithography and Ion Beam Etching

Optical lithography or photolithography is a microfabrication process in which a pattern imprinted on a mask, called photolitographic mask, is transfered to a substrate covered with a thin layer of photoreresistive material. This transfer is achieved by exposing the mask to radiation, which in turn impresses the corresponding regions of the photosensitive layer, as illustrated in Figure 2.3. The unexposed parts of the resist are then removed using a developing fluid. It is to be noted that the processes described above is valid when using a positive photoresist, otherwise, in the case of a negative photoresist, the exposed parts of

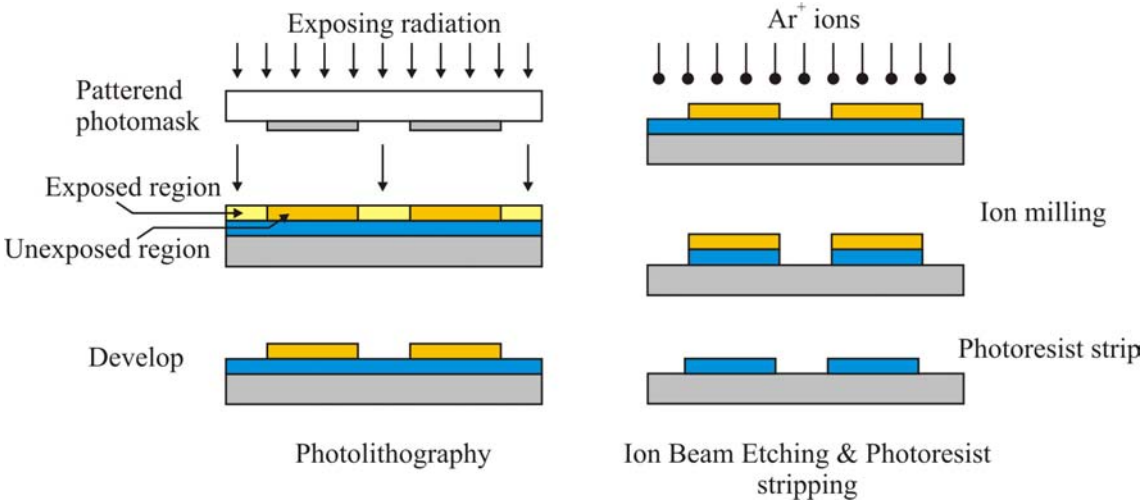

Figure 2.3: Schematic presentation of the photolithografic and ion beam etching processes (adapted from [3])

the resist are soluble and are removed by the developer. Also, in our case, resist is deposited on a substrate upon which we have already grown the films that we desire to structure. The next step of the lithographic process consists in actually defining the pattern onto the thin films. This can be achieved either by chemical route, or, as in our case by ion beam etching. Ion beam etching, illustrated in Figure 2.3, consists removing the film from the areas that are not covered by the resist, by accelerating Ar^+ ions toward the film. The ion remove parts of the film upon impact in by sputtering, a process descried in more detail, in Section 2.1, dedicated to thin film growth techniques.

As far as the hardware is concerned, we have used a SÜSS Microtech MJB4 Mask Aligner for photolithography, and a home-made ion beam etching set-up, equipped with a Kauffman ion gun. The sample holder in the ion beam etching chamber allowed for continuous rotation of the sample, around an axis perpendicular to it, so that it ensured uniform etching. The sample holder also permits for rotations so that the samples make a certain angle with respect to the ion trajectory, which allows for selective etching.

In the present thesis the masks were used to define the superconducting layer into stripes of well know geometrical dimensions, so that quantitative analysis of the electric transport related physical quantities, such as electrical resistivity, ρ, and critical current density, J_c, could be performed. Also photolithography was employed in order to structure magnetic dots on top of the superconducting stripes, so as to study the interaction between the magnetic structures and the vortices within the superconducting material. The design of the lithographic masks constituted a part of the present thesis. The mask drawings were performed with the aid of the Layout Editor software [4].

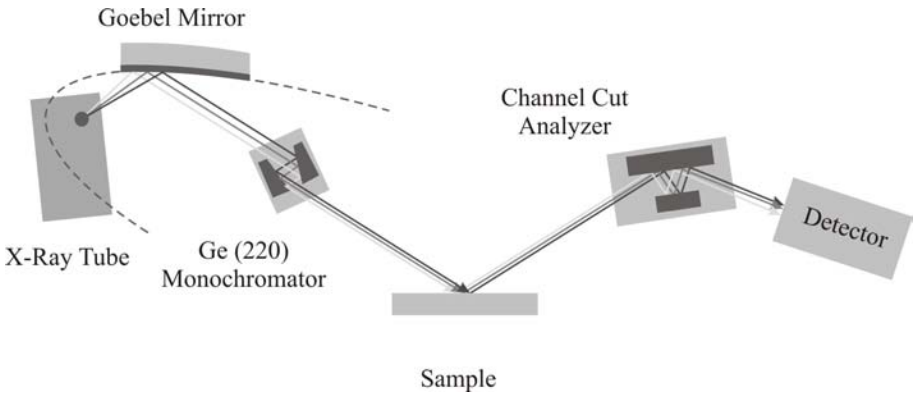

Figure 2.4: High resolution X-ray diffractometer (Adapted from [6]).

2.3 High Resolution X-Ray Diffraction

The present thesis is mainly focused on the growth and characterization of epitaxial thin films and epitaxial heterostructures. Epitaxial thin films represent thin films of high structural order, deposited on top of single crystal substrates. As in the case of x-ray diffraction measurements on powder, polycrystalline films, etc., structural information is extracted from the position, intensity and width of Bragg peaks. However, special optics need to be employed in order to measure epitaxial thin film system, as very closely spaced peaks, which appear in the diffraction pattern of epilayer-substrate systems, need to be resolved. X-ray diffraction in this configuration is referred to as high resolution X-ray diffraction (HRXRD). The precision $\Delta d/d$ by which interplanar spacings may be determined is given by [5]:

$$\frac{\Delta d}{d} = \frac{\Delta \lambda}{\lambda} + \frac{\delta}{\tan \theta}, \tag{2.1}$$

where $\Delta\lambda$ is the spectral width of the radiation and δ is the beam divergence. In order to attain low $\Delta d/d$ values X-ray diffraction optic elements are used. They are described in the following Section. The next Sections are dedicated to describing different types of measurements and the information that they provide on the structural characteristics of the epitaxial thin films.

2.3.1 HRXRD Diffractometer

For the X-ray diffraction measurements of our epitaxial thin films we have used a Bruker AXS D8 Discover diffractometer equipped with high resolution optic components. The high resolution configuration consisted of a Goebel mirror and a Ge monochromator, as tube optics, and a channel cut analyzer or a variable slit set-up on the detector. This configuration is schematically presented in Figure 2.4. The Goebel mirror [5], also known as laterally

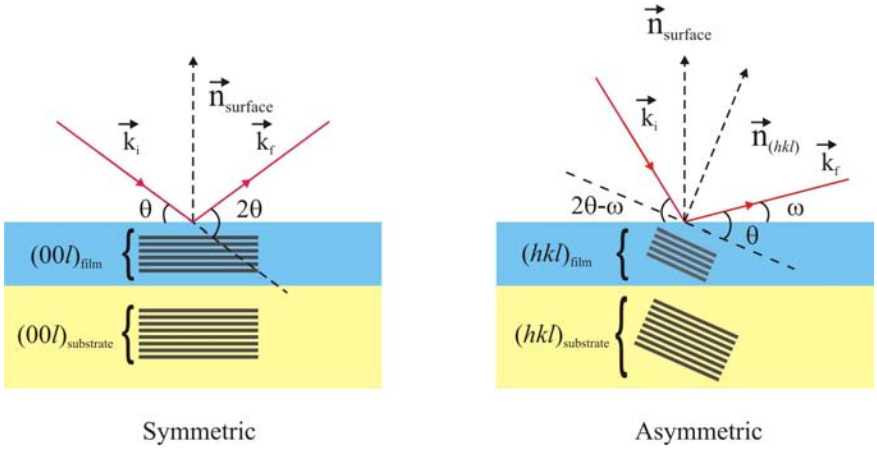

Figure 2.5: Symmetric (left) and asymmetric (right) X-ray diffraction measurements on epitaxial thin films.

graded multilayer mirror (LGMM) is an X-ray optics component designed for reduction of the beam divergence, δ. The device is constructed as an ellipse segment, having the X-ray tube in the ellipse focus. The mirror consists of an alternating multilayer structure, having the layer period adapted in such a way that the Bragg condition is fulfilled for all incidence angles of the divergent X-ray beam. In this way the beam exits the Goebel mirror as a parallel beam, with a divergence of only a few 0.01°. Next to the Goebel mirror a monochromator is mounted. In our case it consists of two Ge crystals, that are positioned in such a way that the beam exiting the mirror suffers a double reflection on them. Additionally, they are disposed in such a way that the incident angle is the Bragg angle of the (220) planes for the Cu Kα_1 wavelength. In this way the only wavelength exiting the monochromator is the one corresponding to Cu Kα_1, reducing thus the wavelength spread, $\Delta\lambda$ of the X-ray radiation. Additional filtering is also provided by the analyzer monochromator that functions under the same physical principles as the monochromator, with the only difference being that the scattered beam suffers a triple reflection on the Ge crystals.

2.3.2 Symmetric and asymmetric X-ray diffraction measurements

In the case of X-ray diffraction on epitaxial thin films, symmetrical $2\theta/\omega$ ($\omega \sim 2\theta/2$) permits to gain information regarding the distance between the planes that are perpendicular with respect to the surface normal of the single crystal substrate. Hence, considering the epitaxial relation between the film and the substrate, according to Bragg's diffraction law:

$$2d_{hkl} \sin\theta = n\lambda \tag{2.2}$$

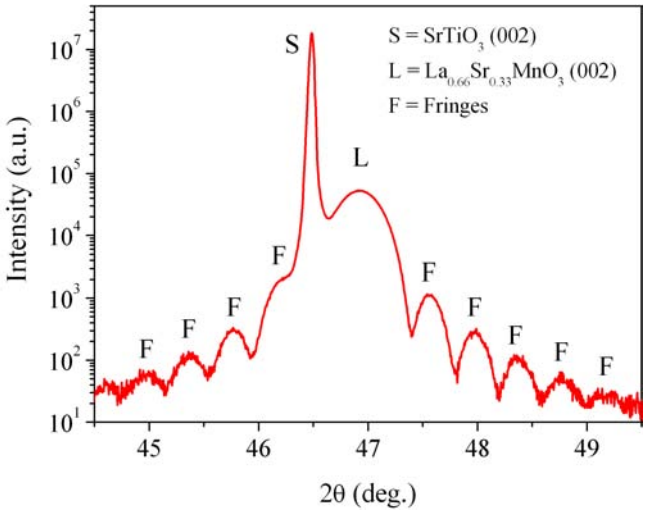

Figure 2.6: Symmetric $2\theta/\omega$ diffraction pattern around the (002) planes of a LSMO epitaxial thin film (L) and of the STO single crystal substrate (S). Additional diffraction fringes (F) may be observed (see text).

the distance d_{hkl} between the (hkl) planes can be determined. It can be observed that in the case of a $(00l)_{film}\|(00l)_{substrate}$ epitaxial relation, performing a symmetric measurement only gives access to the out-of-plane lattice parameter, as shown in Figure 2.5(left). In order to be able to measure the in-plane lattice parameters, asymmetrical measurements have to be performed, Figure 2.5(right). These consist in measurements in which $\omega \neq 2\theta/2$, around crystal planes that are not parallel with the substrate orientation, *e.g.* $(h0l)$, $(0kl)$ or (hkl). Even though Figure 2.5, refers to the situation where epitaxy is determined by $(00l)_{film}\|(00l)_{substrate}$, the principles of symmetric and asymmetric measurements can be applicable to any type of film-substrate epitaxial relation. However asymmetric measurements can be hindered by geometric factors, such as ω being less than zero, for the diffraction condition to be fulfilled. An example of a symmetric $2\theta/\omega$ scan performed with a diffractometer equipped with high resolution optics, as described in the previous paragraph, is shown in Figure 2.6. The measurement was performed around the (002) peak of a thin $La_{0.66}Sr_{0.33}MnO_3$ (LSMO) layer deposited on top of a $SrTiO_3$ (STO) (001) single crystal substrate. In this particular system $(001)_{film}\|(001)_{substrate}$. Besides the substrate and layer peaks, additional peaks may be observed. This fringing comes from the fact that the high structural quality of the films determines a Frauhoffer-like diffraction of the x-ray radiation, where the slit width is the actual film thickness. In this way, one is able to determine the film thickness from the angular spacing of two adjacent fringes. The fringing can only be observed if the density of crystalline disorder associated with dislocations, mosaicity, surface roughness, etc., is not too strong.

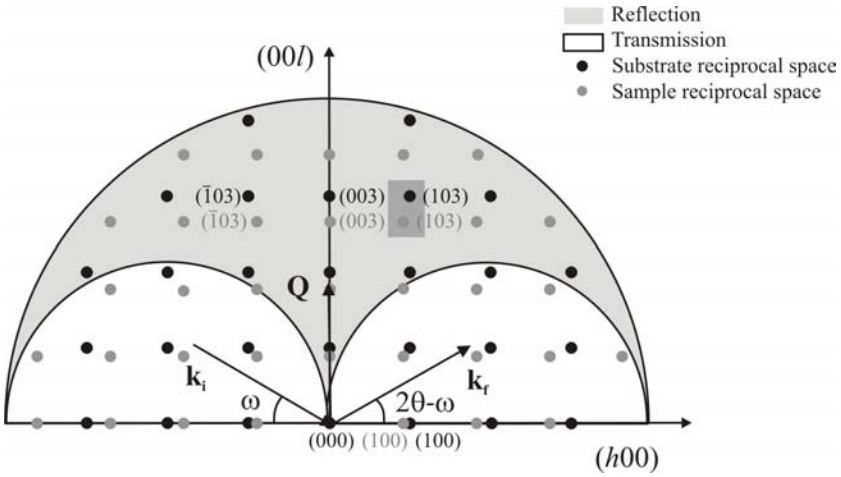

Figure 2.7: Reciprocal space of a single crystal substrate and an epitaxial film.

2.3.3 Reciprocal Space Mapping

Reciprocal Space Mapping is a high resolution X-ray diffraction measurement technique in which one measures an area of the reciprocal space, around certain Bragg reflections. This is achieved by a combination of ω and $2\theta/\omega$ (symmetric or asymmetric) scans. One can imagine diffraction measurements in the k-space, where k is the X-ray wave vector. The result of such a measurement is $\mathbf{Q}$=$\mathbf{k}_f$-$\mathbf{k}_i$. Because of this relation, k-space is also called Q-space or moment transfer space. The relation with the traditional ω and 2θ variables is given by

$$Q_x = k[\cos(\theta - \omega) - \cos(\theta + \omega)] \tag{2.3}$$

$$Q_z = k[\sin(\theta - \omega) + \sin(\theta + \omega)],$$

where x and z represent directions in the sample reference frame. If $\mathbf{Q}$ is a reciprocal space vector, then the Ewald selection rule is fulfilled, so that we would obtain diffraction on a certain crystal lattice plane family. In Figure 2.7 we have represented a fictitious reciprocal space of an epitaxial film (gray) superimposed on the substrate reciprocal space (black). The film growth is determined by the $(001)_{film} \| (001)_{substrate}$ relation. In a Reciprocal Space Mapping experiment one would measure an area of the reciprocal space, like the one represented by the dark gray rectangle of Figure 2.7. Since this kind of measurement is a combination of linear measurements, it provides simultaneous information on the lattice parameters of the substrate and film, the strain of the film and also on the texture, or mosaicity of the film.

X-ray reflection is limited for ω taking values between 0 and 2θ, light gray region in Figure 2.7. Outside these values, instead of reflection one would obtain a transmission of the X-rays through the sample, as the incident or exit beams would be situated below the

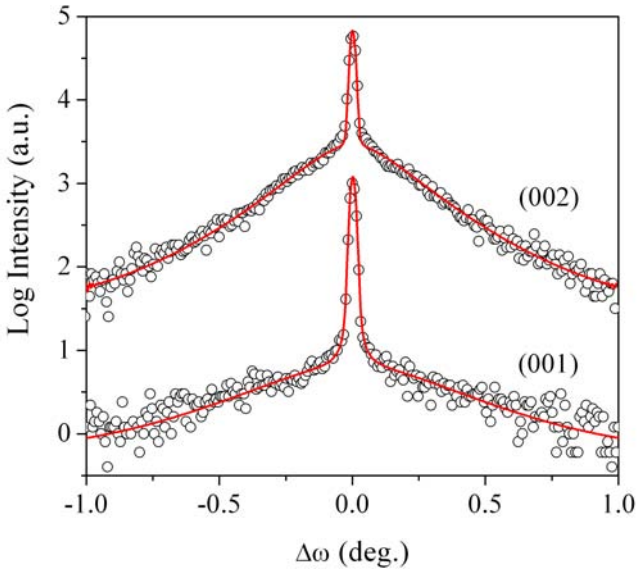

Figure 2.8: ω-scans (rocking curves) around the (001) and (002) peaks of epitaxial thin LSMO films deposited on STO(001) substrate (open circles) and the corresponding simulation (red line).

sample surface.

2.3.4 Epitaxial thin film texture characterization

Epitaxial thin films are formed of highly oriented crystallites. However, these crystallites have a slight misorientation both in the out-of-plane direction, as well as in-plane, which both determine the film's texture. The epitaxial quality of a thin film is reflected by the angular distribution of crystallites in the two afore mentioned directions. For each direction there is a specific measurement method which quantifies the respective angular distribution.

In the out-of plane direction the measurement of the angular distribution is done by performing the so-called "rocking curves", or ω-scans. This type of scan is done by positioning the tube and detector at an angle 2θ, corresponding to the plane family parallel to the film surface, and then measuring the intensity varying ω, around the θ value. In this way one is really measuring the out-of-plane angle distribution of the crystallites of the film. Usually, the parameter that describes the epitaxial quality is the FWHM of the obtained distribution. An interesting feature, observed in many epitaxial thin film, systems is the two-component rocking curve, as the ones presented in Figure 2.8. As it can be seen the peak exhibits a profile comprised of a narrow, high intensity component corresponding to the coherent scattering part of the radiation, and a broad, low intensity component, corresponding to a diffuse scattering part. The presence of the diffuse scattering component stems from the existence of distorted regions, of limited spatial extension, in the films. These regions are situated around defects such as dislocations, grain boundaries, chemical inhomogeneities, etc. The

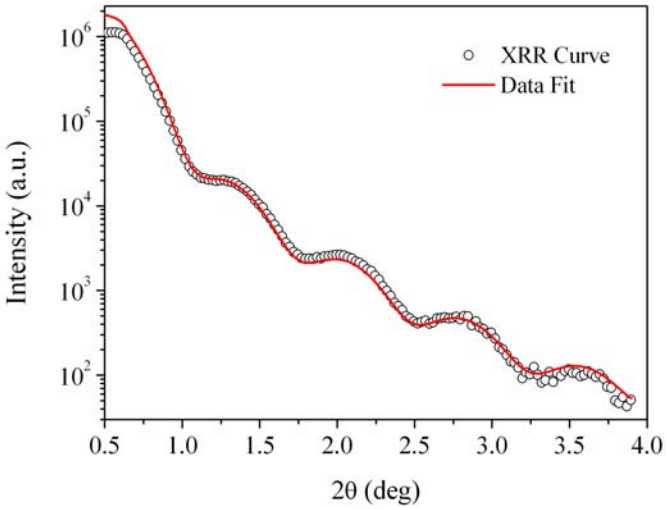

Figure 2.9: X-ray reflectometry measurement on a LSMO epitaxial thin film deposited on a STO(001).

coherent part originates from the long-range order, inherent in high-quality crystalline structures. Quantitative information regarding the spatial and statistical properties of the strain field, as well as regarding the in-plane coherence length, "crystallite" size, can be deduced from the numerical simulation of such ω-scans [7]. With respect to the in-plane distribution of crystallites, ϕ-scans (not shown here) are used to describe their angular distribution in this direction. As in the case of ω scans, this measurement is performed by setting the 2θ angle to a plane, that in this case corresponds to a plane that is not parallel to the film surface, but also has an in-plane component. Besides the in-plane angular distribution, performing such kind of scans on both the film and substrate, provides also the epitaxial relation between the two.

2.3.5 X-Ray Reflectometry (XRR)

X Ray Reflectometry is an non-destructive technique that allows the investigation of thin films in relation to their thickness, composition and roughness. It consists of performing an X-ray reflection experiment around the total reflection angle, also called the critical angle. A typical XRR measurement is shown in Figure 2.9, performed on a thin layer of LSMO deposited on an STO substrate. As it can be seen for angles that are smaller than the critical angle the intensity of the reflected radiation is maximum as one would expect since there is no refraction in the film. As the critical angle is surpassed, the intensity decreases as refraction occurs. The typical features of an XRR measurement are the fringes visible at low 2θ angles. The origin of the fringes stems from the interference of the radiation reflected from the film and the radiation that is reflected from the substrate, at the film-substrate interface. The condition for a constructive interference between the two is that the difference

in optical path of the two rays be an integer of λ. This requirement is the analogous of the Bragg relation, where the distance between the crystal planes, in case of the latter is replaced by the thickness of the film in the case of the former. Thus, from the distance between two consecutive intensity maxima, one can calculate the film thickness accordingly. Also, it can be noticed that the critical reflection angle is dependent on the material of the thin film. This is due to the fact that the refraction index, n, is material dependent, and more specifically is dependent on the material density and the electronic density. The critical reflection angle and the refraction index are connected by Snell's law. In this sense, XRR is considered to be a technique that may be used for compositional studies, through the measurement of the critical reflection angle. As far as thin film and interface morphology characterization are concerned, the overall intensity decay of the reflected X-ray radiation is related to the surface roughness through dispersion. Roughness, understood as large deviations of the film surface normal on a lateral scale of a few nanometers, leads to the dispersion of the reflected radiation which in turn leads to a more rapid decay of the radiation intensity as a function of the incidence angle. Fitting of the XRR measurements on the deposited films, in order to extract quantitative information about the film thickness and morphology, was performed using the LEPTOS software.

2.4 Atomic Force Microscopy

Atomic force microscopy is a very powerful technique used to provide quantitative information about the surface topography of thin films. The principle behind this technique is to use the forces that act between a small probe and the studied surface, when the two are very close or in contact with each other, in order to trace the topography of the surface. In practice this is achieved using an experimental set-up that is summarized in Figure 2.10a. The simplest operation mode of an AFM is the so-called contact mode, in which the probe, *i.e.* tip, is brought into contact with the sample surface and, by means of piezoelectric drives, it is moved in the x-y, surface in-plane direction. As the tip moves, it is deflected, together with the cantilever, by surface irregularities. The deflection amplitude, which is in fact a profile line of the surface, is measured by a reflecting a laser beam from the cantilever into a set of four photodiodes. The topographic information is thus transformed into an electric signal, which is in turn used to recreate a surface image on a display, providing at the same time information for the feedback loop controlling the tip movement. Although simple, the contact operation mode has some drawbacks. Because the tip and surface are in contact, this may lead to the damaging of the tip, creating artifacts and degrading image resolution. Also, the surfaces that have been exposed to air tend to form a thin layer of water and other contaminants on top. An AFM tip touching the contaminated surface will cause the formation of a water meniscus. The surface tension thus created provides an additional force

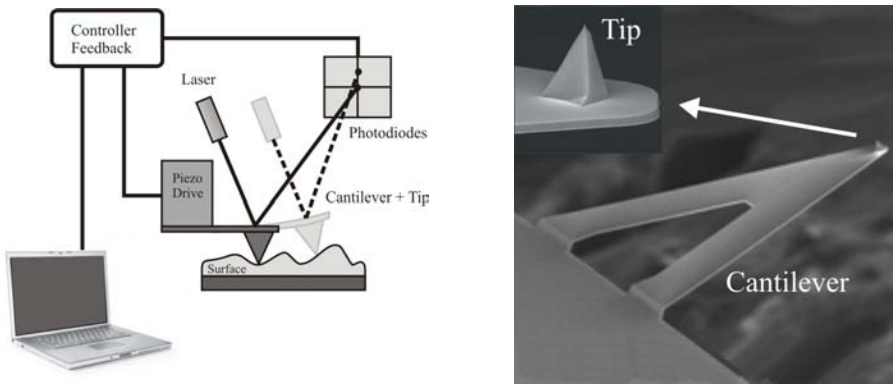

(a) **(b)**

Figure 2.10: (a) Principle of operation of an AFM; (b) Cantilever and tip.

that influences the deflection of the tip, and thus the out-come of the AFM measurement.

To prevent tip and sample damage, but most importantly to increase image resolution and provide the possibility of imaging fluid surfaces, the dynamic modes of AFM were developed. As opposed to the static, *i.e.* contact mode, in the dynamic regime the cantilever is oscillated at, or near the resonance frequency. The oscillation parameters of the cantilever are then used to provide topographical information about the surface. Depending on the parameters used to provide for the feedback loop there are two separate dynamic modes: amplitude modulated mode (AM-AFM) and frequency modulated mode (FM-AFM). Besides the difference in the feedback parameters there is another fundamental difference between the two modes, which consists in the region of the Lennard-Jones potential in which they operate. The Lennard-Jones potential is tip-surface interaction potential as a function of the distance between the two. It is composed of two terms: a repulsive and an attractive component. The repulsive interaction is of short range and stems from the Pauli repulsion as the electronic orbitals of the tip and surface overlap. The attractive long range interaction is due to the Van der Waals forces which are a sum of dipolar interaction forces, the most common of which being the London dispersion force, which is the interaction between instantaneous, self-polarized, dipoles [8]. It is quite clear that in the static, contact regime, the AFM operates in the repulsive branch of the interaction potential, corresponding to very small separation of the tip and surface. The amplitude modulated mode is also known as intermittent contact mode or the Tapping mode. The name comes from the fact that the cantilever oscillates above the sample and then lowered until it comes into contact with the surface, experiencing thus only intermittent contact with it. Consequently, this mode operates both in repulsive and attractive branches of the potential. As the tip is lowered its oscillation amplitude is reduced. During the operation the controller acts as to maintain the oscillation amplitude constant. In the frequency modulated mode, or the non-contact mode, the tip oscillates at a certain height above the surface, experiencing only the attractive van der Waals forces. The presence

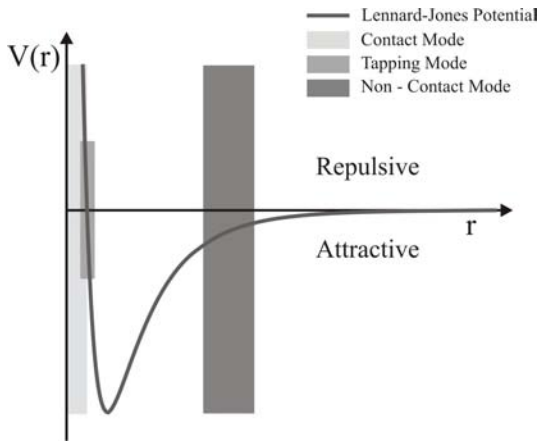

Figure 2.11: Lennard-Jones interaction potential.

of the interaction potential produces shifts in the resonance frequency of the cantilever. In this mode, the controller is set to maintain a constant oscillation frequency. The non-contact mode is operated in vacuum and it's the method that produces routinely atomic resolution images. However, the most common techniques for thin film surface investigations are the Contact and Tapping modes. Throughout the present thesis the AFM images were obtained in the contact or Tapping mode, unless specified otherwise.

2.4.1 Magnetic Force Microscopy

Depending on the nature of the tip and the surface under investigation, the principles of the AFM can be used to probe other forces that appear between the two, besides the van der Waals forces. Such forces include electric, magnetic or friction forces, and they give rise to additional modes of AFM operation. When dealing with magnetic thin films, one can have access to the magnetic domain structure by performing AFM measurements using a tip that has a magnetic coating and measuring the magnetic interaction force between the magnetization of the tip and the stray field of the domains within the film. This AFM mode bears the name of Magnetic Force Microscopy, MFM. The operation of the MFM is summarized in Figure 2.12a. First, the tip traces the topography of the surface (1) and then it is raised at a certain distance above the sample (2), retracing the same line scan, (3). As it is shown in Figure 2.12b, van der Waals forces are short range, while magnetic interaction is long range, so in order to eliminate the van der Waals component of the tip sample interaction, the tip is raised above the surface where only the magnetic force is present. Finally, the tip is then lowered (4) to proceed to the next line scan.

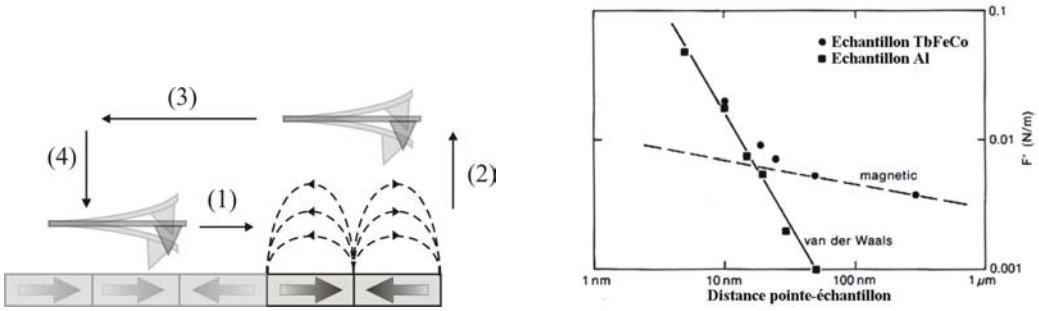

Figure 2.12: (a) Principle of operation of an MFM in the Interleave mode, adapted from [9]; (b) Magnetic and Van der Waals forces as a function of the tip-sample distance. Taken from [10].

2.5 X-Ray Photoelectron Spectroscopy

X-ray photoelectron spectroscopy (XPS) is an analysis technique which allows for the qualitative and quantitative determination of the electronic structure of materials. The physical phenomenon that lies behind this technique is photoemission. Essentially, photoemission is the process in which electrons are emitted from a bulk material after absorbing the energy of photons of an incident radiation beam, represented by X-rays, in the case of the XPS. This phenomena is described, from the conservation of energy point of view, by the Einstein equation:

$$h\nu = E^1_{kin} + \phi_S + E^F_B(k), \tag{2.4}$$

where ϕ_S represents the sample work function, $h\nu$ the incident photon energy, which for most of the XPS systems lies in the 1-10 keV region. E^1_{kin} is the photoelectron kinetic energy and $E^F_B(k)$ is the binding energy of the electron. The binding energy is given by Koopman's theorem as

$$E^F_B(k) = E^f_{tot} - E^i_{tot} \tag{2.5}$$

That is to say, the binding energy represents the difference between the system in the initial state and the energy of the system in the final state, which has one electron less. Since every chemical element has a unique electronic structure, the electrons will be emitted having specific kinetic energies. In photoelectron spectroscopy, one analyzes the kinetic energy of the emitted electrons, from which the binding energy spectrum of the electrons is determined. The determination of the binding energy from the corresponding kinetic energies of the expelled electrons is schematically presented in Figure 3.37. In the case of solid samples, as was the case for our thin film structures, electrical contact is made between the sample and the spectrometer. This ensures that the sample and spectrometer are in thermodynamic equilibrium, so that the electrochemical potentials or Fermi levels are equal [11]. An electron

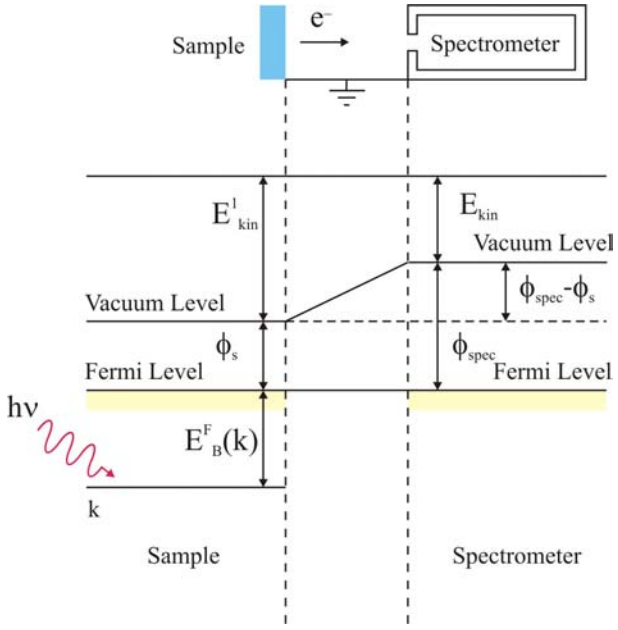

Figure 2.13: Energetic representation of the XPS operation principle. Adapted from [11].

having E^1_{kin} at the sample surface, passing to the spectrometer will feel a potential energy difference of $\phi_{spec} - \phi_S$, Figure 3.37. Hence, the spectrometer will measure a different kinetic energy, E_{kin}, given by the expression

$$E_{kin} = E^1_{kin} + (\phi_S - \phi_{spec}) \tag{2.6}$$

Substituting the above relation in Equations 2.4 and 2.5 will yield the binding energy as a function only of the kinetic energy measured by the spectrometer and the spectrometer work function, which eliminates the need of knowing the sample work function:

$$h\nu = E^F_B(k) + E_{kin} + \phi_{spec} \tag{2.7}$$

From the obtained binding energy spectrum one can determine quantitatively the chemical composition [12], $C_i(\%)$, with an accuracy of approximately 0.5 at.%. This is achieved by determining the normalized area of each peak, which is the actual area of the peak divided by correction factors, as in the expression below

$$Normalized\ Area = \frac{Area\ of\ Photoemission\ Peak}{Relative\ Sensitivity \times Transmission\ Function} \tag{2.8}$$

$$C_i(\%) = \frac{Normalized\ Area_i}{\sum_{i=1}^{N} Normalized\ Area_i} \tag{2.9}$$

The actual concentration is the ratio between the normalized area of the peak corresponding to a certain element and the sum of all the normalized areas of the rest of the measured peaks. From a qualitative point of view, an XPS analysis can also give information on the chemical state of the ions within a sample, hybridization or the chemical environment around a certain ion. This is achieved due to the existence of binding energy shifts, the so called chemical shifts. The effect consists of a modification of the electronic structure, and thus of electronic binding energies, of an ion when, for example, it participates in a chemical bond. The bond rearranges the electrons, thus modifying the Coulomb interaction among electrons and between the electrons and nuclei, changing their respective energies. This results in a shift of the energies of the electrons, *i.e.* chemical shift. Since the shift is sensitive to its particular cause, one can evidence for example oxidation within the sample or other chemical state variations.

2.6 Vibrating Sample Magnetometry

Vibrating Sample Magnetometer is an instrument used for measuring the magnetic properties of samples, and its operating principle is based on the electromagnetic induction principle, as described by the Lenz law. From the experimental point of view, the magnetic sample one wishes to characterize is placed between the poles of an electromagnet, as shown in Figure 2.14a. The sample is mounted at the end of a quartz or plastic rod, which in turn is fixed on a vibrator head. The vibrator is used in order to induce in the sample a periodic, vertical movement. As the sample vibrates a magnetic flux variation is created,

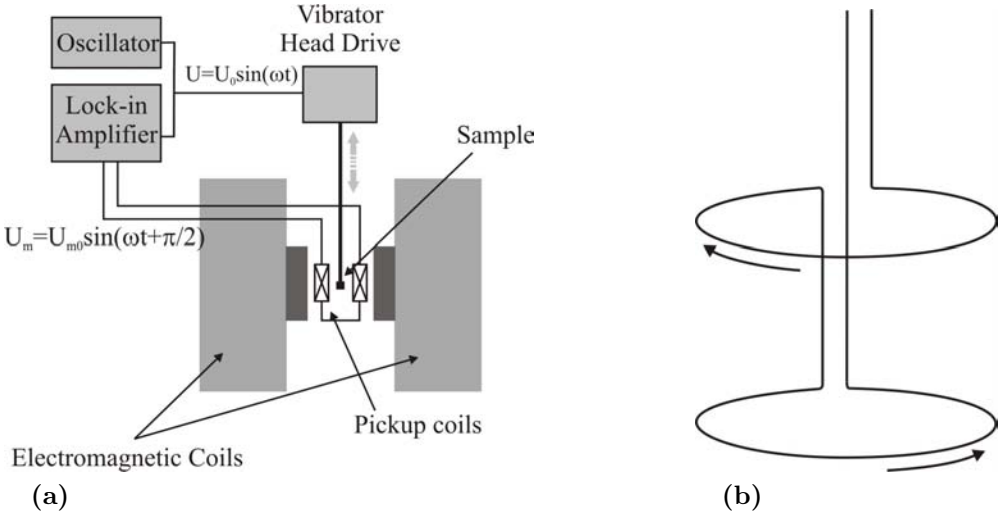

Figure 2.14: Principle of operation of a VSM (a) and (b) schematic view of a first order gradiometer.

which induces a voltage on the coils, called pick-up coils, placed in the vicinity of the sample.

As the sample is vibrating with the frequency set by the vibrator, ν, the flux is oscillating with the same frequency, which results in an induced voltage which is $\pi/2$ out of phase with respect to ν. A lock-in amplifier is used to measure only this signal, $\pi/2$ out of phase with a reference signal, the signal of the vibrating head. The induced signal is proportional with the sample's magnetic moment. In order to establish a link between the magnetic moment and the induced voltage, a calibration is required to be performed on a known sample, which is typically a Ni sphere. An additional feature of the pick-up coils is that they are connected in a 1^{st} order gradiometer configuration, Figure 2.14b so as to eliminate any parasitic voltage signals induced by electromagnetic noise.

2.7 SQUID Magnetometry

The Superconducting Quantum Interference Device, or SQUID, is the most sensitive up to date magnetic sensors, achieving resolutions of several fT. The high resolution makes the SQUID the sensor of choice when dealing with magnetic systems with low magnetic moment, such as thin films. The principle of operation of such a device is based on two features of the superconducting state. One is flux quantization and the other is the electrical characteristics of Josephson junctions (tunnel junctions having superconducting electrodes). The characteristics of the Josephson junctions, Figure 2.15, are given by the so called Josephson relations, which give the expressions for the current passing through and voltage across such a junction:

$$j = J_c \sin\varphi \tag{2.10}$$

$$v = \frac{\hbar}{2e}\frac{\partial\varphi}{\partial t}.$$

In the above expressions, φ is the phase difference of the superconducting wave function across the junction, while J_c is the critical current density of the junction. Flux quantization is a phenomenon that appears when a superconducting ring is placed inside a magnetic field. It can be shown that the magnetic flux inside the ring takes only integer values of Φ_0, a quantity know as the fundamental flux quanta. In other words:

$$\Phi = n\frac{h}{2e} = n\Phi_0. \tag{2.11}$$

When placed inside a magnetic field, the phase variation of the superconducting wave function across a Josephson junction, interrupting a superconducting ring, is given by the expression:

$$2\pi n = 2\pi\frac{\Phi}{\Phi_0} - \varphi, \tag{2.12}$$

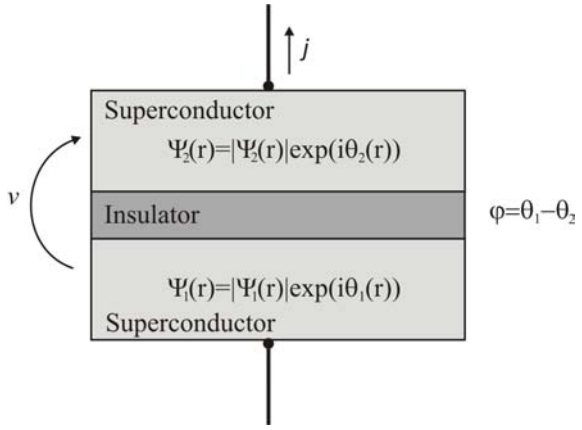

Figure 2.15: Schematic representation of a Josephson junction

where Φ is the magnetic flux within the ring. Taking into consideration the above expressions, one can arrive to the Josephson expression for the current, when the junction is under the influence of an external magnetic field, namely:

$$j = J_c \sin(2\pi \frac{\Phi}{\Phi_0}) \tag{2.13}$$

The SQUID configuration which will be dealt with in this section is the so called DC-SQUID. Such a device consists of two parallel Josephson junctions, a and b, as presented in Figure 2.16a. The external magnetic field, which is to be determined, creates a magnetic flux, which in turn, similarly to the expression presented earlier, leads to a phase shift in the two junctions, equal to:

$$\varphi_a - \varphi_b = 2\pi \frac{\Phi}{\Phi_0} \tag{2.14}$$

The total current passing through the device is given by:

$$I = I_1 + I_2 = I_a \sin(\varphi_a) + I_b \sin(\varphi_b) = I_a \sin(\varphi_a) + I_b \sin(\varphi_a - 2\pi \frac{\Phi}{\Phi_0}) \tag{2.15}$$

The total magnetic flux through the ring in Figure 2.16a, is given by the sum of the external magnetic flux and the flux created by the screening current, i

$$\Phi = \Phi_{ext} + Li \tag{2.16}$$

Considering that the inductance L, of the loop is small, we find that the flux is given just by the external magnetic field component, Φ_{ext}, simplifying greatly the further analysis of the device. For a given external magnetic flux, the maximum of the current through the device

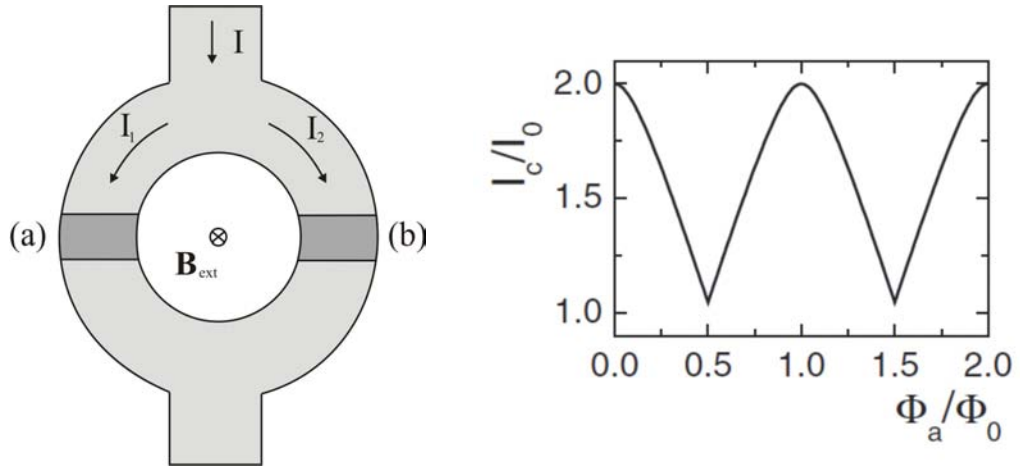

(a) (b)

Figure 2.16: (a) Schematic representation of a DC SQUID (Adapted from [13]); (b) Maximum current through a DC SQUID as a function of the external magnetic flux (Taken from [13]).

is obtained for a phase difference of

$$\varphi_a = \frac{\pi}{2} - \frac{\pi\Phi_{ext}}{\Phi_0} \tag{2.17}$$

This value yields a value of maximum current of

$$I = I_a|\cos(\frac{\Phi_{ext}}{\Phi_0})| \tag{2.18}$$

where we have considered a symmetric configuration in which $I_a = I_b$. This law, presented in Figure 2.16b, is at the core of the DC SQUID field sensing mechanism, linking the external flux of the external magnetic field, which is to be measured, to the current passing through the device.

Besides the SQUID sensor itself, commercial SQUID devices, Figure 2.17, include a so called flux transformer. The flux transformer consists of two connected superconducting coils, one for signal pickup and one for coupling the signal to the SQUID loop. A magnetic flux caught by the large pickup loop produces a circulating current, which in turn creates a magnetic flux in the input coil coupling it to the SQUID loop. Because of the low inductance value of the SQUID, it is difficult to couple directly the magnetic flux to the loop without the use of a flux transformer. In addition, another advantage of the use of a flux transformer, lies in the particular geometry of the pickup loop, second order gradiometer, Figure 2.18 (lower panel), which allows for magnetic measurements of magnetic samples in magnetic fields, by discriminating between the two magnetic sources (sample and field).

The SQUID system used for the measurements that are presented in the current thesis was a Quantum Design MPMS, a model which allowed for magnetic characterizations in

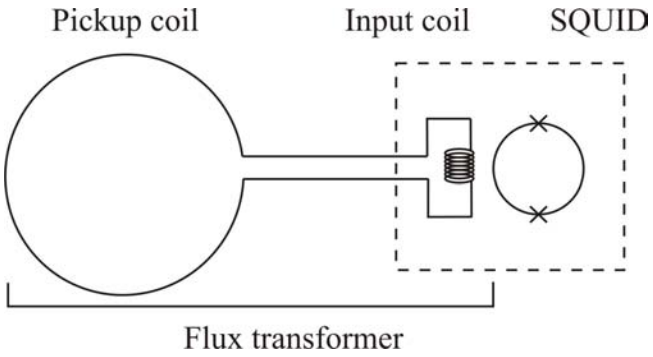

Figure 2.17: Schematic representation of a SQUID measurement set-up.

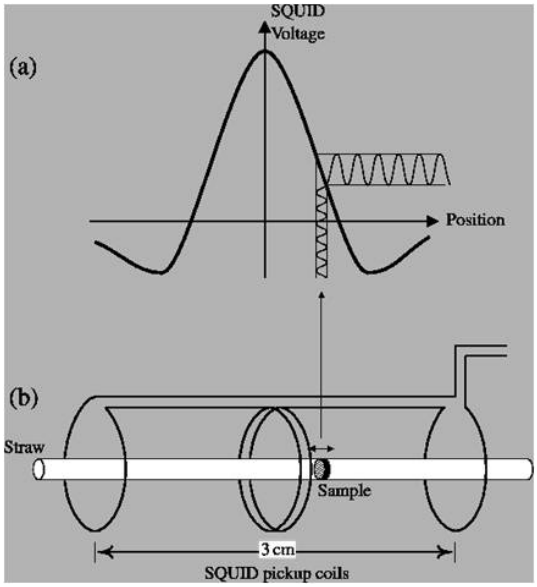

Figure 2.18: Illustration of an RSO measurement with a small amplitude. (a) Shows the ideal SQUID response for a dipole and (b) shows the movement of the sample within the SQUID pickup coils. Taken from [14].

magnetic fields up to 7 Tesla. The temperature range for the sample measurement was between 2.5 - 400K. A distinct feature of this system was the fact that it included a phase sensitive measurement, by inducing a small amplitude, periodic displacement of the sample. The sample movement results in an AC signal that is detected by the DC SQUID sensor by performing phase sensitive measurements. This feature is called Reciprocating Sample Option (RSO) and it allows for sensitivities of up to 1×10^{-8} emu. The RSO feature can perform two types of measurements. One is the RSO Center Scan, while the second, illustrated in Figure 2.18, is the RSO Maximum Slope Technique.

2.8 Résumé de chapitre en français

Ce chapitre introduit les techniques expérimentales utilisées dans le cadre de cette thèse. Le premier paragraphe présente les principes et les spécificités de la technique de pulvérisation cathodique DC et celle des dépôts par ablation laser à impulsions (PLD). Le deuxième paragraphe illustre les principes de la photolithographie et de la lithographie optique.

Dans le paragraphe suivant nous introduisons la technique de diffraction des rayons X à haute résolution. Les différents types de configurations de mesure sont discutés : $2\theta/\omega$, la cartographie de l'espace réciproque, la technique de caractérisation de la texture dans les couches minces épitaxiées, la réflectométrie X.

Le paragraphe suivant introduit la microscopie à force atomique et ses différents modes et options de mesure (mode contact, mode tapping, mode de modulation en fréquence et en amplitude, le mode *lift/interleave* dédié à la microscopie de force magnétique).

Dans le paragraphe suivant nous introduisons les principes de la spectroscopie de photoémission des photoélectrons X et ses différentes options d'analyses. Les derniers deux paragraphes expliquent les principes de fonctionnement pour deux types de magnétomètres utilisés pour effectuer les mesures magnétiques sur les films élaborés dans le cadre de cette thèse. Le premier type de magnétomètre est le magnétomètre à échantillon vibrant (VSM). Le deuxième est le magnétomètre SQUID (abréviation de l'anglais : Superconducting Quantum Interference Device). Une attention toute particulière a été portée au fonctionnement du SQUID, étant donné le cadre spécifique de cette thèse qui se situe à la frontière entre magnétisme et supraconductivité.

Bibliography

[1] S. A. Campbell, *The Science and Engineering of Microelectronic Fabrication*, Oxford University Press (2001);

[2] D. P. Norton, *Pulsed Laser Deposition of Thin Films*, R. Eason (ed.), Wiley (2007);

[3] S. W. Jones, *Photolithography*, IC Knowledge LLC (2008)

[4] Layout Editor, MEMS/IC design software, http:\www.layouteditor.net;

[5] M. Birkholz, *Thin Film Analysis by X-Ray Scattering*, Wiley-VCH (2006);

[6] Bruker AXS, *Diffraction Solutions for Material Rsearch - D8 DISCOVER* Brochure;

[7] A. Boulle, R. Guinebretière, A. Dauger, *J. Phys. D: Appl. Phys.* **38**, 3907 (2005);

[8] Ron Reifenberger (2010), *ME 597 Lecture 5: Interaction Forces I*, http://nanohub.org/resources/9713;

[9] *Magnetic Force Microscopy* in *Dimension 3100 - Manual*, Veeco Instruments (2004);

[10] M. Hehn, *Elaboration, étude des propriétés structurales et magnétique de couches et réseaux de plots submicronique à base de cobalt*, Ph.D Thesis, Université "Louis Pasteur", Strasbourg (1997);

[11] T. L. Alford, L. C. Feldman, J. W. Mayer, *Fundamentals of Nanoscale Film Analysis*, Springer (2007);

[12] D. Zemlyanov, *Introduction to X-ray Photoelectron Spectroscopy and to XPS Applications*, http://nanohub.org/resources/2668;

[13] B. Chesca, R. Kleiner, D. Koelle, *SQUID Theory* in *The SQUID Handbook, Vol. I*, J. Clarke, A. I. Braginski (eds.), Wiley-VCH (2004);

[14] J. Bland, *A Mössbauer Spectroscopy and Magnetometry Study of Magnetic Multilayers and Oxides*, Ph. D. Thesis, University of Liverpool (2002).

Chapter 3

Elaboration and characterization of epitaxial $La_{1-x}Sr_xMnO_3$ thin films

In the present Chapter the elaboration and characterization of thin epitaxial films is presented. Due to their structural compatibility with YBCO thin films and their ferromagnetic nature at low temperatures, LSMO thin films represent a straightforward choice in studying the magnetic pinning of vortices in YBCO layers. An up-to-date overview of the scientific literature concerning LSMO thin films is given, focusing on issues that are relevant in the context of magnetic pinning. Growth studies of LSMO thin films are also presented with detailed morphological, structural and electrical characterization. An important result of our studies is represented by LSMO thin films having a modulated surface morphology which will be considered in the elaboration of LSMO/YBCO bi-layers for pinning studies in YBCO films. The last Section is devoted to the study of oxygen incorporation effects in LSMO thin films. This topic is of particular importance in the field of doped manganites, as the oxygen content in these systems strongly affects their physical properties. Although a widely studied topic, an original approach based on the numerical simulations of LSMO ω-scans was adopted, in order to characterize the structural effects of oxygen incorporation on the LSMO lattice.

3.1 Introduction to $La_{1-x}Sr_xMnO_3$

Divalent ion doped rare earth manganites having the formula $R_{1-x}A_xMnO_3$, where R is a rare earth such as La, Nd, Pr and A is a divalent substitution ion, Sr, Ca, Ba, have been intensely investigated in the last decade due to their so-called "colossal magnetoresistance effect" (CMR) and their theoretical 100% spin polarization [1]. The two exceptional features recommended these materials as an obvious, strightforward choice in the elaboration of magnetoelectronic, *i.e.* spintronic, devices, such as magnetic sensors, magnetic

tunnel junctions for MRAM (magnetic random access memory) applications, or magnetic read heads for hard-disks. Among the plethora of materials that enter the category of doped rare earth manganites, $La_{0.66}Sr_{0.33}MnO_3$ (LSMO) is thought to be the ideal candidate for the above applications, having the highest bulk Curie temperature, ∼360K. Various aplications using LSMO thin films have been published so-far, including magnetic tunnel junctions [2], spin valve structures [3, 4], bolometers [6] or Schottky barriers [5]. Even though promising results were obtained, up to now LSMO failed to be incorporated in commercial sensors or tunnel junctions. One of the reasons for this is the high sensitivity of the LSMO transport and magnetic properties around room temperature [7]. Another is the difficulty in obtaining high quality LSMO surfaces and interfaces. It has been shown that in a LSMO/STO/LSMO tunnel junction, a crucial role in determining its magnetoelectric response, is played by the termination layers of LSMO at LSMO/STO interfaces [8].

3.1.1 Structural properties

Lanthanum manganite, $LaMnO_3$, crystallizes in a perovskite-like structure that is nearly cubic. Pervoskite structures are determined by the so-called tolerance factor, t, defined as:

$$t = \frac{r(A) + r(O)}{\sqrt{2}(r(B) + r(A))}, \tag{3.1}$$

where r is the ionic radius of the three constituent elements A, B and O of the ABO_3 lattice. This tolerance factor has a value comprised between 0.89 and 1.02 for slightly distorted prevoskite structures and 1 for the cubic perovskite. The latter is schematically presented in Figure 3.1. In the case of $LaMnO_3$, La occupies the corners of the lattice, while Mn is placed in the center of an O octahedron. The octahedral surrounding of Mn plays an important role in determining some of the physical properties of doped LMO. Upon doping, Sr occupies the La corner sites. Strictly speaking, for a Sr doping level of x=0.33%, $La_{0.66}Sr_{0.33}MnO_3$ has a rhomohedral crystal structure. For partcical purposes however, the structure is often regarded as being pseudo-cubic, having the pseudo-cubic lattice parameter a=3.873 Åand angle of 90°+γ =90.26° [9, 10].

When LSMO is epitaxially grown on different single crystal substrate, its structure suffers distortions that modify its crystal structure. Doped manganites are a class of materials in which the structural, magnetic and electric properties are closely related, so it is important to understand the structural response of LSMO when subjected to different substrate induced strains. The most common substrates that LSMO has been grown upon are: $SrTiO_3$ (STO) [15, 10, 17, 23, 18, 19, 20], $LaAlO_3$ (LAO) [21, 22, 23], MgO [11], $NdGaO_3$ (NGO) [12] and $(LaAlO_3)_3(Sr_2AlTaO_6)_7$ (LSAT) [13, 14]. Recently, in the attempt for LSMO integration in the semiconducting industry, thin films have also been grown on STO buffered Si substrates

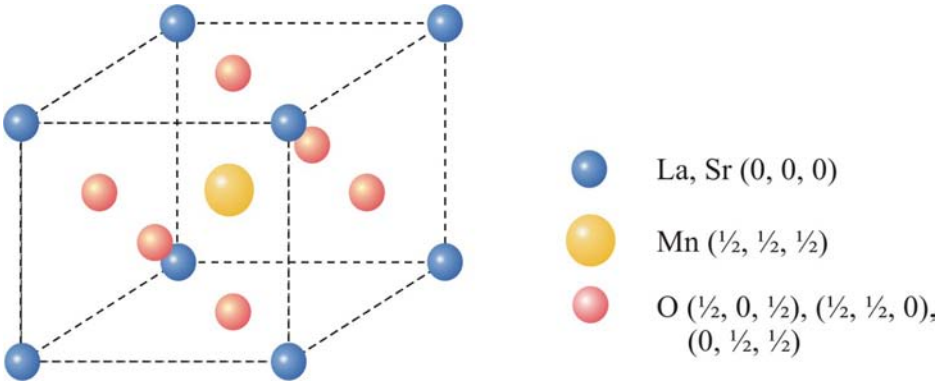

Figure 3.1: Unit cell of the perovskite-like lattice of LSMO.

[16]. The misfit parameter, δ, defined as

$$\delta = \frac{(a_F - a_S)}{a_S}, \tag{3.2}$$

gives the substrate and lattice mismatch, in the case of substrates having cubic lattices. If the misfit parameter is positive, like in the case of LAO(001) substrates, δ=0.022, the film is subjected to compressive strain in the in-plane direction. If on the other hand, δ has a negative value, the case of STO(001), δ=-0.008, the film grows under an in-plane tensile strain. Of course, the above considerations refer to epitaxial LSMO layers grown pseudomorphically on the respective substrates. Having a positive Poisson ratio of ν=0.4 [71] the resulting LSMO lattices on LAO and STO will consequently be tetragonal, having in the first case $a_{in-plane} < a_{out-of-plane}$. In the case of the tetragonal LSMO films grown on STO(001), $a_{in-plane} > a_{out-of-plane}$. In general, throughout the manuscript we will denote $a_{in-plane}$ as simply a, and $a_{out-of-plane}$ as c. If the substrate lattice is not cubic, for example in the case of NGO which has an orthorhombic lattice, LSMO grown on NGO (110) will experience different in-plane lattice strains, leading to an orthorhombic distortion of the lattice. The latter case will also be dealt with in the Section concerning the magnetic anisotropy of epitaxial LSMO thin films.

Another contribution to the lattice distortion comes from the Jahn-Teller effect. Schematically presented in Figure 3.2 the Jahn-Teller effect in doped manganites consists in the deformation of the MnO_6 so as the degeneracy of the e_g levels is lifted. The decrease of the electronic energy is greater than the increase in the elastic energy stored in the deformed state of the octahedron, so that this deformation is energetically favorable.

3.1.2 Magnetic Properties

The magnetic properties of manganites is determined by the specific exchange interactions that occur between Mn ion spins. These interactions are mediated by the oxygen ion, or

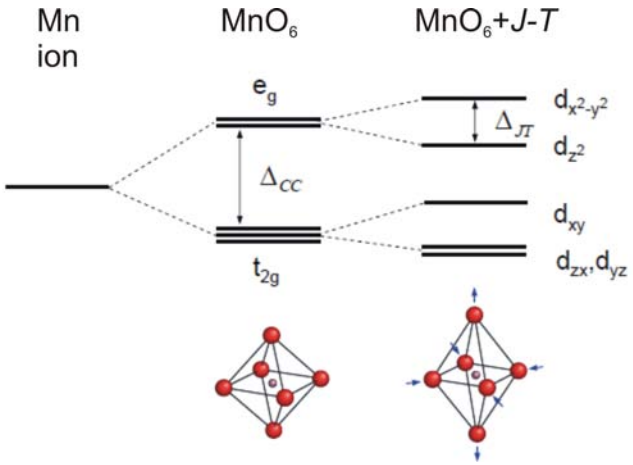

Figure 3.2: Jahn-Teller distortion of the MnO_6 octahedron and the corresponding e_g energy level modification. Adapted from [24].

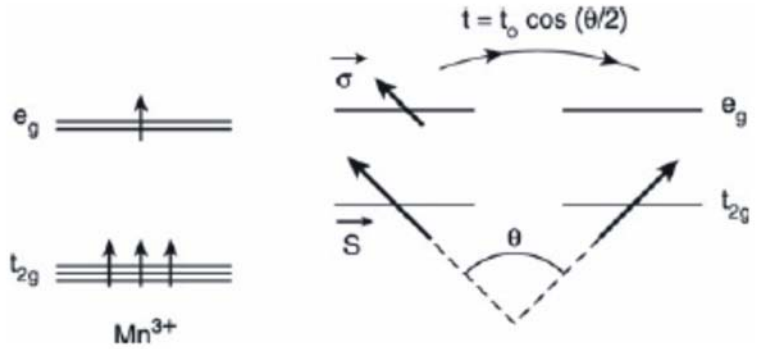

Figure 3.3: Schematic representation of the double exchange mechanism. Taken from [33].

more precisely by the overlap between the d Mn orbitals and the p O orbitals. Superexchange interactions take place between Mn ions having the same valence state, Mn^{3+}, or Mn^{4+} in Mn-O-Mn bonds. Without going into details the superexchange interaction stabilizes an anti-ferromagnetic spin configuration in the case of Mn^{4+}-O-Mn^{4+}, whereas it may be either ferromagnetic or anti-ferromagnetic in the Mn^{3+}-O-Mn^{3+} bond. The latter is the case for the LSMO end member $LaMnO_3$, in which both states F and AF coexist.

Divalent ion doping of end member rare earth manganites, such as La^{2+} doping of $LaMnO_3$, creates Mn^{4+} within the compound, forming thus Mn^{3+}-O-Mn^{4+} bonds. In order to explain ferromagnetism in LSMO, Zener [25, 26] proposed the so-called *double exchange* interaction between Mn^{3+} and Mn^{4+} ions. It consists of the simultaneous transfer of e_g electron from a Mn^{3+} ion on the O p-orbital and from the O p-orbital to an empty e_g level of a Mn^{4+} ion. Hund's rule coupling is a very important factor in determining the double exchange interaction. Hund coupling consists in the parallel spin alignment of the e_g electron to the three core t_{2g} electrons of Mn^{3+}. Anderson and Hasegawa [27] have shown that

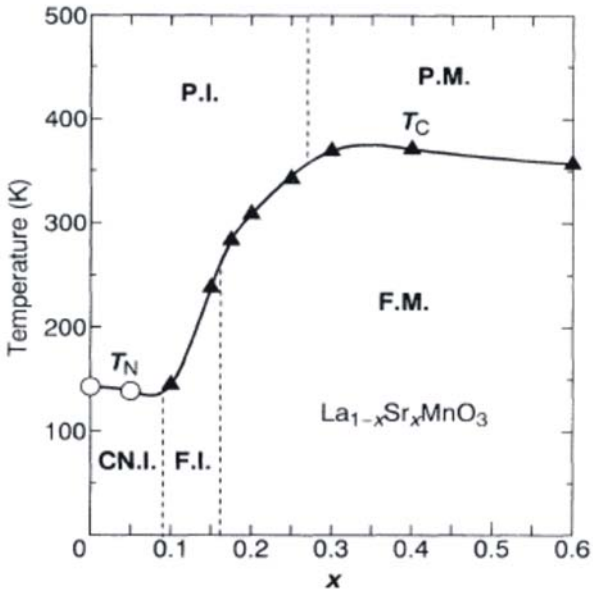

Figure 3.4: The magnetic and electric phase diagram of the $La_{1-x}Sr_xMnO_3$ compound, as measured by Urushibara *et al.* [28].

the probability of the e_g electron transfer in the case of strong Hund coupling is $t_0 \sin(\theta/2)$, where θ is the angle made by the core t_{2g} electron spins of neighboring Mn^{3+} and Mn^{4+} ions. The e_g electron transfer to an adjacent Mn^{4+} free e_g level is favored if the core t_{2g} electron spins are parallel for both Mn ions. This coupling has a crucial importance of the electric characteristics of LSMO, and doped manganites in general, and is schematically presented in Figure 3.3.

Urushibara *et al.* [28] constructed a magnetic and electric phase diagram of LSMO as a function of the Sr doping x, *i.e.* of the Mn^{4+} ion concentration with respect to Mn^{3+}. Their result is shown in Figure 3.4. As the doping concentration increases the magnetic order changes from anti-ferromagnetic to ferromagnetic, at x=0.33 having the highest Curie temperature, T_C~360 K. For x <0.1, LSMO becomes an antiferromagnet below the Neel temperature of ~150 K.

Kubo and Ohata [29] treated the double exchange interaction from the quantum mechanical point of view, writing the Hamiltonian as composed from an intra-atomic exchange term related to Hund coupling and a electronic transfer term, proportional to a transfer matrix element, t_{ij}. The $M(T)$ dependence deduced from statistical considerations is presented in Figure 3.5a. Good agreement with experimental data can be observed, Figure 3.5a. Boschker *et al.* [30] interpreted their magnetization data using the Weiss model for ferromagnetism with the Brillouin function. Figure 3.5b shows the theoretical curves for different values of the total angular momentum, J. The best fit was obtained for J=4, an intermediate value between the quantum mechanical picture, J=1/2, and the classical one, $J \to \infty$. The

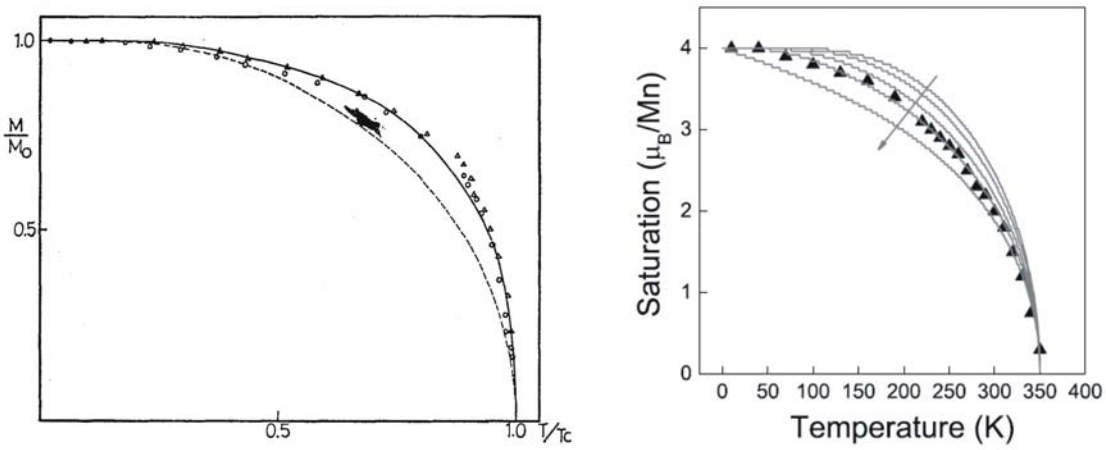

(a) **(b)**

Figure 3.5: (a) M(T) curve calculated within the quantum mechanical mode proposed by Kubo and Ohata [29] (solid line), experimental data obtained on $La_{0.62}Pb_{0.38}MnO_3$ (circles) and M(T) curve calculated with the Heisenberg model (dotted line), for comparison. Taken from [29]. (b) M(T) curve of a LSMO epitaxial thin film and the corresponding fit, see text. The continuous lines represent the fits for different values of J. Taken from [30].

authors argue that this result could originate from spin wave excitations.

An important effect that is in close relationship with the electron transfer between the Mn^{3+} and Mn^{4+} is the Jahn-Teller effect. The Jahn-Teller effect is present in the case of Mn^{3+} ions and it consists of a deformation of the oxygen octahedron surrounding them. The deformation consists of an elongation of the octahedron along a certain axis which modifies the crystal field sensed by the metallic ion. The change of crystal field affects the the energy levels so as to lift the degeneracy of the two e_g levels, by splitting them into states symmetric in energy to the initial value. The single e_g electronic energy is thus reduced. In an double exchange type electron transfer from Mn^{3+} to Mn^{4+} the Jahn-Teller octahedron distortion is "displaced" to the new Mn^{3+}. The electron and lattice distortion travel together and form a quasiparticle called *Jahn-Teller polaron*. In this case, and in metallic manganites in general, the Jahn-Teller effect is dynamic and results in an average distortion of all O_6 octahedron. In the case of LMO, where only Mn^{3+} ions are present, the effect is static and long-range.

We have presented above some of the key factors that determine the magnetic and electric properties of doped manganites. Other contributions arise from: Heisenberg magnetic coupling between the nearest-neighbor localized spins and Coulomb interaction among e_g electrons.

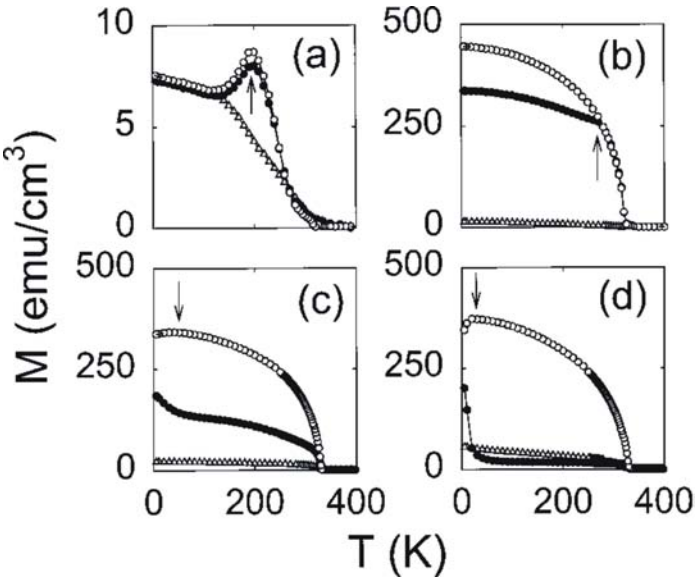

Figure 3.6: Field-cooled temperature-dependent magnetization at 5 Oe of 250Å$La_{0.67}Sr_{0.33}MnO_3$ epitaxial films grown on (a) (001) $LaAlO_3$, (b) (001) $SrTiO_3$, (c) (001) LSAT, and (d) (110) $NdGaO_3$ substrates. The responses were measured along three symmetry directions. The directions with respect to the substrate are: for (a) and (b), in-plane [110] (open circles), in-plane [100] (closed circles), and out-of-plane [001] (triangles), and for (c) and (d), in-plane edge directions (circles), and out-of-plane (triangles). Arrows indicate the spin reorientation transitions. Taken from [23].

Magnetic Anisotropy

The magnetic anisotropy of doped manganites in general is an example of the close relationship that exists between the structural properties of the compounds and their magnetic properties. According to the structural phase of a manganite an array of different magnetic anisotropies can be stabilized. In the present section we will limit our literature overview to the case of thin films, as thin films are the main concern of the thesis. Also, thin films, due to their intrinsic nature, are systems in which the crystal structure is highly modulable through the choice of substrate and of the deposition conditions, allowing for a thorough assessment of the influence of the lattice structure on magnetic anisotropy.

Tsui *et al.* [23] studied the effects of substrate induced strain in LSMO thin films deposited on (001) STO, LAO, NGO and LSAT. Their results are presented in Figure 3.6. They measured the magnetization as function of temperature for three crystallographic directions: two in-plane, [110], [100] and one out-of-plane, [001]. In the case of LSMO epitaxial films deposited on LAO, Fig. 3.6a, the magnetization along the in-plane directions of the film rises abruptly as the temperature is decreased and reaches a peak value at 200K, temperature beyond which both in-plane magnetization values decrease. The out-of-plane magnetization, on the other hand, increases rather linearly as a function of temperature. The larger in-plane magnetization down to 200 K indicates an in-plane easy axis originating from demagnetiza-

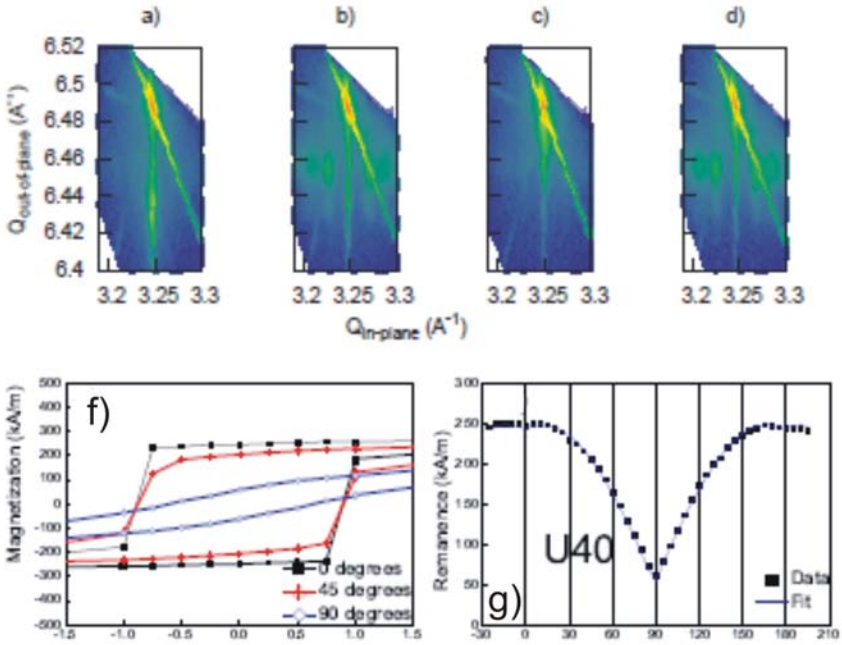

Figure 3.7: Reciprocal space maps around the (a) $(204)_c$, (b) $(024)_c$, (c) $(\bar{2}04)_c$ and (d) $(0\bar{2}4)_c$ LSAT reflections of the 40 nm thick sample grown on a smooth substrate. In (a) and (c) the dissimilar spacing of the $(260)_o$ and $(620)_o$ LSMO reflections is clearly observed while in (b) and (d) satellites are present next to the $(444)_o$ and $(44\bar{4})_o$ LSMO reflections. Magnetization loops with the field aligned with 3 high symmetry directions (f) and (g) remanence versus field angle dependence. Taken from [14].

tion effects. The behavior below 200 K suggests the existence of a perpendicular anisotropy having the [001] easy axis. This conclusion is supported by the *M-H* loops, not shown here. As far as the film grown on STO (001), Fig. 3.6b, as the temperature drops, the magnetization dependence of along [110] parts with the magnetization along [100] around ∼250 K, suggesting a biaxial anisotropy, having easy axes the [110] in-plane direction. For the films grow on LSAT and NGO, respectively, the results show similar behavior of the two. Both films have a biaxial anisotropy along [110] directions and an additional uniaxial anisotropy superimposed, along [100]. In the case of (001) LSAT, Boschker *et al.* [14] show that the presence of the uniaxial anisotropy is due to the orthorhombic structure of LSMO epitaxial films. The orthorhombic structure is determined by recording reciprocal space maps around the asymmetric substrate and film peaks in positive and negative configurations. Remanence measurements were recorded for different field orientations, Figure 3.7g. The results show a strong uniaxial anisotropy axis along [001] direction, as the maximum in the magnetization remanence is located a 0° and 180°, respectively. Local minima are also observed originating from a low biaxial anisotropy along [110]. Anisotropic substrate induced strain can also cause the growth of orthorhombic LSMO films. This is the case when LSMO is grown on (110) NGO [12]. The film-substrate lattice mismatch along the $[1\bar{1}0]$ direction

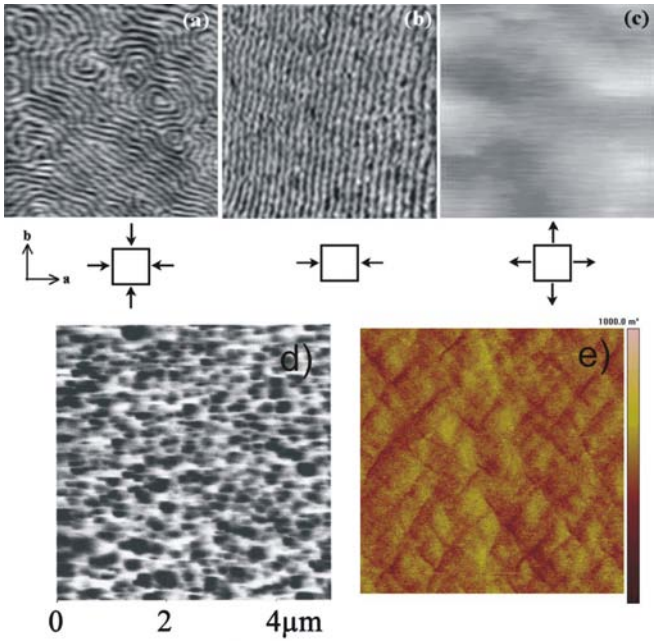

Figure 3.8: MFM images of $La_{0.7}Sr_{0.3}MnO_3$ thin films, taken in zero applied field at room temperature, on various substrates of (a) LAO, (b) NGO, and (c) STO. The scan size is $4\mu m \times 4\mu m$. Taken from [20]. MFM images of LSMO thin films deposited on LAO (d) substrates recorded at RT without an external field. The scan size is $5\mu m \times 5\mu m$. Taken from [22]. (e) AFM image with a NiCo MFM tip shows the surface steps on a 20 nm $La_{0.67}Sr_{0.33}MnO_3$ film on a $SrTiO_3$ substrate. The scan size is $4\mu m \times 4\mu m$ in an applied magnetic field of 5.6kA/m. Taken from [31].

is of -0.47% and -0.70% along [001], both lying in-plane. The XRD measurments used to determine the directions of the crystal axes of the NGO, the structure of the LSMO film and the corresponding lengths of the lattice vectors, reveal that the film grows coherently on the substrate, resulting in different lattice parameters along the two directions. This lattice parameter anisotropy leads to the formation of an in-plane uniaxial magnetic anisotropy having the $[1\bar{1}0]$ direction as an easy axis. Different magnetic anisotropy configurations give rise to specific magnetic domain configuration patterns. Dho *et al.* [20] studied the influence of strain-induced magnetic anisotropy on the magnetic domains of epitaxial LSMO thin films deposited on (001)LAO, (110)NGO and (001)STO substrates. The MFM images obtained on the three systems are shown in Figure 3.8(a)-(c). It can be seen that in the case of the LSMO thin films that are subjected to in-plane compressive strain, as is the case for LSMO grown on LAO and NGO, the domain pattern takes the form of stripes. *Stripe domains* are characteristic for films possessing an out-of-plane magnetic anisotropy. In the case of the films deposited on (001)LAO the stripes are arranged in a maze-like pattern, while in the case of the domains of the film grown on (110)NGO the stripes are parallel and are aligned along a well defined direction. The authors point out that this behavior is due to the fact that LSMO is isotropically subjected to a tensile strain when deposited on LAO,

while in the case of an (110)NGO substrate the strain manifests itself on only one direction, thus giving rise to an in-plane structural anisotropy. The uniaxial compressive strain results in a preferential in-plane axis responsible for the alignment of the stripes. For the LSMO films grown on STO, the tensile strain determines a biaxial in-plane magnetic anisotropy which fixes the magnetization of the film parallel to the surface plane. This arrangement results in the so-called *feather*-like domain configuration. This pattern is described by the absence of strong magnetic contrast in the MFM images and relatively large magnetic domains. The feather-like domains were also observed on epitaxial LSMO thin films deposited on (001)STO substrates by Desfeux *et al.* [22]. However, as far as the LSMO thin films grown on (001)LAO substrates are concerned, they found that the maze-like character of the domains was replaced by a *bubble* domain configuration, Figure 3.8d. Both patterns are characteristic of films with out-of-plane magnetic anisotropy. The observation of the bubble domains was attributed to the structural transition that occurs in LAO at the LSMO growth temperature.

Houwman *et al.* [31] did not observe the typical feather-like domain structure of LSMO thin films grown on (001)STO substrates. In their MFM study they employed soft NiCo covered tips, which had a low coercivity (∼0.16 kA/m). Thick coated NiCo tips were found to be the ideal choice in imaging LSMO samples as they had a sufficiently high magnetic moment so as to detect a measurable signal and a sufficiently small coercive field not to disturb the magnetic features during scanning. Figure 3.8e presents an MFM image obtained on a 20 nm thick LSMO thin film. The domain pattern described as a *checkerboard* configuration consisting of bright rectangular regions separated by dark stripes. As it has been shown before, the magnetization of LSMO thin films lies in the in-plane direction of the film, while at the domain border the magnetization is oriented in the out-of plane direction. The authors argue that the out-of-plane orientation of the magnetization is due to that fact that the perpendicular uniaxial anisotropy is not totally annihilated by the in-plane biaxial anisotropy.

Another important role played on the magnetic anisotropy of LSMO thin films is the vicinal step formation on the substrates upon which LSMO is grown. Mathews *et al.* [18] deposited LSMO thin films on vicinal (001)STO substrates. Angular remanence measurements indicate the existence of an uniaxial anisotropy having the easy axis parallel to the vicinal steps and a hard axis perpendicular to them, Figure 3.9a. Substrate terraces induce magnetocrystalline uniaxial anisotropy in thin films because of the presence of broken bonds at step edges [32]. Perna *et al.* [19] studied the evolution of the uniaxial anisotropy as a function of the substrate miscut angle. For a 2° miscut angle both a biaxial and an uniaxial anisotropy are present in the film, Figure 3.9b upper graph. As the miscut angle is increased to 4° the number of steps increases so that the uniaxial anisotropy is dominant over the biaxial one, as can be seen from Figure 3.9b, lower graph.

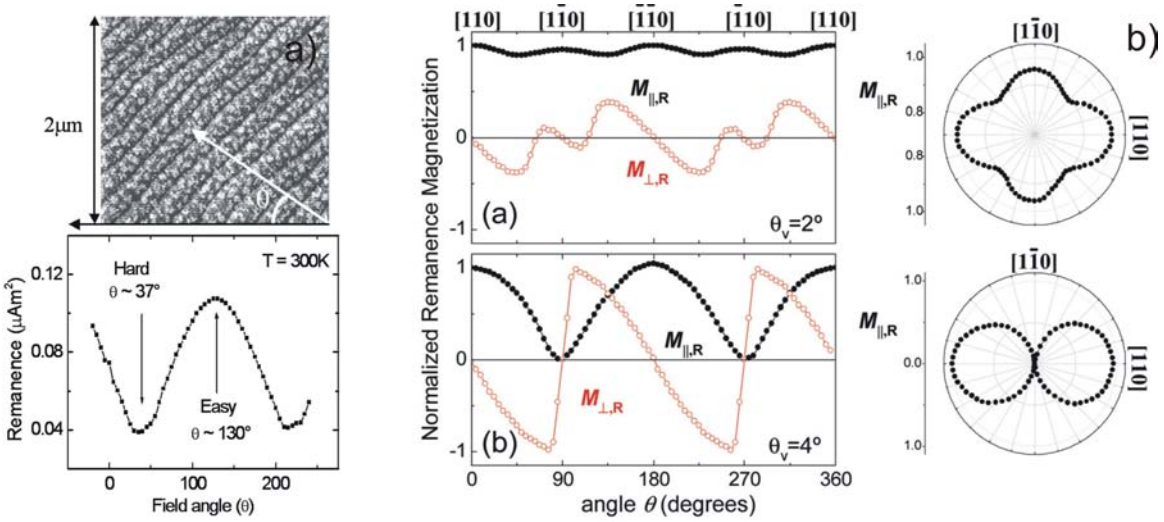

Figure 3.9: (a)Remanence vs. in-plane field angle of a 25 nm thick LSMO film at room temperature (bottom panel). Arrows denote easy and hard directions. AFM image of the same film (top panel) with the step direction θ=133±5°. The gray scale range is from 0 to 2nm. Taken from [18]. (b)Angular dependence of the normalized remanence magnetization ($M_{||,R}$=M_S and $M_{\perp,R}$=M_S) of 120-nm-thick LSMO films grown onto a vicinal θ_v=2° and θ_v=4° STO(001) surfaces. The right panels show the corresponding polar-plot representations of $M_{||,R}$. Note that different scale is adopted for the 2° miscut film. Taken from [19].

3.1.3 Electric Properties

The electric properties of LSMO are in direct correlation with its structural and magnetic properties. In the present Section we will give a brief account of the electrical behavior of $La_{0.66}Sr_{0.33}MnO_3$ and doped manganites in general, referring to the mechanism of metallic conduction and their insulating character above the metal-insulator transition temperature, the different models that are used in modeling their respective electric properties. Also an overview is given on probably the most spectacular property of doped manganites, colossal magnetoresistance (CMR).

As it could be seen from the magnetic and electric phase diagram proposed by Urushibara *et al.* around optimum doping x=0.33, in the ferromagnetic state LSMO has a metallic character, while above the Curie temperature, in the paramagnetic state the electrical behavior is insulating. Metallic conduction in the ferromagnetic state can be readily understood within the framework of the double exchange model, and strong Hund coupling. Ferromagnetic order within the material results in the alignment of the t_{2g} core spins. With the core spins aligned, the e_g electron which is transfered between Mn ions, reaches a maximum transition probability, $t = t_0$, and thus gains a "free electron"-like delocalized character. It is then evident that these electrons are the ones that participate in the electric transport giving it a metallic character. On the other side, as the temperature rises towards the critical Curie temperature, the core spins tend towards a thermally induced disorder, which in turn causes

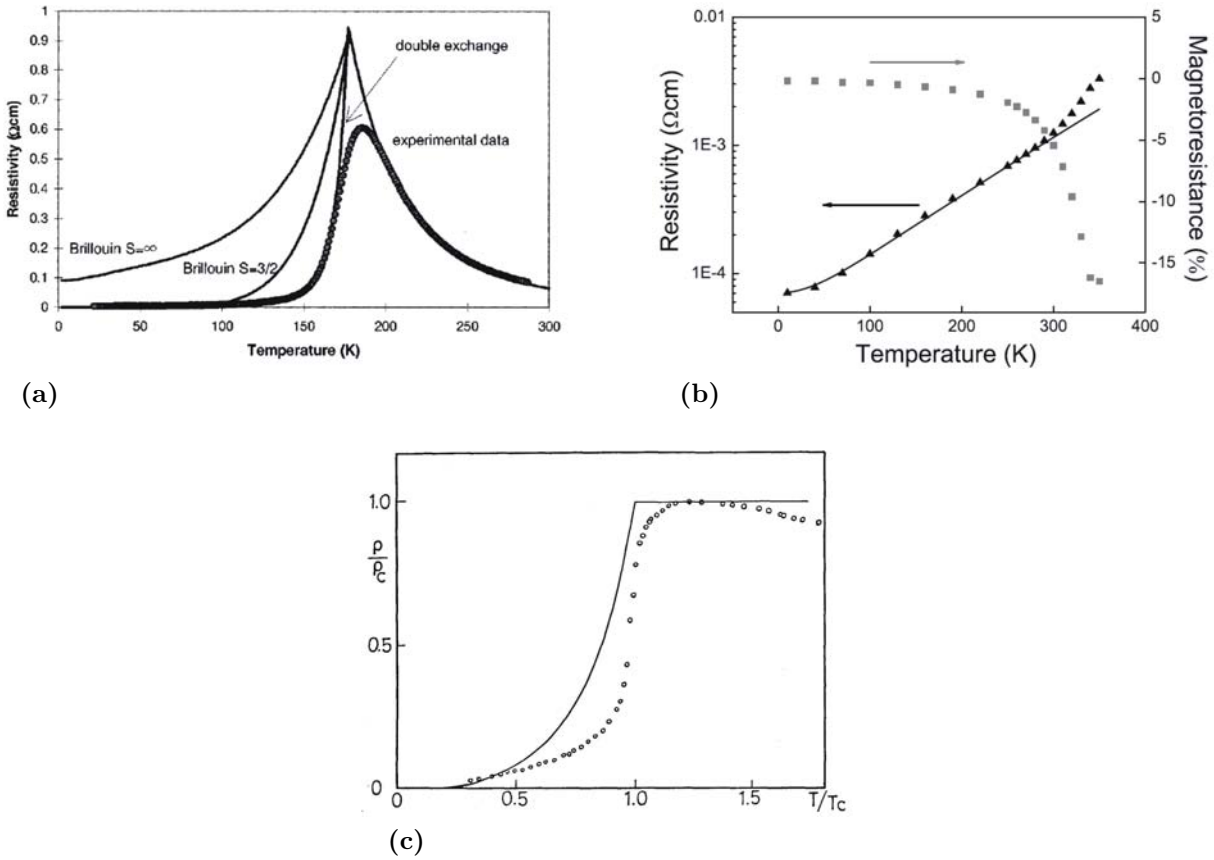

Figure 3.10: (a) Comparison of the magnetic localization model 3.3 with data measured on a $La_{0.7}Ca_{0.3}MnO_3$ thin film. The three curves are fits obtained using magnetizations from a Brillouin function with S=3/2 and S=∞ (large spin clusters) and the double exchange model [29] , taken from [38]; (b) $\rho(T)$ and $MR(T)$ dependencies for a thin $La_{0.67}Sr_{0.33}MnO_3$ epitaxial film and the corresponding fit using Eq. 3.4, taken from [30]; (c) Temperature dependence of the normalized resistivity of $La_{0.69}Pb_{0.31}MnO_3$ (circles) and the corresponding fit (line) using Eq. 3.5, taken from [29].

a decrease of the e_g electron transfer rate. The decrease of electron mobility results in the increase of the electrical resistance and the insulating behavior at high temperatures, *i.e.* $T > T_C$.

Several models were developed in order to quantitatively describe the the electrical characteristics, electrical resistivity vs. temperature, $\rho(T)$, of LSMO in different temperature regimes. For the high temperature range in the paramagnetic regime, $T > T_C$, these models include the common thermal activation law, small adiabatic polaron hopping or Mott's *variable range hopping*, VRH. Each of these mechanisms has a precise physical foundation [33]. In the case of the thermal activation law Zhuang *et al.* [34] have shown the existence of a pseudogap at the Fermi level in the paramagnetic phase. The concept of polaron has been introduced in 1959 by Holstein [35] to describe charge carriers that are "clothed" by a lattice distortion. A polaron is said to be in the adiabatic limit when the charge carrier can hop

to an adjacent site which, in the virtue of thermal energy, has suffered the necessary lattice distortion [42]. The Holstein polaron theory is constructed in the following approximations [39]: *i*)polaron hopping is always taking place to the nearest neighbor site; *ii*) all lattice sites are equivalent; *iii*) polaron-polaron interaction is neglected, the theory describes a non-interacting polaron gas. On the contrary, in the variable range hopping model, the lattice sites are not equivalent due to the chemical environment, and also to magnetic disorder, in the case of doped manganites in the paramagnetic region. Additionally, charge hopping is not fixed to the nearest neighboring Mn sites.

At its origin Mott proposed this model for doped semiconductors [36, 37]. Qualitatively, this model can be understood as follows, random distribution of the divalent doping elements within the crystal lattice determines a redistribution of energy levels through an alteration of the crystal field from Mn site to site. If the thermal energy of the system is high enough to permit the electrons to jump to an adjacent lattice site, which is presumed here to have a higher energy, due to the crystal surrounding, the electron will act accordingly. If however, the energy difference between states is higher than k_BT, the electron will hop to a farther site for which the energy of the empty state lies within the thermal energy range. The electron thus hops to an energetically suitable site, hence the name variable range hopping. Viret *et al.* [38] used an adapted VRH model to describe the the transport properties of different mixed valence manganites. Their model takes into consideration the localization of carriers not only due to chemical disorder but also on magnetic disorder which is induced as the temperature reaches T_C, coming from the ferromagnetic region. The expression for the resistivity under these assumptions is:

$$\ln(\rho/\rho_\infty) = \{[T_0(1 - M/M_s)^2]/T\}^{1/4} \tag{3.3}$$

One can see that the the magnetic localization term becomes important as the magnetization decreases and so electrons are trapped on local ferromagnetic regions, in an overall imperfect ferromagnetic order. Electron hopping is thus governed both by chemical disorder induced level energy difference and by the magnetic disorder. Taking into account the double exchange theory, the electron will jump to a site for which the transfer probability is maximum, *i.e.* the core spins of the two sites are parallel. Figure 3.10a show the results obtained by the authors on $La_{0.67}Ca_{0.33}MnO_3$ thin films. The best result is obtained the double exchange model of *M(T)* developed by Kubo and Ohata [29]. As the temperature is higher than T_C, the magnetization is zero, and so the classic VRH model describes electronic transport. Sun *et al.* [39] circumvented the hypotheses of the polaronic model, which are to strict to be useful with respect to the doped manganites, by developing a so-called VRH of small polarons. Good results were obtained in interpreting the $\rho(T)$ data on some manganite systems.

As far as the low temperature regime is concerned, besides the magnetic VRH model described above, other mechanisms have been proposed. Although not the first, Boschker *et al.* [30] describe the low temperature part of the resistivity as:

$$\rho(T) = \rho_0 + aT^2 + bT^5, \tag{3.4}$$

where ρ_0 is the temperature independent impurity scattering term, the T^2 term describes the electron-electron scattering, while the T^5 term represents electron-phonon scattering. Other scattering mechanisms include the electron-magnon scattering, described by Kubo and Ohata [29] as being proportional to $T^{9/2}$. Their model also took into consideration the electron-electron scattering:

$$\rho(T) = \rho_0 + aT^2 + cT^{9/2}. \tag{3.5}$$

Figure 3.10 shows the three different low temperature models.

Sirena *et al.* [40] a used the VRH model in order to determine the T_0 parameter in LSMO epitaxial thin films that suffered oxygen implantation. T_0 was used as a measure of structural disorder induced by the implantation. As expected, the level of disorder and, consequently, T_0 increases, as the irradiation current density increase. Good agreement also exists between the resistivity data and the model used by Boschker *et al.* [30], Figure 3.10b. On the contrary, the expression proposed by Kubo and Ohata [29] fits resistivity data only in the low temperature end, departing from the data as the temperature increases, Figure 3.10c.

Dagotto *et al.* [41] in their extensive review of transport properties of colossal magnetoresistance materials, stress out the key role played by the existence of inhomogeneities. The authors argue that the ground state of manganites has the tendency towards phase separation which involves the co-existence of metallic ferromagnetic and antiferromagnetic charge and orbital ordered insulating domains. Other reviews that concern the transport properties of doped manganites include the ones by Salomon and Jamie[42] and Ziese[43].

Colossal Magnetoresistance, CMR

Colossal magnetoresistance represents the property of mixed-valence manganites that triggered the impressive body of work concerning this class of materials. Magnetoresistance ratio is defined as $\Delta R/R(H) = (R(0) - R(H))/R(H)$, where $R(0)$ and $R(H)$ represent the electrical resistances in zero field and an applied field, H. Although magnetoresitance had been observed for the first time by Searle and Wang [44] in $La_{1-x}Pb_xMnO_3$, the truly colossal magnetoresistance ratio has been determined by Jin *et al.* [45] in $La_{0.67}Ca_{0.33}MnO_3$ as being an impressive 127,000%, corresponding to more than 1000-fold change in resistance, Figure 3.11. An impressive MR ratio of 10^6% was obtained by Xiong *et al.* [46] on

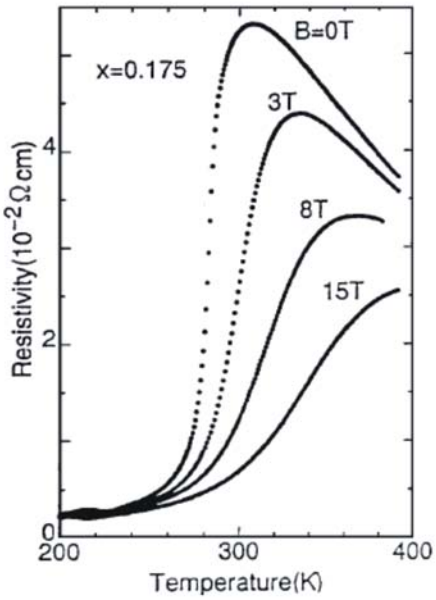

Figure 3.11: Temperature dependence of the resistivity in magnetic fields corresponding to $La_{1-x}Sr_xMnO_3$ at x=0.175. Taken from [47].

$Nd_{0.7}Sr_{0.3}MnO_3$ thin films. The phenomenology of CMR can be qualitatively be understood within the framework set by the double exchange interaction. As previously shown, the double exchange mechanism consists in the transfer of an e_g from a Mn^{3+} ion to a Mn^{4+} ion via an O^{2-} ion. This transfer is governed by the relative spin orientation of the core t_{2g} of the two Mn ions. As the temperature rises towards the Curie temperature, the spins tend towards the paramagnetic disorder so that electronic transfer is empeded leading to a resistivity increase. Applying a magnetic field in the temperature range around T_C, the core spins align themselves along the field and so electronic transfer is favoured, decreasing the electrical resistivity. The resistivity decrease can be dramatic and thus the term of colossal magnetoresistance.

3.2 Elaboration and characterization of $La_{1-x}Sr_xMnO_3$ epitaxial thin films

The present section gives an account of the deposition and characterization of thin $La_{0.66}Sr_{0.33}MnO_3$ (LSMO) epitaxial films. The main goal of our research, is the optimization of the physical properties, *i.e.* morphological, structural and electrical, of the LSMO thin films, in order to make them suitable for the desired purpose, magnetic pinning in HTS. Also, we have set out to understand various aspects of LSMO thin film growth processes that are relevant to the films' subsequent properties.

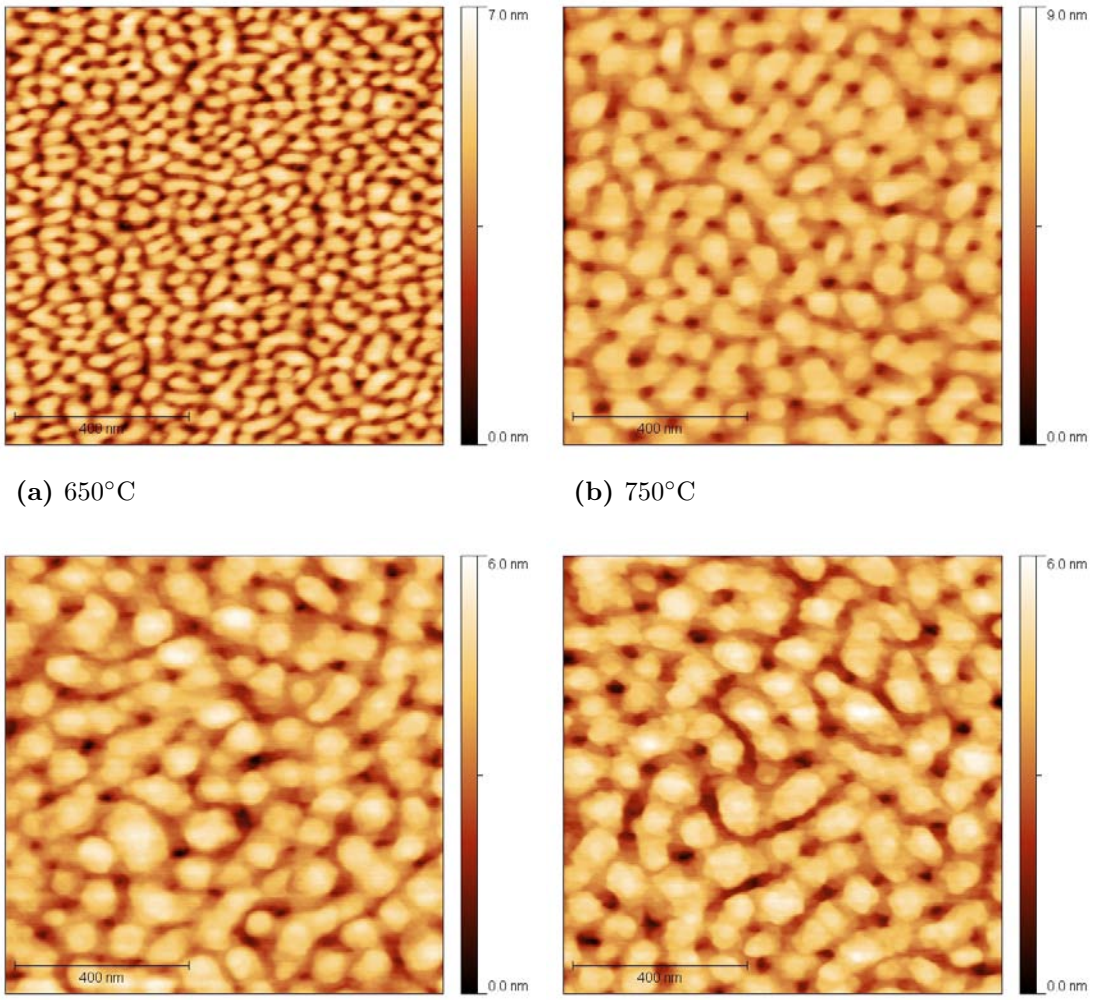

(a) 650°C **(b)** 750°C

(c) 800°C **(d)** 825°C

Figure 3.12: 1μm×1μm AFM images of the LSMO thin films deposited at different substrate temperatures.

The LSMO epitaxial thin films were deposited by dc magnetron sputtering in an Ar:O_2 (3:1) gas mixture at a total pressure of 40 mTorr, from a stoichiometric, 2 inch $La_{0.66}Sr_{0.33}MnO_3$ target. The magnetron was operated at 25 W. The substrate was heated to the deposition temperature (650 °C - 825 °C) at a rate of 10 °C/min in a background pressure around 10^{-7} Torr. After the deposition the films were cooled down in 520 Torr of oxygen and annealed *in-situ* at 550 °C for half an hour. Annealing at 550 °C was included in order to simulate the deposition of the LSMO/YBCO heterostructure, since it is known that YBCO thin films need annealing in this temperature range in oxygen to stabilize the orthorhombic superconducting phase.

3.2.1 Morphological properties of LSMO thin films

It is well known that the deposition parameters are strongly correlated with the growth mechanisms of thin films which in turn affect the film morphology. In our study regarding the morphology, we have mainly focused on the role of the following parameters: substrate temperature, film thickness, substrate morphology and target-substrate distance.

The role of substrate temperature on the morphology of the films

In order to perform this study we have chosen four deposition temperatures: 650, 750, 800 and 825 °C. All the other parameters of the process were kept constant. The thickness of the as deposited films is of about 25 nm, as evaluated from XRR data. In Figure 3.12 we present the as obtained AFM images of the samples grown at the different temperatures. As it can be seen the surface of the film grown at 650 °C is formed of small and relatively independent grains. This can be attributed to the fact that at low deposition temperatures the mobility of the ad-atoms on substrate surface is reduced leading to a 3D growth mode in which cluster formation is favored. As the temperature is increased to 750 °C the surface evolves in a way that clusters appear to be larger in size and they are interconnected among themselves by the layer immediately below. However, this interconnection layer is not continuous and holes can be seen uniformly spread on the surface. The presence of these holes is an indication of the growth mode, studied in more detail in the next section, which can be either a Stranski-Krastanov combined layer by layer and island growth, or pure island growth with coalesced grains, favored by the higher deposition temperature. Increasing the temperature to 800 °C and 825 °C, respectively, further increase of grain size is observed, accompanied by a decrease in the number of holes present on the film surface.

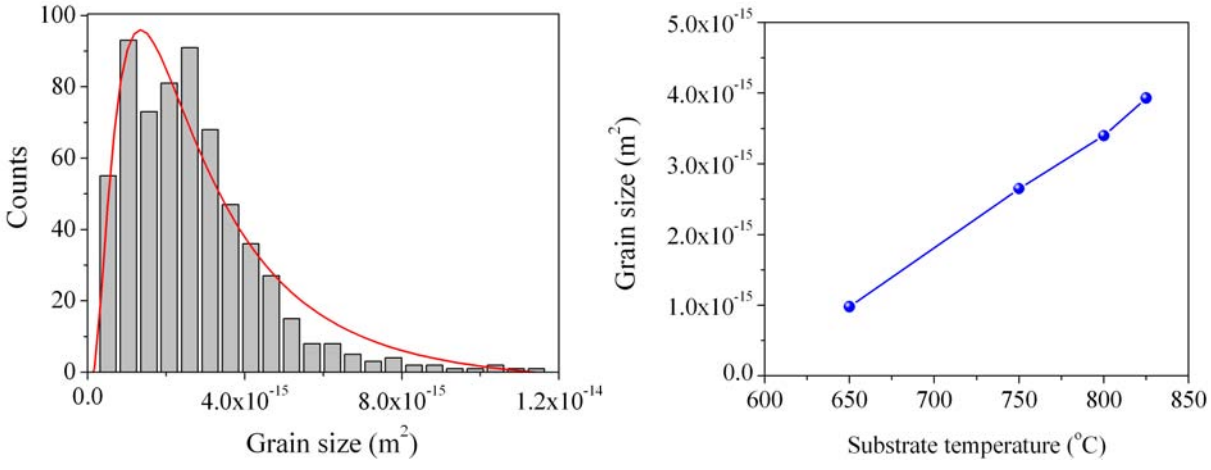

Figure 3.13: (a) Number of grain counts versus grain area and the log normal distribution fit for the LSMO film deposited at 750 °C; (b) Grain size evolution as a function of temperature.

Table 3.1: Morphological parameters of the LSMO films deposited at various temperatures.

Temperature (°C)	RMS roughness (nm)	P-V distance (nm)
650	1.18	6.81
750	1.11	7.48
800	0.83	5.8
825	0.89	3.66

In order to study the evolution of the size of surface grains, a parameter which best describes the evolution of the surface as a function of temperature, we have employed a thresholding technique to measure the grain surface. Thresholding implies a choosing a relevant height limit for a AFM image and considering that any surfaces that have a height higher than the selected threshold represent the grains in the film. In the case of LSMO thin films, Figure 3.12 the use of this simple algorithm is justified by the high uniformity of the film, in the sense that no waviness of the film is present, combined with a very clear surface grain separation. The results were then fitted using a log-normal distribution function, Figure 3.13a, in order to determine the mean grain area. The results of the fits are given in Figure 3.13b. A linear increase of the grain size is observed as function of the substrate temperature. However, no coalescence of the surface grains occurs within the studied temperature range.

As far as typical morphological parameters, RMS roughness and peak-to-valley distances, they are summarized in Table 3.1. Both film roughness and maximum height values show a decrease as deposition temperature is increased indicating higher morphological quality. This suggests that a further increase in film quality can be obtained if the substrate temperature is further increased. This further increase is limited by technical issues.

The role of film thickness on the morphology of the films

The main goal in studying the morphology as a function of film thickness is to determine the growth mechanisms of the LSMO epitaxial layers on STO (001) substrates. For this purpose we have prepared four films varying their respective thicknesses by adjusting the deposition time and measuring thicknesses of the resulting films by X-Ray Reflectometry (XRR). The times chosen were: 0.1 h, 0.5 h, 1 h and 2 h corresponding to thicknesses of 7 nm, 30 nm and 56 nm. The XRR measurements are presented in Figure 3.14. For the film deposited for 2 h the lack of oscillations in the reflectometry curve prevents us from estimating its thickness. However, fitting the existing data with a linear function, a 110 nm thickness was estimated for the 2 h deposited film.

The AFM images are presented in Figure 3.15. In the 7 nm thick film, the surface

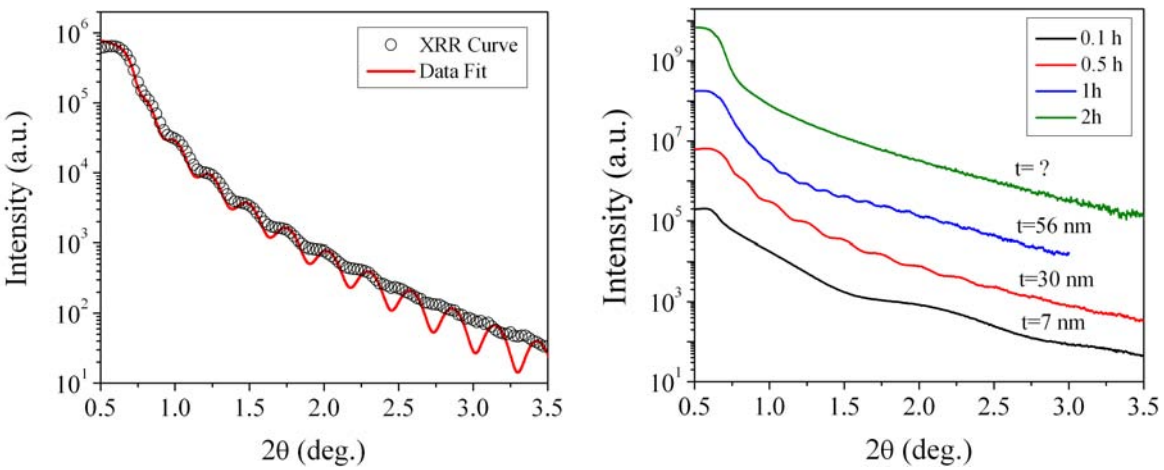

(a) (b)

Figure 3.14: (a) Typical XRR curve for the LSMO thin films and the curve fit used for thickness determination; (b) XRR curves for LSMO thin films of various thicknesses.

exhibits a grainy structure, with the top grains, having approximately 1nm in height, not coalesced. This however does not permit us to drawn any definitive conclusion about the growth mode of the LSMO films. The layer by layer growth is excluded from the start, since grains are formed on the surface, leaving us with the two other mechanisms of film formation, Volmer-Weber, three-dimensional mode and combined layer by layer and island growth, Stranski-Krastanov mode. The problem with the latter is that the critical thickness of the transition from two-dimensional growth to a three dimensional one is typically of about one or two monolayers [50]. Since the holes present in the film have a maximum height of 2 nm it is impossible to distinguish whether we are dealing with a layer by layer followed by island growth mechanism or a pure island growth mode with the bottom islands coalesced.

Further increasing the film thickness grain coalescence is enhanced, Figure 3.15c, leading to a large grain structure. At the highest value of the thickness grain size is reduced by the enlargement of the surface of the holes, Figure 3.15d present on the surfaces of the films. It is to be noted that the holes were observed for all the films studied. The presence of the holes is intrinsic to growth mechanism, their evolution however is related to a well-known phenomena in thin film processes, that is the shadowing effect [50]. Shadowing comes from the fact that particles arriving on the surface do not have a trajectory perpendicular to the film but are incident under a certain angle, which leads upon increasing film thickness, to a preferential distribution, giving thus rise to an increase in the depth of the holes. This can be observed from the evolution of the peak-to-valley distance as it increases with thickness. In summary, two competing effects are observed: one is the coalescence of the grains and the other is the shadowing effect. While the first tends to reduce the number of holes, evident for the 30 nm and 56 nm films, in which the number of holes decreases by about 30% from 159

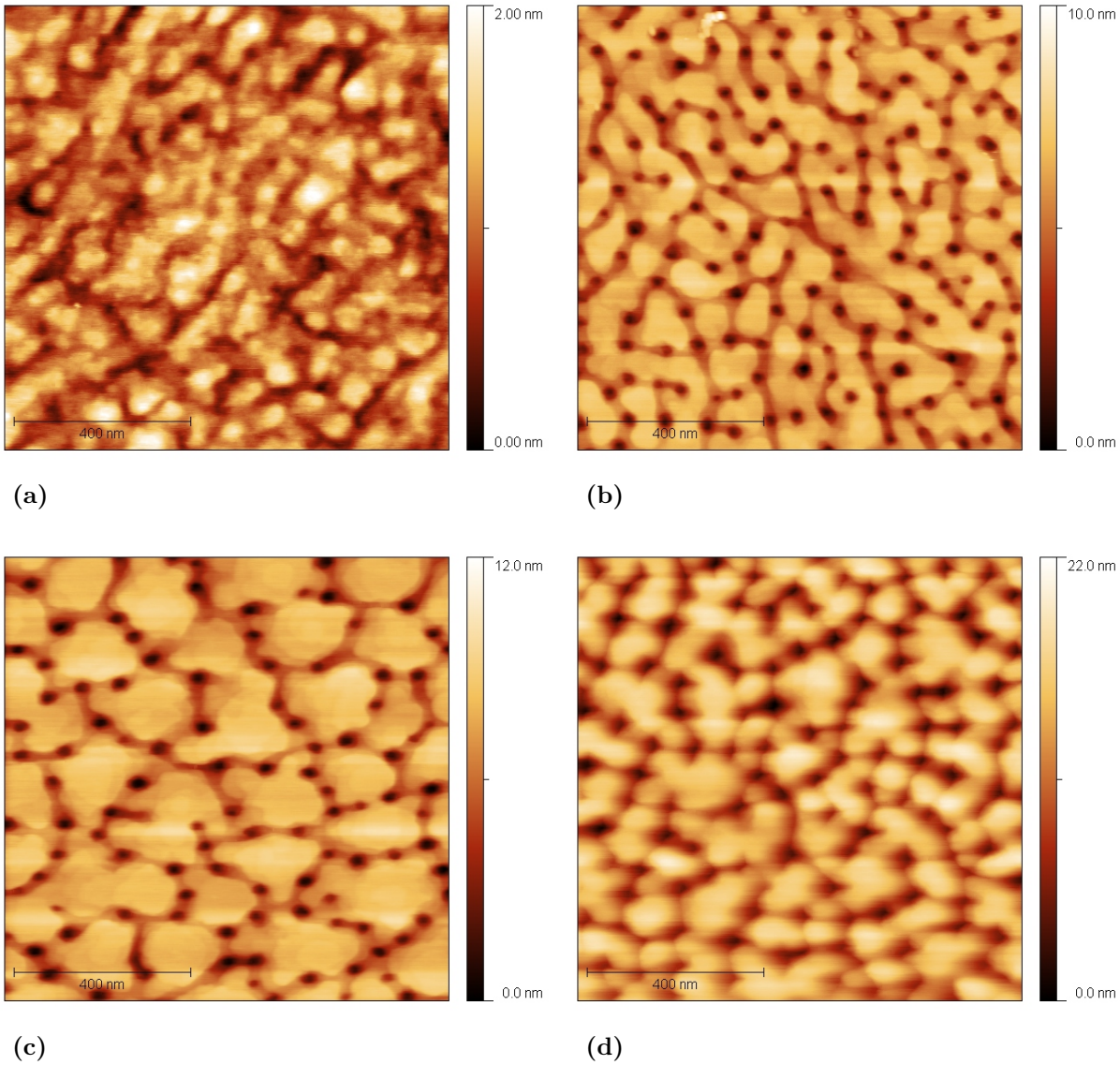

Figure 3.15: 1μm×1μm AFM images of the LSMO thin films deposited for different times corresponding to different thicknesses (a) 7 nm, (b) 30 nm, (c) 56 nm and (d) 110 nm.

Table 3.2: Morphological parameters of the LSMO films having different thicknesses.

Film thickness (nm)	RMS Roughness (nm)	P-V distance (nm)	Threshold Criterium (nm)	Nr. of Holes	Perentage of Total Area (%)
7	0.29	2	1	92	43.4
30	1.3	6.6	4	159	13.9
56	1.67	9.75	4	106	7.1
110	3.45	19.82	9	124	16.4

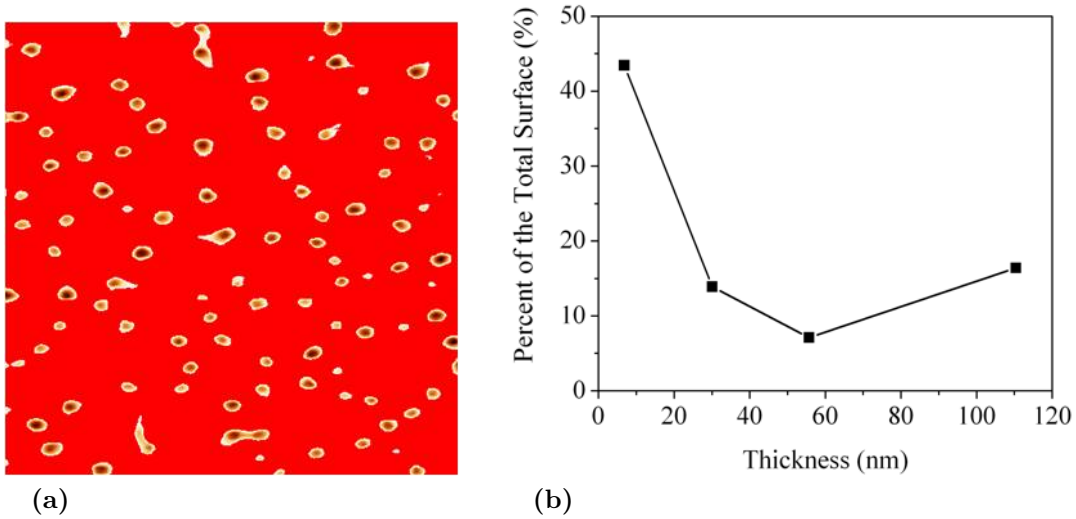

Figure 3.16: (a) Typical processed image for number of hole determination; (b) The variation of the percent of the surface covered by holes as a function of film thickness. The line between pints is to guide the eyes.

to 106 holes, the other leads with the increase in peak-to-valley distance and the enlargement of the hole area. The percentage of the film area "covered" by holes reaches a minimum of 7.1% at 55.7 nm only to rise again for the 110 nm film up to 16.4%, suggesting the predominance of shadowing. To better illustrate this we have applied the same algorithm as the one presented in the previous section to determine the number of holes and the percent of the total area that they occupy. Figure 3.16 presents the results of this analysis.

The role of substrate treatment on the morphology of the films

For a better control of film morphology and a better understanding of the deposition processes many groups have performed a surface treatment of the STO (001) [51, 52] substrates in order to reveal the step structure of the substrate surface and obtain a uniform TiO_2 termination layer. We have treated our substrates for 10 sec in a NH_4 buffered HF solution, and then annealed them at 950 °C for 12 min. in flowing oxygen, 15 l/h. AFM investigation of the as treated (001)STO surface is presented in Figure 3.17a. As it can be seen, after the thermo-chemical treatment of the substrate surface, atomically flat surfaces are present. On top of the as treated substrate we have deposited an approximately 25 nm thick LSMO film at 800 °C. The AFM image of the resulted film is presented in Figure 3.17b. For comparison, the film presented in Figure 3.12c is a film deposited under the same conditions on an untreated STO substrate. The morphological features exhibited by the two films are similar, and they were discussed in the previous section. The difference comes from the arrangement of the grains present at the films' surface. In the case of the untreated

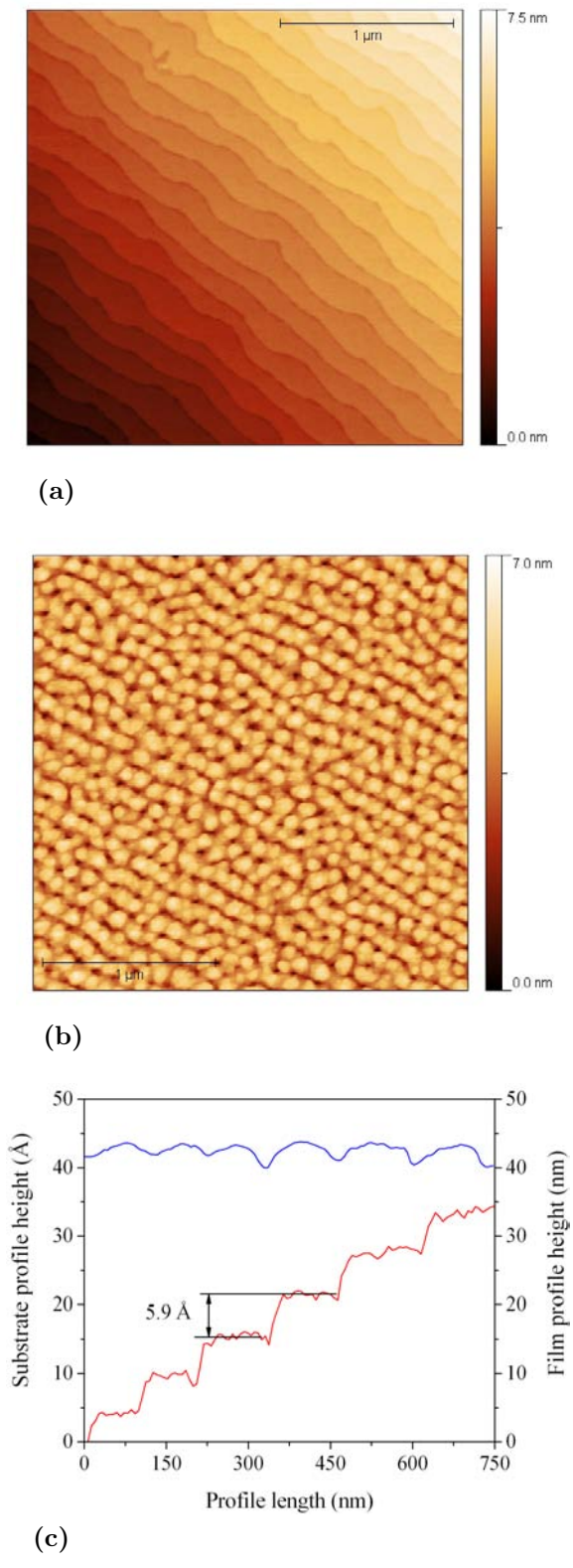

Figure 3.17: (a) Treated STO(001) surface, image shows steps revealed after treatment; (b) LSMO thin film deposited on top of the treated STO substrate, presented in (a); (c) LSMO grain (blue) periodicity and STO step (red) periodicity coincide.

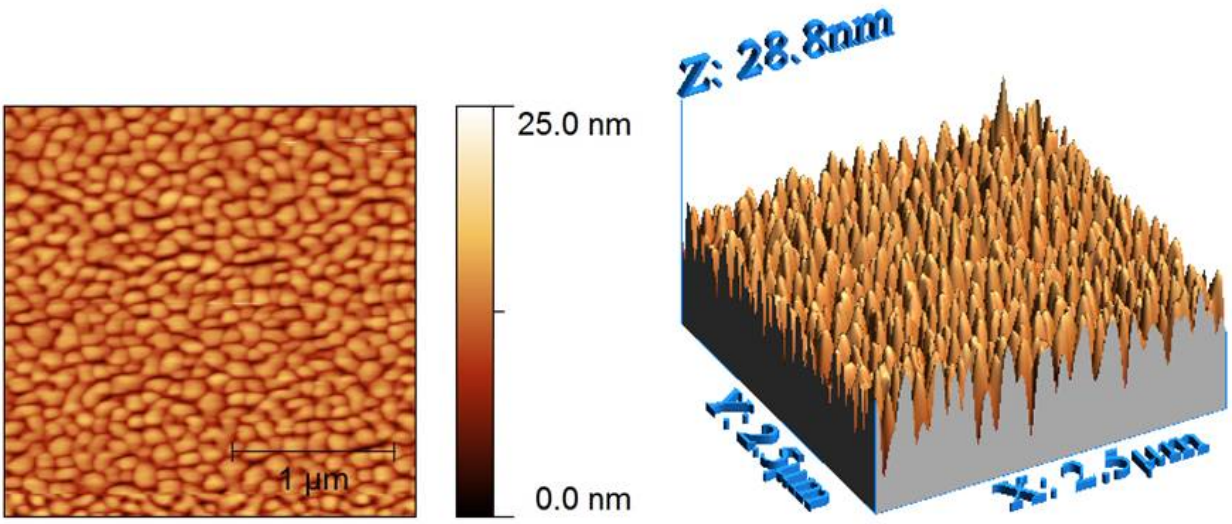

(a) **(b)**

Figure 3.18: (a)LSMO film grown at a target-substrate distance of 5.5cm. Surface shows grains separated by deep (20nm) crevasses. (b) 3D image of the film reveals columnar growth of the grains, typical of zone I of the SZD.

substrate they are randomly distributed on the surface, while on the substrate they arrange themselves along the step surface, and their lateral dimensions are of the order of magnitude of one step, as shown in the image presented in Figure 3.17c. This periodicity is a suggestion that the nucleation and growth process are step-mediated, that is adatoms migrate to step sites and nucleate grains which in turn grow up to the step's edge [53].

3.2.2 The influence of target-substrate distance on the morphology of the films

Studies performed on LSMO thin films grown on STO (001) by PLD have demonstrated that film morphology dramatically depends on the target-substrate distance during the film deposition. Haghiri-Gosnet *et al.* [54] , using Structure Zone Diagrams proposed by Thorton [84], have shown that LSMO switches from a zone T morphology to zone II with exceptional flatness, upon the reduction of the target-substrate distance (d_{T-S}). Following their conclusions, we have reduced the d_{T-S} from 8.5 cm to 5.5 cm. The result is presented in the Figure 3.18. Film quality is very poor with respect to the film deposited at 8.5 cm away from the target. This could be caused by a high deposition rate which causes grains to grow very fast leaving large holes in the film, as illustrated by the high peak-to-valley distance, 21 nm. The film morphology suggests a columnar growth (Fig. 3.18b), which is typical for zone I of the structure zone diagram.

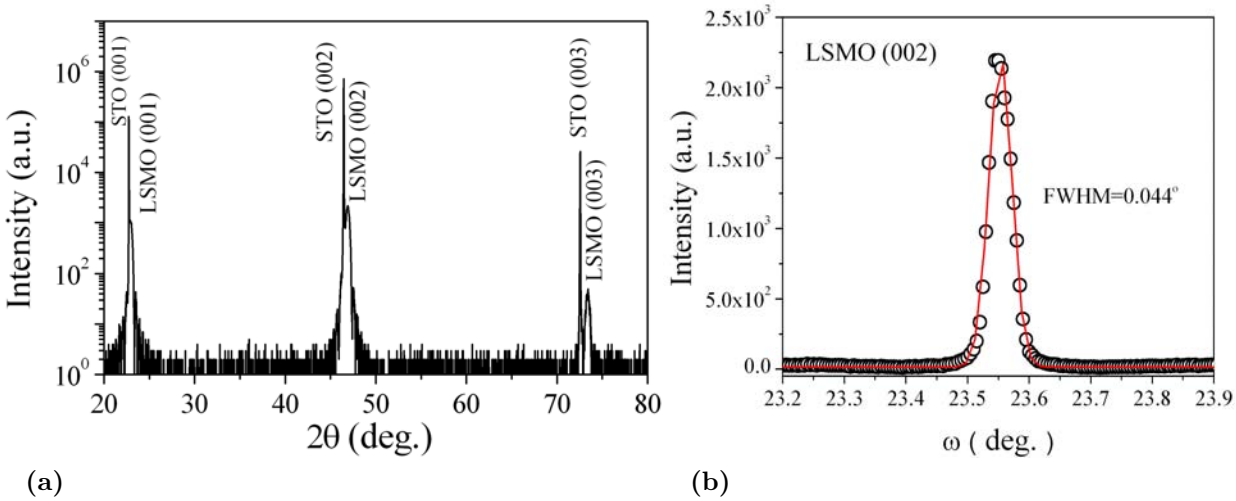

Figure 3.19: (a) Typical $2\theta/\omega$-scan of a LSMO thin epitaxial film grown on STO (001) substrate;(b) ω-scan of the (002) LSMO peak.

3.2.3 Structural properties of epitaxial LSMO thin films

General structural properties of LSMO epitaxial thin films

A typical $2\theta/\omega$ scan for a LSMO film grown on a STO(001) substrate is shown in Figure 3.19a. The XRD pattern exhibits only (00l) LSMO reflexions indicating that the LSMO film grows epitaxially on the substrate. The ω-scan on the (002) LSMO peak has a FWHM of 0.04°, as determined from a Gaussian fit of the profile, demonstrating an excellent out-of-plane alignment of the film. The ω-scans, revealed also the presence of two satellite peaks,

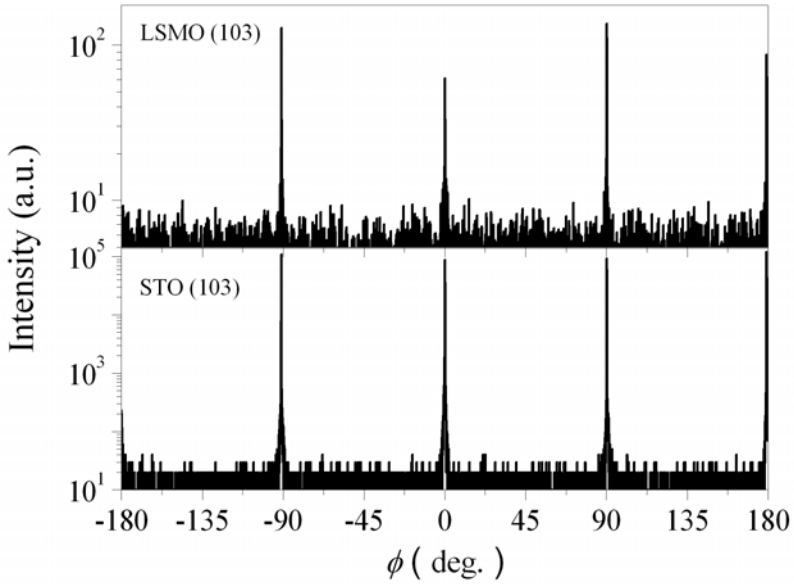

Figure 3.20: ϕ-scan around the (103) peak of STO and LSMO show a $[100]_f \| [100]_s$ in-plane orientation relationship.

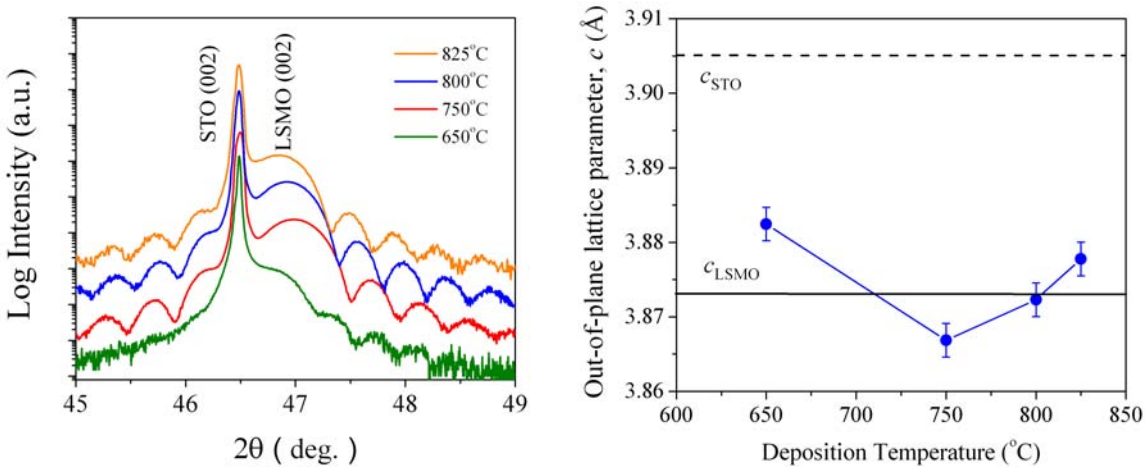

Figure 3.21: (a) $2\theta/\omega$-scan around the (002) peaks of the STO substrate and the LSMO film, respectively, deposited at different temperatures. (b) Evolution of the out-of-plane parameter, c, as a function of the deposition temperature. The uncertainty in the lattice parameter, c, evaluation was deduced from Eq. 2.1.

not shown in Figure 3.19b, which will be discussed in a following paragraph. In order to determine the in-plane orientation of the epitaxial LSMO thin films with respect to the STO substrate, we have performed ϕ-scans on the (103) peak of LSMO and STO, respectively. A typical ϕ-scan is shown in Figure 3.20. As it can be seen, the film-substrate orientation relationship is $[100]_f \| [100]_s$. The mean FWHM value of the ϕ-scan peaks is of 0.08° for the STO substrate and of 0.1° for the LSMO film, determined by averaging the FWHM of the four peaks in Figure 3.20. The small difference between the FWHM values of the substrate and film is an indication of the high degree of in-plane orientation of the LSMO film. The $2\theta/\omega$ and ϕ-scans have revealed that the LSMO films are epitaxially grown on STO (001)with a $(001)[100]_f \| (001)[100]_s$ epitaxial relationship.

Evolution of the structural parameters of LSMO thin films as a function of deposition temperature

It has been established that the structural parameters of the LSMO thin epitaxial films are highly sensitive to a series of deposition parameters. One of them is the substrate on which they are deposited, which because of lattice mismatch, causes different types of strains in the film. This is due to the fact that, upon growth, the film tends to adapt its lattice parameters to those of the substrate. For example, for films deposited on $LaAlO_3$ substrates, which have a lattice constant smaller than that of LSMO with a mismatch of -2.24%, the strain is compressive, while on the other hand, in the case of $SrTiO_3$ the mismatch is 0.41% yielding a tensile strain in the films. Besides substrate induced strain, the oxygen content of the film strongly affect their structure, as will be shown later in this Chapter. The oxygen

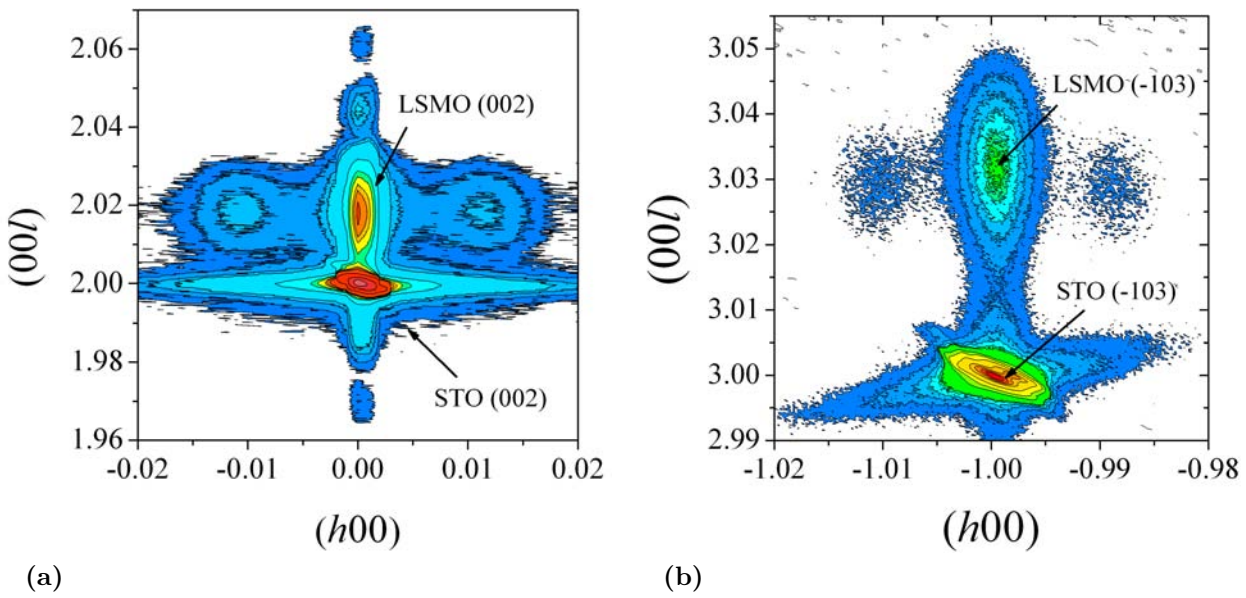

Figure 3.22: Reciprocal Space Maps of the STO//LSMO substrate-film system, around the: a) (002) and b) (103) peaks.

stoichiometry is controlled by the partial oxygen pressure during deposition, post-deposition annealing and substrate temperature. Also, it has been shown that film thickness influences the structural behavior of the films, since the structural parameters tend to relax to their bulk value as the thickness is increased.

In order to study the influence of the deposition temperature on the lattice parameters of our films, four LSMO films were deposited at 650, 750, 800 and 825 °C, in the conditions mentioned in the previous chapter. The $2\theta/\omega$-measurements of the LSMO (002) peak are presented in Figure 3.21a, together with the evaluation of the out-of-plane lattice parameter, c, Figure 3.21b. It can be observed that there is an abrupt decrease of the lattice parameter from 3.882±0.002 Å, for the film deposited at 650 °C, to 3.867±0.002 Å, for the film deposited at 750 °C. This can be explained by the fact that increasing the deposition temperature the oxygen content increases. In turn, this leads to a transformation of the valence state of the manganese ions from Mn^{3+} to Mn^{4+}, according to the valance balance. However their respective ionic radii are different: Mn^{3+} has a radius of 0.07 nm, while Mn^{4+} has a radius of 0.05 nm. The decrease of the lattice parameter induced by the change of the valance state of manganese is only partially compensated by the increase caused by the absorption of an O^{2-} ion in the lattice, leading thus to a net decrease of the lattice parameter [56]. As the deposition temperature is further increased an increase of c is observed. This increase has been previously observed by Sun *et al.* [57] when annealing $La_{0.66}Ca_{0.33}MnO_3$ films in vacuum, and it was attributed to oxygen release. This effect was more pronounced in films deposited on STO substrates as the lattice mismatch was higher in this case. In view of these observations, we may suppose that high deposition temperatures, 825 °C, and relatively low

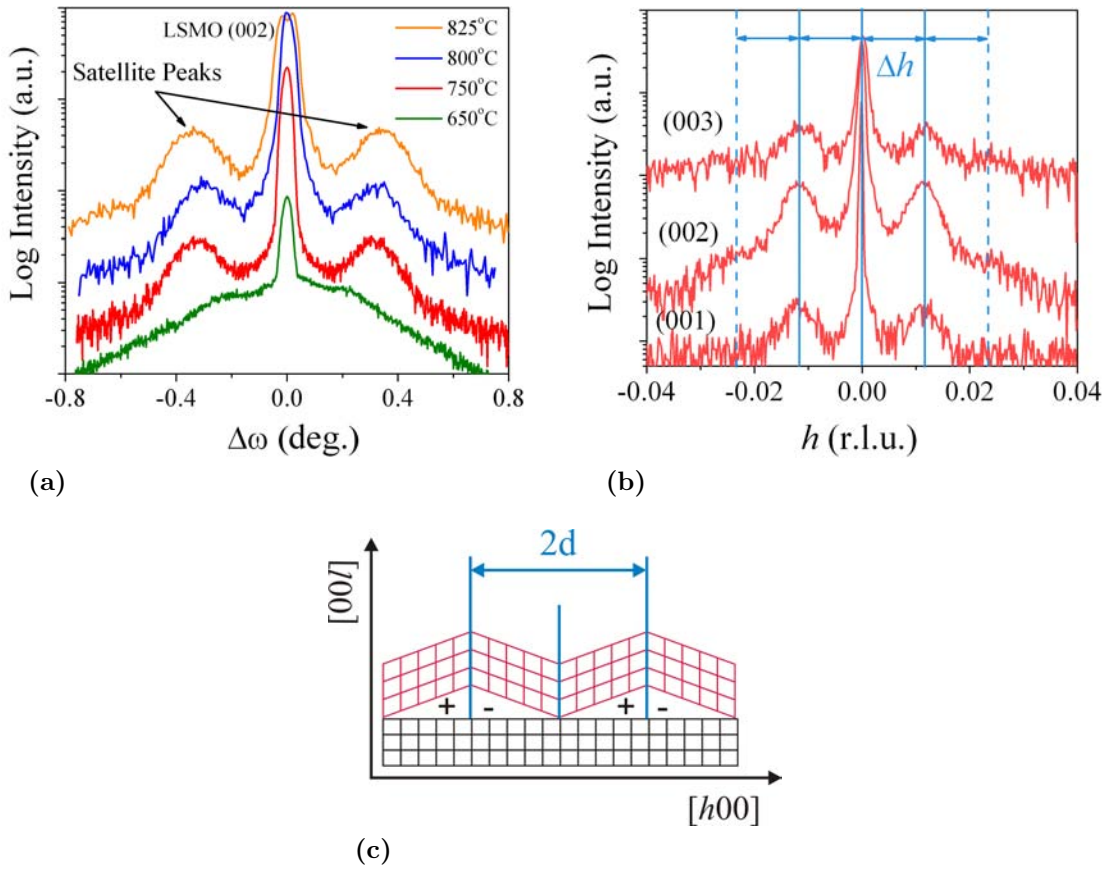

Figure 3.23: (a) Rocking curves around the LSMO (002) peak for films deposited at different temperatures, showing that twinning occurs between 650°C and 750°C. (b) h-scan, indicating the periodic nature of film twinning and a scheme representing periodic twinning of a film, (c.

deposition pressures, 40mTorr, prevent the attainment of desired oxygen stoichiometry, and thus an increase of the out-of-plane lattice parameter. Another interesting observation is that in the diffractogram of the film deposited at 650 °C, the higher order diffraction fringes are not visible for lower values of 2θ. This fact could arise due to structural inhomogeneities of the film and were previously reported on Ir thin films [58]. The hypothesis is sustained by the R vs. T measurements which indicate a double transition temperature for this film.

As far as the in-plane lattice parameter is concerned, in order to determine its value, we have performed studies on the (002) and ($\bar{1}03$) lattice planes. They consisted in mapping the reciprocal space around the respective reflections. The results for the film deposited at 800 °C are presented in the Figure 3.22. The ($\bar{1}03$) peak of LSMO has the same in plane position as the ($\bar{1}03$) STO peak. This is an indication that the LSMO film is fully stressed in plane. Thus, the lattice constant is equal to that of the substrate, 3.905 Å. This is found to be true for all the other samples. A distinct characteristic of our maps consists in the presence of two satellite peaks. Their origin is investigated in the next Section.

Periodic twinning of LSMO thin epitaxial films

Upon performing ω-scans around the LSMO (002) peak, in order to determine the out of plane distribution of film crystallites, two satellite peaks were observed around the central peak. The evolution of the peaks as a function of deposition temperature is presented in the Figure 3.23a. At 650 °C, these peaks can be barely observed, while at 750 °C they are clearly visible. These peaks originate from the existence of out of plane twinning of the LSMO thin films. Besides the elastic, normal, strains that are due to the lattice parameter mismatch of the film and the substrate, there is another type of distortion in coherent LSMO films, elastic shear [9]. This distortion is due to the rhombohedral symmetry of LSMO at room temperature, when it is deposited onto a cubic substrate, which is the case of STO (001). The contribution in elastic energy that results from the mismatch in the magnitude of lattice parameters can be diminished by the formation of misfit dislocations at the film/substrate interface. The distortion related to shear strain can be reduced by the formation of structural domains with an alternating sign of shear [59]. These structural domains can also be called twins since the crystallographic orientation of neighboring domains is similar to that of twins. However, Gebhardt *et al.* [59] made a distinction between a periodic microtwinning of the films and tilted twin domains. The first, due to their periodicity, give rise to satellite peaks which emerge with a constant in-plane momentum transfer Δk, irrespective of the diffraction plane, implying periodic height modulation. This behavior is encountered in relatively thin films, up to 30 nm. In thicker films, the situation is different, in the sense that the tilted lattice planes evolve into large, tilted domains. They give rise to the observation of twinned peaks, but their position varies according to the lattice plane investigated. In order to elucidate the nature of the observed satellite peaks, we have performed reciprocal space scans in the h-direction, h-scans on the (001), (002) and (003) planes. Our measurements, Figure 3.23b, reveal that the position of the additional peaks does not vary as a function of the lattice plane investigated, suggesting that our film has been subjected to periodic twinning, represented schematically in Figure 3.23c. This result is somewhat to be expected since we are dealing with films having around 25 nm in thickness. In order to determine the direction in which the periodic twinning takes place we have performed ω-scans at various values of the ϕ angle, which is the angle between sample orientation and in-plane axes [100], or [010]. The results, Figure 3.24a, are indicating that the twinning occurs both in the [100] and the [010] directions. Each of the two branches observed in Figure 3.24b correspond to one of the twinning directions, Figure 3.24c. Similar results, have been previously obtained by Pflanz and Moritz [60] in their theoretical study of surface faceting. However, in our case it is clear that we are not dealing with surface faceting since the additional peaks have the same position, namely (002). We do not exclude the possibility of film twinning occurring in the plane of the film [59, 61], but our measurements do not permit to draw us such a

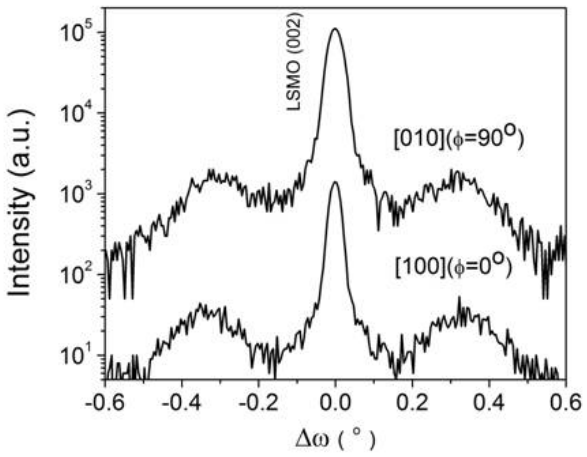

(a)

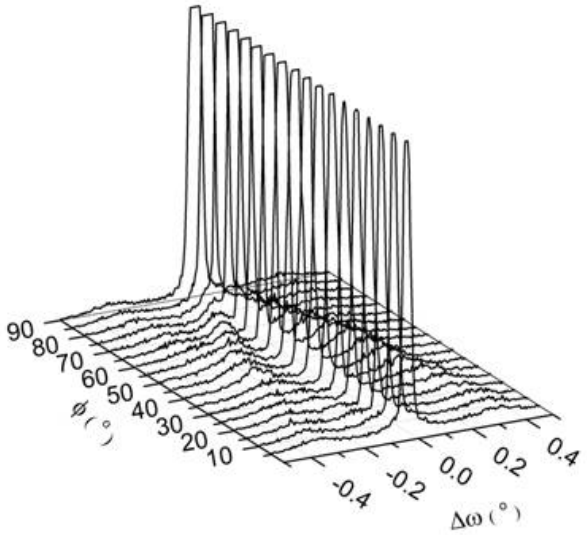

(b)

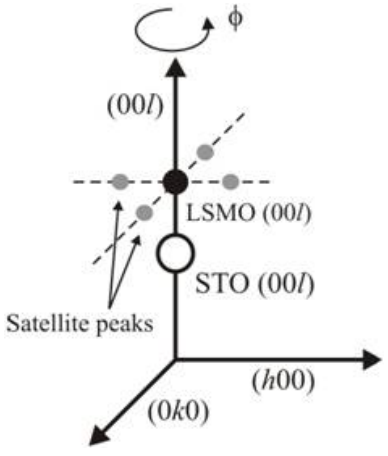

(c)

Figure 3.24: (a) Rocking curves around the LSMO (002) peak along the [100] and [010] crystallographic directions. (b) Rocking curves around the LSMO (002) peak, with different in-plane orientation of the film, revealing the twinning directions of the film. (c) Diagram of the reciprocal space of the STO//LSMO substrate-film system, with periodic twinning of the film.

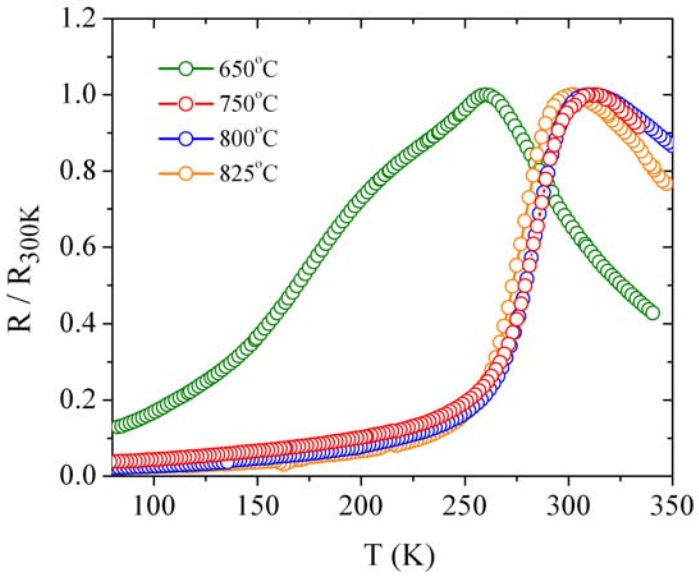

Figure 3.25: Normalized Rvs.T measurements of LSMO thin films deposited at various temperatures.

conclusion, since we are studying the films on the out-of-plane direction. Further studies have to be carried out in order to determine a link between twin domains and electric and magnetic properties of our films. As we have stated previously, these properties are highly dependent, due to their origin, to structural features of the film. Other studies could include the influence of film thickness, and substrate temperature on crystallite twinning, as we have observed that high substrate temperatures favor twin formation. Also, Jin *et al.*[61] have shown that films tend to relax, by twin formation as their thickness increases.

3.2.4 Electrical characterization of LSMO epitaxial thin films

In order to evaluate the transport properties of the deposited LSMO thin films we have performed R(T) measurements on our samples, in the 80-340 K range, using the four probe technique. No lithographic process was performed on the films prior to their measurement. Transport characteristics are crucial to the evaluation of film properties, as the presence of a metal-insulator transition is an indication of the ferromagnetic-paramagnetic transition. Also, lattice strains induced by substrate-film lattice mismatch, film thickness, oxygen content and so on, are intimately related to the magnetic and transport properties, because of the mechanisms that generate ferromagnetism and metallic conductivity in such systems.

For our preliminary electrical study, shown in Figure 3.25, we have chosen to investigate the role of the deposition temperature on the temperature dependence of resistance, linking this behavior to the structural findings presented in the previous chapter. As it can be observed from Table 3.3, the variation of the metal-insulator transition temperature, T_{MI},

Table 3.3: Variation of the metal-insulator transition temperature and out-of-plane lattice parameter as a function of the film deposition temperature.

Deposition Temperature (°C)	Metal-insulator transition temperature, T_{MI} (K)	Out-of-plane lattice parameter, c (Å)
650	260	3.882
750	311	3.867
800	310	3.872
825	303	3.877

defined as the temperature for which the maximum in resistance is achieved, closely follows the behavior of the out of plane lattice parameter, c. As c decreases from 3.882 Åto 3.867 Å, there is a dramatic increase in the transition temperature from 260 K to 311 K. Also an interesting feature on the R(T) dependence for the film deposited at 650 °C is the presence of kink, around 200 K, which is an indication of the presence of a second transition, having a lower transition temperature, due to the existence of a secondary phase(s). This dependence confirms the hypothesis stated in the paragraph concerning the structural analysis of the films. As the deposition temperature is increased from 750 to 800 °C, the transition temperature remains relatively constant, approximately 310 K. It is to be noted that the lattice parameter exhibits only 0.13% increase. For the film deposited at 825 °C, the increase of c, is accompanied by decrease of the transition temperature to 303 K. Sun *et.al.* [57] argue that annealing in vacuum leads to the release of oxygen which, besides expanding the lattice, leads to the decrease of T_{MI}, as Mn^{4+} changes to Mn^{3+}. As stated before, it is our belief that the deposition of LSMO films in relatively low pressure, 40 mTorr of argon and oxygen mixture, at high 825 °C, temperature may cause oxygen release which leads to the observed behavior.

The preliminary study presented above is an indication that the electrical properties of LSMO thin films are highly sensitive to deposition conditions, which in turn determine the structure of the films, and especially to the stabilization of the oxygen stoichiometry. Oxygen content dependent electrical properties are expected since the metallic conduction mechanism as well as ferromagnetism are determined by the presence of O^{2-} ions in the lattice. In order to quantify systematically the influence of oxygen content on the physical properties, in the next Section we have performed annealing studies of LSMO thin films in different O_2:Ar gas mixtures.

3.3 Oxygen incorporation effects on $La_{1-x}Sr_xMnO_3$ epitaxial thin films

From a chemical point of view $La_{1-x}Sr_xMnO_3$ is substitutional solid solution, in which divalent Sr^{2+} ions substitute trivalent La^{3+} ions at their respective lattice sites. In the end member $LaMnO_3$, the manganese ions have a +3 valence state. Upon substitution with divalent ions, *e.g.* Sr, Ca, Ba, the Mn^{3+} state changes to Mn^{4+} in order to preserve the overall charge balance. The resulting Mn^{4+}/Mn^{3+} ratio corresponds to the doping degree, *i.e.* to $x/(1-x)$, so that the chemical formula can be written as $La^{3+}_{1-x}Sr^{2+}_{x}Mn^{3+}_{x}Mn^{4+}_{1-x}O^{2-}_{3}$ or, alternatively, as $(La^{3+}Mn^{3+}O4^{2-}_{3})_{1-x}(Sr^{2+}Mn^{4+}O^{2-}_{3})_{x}$.

Introducing Mn^{4+} valence ions in the crystal lattice, plays a crucial role in determining the physical properties of the compound. Namely, through the mechanism of double exchange, first described by Zener [25, 26], the extra electron present in Mn^{3+}, occupying a e_g energy level, can be transferred to a neighboring Mn^{4+} e_g empty level, by means of a double exchange of electrons mediated by the O^{2-} ion present in a Mn^{4+}-O^{2-}-Mn^{3+} bond. Anderson and Hasegawa [27] have shown that electron transport is a function of the relative angle between the "core" t_{2g} electrons of the two Mn ions. This fact, corroborated with the Hund coupling that exists between the e_g electron and the three t_{2g} electrons, explains the existence of a ferromagnetic metallic state and a paramagnetic insulating one for optimum doped manganites. Also, one of the most interesting properties of doped manganites, colossal magnetoresistance, can be explained within the framework of the double exchange model, as an external magnetic field acts as to align the t_{2g} core spins, enhancing e_g electron mobility, determining thus a dramatic electrical resistance drop, ∼1000%, *i.e.* colossal, in the vicinity of the Curie temperature, Jin *et al.* [45].

3.3.1 $La_{1-x}Sr_xMnO_{3+d}$ defect model

Roosmalen *et al.* [62] published a series of articles concerning a defect model for $LaMnO_3$ when it is subjected to an excess in the oxygen stoichiometry, d. From neutron diffraction data, thermogravimetry, titration methods and charge balance they have constructed a model in which the presence of an excess in oxygen concentration leads to the formation of an equal number of La and Mn vacancies accompanied by a change in the Mn valance state from +3 to +4, increasing thus the overall Mn^{4+}/Mn^{3+} ratio. The defect equation reaction that they proposed was:

$$LaMnO_3 + \frac{d}{2}O_2 \rightarrow (La\square'''_{d/3})(Mn^{\bullet}_{1-2d}Mn^{\circ}_{2d}\square'''_{d/3})O_{3+d}. \tag{3.6}$$

From the above equation, it can be seen that an excess d of oxygen produces cationic vacancies, on La and Mn sites, denoted by □. Both type of vacancies have the same charge,

3+, symbolized by $'''$. Besides vacancy creation, the presence of extra oxygen in the lattice produces Mn^{4+} ions, $Mn^{\bullet}$. The Mn^{3+} ions are denoted as Mn°.

The Roosmalen equation can be rewritten in the conventional Kröger-Vink notation, the standard in expressing defect reactions as:

$$6Mn_{Mn} + \frac{3}{2}O_2 \leftarrow V_{Mn}''' + V_{La}''' + 6Mn_{Mn}^{\bullet} + LaMnO_3. \tag{3.7}$$

In equation 3.7 vacancies are marked as V and the corresponding negative charge, $'''$. Also, Mn^{3+} is considered to be "neutral", so that Mn^{4+} has only one extra positive charge, $\bullet$. Equation 3.7 does not change the results of Roosmalen *et al.* [62] as the result of excess oxygen is the same, *i.e.* creation of equal amounts of La and Mn vacancies and creation on Mn^{4+} ions. In their papers Roosmalen *et al.* [62] also studied the effects of excess oxygen incorporation in Sr doped LMO, $La_{1-x}Sr_xMnO_3$. As is to be expected, qualitatively the results are the same as in the case of LMO:

$$6Mn_{Mn} + \frac{3}{2}O_2(g) \rightarrow V_{Mn}''' + V_{Mn}'''' + V_{La}''' + V_{Sr}'' + 6Mn_{Mn}^{\bullet} + La_{(1-x)}Sr_xMnO_3, \tag{3.8}$$

that is, cationic, La, Sr and Mn, vacancies are produced and also supplementary Mn^{4+} ions. In the case of LSMO, the Mn^{4+}/Mn^{3+} ionic ratio is $x + 2d/(1 - x - 2d)$.

From the above studies the main conclusion that can be drawn is that there are two mechanisms that can alter the hole doping in LSMO: the first is straight forward by divalent ion doping, while the second is by creating an oxygen excess in the LSMO lattice. However, the latter has side effects in terms of lattice defects, as vacancies are created within the crystal strucutre. In the present Chapter we set out to investigate the effects of oxygen incorporation in epitaxial LSMO thin films deposited on STO (001) substrates. We study the influence of oxygen on the structural, magnetic and electric properties. An original approach is proposed in the evaluation of the structural effects that excess oxygen produces in the film lattice. Using the model proposed by Boulle *et al.* [76] the measured two-component rocking curves were simulated in order to extract the correlation length of and mosaicity created by the oxygen induced cationic vacancies. As it will be seen LSMO thin films are quite susceptible to oxygen incorporation and their properties may suffer important variations with the oxygen content. In order to obtain reproducible films for more sensitive applications, like tunnel junctions or spin valve systems, a systematic study of these effects is necessary.

3.3.2 Overview of oxygen incorporation effects in doped lanthanum manganites

The electric, magnetic and structural properties of epitaxial manganite thin films can be modified by the amount of oxygen doping and additionally by means of the lattice distortion caused by the mismatch between lattice parameters of the film and those of the substrate, respectively. For example, a whole range of magnetic anisotropies in LSMO thin films have been stabilized changing the substrate on which the films were grown: on LAO (001) the films are subjected to compressive strain that lead to an out of plane magnetic easy axis, Dörr [55], on STO (001) the film is subjected to tensile strain and it exhibits biaxial anisotropy Suzuki *et al.* [65], while recently, on NGO (001) and (011) there have been reports of uniaxial in plane anisotropy, Boschker *et al.* [12]

In doped lanthanum manganite thin films oxygen content plays an important role in determining their physical properties as it acts both on the Mn^{4+}/Mn^{3+} ratio as well as on the lattice distortion, modifying the c/a ratio, usually through the alteration of out-of-plane parameter, c, as the in-plane parameter, a, matches the one of the substrate for film thicknesses that are situated below the critical value at which relaxation occurs. There have been papers that have tried to distinguish between the two effects by depositing films on different substrates and varying the oxygen pressure during deposition and by post-deposition annealing. Sakai *et al.* [64], have deposited $La_{0.6}Sr_{0.4}MnO_{3-d}$ thin films on STO (001) and LAO (001) substrates at 750 °C varying the oxygen pressure during deposition and subsequent oxygen annealing from 0.3 to 300 mTorr. They found there is a limiting oxygen pressure around the value of 3 mTorr above which the lattice easily incorporates oxygen. For oxygen deficient samples, oxygen incorporation results in an improvement of structural quality, as the FWHM of the rocking curves decreases with increasing the oxygen content. This fact is consistent with the findings of Sirena *et al.* [78], which pointed out that in the films that have oxygen vacancies and are subjected to oxygen annealing, their respective coercive fields decrease as the number of oxygen vacancies decreases. The coercive field of magnetic films is sensitive to structural defects, as the latter act as to pin domain walls. Another interesting fact pointed out by Sakai *et al.* [64], is for the LSMO film deposited on LAO (001) where they found a Mn^{4+} content of 0.175, for which, from the phase diagram determined by Urushibara *et al.* [28], the film should have been an antiferromagnetic insulator. However, the film exhibited a metal-insulator transition, a phenomenon which the authors attributed to the substrate induced compressive strain on the film. For under-doped manganite thin films (x<0.3), Murugavel *et al.* [68], conducted an extensive study on $La_{1-x}Ca_xMnO_3$, $La_{1-x}Ba_xMnO_3$ and $LaMnO_3$ deposited on STO, LAO and LSAT substrates. After deposition they performed an annealing of the films in flowing oxygen at atmospheric pressure at temperatures varying from 750-900 °C. In all their samples they observed a systematic

increase of the metal-insulator transition temperature, T_{MI}, with the increase of the annealing temperature. All of the measured T_{MI} were higher than the temperatures reported in the literature for bulk samples having the same doping level. They concluded thus, that in the under-doped regime, the enhancement of the transition temperature is not related to the substrate induced strain, as in the case of Sakai*et al.* [64], but rather to an oxygen excess that increases the Mn^{4+}/Mn^{3+} ratio, as pointed out by Dabrowski et al. [70]. An increase in the Mn ionic ratio corresponds to an increase in the hole doping level.

Prellier *et al.* [67], have studied the properties of $La_{1-x}Ca_xMnO_3$ thin films, varying x from 0.1 to 0.5, annealing them in pure oxygen and pure argon at 800 °C for 10 h. As confirmed by Murugavel *et al.* [68], in the under-doped regime there is quite a dramatic increase of T_{MI}, from 240 K to 270 K, for the as-deposited and oxygen annealed film. The saturation magnetization value is 3.75 μ_B for the as-deposited films, and it decreased to 3.59 μ_B after oxygen annealing. Again, this decrease has been ascribed to the increase of Mn^{4+} content, as oxygen incorporation created cationic vacancies. The transition temperature increase is not as evident for the sample having a doping level of x =0.5. The authors noted that oxygen annealing produces a shift in the magnetic phase diagram of the oxygen annealed samples compared to that of bulk material, as high transition temperatures can be achieved at lower concentrations of Ca, by means of excess oxygen in the lattice. Another interesting fact pointed out in the paper is that temperature alone, for the samples annealed in argon, changes only to a little extent the transition temperature of the film with respect to the as-deposited one.

3.3.3 Experimental

The LSMO epitaxial thin films were deposited by means of DC Sputtering on (001) $SrTiO_3$ (STO) single crystal substrate in a mixture of Ar and O_2, with a 3:1 ratio at a total pressure of 40 mTorr, from a stoichiometric, 2 inch $La_{0.66}Sr_{0.33}MnO_3$ target. The deposition was performed at a substrate temperature of 650°C. During cooling, at a rate of 10°C /min., an additional annealing sequence was performed at 550°C for 30 min. in 520 Torr of oxygen atmosphere. In order to study the oxygen incorporation effects in LSMO, the film was cut into pieces of about 5×5 mm^2 which were subsequently annealed at 900°C for 1 hour in flowing annealing gas comprised of an Ar and O_2 mixture in a (100%-x):x ratio, with x taking the values 0%, 3%, 10%, 25% and 100%. The structural, X-ray characterization of the films was carried out using a Bruker AXS D8 Discover diffractometer in a high resolution X-ray diffraction (HRXRD) configuration. The magnetic characterization was performed using a Quantum Design SQUID magnetometer. The Mn^{3+}/Mn^{4+} of the samples was determined by X-ray Photoelectron Spectroscopy of the Mn 2p core level lines. Ar^+ ion etching was performed in order to remove contamination layers. The samples were subjected to consec-

utive etchings until, by performing an additional milling, the measured spectra remained unchanged in shape and intensity. Morphology characterizations were performed by means of AFM microscopy in the Contact mode. Electrical measurements were performed in a cryogen-free set-up using the four probe method.

3.3.4 Results and Discussion

Morphologic characterization

The morphologic characterization of the samples was performed by means of AFM in the contact mode. For the measurements we have used the so-called ultra-sharp tips having the tip radius of ∼2 nm. The results for as deposited and annealed samples are shown in Figure 3.26. The morphology of the as deposited film is characterized by the presence of surface grains. The root-mean-square, RMS, roughness is around 2 Å. This very low value is typical for low crystal quality thin films, which is to be expected for the as deposited film, which was grown at 650 °C. As the annealing process is performed, the microstructure changes completely. All the films exhibit a terraced surface, with steps having different widths and edge shapes. A particular feature is present on the surface of the 0% and 3% oxygen annealed films. It can be seen that in both cases small grains may be observed on the otherwise flat step surface. These outgrowths have been studied extensively by Moreno *et al.* [66] on chemically deposited LSMO thin films on STO(001) substrates. HR-TEM and EELS analyses have shown that the outgrowths were La-Sr oxide (LSO) nanoislands. They argue that within the body of the film a phase separation of two dissimilar crystalographic structures occurs. The formation of the nano-islands is seen as the result of the minority phase diffusion towards the surface of the film. This mechanism can be supported for the 0% O_2 annealed film, for which we will show from M(T) measurements that there is, most likley, a distribution of phases that coexist within the film. For the 3% O_2 film the explanation may not be as straight forward. It can be seen from the AFM images that the two morphologies are not similar, as in the case of the 3% film the steps are not very well defined, so that the surface grains may constitute a prelimiary stage towards step formation. The 10%, 25% and 100% oxygen annealed films display the terraced surface without any out-croppings. The edges of the terraces have a different shapes, ranging from rounded features to sharp edges, as is the case of the 100% film. From these images it is impossible to draw any quantitative conclusion with respect to the variation of the edges' shapes. However, qualitatively, we suspect that the driving force behind this evolution is the change of chemical composition of the films, oxygen content wise, which in turn determies a change of the surface energies. A variation of the surface energy may give rise to different step formations.

As a conclusion, our study reveals that upon annealing, irrespective of the annealing gas composition, the poorly defined film morphology evolves into a terraced surface. Pure

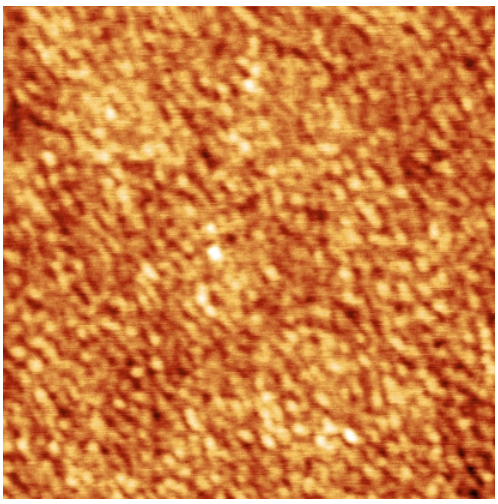

(a) As deposited

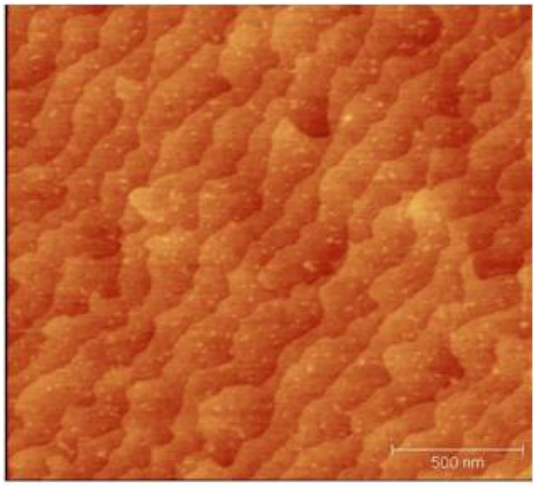

(b) 0% O_2

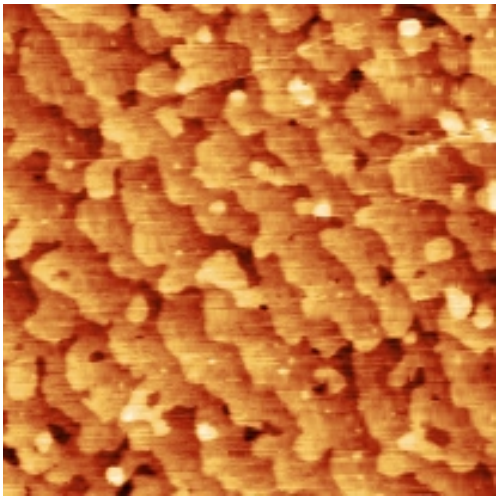

(c) 3% O_2

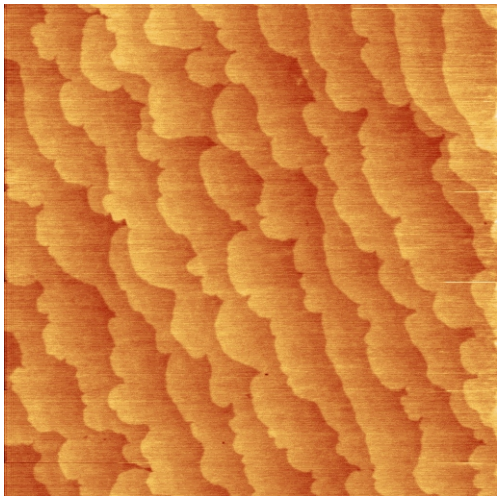

(d) 10% O_2

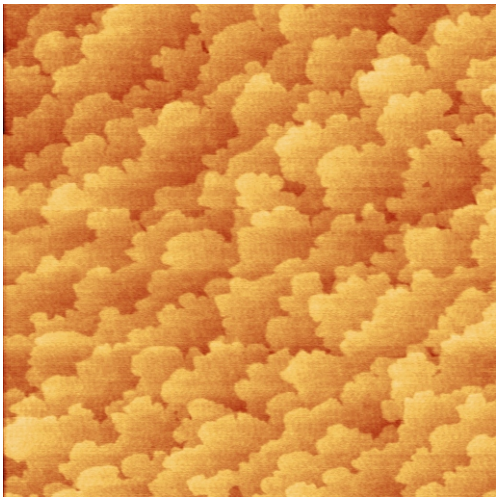

(e) 25% O_2

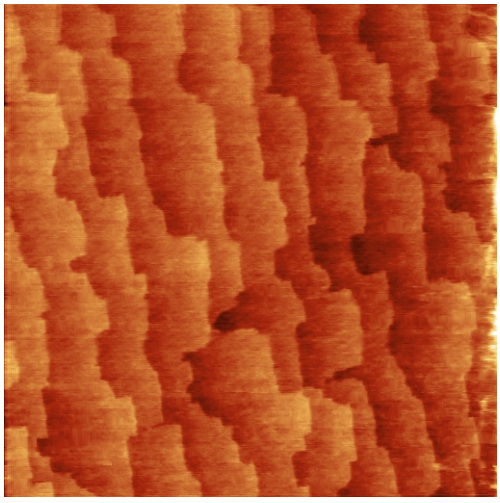

(f) 100% O_2

Figure 3.26: 2μm$\times$ 2μm AFM images of the as-deposited and annealed films

Ar annealing results in outgrowth formation on the step surface, which may originate from an inhomogeneous film phase. Minority phases may diffuse towards the surface leading to nano-island formation. Also, different gas compositions lead to a different oxygen stoichiometry films, which in turn, modifying the film surface energies results in different terrace edge shapes. From the device application point of view, where defect free, chemically pure surfaces are required, our study helps define the appropriate annealing conditions window for good morphological quality films, for 900 °C annealing, oxygen concentrations of the annealing gas above 3%. However, steps widths of ∼100 nm may be too narrow for heterostructure applications, such as spin valves or tunnel junctions, as at the step edges dislocations may form. These defects may subsequently act as scattering centers which reduce the spin coherence length, crucial for developing effective spintronic devices.

HRXRD characterization

$2\theta/\omega$ Scans

Figure 3.27 shows the evolution of the $2\theta/\omega$ scans of the (002) LSMO peak for the different compositions of the annealing gas. All curves could be fitted with a simple semi-kinematical film/substrate model [69]. It turned out that the film and substrate diffract coherently indicating a high structural quality of the films. The film thicknesses are in the 29-31 nm range and the films roughness is less than 1.2 nm. As the oxygen content of the annealing

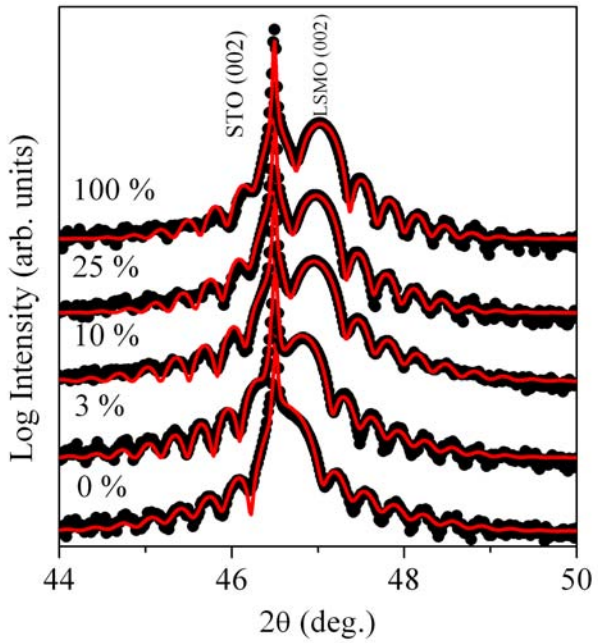

Figure 3.27: $2\theta/\omega$ scans around the (002) peaks of the LSMO films and STO substrate for different values of x=0%, 3%, 10%, 25% and 100% (balck) and the corresponding simulated curves (red).

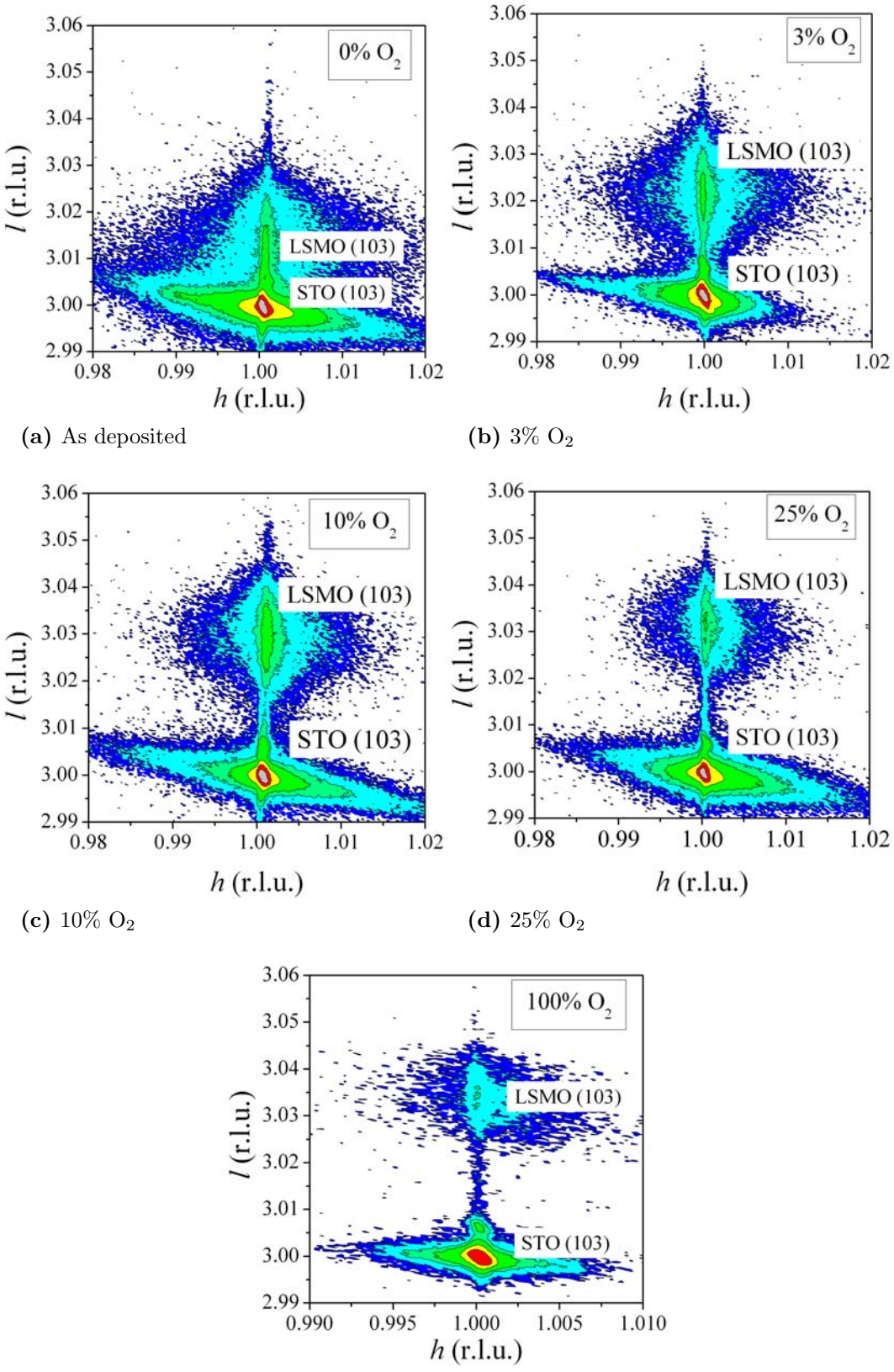

(a) As deposited

(b) 3% O_2

(c) 10% O_2

(d) 25% O_2

(e) 100% O_2

Figure 3.28: Reciprocal space maps around the (103) peaks of the STO substrate and LSMO thin films annealed in (a) 0%, (b) 3%, (c) 10%, (d) 25%, (e) 100% oxygen.

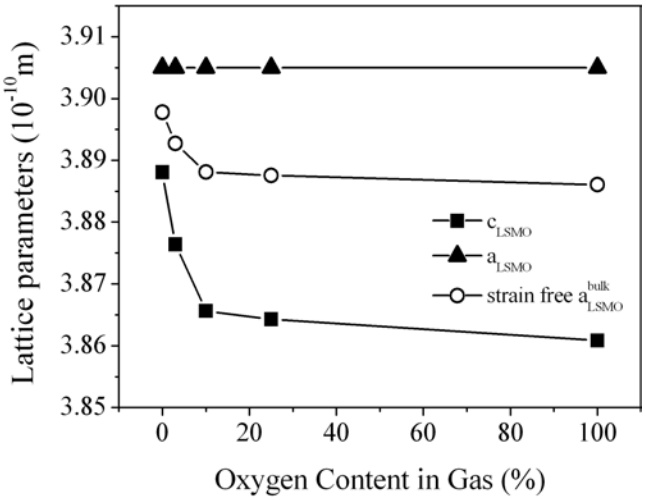

Figure 3.29: LSMO thin films lattice parameters evolution as a function of the oxygen content in the annealing gas.

gas increases one can observe a tendency of the (002) LSMO peak to shift towards higher 2θ values, indication of a decrease of the out-of-plane LSMO lattice parameter, c. The decrease of c is generally regarded as an indication of oxygen incorporation in the LSMO lattice, as the Mn^{3+} valence state changes to Mn^{4+}, which has a lower ionic radius [56]. Dabrowski *et. al.* [70] suggested that the decrease in the lattice parameter can be also ascribed to the creation of vacancies in the lattice due to the excess of oxygen. On the other hand, the observed evolution of the c parameter might also be due to an evolution of the state of strain of the film. In order to discriminate between both contributions we recorded reciprocal space maps around the (103) LSMO and STO reflections. In Figure 3.28 is shown the reciprocal space map for the films annealed in pure argon and argon and oxygen mixtures. As it can be seen, the peaks of the film and substrate have the same value of h, namely 1, indicating that the two lattices are perfectly matched in the in-plane direction, having the lattice constant of the STO substrate, 3.905 Å. In all cases the films are fully strained and the corresponding in-plane strain is $e_{xx} = (a_{STO} - a^{bulk}_{LSMO})/a^{bulk}_{LSMO}$.The strain free parameter of LSMO is denoted a^{bulk}_{LSMO}, so as to distinguish it from the measured (strained) values a and c. Since the same result was found to be true for all the annealed samples, this is a clear indication that the observed evolution of the c parameter is solely related to compositional changes, namely oxygen content. The influence of the oxygen content on the in-plane and out-of-plane lattice parameter is presented in Figure 3.29. We deduce the influence of the oxygen incorporation only, *i.e.* without the effect of strain, according to $a^{bulk}_{LSMO} = (c + \nu_2 a_{STO})/(1 + \nu_2)$, where ν_2 is the biaxial Poisson's ratio which is related to the uniaxial Poisson's ratio through $\nu_2 = 2\nu/(1-\nu)$. In the case of LSMO we have $\nu = 0.4$ [71], and the parameter c is obtained either from the reciprocal space map (Figure 3.28) or from the $2\theta/\omega$ scan (Figure 3.27). It can be seen that the strain free lattice parameter decreases as a function of the oxygen

content in the treatment gas, following two regimes. The first, up to 10%, is characterized by strong decrease of the lattice parameter, indicating a pronounced oxygen incorporation effect in the film lattice. In the second regime, from 10% to 100% oxygen content, the lattice parameter exhibits only a slight decrease. The overall behavior is similar with the random-defect model in LSMO[72] in which the abrupt decrease corresponds to oxygen incorporation in the oxygen deficient phase, while the mild decrease is due to oxygen over-doping.

ω Scans

The ω-scans around the (002) LSMO peaks of the annealed samples are presented in Figure 3.30. All peaks exhibit a profile comprised of a narrow, high intensity component and a broad, low intensity component. The two-component rocking curves of epitaxial thin films have been observed in a wide variety of thin film systems [73, 74, 75]. The presence of the diffuse scattering component stems from the existence of distorted regions (of limited spatial extension) in the film. These regions are situated around defects such as dislocations, grain boundaries, chemical inhomogeneities, etc. The defects are therefore sources of heterogeneous strain in the film, opposed to the growth related homogeneous strain. The coherent part originates from the long-range order inherent in high-quality epitaxial films. Quantitative information regarding the spatial and statistical properties of the strain field, as well as regarding the in-plane coherence length ("crystallite" size) can be deduced from the numerical simulation of such ω-scans [76] in form of the defect correlation length, ξ, and the level of disorder, σ_∞.

Miceli *et al.* [85] were the first to propose a phenomenological theory of the two-

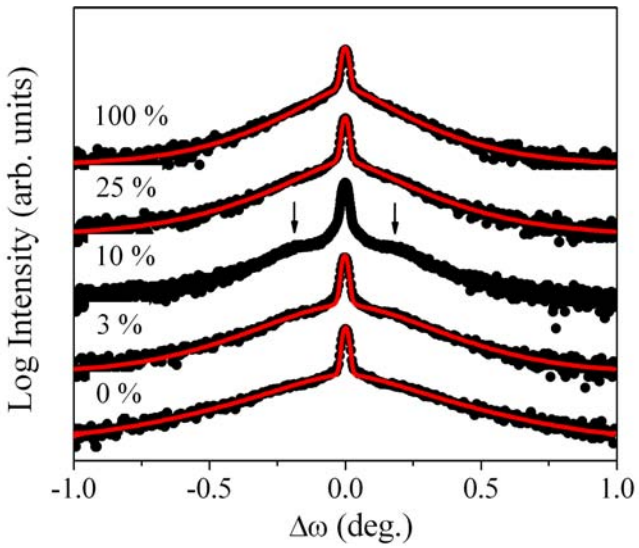

Figure 3.30: Rocking curves around the (002) peak of the annealed LSMO thin films (black) and the simulated curves (red).

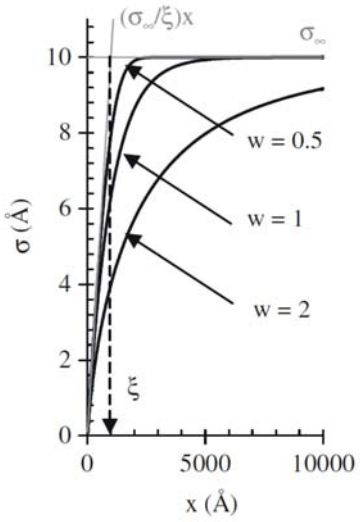

Figure 3.31: Plot of the displacement-difference correlation function $\sigma(x)$ versus x for different values of the width parameter w. Decreasing w results in a more abrupt transition from the correlated to the uncorrelated disorder regime. The asymptotic behaviours for $x \ll \xi(\sigma(x) = \sigma_\infty(x/\xi))$ and for $x \gg \xi(\sigma(x) = \sigma_\infty)$ are shown as grey lines. The x-position of the intersection of the two asymptotic lines correspond to the defect correlation length, ξ.

component profiles. They distinguished between two cases, one of weak disorder, in which the width of the diffuse scattering peak is related to the defect correlation length, $\Delta Q_x = 2\pi/\xi$, and a strong disorder case, where the width of the diffuse scattering peak, expressed as a function of the scattering vector Q_x, is given by the strain, or mosaicity of the defects, $\Delta Q_x = \omega h$, ω being the mosaicity, while h is the length of the reciprocal lattice vector. The use of this approach is limited to the two extreme cases of disorder, so that in an intermediate case ξ and ω cannot be evaluated separately. Also, a separation of the two components of the rocking curves, through fitting algorithms may lead to an erroneous evaluation of the diffuse scattering component through the arbitrary choice of the fitting functions (Gaussian, Lorentzian or Voigt).

In order to overcome these shortcomings, Boulle *et al.* [76] proposed the direct modeling of experimental diffraction profiles. The proposed scattering model makes use of the Lèvy-stable distribution function in order to describe the statistical properties of the strain fields. Also, the effects of the finite size domains, *i.e.* crystallites, over which the diffraction process is coherent, are taken into account. The spatial properties of the of the strain field, responsible for the occurrence of the of the two-component profiles are described by the so-called *displacement-difference correlation function*, $\sigma(x)$. This function is defined as $\sigma(x) = \langle [u_z(x) - u_z(0)]^2 \rangle$, where $u_z(x)$ is the deviation from the average lattice position, along the normal direction, z, with respect to the film surface, at point x. The authors

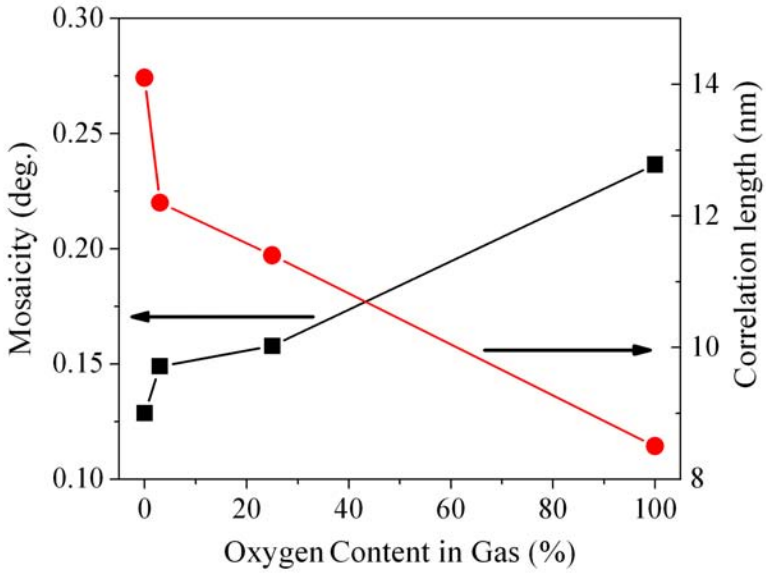

Figure 3.32: Evolution of the mosaicity and correlation length of the defects, as obtained by fitting the rocking curves around the (002) and (001) peaks of the LSMO films.

propose the following form of the correlation function:

$$\sigma(x) = \sigma_\infty \left\{ 1 - \exp\left[-\left(\frac{x}{\xi}\right)^{1/w} \right] \right\}^{Hw} . \tag{3.9}$$

In Equation 3.9, ξ is the correlation length, meaning that for $x < \xi$ the lattice displacements, $u_z(x)$, are correlated, while for $x > \xi$, the displacements are uncorrelated. As a consequence, the correlation length corresponds to the spatial extension of the strain field created by defects. The parameter w, represents the transition width between the correlated and uncorrelated regimes. The different dependencies of $\sigma(x)$ on w are shown in Figure 3.31. H depends on the nature of the disorder and takes the value of 1 in the correlated regime, for which the characteristic strain created by the defect is obtained to be $\epsilon_{xz} = \sigma_\infty/\xi$, also referred to as the mosaicity.

In the present case a good agreement between the calculated and the observed curves could be obtained assuming a Gaussian distribution of strain and crystallites having a parallelipipedic shape. The strain field is characterized by the in-plane correlation length ξ, below which the lattice displacements are correlated, which in the case of a symmetrical reflection, correspond to the root-mean-squared (r.m.s) rotations, *i.e.* the mosaicity. This mosaicity gives rise to the diffuse peak. Above the correlation length ξ, the displacements are uncorrelated so that the mosaicity drops down to zero, which gives rise to the coherent peak. The correlation length ξ can be regarded as a "mean distance" between defects [77].

The simulation of several (00l) reflections is necessary in order to determine the different parameters entering the model. We here used the (001) and (002) reflections. Finally, it is to be noticed that the ω-scan of the film annealed in 10% oxygen could not be simulated properly with the described model, as it exhibited an additional signal, giving rise to two shoulders indicated by the arrows in Figure 3.30. The presence of such distinct features in epitaxial LSMO thin films has been attributed to the presence of periodic microtwinning [59]. The evolution of the mosaicity and the correlation length as a function of oxygen content are presented in Figure 3.32. Starting from $x = 3\%$ the correlation length of the defects decreases, while the mosaicity increases. This evolution can be interpreted as follows: as oxygen incorporation in the film lattice increases, due to higher oxygen concentration in the annealing gas, a greater number of cationic vacancies form, according to the defect model (1). These vacancies act as defects, locally distorting the lattice, giving rise to the diffuse scattering component of the rocking curves. As the defect density increases the mosaicity increases, *i.e.* the strength of the defects increases. Concomitantly, the distance between defects decreases, *i.e.* the extension of the distortion field of an individual defect is reduced by the presence of adjacent distortions.

Magnetic properties

In order to demonstrate the validity of our interpretation we have conducted a series of magnetic measurements, as well as a XPS investigation on our samples, from which we have evaluated physical quantities that are dependent both on oxygen and defect concentration, such as Curie temperature, T_C, the coercive field and the Mn^{3+}/Mn^{4+} ionic ratio.

The temperature dependence of the magnetization, M(T), for the annealed films is presented in Figure 3.33. From the derivative of the M(T) curves, the ferromagnetic-paramagnetic transition width was investigated, taking as a parameter the full-width-at-half-maximum (FWHM) of the dM/dT peak around the inflexion point of the M(T) curves, Figure 3.34a. The behavior of the FWHM also suggests the existence of the two oxygen incorporation regimes, in agreement with the structural studies. Thus, for the films annealed in up to 10% oxygen concentration, the FWHM decreases, *i.e.* the ferromagnetic-paramagnetic transition becomes narrower as a function of temperature. This behaviour can be ascribed to an evolution of the films towards a low defect density and possibly oxygen stoichiometric phase. The large FWHM value of the 0% oxygen content annealed sample is an indication that the film exhibits multiple magnetic phases, having different Curie temperatures. These phases could in turn come from the existence of slight local compositional and/or structural variations within the film. It is to be noted that such local inhomogenities can hardly be evidenced by the HRXRD measurement, which might explain the contradiction between the high value of the coherence length, determined from the ω-scan, and the value of FWHM of

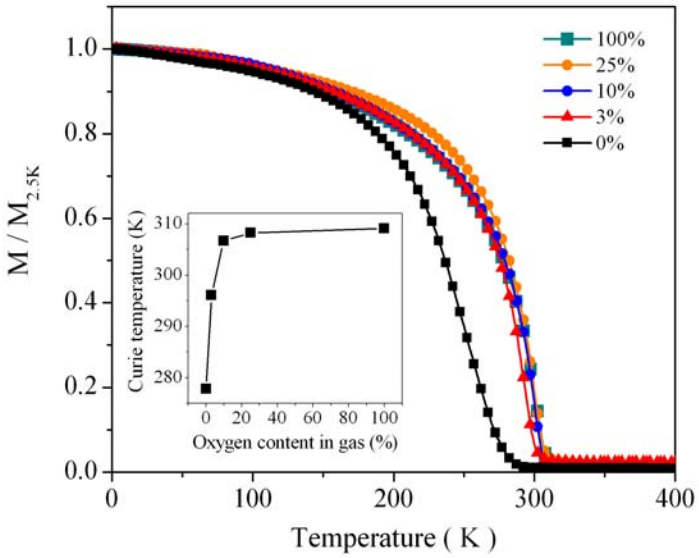

Figure 3.33: M(T) curves for the annealed samples; Curie temperature evolution as a function of the oxygen content in the annealing gas (inset).

dM/dT peak, in the case of the film annealed in pure argon. On the other hand, for oxygen concentrations above 10%, a slight increase of the FWHM is noted. This trend can be interpreted as the effect of oxygen over-doping which creates cationic vacancies in the film crystal structures. Taking into account the above considerations, we can conclude that in the first regime oxygen annealing acts as to homogenize the films into a single phase with recovered oxygen stoichiometry, while the second regime is governed by uniform oxygen incorporation in the single phase films, leading to oxygen over-doped, $La_{(1-x)}Sr_xMnO_{3+d}$films.

The Curie temperatures were determined by linear extrapolation of the M(T) curves around the inflexion points and are presented in the inset of Figure 3.33. A pronounced increase of T_C is observed from 278 K, corresponding to the film annealed in Ar, to 307 K, for the film annealed in 10% oxygen, as the structure evolves to a single phase possibly having stoichiometric oxygen content. Above 10% oxygen content, the increase is slower, reaching a maximum value, for 100% oxygen annealed film, of 309 K. The slight increase observed above 10% oxygen content, suggests a hole doping effect of oxygen excess in a sub-optimum (x <0.33), cationic, *i.e.* strontium, doped phase. A similar effect was also observed by Murugavel *et. al.* [68] in their studies of oxygen annealing effects on cationic under-doped $La_{(1-x)}Ca_xMnO_3$ films, where the dramatic increase of the metal-insulator transition temperature, T_{MI}, from 240K for the as-deposited to 270K for oxygen annealed film was ascribed to the effective hole doping originating from oxygen excess in the film lattice. The lack of the exact Sr concentration value of our films prevents us from making any quantitative evaluation of the amount of excess oxygen in the annealed films, based on the T_C value. There have also been results [70] on oxygen incorporation effects in LSMO, in which above

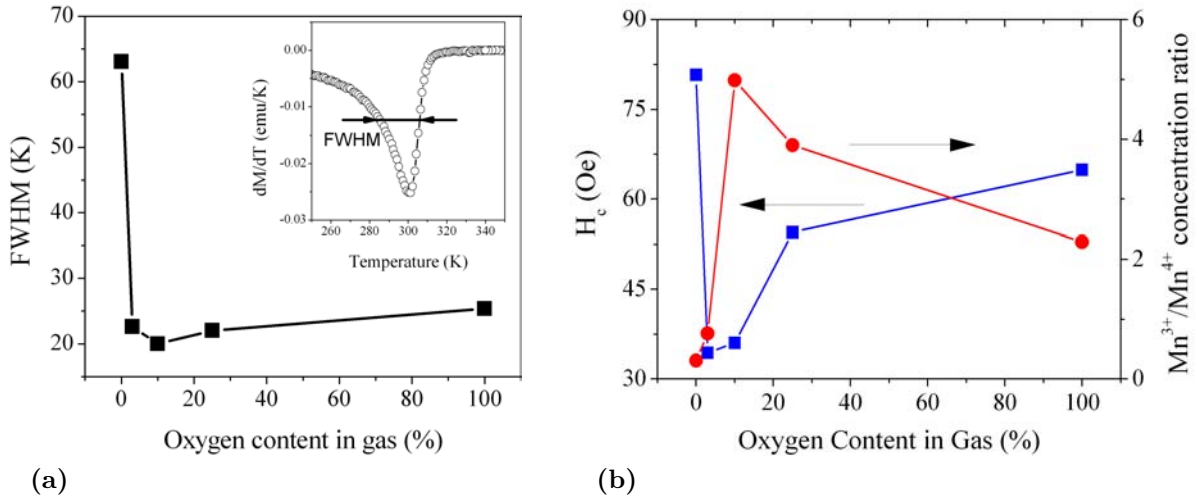

Figure 3.34: (a) Full-width-at-half-maximum (FWHM) of the dM/dT peak around the inflexion point of the M(T) curves; dM/dT curve for the 10% oxygen annealed film (inset);(b) Evolution of the coercive field and of the Mn^{3+}/Mn^{4+} ratio, determined by XPS measurements, as a function of oxygen concentration of the annealing gas.

a certain oxygen doping level, due to the induced structural defects, the Curie temperature experienced a decrease. However, it seems that in our case, this critical level of doping is not attained.

As far as the coercive field of the LSMO films is concerned, Sirena *et. al.* [78] studied the effect oxygen incorporation in LSMO thin films, which were initially oxygen deficient, on the coercive field. They concluded that upon oxygen annealing, the coercive field of the films decreases. Considering domain wall pinning on structural defects as the main mechanism of coercivity, they attributed their result to the fact that oxygen incorporation in oxygen deficient samples results in a reduction of the number of oxygen vacancies, *i.e.* structural defects, leading thus to a reduction of coercive field. The evolution of the coercive field as a function of the annealing conditions is given in Figure 3.34b, evaluated from hysteresis loops performed at 5 K. The coercive field decreases from a value of 80 Oe for the argon annealed sample, to 35 Oe, for the film annealed in 3% oxygen. The coercive field in case of the 10% film is close to this value, 36 Oe. For the 25% and 100% oxygen annealed films the value of the coercive field increase to 55 Oe and 64 Oe, respectively. Following the arguments used by Sirena *et. al.* [78], we can explain the decrease of the coercive field by the structural evolution of the LSMO thin films towards a single, low defect phase, up to 10%. For the 25% and 100% the increase of the coercive field is related to the increase of the defect density due to oxygen over-doping, as revealed by the decrease of the coherence length, Figure 3.32.

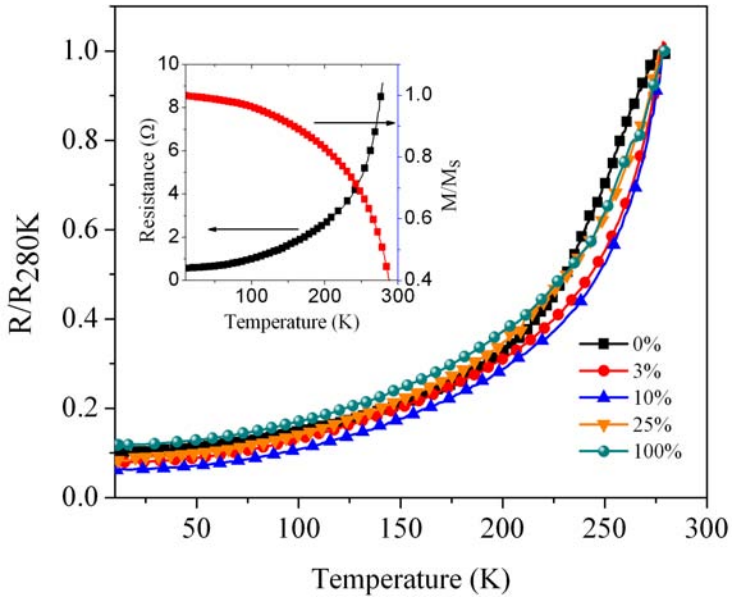

Figure 3.35: Resistance vs. temperature dependence of the annealed samples. (inset) Magnetization and resistance temperature dependence of the 10% oxygen annealed film.

Electrical characterization

The electrical characterization of the samples consisted of resistance measurements. The measurements were performed as a function of temperature in the 10-280 K range. The results are shown in Figure3.35. As it was to be expected the critical metal-insulator transition temperature was not reached. All the curves exhibit the characteristic resistance increase as the temperature tends towards T_{MI}. As it was mentioned in the introduction to LSMO chapter, this part of the R vs. T curve is referred to as metallic, even though the behavior of the resistance is not strictly linear even for low temperatures, *e.g.* 0-100 K. The Figure 3.35 inset demonstrates the close relationship that exists between the magnetic and electric properties of the LSMO thin films. As the magnetization decreases, due to the thermal fluctuations, the resistance of the sample rises. This behavior can be qualitatively be understood within the double exchange model. This was already reviewed in the introductory chapter so that we will only briefly touch upon it. Thermal fluctuations act as to produce disorder of the core t_{2g} spins. The e_g electron delocalization, responsible for metallic conduction, will be thus impeded as it depends on the relative angle between the t_2g spins, in the sense that electronic transfer probability is maximum for parallel core spin alignment.

Several models are used for the quantitative interpretation of the ρ(T) data. Recently, Sirena *et al.* [40] have used the VRH model to describe their data obtained on LSMO epitaxial thin films that were subjected to oxygen ion implantation. They use the "classic" VRH model, without taking into consideration magnetic disorder, to interpret the low temperature resistivity values. Their assumption is justified, as magnetization can be assumed

as constant in the low temperature range. The potential fluctuations due to the presence of defects tend to localize the electrons, described by a $\psi = \psi_0 \exp(-\alpha r)$ wave function. The resistivity expression as a function of temperature of the VRH model is:

$$\rho = \rho_0 \exp(T_0/T)^{\frac{1}{4}}. \tag{3.10}$$

T_0 is a term proportional to α^3, the inverse of the electron localization volume. Accordingly, T_0 is a measure of the disorder in the system. Of course, the disorder is due to the random distribution of the dopant within the lattice, but is assumed to be constant for all the studied samples. Ion implantation is also a source of disorder, so that the evolution of T_0 is a measure of the effects of ion implantation. As the ion density increases the defect density increases so that T_0 increases as a sign of the localization volume decrease. Following the arguments proposed by Sirena *et al.* [40] we set out to investigate the R(T) obtained on the annealed LSMO films in order to evaluate the influence of the oxygen induced defect creation on the localization volume of the e_g electrons. In our endeavor we used the modified VRH model proposed by Viret *et al.* [38] in which the magnetic contribution to the potential variation is also taken into account. The model, having the expression given below, allows for fitting in wider temperature range than the original VRH model, which is an important advantage, since in our study the measurements were not performed at temperatures lower than 10K, where only structural effects are present. The resistivity expression according to this model, also given in the introductory chapter on LSMO, is:

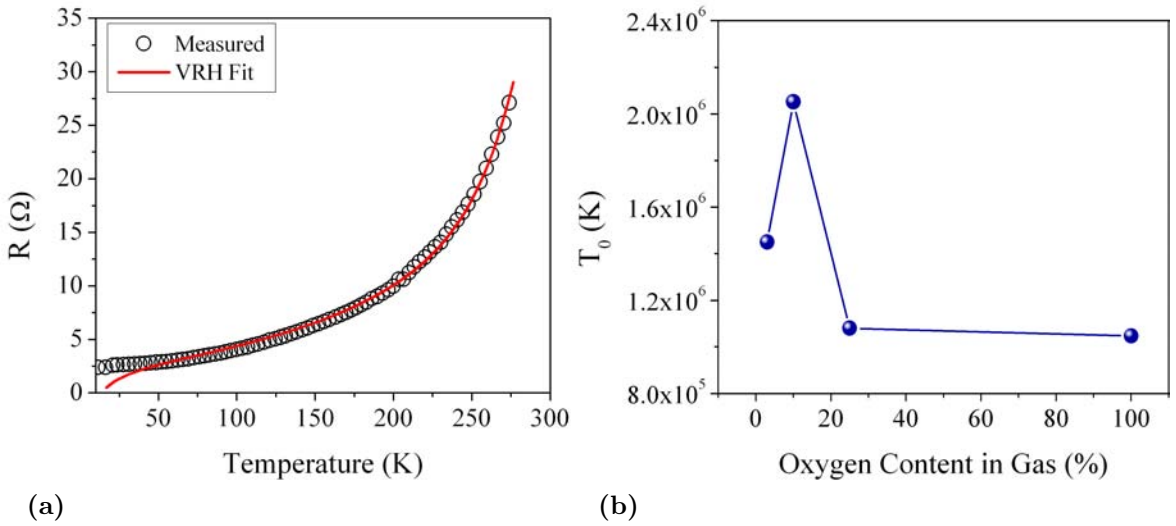

Figure 3.36: (a) Experimental data and fit according the variable range hopping for the 25% oxygen annealed film; (b) T_0 variation as a function of the oxygen content of the annealing gas.

$$\rho = \rho_0 \exp\left(\frac{T_0}{T}[1-(M/M_s)^2]\right)^{\frac{1}{4}}. \tag{3.11}$$

Figure 3.36 presents the result obtained by using the model above to interpret the $R(T)$ experimental data. Although good agreement between theory and experiment exists in the higher temperature range, for low temperatures a slight discrepancy seems to exist between the two. The fit shown in Fig. 3.36a is the best obtained on this set of samples. The overall poor fitting results point to the conclusion that the conduction mechanism in our films is more complex and probably is a superposition of different contributions. This conclusion is also supported by the results of the T_0 parameter estimation, obtained from the fits. Its variation is completely the inverse of the expected behavior. From the 3% O_2 annealed sample to the 10% one, where according to the previous analyses oxygen incorporation acts as to homogenize and possibly to restore its stoichiometry, T_0 increases. This increase means that α increases as well, so that the localization volume decreases. On the other hand, up to the 100% film, T_0 decrease. This variation contardicts our measuremts which have indicated defect formation due to oxygen over-dopping, which would lead to an increase of T_0, *i.e.* a stronger localization of the carriers.

As a conclusion, although a qualitative agreement exists between the magnetic VRH model and the measured R(T) curves, quantitatively important differences exist between the two. This fact leads to erroneous evaluation of the T_0 parameter, and hence any attempt for disorder quantification from the resistance data proves to be fruitless.

XPS characterization

The composition of the samples was analyzed by X-ray Photoelectron Spectroscopy (XPS) of Mn 2p and O 1s core-levels lines combined with controlled Ar+ ions etching of samples. The etching was performed in order to remove the contamination layers and to avoid the surface effects on manganese and oxygen ions concentrations respectively. The samples were subject of consecutive Ar ions etchings until, for each sample, by doing any additional sputtering the spectra remained unchanged in shape and intensity The excitation was made by using the Al anode of the X-rays source ($h\nu$ = 1486.3 eV). CASA software was utilized to deconvolute and fit the experimental data.

As an example the XPS recorded spectra of Mn 2p core-level doublet for the sample annealed at 3% O2 together with the corresponding deconvolutions and fitted curve are shown in Figure 3.37a. As one can see the deconvolution was performed using two components corresponding to Mn^{3+} and Mn^{4+} states respectively, each having additional satellite peaks around 645 and 658 eV. The low energy peaks (A) belongs to Mn^{3+} ions while the higher energy peaks (B) are attributed to Mn^{4+}. The restrictions used for fitting the Mn 2p XPS spectra concern the relation between the areas of the two components, namely $A_{1/2} = A_{3/2}/2$,

Table 3.4: XPS Results.

	0% O_2	3% O_2	10% O_2	25% O_2	100% O_2
Mn^{4+}/Mn_{tot}	0.763	0.567	0.167	0.203	0.318
$O(A)/O_{tot}$	0.784	0.587	0.180	0.211	0.303
μ_B/f.u.	3.236	3.433	3.833	3.796	3.696

the rations between (3/2) and (1/2) linewidths which were set between 1.05 - 1.25 and the doublet separation which was restricted to ∼11.8 eV [79, 80, 81, 82, 83].

The deconvolution of the O 1s core level line of the same 3% O2 annealed sample can be seen in Fig. 3.37b. Here the large peak labeled C is attributed to the oxygen contamination originating from various sources lake: oxide of the Mo support, adsorbed oxygen onto the conductive carbon tape which was used to ensure the neutrality of the sample, etc.

The outer shell orbital of an oxygen ion connected to some Mn^{4+} neighbor ions is much more delocalized that in the case of the Mn^{3+} neighbor ions due to the double exchange interactions specific to the perovskite manganites. A stronger electronic delocalization of the outer shells splits the XPS O 1s core level peak to lower binding energies ("less negative" charge) as compared to the O 1s core level of an manganese ion connected mainly, statistically speaking, to some Mn^{3+} type neighbors. In the last case one have a much localized charge cloud at the oxygen position which, in turns, appears to be "more negative" that the oxygen ions with delocalized electronic clouds. Therefore, the peak labeled B can be attributed to the O^{2-} ions connected to Mn^{3+} ions while the peak labeled A can be seen as belonging to oxygen ions bound primarily to the Mn^{4+} ions.

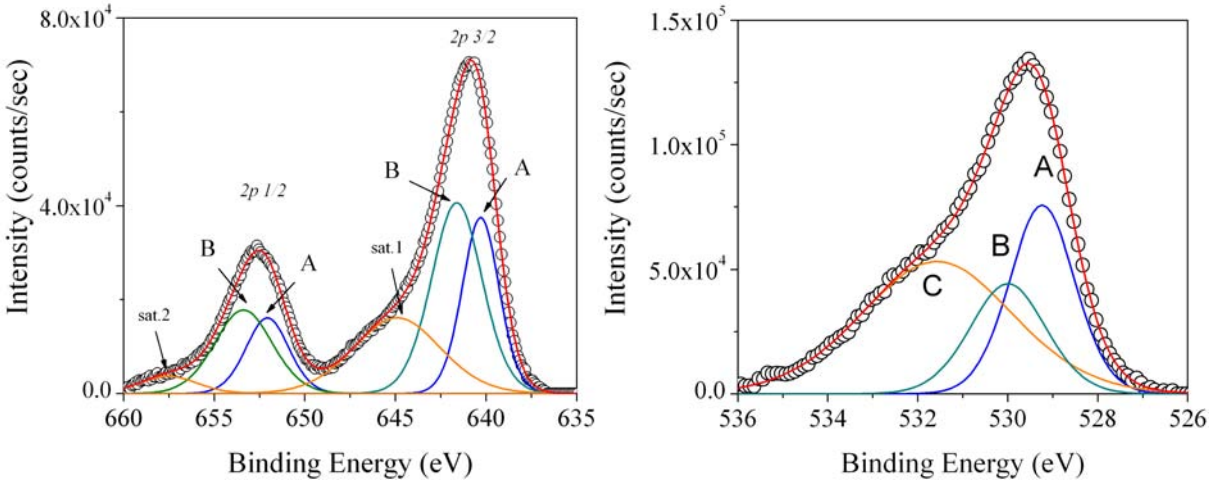

(a) As deposited **(b)** 3% O_2

Figure 3.37: XPS measurements of the Mn^{3+}, Mn^{4+} (a) and oxygen (b) with the corresponding fits.

The integral intensities were calibrated by using the real sensitivity, transmission and electronic mean free path factors. In Table 3.4 the Mn^{4+} concentrations are presented, together with the oxygen ions concentrations connected to the Mn^{4+} ions. One can observe a quite good concordance between the values determined from XPS line analysis of Mn 2p and O 1s core levels respectively. The last row shows the calculated magnetic moments in Bohr magnetons (μ_B)/formula unit (f.u.), based on Mn^{4+}/Mn^{3+} concentrations, as resulted from XPS data.

The existence of the oxygen over-doping regime is thus confirmed by the XPS measurements. From the fitting of the obtained XPS spectra the Mn^{3+}/Mn^{4+} ionic ratio in the films was determined, Figure 4.6. A decrease of the ionic ratio is observed starting from the 10% oxygen annealed film. This is in good agreement with the previous findings, in the sense that the increase of the Mn^{4+} ionic fraction is due to the presence of excess oxygen in the film lattice [62]. The origin of the increase of the ionic ratio, for the films annealed in 0% and 3% oxygen, remains unclear, even though the high concentration of Mn^{4+} in the 0% film can be attributed to the fact that the film is a mixture of LSMO phases, and therefore Mn^{4+} rich regions may exist within the film.

The results of the studies regarding the oxygen incorporation in LSMO thin films have been the subject of a publication, T. Petrişor Jr. *et al.*, *Oxygen incorporation effects in annealed epitaxial* $La_{1-x}Sr_xMnO_3$ *thin films*, J. Appl. Phys. **109**, 123913 (2011).

3.4 Résumé de chapitre en français

Ce chapitre est consacré à l'étude d'un système magnétique de type pérovskite qui présentera une très bonne compatibilité structurale en termes d'épitaxie avec le $YBa_2Cu_3O_7$. Cela est très important vis-à-vis de l'objectif scientifique de cette thèse concernant la réalisation des systèmes hybrides d'interface entre un film magnétique et un autre supraconducteur.

Le système choisi dans notre étude est le système épitaxial $La_{1-x}Sr_xMnO_3$(LSMO). Le chapitre est structuré en trois grandes parties: une introduction générale, un paragraphe consacré à la croissance et aux études structurales et cristallographiques et un dernier paragraphe consacre à une étude très détaillée sur les effets de l'incorporation de l'oxygène sur les propriétés des films épitaxiales de LSMO.

L'introduction présente, par une ample étude bibliographique, des généralités sur les propriétés structurales, magnétiques et électriques du LSMO. Dans ces systèmes les interactions de double-échange, moyennés par l'oxygène, gouvernent les propriétés magnétiques et électriques. Une transition de type métal isolateur accompagnée d'une transition ferromagnétique-paramagnétique apparaît, au-delà d'une température critique T_c qui est directement corrélée à la qualité structurale des films et à la stchiométrie précise en oxygène. Toujours dans cette introduction, des aspects concernant les propriétés d'anisotropie magnétique

des films de LSMO sont discutés.

Un deuxième paragraphe contient une présentation détaillé de la croissance des films de LSMO élaborés dans le cadre de cette thèse ainsi que les résultats des études de caractérisation structurale (cristallographie et morphologique) et du transport électrique de ces films. Les films de LSMO étudiés ont été élaborés par la pulvérisation cathodique (DC) sur un substrat de $SrTiO_3$. Selon les études faites le substrat est chauffé à une température comprise entre 650 et 825 °C. Les films sont déposes dans un mélange de Ar:O_2 (3 :1) à une pression de 40mbar. L'étape finale consiste dans un refroidissement sous oxygène suivi d'un recuit à 550°C pendant une demi-heure. Le dernier recuit est introduit dans la séquence de l'élaboration pour le cas ou un film de $YBa_2Cu_3O_7$ sera déposé ultérieurement sur le LSMO, sachant que dans la phase de l'élaboration du supraconducteur un recuit à 450 °C sous oxygène sera nécessaire afin de stabiliser la phase supraconductrice avec une structure orthorhombique.

La caractérisation de la morphologie des films de LSMO a été effectuée par la microscopie à force atomique en utilisant un microscope AFM modèle Veeco Dimension 3100. Les propriétés structurales ont été déterminées avec un diffractomètre de type Bruker AXS D8 Discover dans une configuration de haute résolution. Un premier résultat de notre analyse montre le rôle de la témpérature du substrat sur la morphologie des films. Un deuxième paramètre important pour la morphologie est l'épaisseur du film. L'objectif principal de l'étude sur la dépendance de la morphologie de l'épaisseur du film a été la détermination des mécanismes de la croissance épitaxiale du LSMO sur les substrats de $SrTiO_3$(001). Un troisième paramètre important pour la morphologie est la topologie de la surface du substrat. Des traitements chimiques et thermiques spécifiques appliqués au substrat nous ont permis d'induire des structures périodiques de terrasses. Ce terrassement du substrat est particulièrement intéressant permettant l'induction, par un mécanisme magnétostatique de type dipolaire, des propriétés d'anisotropie magnétique dans les films magnétiques déposés ultérieurement sur les substrats. Un dernier paramètre, identifié comme important pour la morphologie des films de LSMO, est la distance substrat-cible pendant la pulvérisation cathodique.

Les études par AFM sur la morphologie des films ont été accompagnées par des études très détaillés de diffraction X (mesures 2θ-ω, rocking curves, réflectométrie, cartographie de l'espace réciproque). Ce type d'étude montre l'évolution des paramètres structuraux des films de LSMO en fonction de leur température de croissance, le "twinning" périodique des films de LSMO, etc.

La dernière partie du deuxième paragraphe du chapitre présente des résultats de la caractérisation électrique des films de LSMO. Les mesures de la variation de la résistance électrique avec la température montrent clairement le régime de transition métal-isolateur et la dépendance de la température critique des paramètres clefs de l'élaboration des films. La

température critique augmente avec l'augmentation de la température de recuit. Cependant, une température trop élevée (825 °C) sera responsable d'une détérioration des propriétés des films. Une piste préliminaire qui se dégage pour expliquer cette détérioration, traduite par une réduction de la T_c, s'oriente sur l'influence de la stœchiométrie de l'oxygène dans le LSMO, élément clef pour les interactions de double échange.

Ainsi, dans le troixième et dernier paragraphe du chapitre, nous présentons les résultats d'une étude exhaustive concernant les effets de l'incorporation contrôlée de l'oxygène sur les propriétés magnétiques des films de LSMO intimement corrélés avec leur structure cristallographique. Ce paragraphe développe le mécanisme des interactions de double échange et, par une étude bibliographique, le rôle de l'incorporation de l'oxygène dans les manganites de lanthane. Le paragraphe continue avec la stratégie expérimentale concernant la préparation proprement dite des échantillons de LSMO avec une concentration variable en oxygène. Cette dernière est obtenue par un traitement thermique spécifique à 900°C pendant une heure dans une atmosphère d'oxygène (mélange de Ar et O2 (100%-x):x avec x= 0, 3, 10, 25, 100%). La caractérisation magnétique des films a été effectuée avec un magnétomètre SQUID ((Quantum Design) à l'Université Henri-Poincaré de Nancy. Le rapport Mn^{3+}/Mn^{4+} a été détermine par des mesures de Photoémission de Photoélectrons X sur les niveaux de cœur Mn 2p.

La caractérisation en diffraction X de type $2\theta/\omega$ scans et la cartographie de l'espace réciproque permettent d'observer et d'extraire l'évolution des paramètres structuraux et du stress dans les films en fonction de leur contenu x en oxygène. L'analyse expérimentale de type rocking curve corrélée avec la simulation numérique des ω scans permetent d'extraire l'évolution de la longueur de corrélation dans le plan et du champ de déformation. Ces paramètres, également reliés à la densité et la distance moyenne entre les défauts structuraux dans les films de LSMO sont contrôlés par la stœchiométrie en oxygène modulable via le paramètre x. Nous démontrons une anti-corrélation entre l'évolution de la longueur de corrélation des défauts, qui décroît avec l'augmentation du taux d'oxygène x dans le gaz pendant le recuit, et la mosaïcité qui présente une variation opposée. Ce type d'analyse structurale a été suivie par une analyse magnétique concernant la variation en température de l'aimantation. A partir des courbes $M(T)$, nous avons étudié la transition ferromagnétique - paramagnétique: la température de cette transition et la largeur en température de la transition. L'évolution de ces deux paramètres avec le taux d'oxygène x lors du recuit a été intimement corrélée avec l'évolution des paramètres structuraux des films. Dans ces analyses, la stœchiométrie des films de LSMO en fonction du paramètre x a été déterminée par XPS qui montre l'évolution du contenu en oxygène dans le LSMO en fonction du taux x qui varie de la sous-stœchiométrie en oxygène vers le sur-dopage. L'analyse XPS permet également de quantifier le rapport Mn^{3+}/Mn^{4+}, important pour expliquer l'évolution des propriétés électriques et magnétiques gouvernés par les interactions de double échange moyennes par

l'oxygène.

Au delà des analyses structurales et magnétiques ce dernier paragraphe présente les résultats des mesures électriques (résistance en fonction de la température). Les courbes R(T) ont été ajustés avec un modèle théorique (modèle VRH) qui rend compte du mécanisme de super-échange, de la localisation et de l'influence des fluctuations thermiques sur la résistance dans le pérovskite LSMO. Dans ce type d'analyse, on voit clairement la corrélation directe entre les mécanismes du magnétisme par super-échange et ceux de la conductibilité électrique.

Le chapitre est clôt avec des conclusions et perspectives en soulignant l'importance des études effectués sur le LSMO pour la philosophie générale de cette thèse, orientée vers la réalisation des systèmes hybrides avec les supraconducteurs. L'analyse très détaillée effectuée ici sur la densité des défauts structuraux dans le LSMO présente une importance majeure pour la réalisation des systèmes d'interface LSMO/YBaCuO. Des structures de LSMO de morphologie modulée vont jouer le rôle des centres d'ancrage ou pinning intrinsèque pour les vortex dans la couche supraconductrice d'$YBa_2Cu_3O_7$ adjacente.

Bibliography

[1] J. M. D. Coey, M. Viret and S. von Molnár, *Adv. Phys.* **48**, 167 (1999);

[2] M. Bowen, M. Bibes, A. Barthélémy, J. P. Contour, A. Anane, Y. Lemaitre and A. Fert *Nearly total spin polarization in $La_{2/3}Sr_{1/3}MnO_3$ from tunneling experiments*, Appl. Phys. Lett. 82, 233 (2003);

[3] V. Dediu, M. Murgia, F. C. Matacotta, C. Taliani and S. Barbanera *Room temperature spin polarized injection in organic semiconductor*, Solid State Comm. **122**, 181 (2002);

[4] Z. H. Xiong, Di Wu, Z. Valy Vardeny and Jiong Shi *Giant magnetoresistence in organic spin-valves*, Nature **427**, 821 (2004);

[5] Y. Hikita, M. Nishikawa, T. Yajima and H. Y. Hwang, *Termination control of the interface dipole in $La_{0.7}Sr_{0.3}MnO_3$/Nb:$SrTiO_3$(001) Schottky junctions*, Phys. Rev. B **79**, 073101 (2009);

[6] L. Méchin, J.-M. Routoure, B. Guillet1, F. Yang, S. Flament, D. Robbes and R. A. Chakalov, *Uncooled bolometer response of a low noise $La_{2/3}Sr_{1/3}MnO_3$ thin film*, Appl. Phys. Lett. **87**, 204103 (2005);

[7] J. M. D. Coey, *Magnetism and Magnetic Materials*, Cambridge University Press (2009);

[8] M. Bowen, J.-L. Maurice, A. Barthélémy, M. Bibes, D. Imhoff, V. Bellini, R. Bertacco, D. Wortmann, P. Seneor, E. Jaquet, A. Vaurès, J. Humbert, j.-P. Contour, C. Colliex, S. Blügel and P. H. Dederichs, *Using half-metallic mnganite interfaces to reveal insights into spintronics*, J. Phys.: Condens Matter. **19**, 315208 (2007);

[9] N. Farag, M. Bobeth, W. Pompe, A. E. Romanov and J. S. Speck, *Model of twinning in epitaxial (001)-oriented $La_{0.67}Sr_{0.33}MnO_3$ thin films*, J. Appl. Phys. **97**, 113516 (2005);

[10] J.-L. Maurice, F. Pailloux, A. Barthélémy, O. Durand, D. Imhoff, R. Lyonnet, A. Rocher and J.-P. Contour, *Strain relaxation in the epitaxy of $La_{2/3}Sr_{1/3}MnO_3$ grown by pulsed layer deposition on $SrTiO_3$*, Philos. Mag. **83**, 3201 (2003);

[11] M. Spanková, S. Chromika, I. Vávra, K. Sedlácková, P. Lobotka, S. Lucas and S. Stancek, *Epitaxial LSMO films grown on MgO single crystalline substrates*, Appl. Surf. Sci. **253**, 7599 (2009);

[12] H. Boschker, M. Mathews, E. P. Houwman, H. Nishikawa, A. Vailionis, G. Koster, G. Rijnders and D. H. A. Blank, *Strong uniaxial in-plane magnetic anisotropy of (001)- and (011)-oriented $La_{0.67}Sr_{0.33}MnO_3$ thin films on $NdGaO_3$ substrates*, Phys. Rev. B **79**, 214425 (2009);

[13] S. Jin, G. Gao, W. Wu and X. Zhou, *Effect of angular-distortion-induced strain on structural and transport properties of epitaxial $La_{0.67}Sr_{0.33}MnO_3$ thin films*, J. Phys. D: Appl. Phys. **40**, 305 (2005);

[14] H. Boschker, M. Mathews, P. Brinks, E. Houwman, G. Koster, D. H. A. Blank, and G. Rijnders, *Uniaxial contribution to the magnetic anisotropy of $La_{0.67}Sr_{0.33}MnO_3$ thin films induced by orthorhombic crystal structure*, arXiv:1009.0815v1 (2010);

[15] F. S. Razavi, G. Gross, H.-U. Habermeier, O. Lebedev, S. Amelinckx, G. Van Tendeloo and A. Vigliante, *Epitaxial strain induced metal insulator transition in $La_{0.9}Sr_{0.1}MnO_3$ and $La_{0.88}Sr_{0.1}MnO_3$ thin films* **76**, 155 (2000);

[16] A. K. Pradhan, D. Hunter, T. Williams, B. Lasley-Hunter, R. Bah, H. Mustafa, R. Rakhimov, J. Zhang, D. J. Sellmyer, E. E. Carpenter, D. R. Sahu, and J.-L. Huang, *Magnetic properties of $La_{0.6}Sr_{0.4}MnO_3$ thin films on $SrTiO_3$ and buffered Si substrates with varying thickness*, J. Appl. Phys. **103**,023914 (2008);

[17] H. Boschker, J. Kautz, E. P. Houwman, G. Koster, D. H. A. Blank and G. Rijnders, *Magnetic anisotropy and magnetization reversal of $La_{0.67}Sr_{0.33}MnO_3$ thin films on $SrTiO_3$ (110)*, J. Appl. Phys. **108**, 103906 (2010);

[18] M. Mathews, F. M. Postma, J. C. Lodder, R. Jansen, G. Rijnders and D. H. A. Blank, *Step-induced uniaxial magnetic anisotropy of $La_{0:67}Sr_{0:33}MnO_3$ thin films*, Appl. Phys. Lett. **87**, 242507 (2005);

[19] P. Perna, C. Rodrigo, E. Jiménez, N. Mikuszeit, F. J. Teran, L. Méchin, J. Camarero and R. Miranda, *Magnetization reversal in half metallic $La_{0.7}Sr_{0.3}MnO_3$ films grown onto vicinal surfaces* (109), 07B107 (2011);

[20] Joonghoe Dho, Y. N. Kim, Y. S. Hwang, J. C. Kim and N. H. Hur, *Strain-induced magnetic stripe domains in $La_{0.7}Sr_{0.3}MnO_3$ thin films* **82**, 1434 (2003);

[21] O. I. Lebedev, G. Van Tendeloo, S. Amelinckx, H. L. Lu, K. M. Krishnan, *High-resolution electron microscopy study of strained epitaxial $La_{0.67}Sr_{0.33}MnO_3$ thin films*, Phil. Mag. A **80**, 673 (2000);

[22] R. Desfeux, S. Bailleul, A. Da Costa, Prellier and A. M. Haghiri-Gosnet, *Substrate effect on the magnetic microstructure of $La_{0.7}Sr_{0.3}MnO_3$ thin films studied by magnetic force microscopy* Appl. Phys. Lett. **78**, 3681 (2001);

[23] F. Tsui, M. C. Smoak, T. K. Nath, C. B. Eom *Strain-dependent magnetic phase diagram of epitaxial $La_{0.67}Sr_{0.33}MnO_3$ thin films*, Appl. Phys. Lett. **76**, 2421 (2000);

[24] M. Gajek, *Etude du filtrage de spin par des barrières multiferroiques*, Ph. D Thesis, Université Pierre et Marie Curie, Paris IV (2007);

[25] C. Zener, *Interaction between the d-Shells in the Transition Metals. II. Ferromagnetic Compounds of Manganese with Perovskite Structure*, Phys. Rev. **82**, 403 (1951);

[26] C. Zener, *Interaction Between the d Shells in the Transition Metals*, Phys. Rev.**81**, 440 (1951);

[27] P. W. Anderson and H. Hasegawa, *Considerations on Double Exchange*, Phys. Rev. **100**, 675 (1955);

[28] A. Urushibara, Y. Moritomo, T. Arima, A. Asamitsu, G. Kido and Y. Tokura, *Insulator-metal transition and giant magnetoresistance in $La_{1-x}Sr_xMnO_3$*, Phys. Rev. B **51**, 14103 (1995);

[29] K. Kubo and N. Ohata, *A Quantum Theory of Double Exchange. I*, J. Phys. Soc. Jap. **33**, 21 (1972);

[30] H. Boschker, M. Huijben, A. Vailionis, J. Verbeeck, S. van Aert, M. Luysberg, S. Bals, G. van Tendeloo, E. P. Houwman, G. Koster, D. H. A. Blank and G Rijnders, J. Phys. D: Appl. Phys. **44**, 205001 (2011);

[31] E. P. Houwman,G. Maris, G. M. De Luca, N. Niermann, G. Rijnders, D. H. A. Blank and S. Speller, *Out-of-plane magnetic domain structure in a thin film of $La_{0.67}Sr_{0.33}MnO_3$ on $SrTiO_3$ (001) observed by magnetic force microscopy*, Phys. Rev. B **77**, 184412 (2008);

[32] D. S. Chuang, C. A. Ballentine and R. C. OHandley, *Surface and step magnetic anisotropy*, Phys.Rev. B **49**, 15084 (1994);

[33] A.-M. Haghiri-Gosnet and J.-P. Renard, *CMR manganites: physics, thin films and devices*, J. Phys. D: Appl. Phys. **36**, R127 (2003);

[34] M. Zhuang, W. Zhang and N. Ming,*Spin-disorder-scattering-induced spectral-weight transfer and pseudogap in doped perovskite* $LaMnO_3$, Phys. Rev. B **56**, 14547 (1997);

[35] T. Holstein, *Studies of polaron motion: Part I. The molecular-crystal model*, Ann. of Phys. **8**, 325 (1959);

[36] N. F. Mott and E. A. Davies, *Electronic Processes in Noncrystalline Solids*, 2nd ed. Oxford University Press (1979);

[37] H. Boettger and V. Bryksin, *Hopping Conduction in Solids*, Akademic-Verlag (1985);

[38] M. Viret, L. Ranno and J. M. D. Coey, *Magnetic localization in mixed valence manganites*, Phys. Rev. B **55**, 8067 (1997);

[39] Y. Sun, X. Xuand Y. Zhang, *Variable-range hopping of small polarons in mixed-valence manganites*, J. Phys.: Condens. Matter. **12**, 10475 (2000);

[40] M. Sirena, A. Zimmers, N. Haberkorn, E. E. Kaul, L. B. Steren, J. Lesueur, T. Wolf, Y. Le Gall, J.-J. Grob and G. Faini, *Influence of ion implantation on the magnetic and transport properties of manganite films*, Phys. Rev. B **81**, 134439 (2010);

[41] E. Dagotto, T. Hotta and A. Moreo, *Colossal magnetoresistant materals: the key role of phase separation*, Phys. Rep. **344**, 1 (2001);

[42] M. B. Salamon and M. Jaime, *The physics of manganites: structure and transport*, Rev. Mod. Phys. **73**, 583 (2001);

[43] M. Ziese, *Extrinsic magnetotransport phenomena in ferromagnetic oxides*, Rep. Prog. Phys. **65**, 143 (2002);

[44] C. W. Searle, S. T. Wang, *Studies of the ionic ferromagnet (La,Pb)*MnO_3 *III. Ferromagnetic resonance studies* , Can. J. Phys. **47**, 2703 (1969);

[45] S. Jin, T. H. Tiefel, M. Mc Cormack, R. A. Fastnacht, R. Ramesh, L. H. Chen, Thousandfold change in resistivity in magnetiresistive La-Ca-Mn-O films, Science **264**, 413 (1994);

[46] G.C. Xiong, Q. Li, H. L. Ju, S. N. Mao, L. Senapati, X. X. Xi, R. L. Greene and T. Venkatesan, *Giant magnetoresistance in epitaxial* $Nd_{0.7}Sr_{0.3}MnO_{3-d}$ *thin films*, Appl. Phys. Lett. **66**, 1427 (1995);

[47] Y. Tokura, A. Urushibara, Y. Moritomo, T. Arima, A. Asamitsu, G. Kido and N. Furukawa, *Giant Magnetotransport Phenomena in Filling-Controlled Kondo Lattice System:* $La_{1-x}Sr_xMnO_3$, J. Phys. Soc. Japan **63**, 3931 (1994).

[48] I. Horcas, R. Fernández, J. M. Gómez-Rodríguez, J. Colchero, J. Gómez-Herrero and A. M. Baro, *Rev. Sci. Intrum.* **78**, 013705 (2007);

[49] http://gwyddion.net/;

[50] M. Ohring *Materials Science of Thin Films - Deposition and Structure* 2nd. Ed., Academic Press (2002);

[51] M. Kawasaki, K. Takahashi, T. Maeda, R. Tsuchiya, M. Shinohara, O. Ishiyama, T. Yonezawa, M. Yoshimoto and H. Koinuma, *Atomic Control of the SrTiO3 Crystal Surface*, Science **266**, 1540 (1994);

[52] T. Ohnishi, K. Shibuya, M. Lippmaa, D. Kobayashi, H. Kumigashira, M. Oshima and H. Koinuma, *Preparation of thermally stable TiO_2-terminated $SrTiO_3$(100) substrate surfaces*, Appl. Phys. Lett. **85**, 272 (2004);

[53] T. Haage, J. Zegenhagen, H.-U. Habermeier and M. Cardona, *Nucleation Mechanism of $YBa_2Cu_3O_{7-d}$ on $SrTiO_3$(001)*, Phys. Rev. Lett. **80**, 4225 (1998);

[54] A. M. Haghiri-Gosnet, J. Wolfman, B. Mercey, Ch. Simon, P. Lecoeur, M. Korzenski, M. Hervieu, R. Desfeux and G. Baldinozzi, *Microstructure and magnetic properties of strained $La_{0.7}Sr_{0.3}MnO_3$ thin films*, J. Appl. Phys. **88**, 4257 (2000);

[55] K. Dörr, *Ferromagnetic manganites: spin-polarized conduction versus competing interactions*, J. Phys. D: Appl. Phys. **39**, R125 (2006);

[56] Y.S. Du, B. Wang, T. Li, D.B. Yu and H. Yan, *Effects of annealing procedures on the structural and magnetic properties of epitaxial $La_{0.7}Sr_{0.3}MnO_3$ films*, J. Magn. Mag. Mat. **297**, 88 (2006);

[57] J. R. Sun, C. F. Yeung, K. Zhao, L. Z. Zhou, C. H. Leung, H. K. Wong and B. G. Shen, *Strain-dependent vacuum annealing effects in $La_{0.67}Ca_{0.33}MnO_{3-d}$ films*, Appl. Phys. Lett. **76**, 1164 (2000);

[58] K. L. Saenger and I. C. Noyan, *Determination of processing damage in thin polycrystalline Ir films using Bragg-peak fringe analysis*, J. Appl. Phys. **89**, 3125 (2001);

[59] U. Gebhardt, N. V. Kasper, A. Vigliante, P. Wochner, H. Dosch, F. S. Razavi and H.-U. Habermeier, *Formation and Thickness Evolution of Periodic Twin Domains in Manganite Films Grown on $SrTiO_3$(001) Substrates*, Phys. Rev. Lett. **98**, 096101 (2007);

[60] S. Pflanz and W. Moritz, *The domain matrix method: a new calculation scheme for diffraction profiles*, Acta Cryst. **A48**, 716 (1992);

[61] S. W. Jin, G. Y. Gao, Z. Huang, Z. Z. Yin, X. Zheng and Wenbin Wu, *Shear-strain-induced low symmetry phase and domain ordering in epitaxial $La_{0.7}Sr_{0.3}MnO_3$ thin films*, Appl. Phys. Lett. **92**, 261901 (2008).

[62] J. A. M. van Roosmalen, E. H. P. Cordfunke, R. B. Helmholdt, H. W. Zandbergen, *The Defect Chemistry of $LaMnO_{3\pm d}$: 2. Structural Aspects of $LaMnO_{3+d}$*, J. Solid State Chem. **110**, 100 (1994); J. A. M. van Roosmalen, E. H. P. Cordfunke, *The Defect Chemistry of $LaMnO_{3\pm d}$: 3. The Density of (La,A)MnO_{3+d} (A = Ca, Sr, Ba)*, J. Solid State Chem. **110**, 106 (1994); J. A. M. van Roosmalen, E. H. P. Cordfunke, *The Defect Chemistry of $LaMnO_{3\pm d}$: 4. Defect Model for $LaMnO_{3+d}$*, J. Solid State Chem. **110**, 109 (1994); J. A. M. van Roosmalen, E. H. P. Cordfunke, *The Defect Chemistry of $LaMnO_{3+d}$: 5. Thermodynamics* , J. Solid State Chem. **110**, 113 (1994);

[63] Mizusaki, J., N. Mori, H. Takai, Y. Yonemura, H. Minamiue, H. Tagawa, M. Dokiya, H. Inaba, K. Naraya, T. Sasamoto, T. Hashimoto, *Oxygen nonstoichiometry and defect equilibrium in the perovskite-type oxides $La_{1-x}Sr_xMnO_{3+d}$*, Solid State Ionics **129**, 163 (2000);

[64] Sakai, J., N. Ito, S. Imai, *Oxygen content of $La_{1-x}Sr_xMnO_{3-y}$ thin films and its relation to electric-magnetic properties*, J. Appl. Phys. **99**, 08Q318 (2006);

[65] Suzuki, Y., H. Y. Hwang, S.-W. Cheong, R. B. van Dover, *The role of strain in magnetic anisotropy of manganite thin films*, Appl. Phys. Lett. **71**, 140 (1997);

[66] C. Moreno, P. Abellan, A. Hassini, A. Ruyter, A. Perez del Pino, F. Sandiumenge, M.-J. Casanove, J. Santiso, T. Puig and X. Obradors, *You have full text access to this contentNanodot Formation: Spontaneous Outcropping of Self-Assembled Insulating Nanodots in Solution-Derived Metallic Ferromagnetic $La_{0.7}Sr_{0.3}MnO_3$ Films* , Adv. Funct. Mater. **19**, 2139 (2009);

[67] W. Prellier, M. Rajesawi, T. Venkatesan, R. L. Greene, *Effects of annealing and strain on $La_{1-x}Ca_xMnO_3$ thin films: A phase diagram in the ferromagnetic region*, Appl. Phys. Lett. **75**, 1446 (1999);

[68] P. Murugavel, J. H. Lee, J.-G. Yoon, T. W. Noh, J.-S. Chung, M. Heu, S. Yoon, *Origin of metalinsulator transition temperature enhancement in underdoped lanthanum manganite films*, Appl. Phys. Lett. **82**, 1908 (2003);

[69] A. Boulle, F. Conchon, R. Guinebretière, *Strain profiles in thin films: influence of a coherently diffracting substrate and thickness fluctuations*, J. Appl. Crystallogr. **42**, 85 (2009);

[70] Dabrowski, B., R. Dybzinski, Z. Bukowski, O. Chmaissen, J. D. Jorgensen, *Oxygen Content and Structures of $La_{1-x}Ca_xMnO_{3+d}$ as a Function of Synthesis Conditions*, J. Solid State Chem. **146**, 448 (1996);

[71] A. Tebano, A. Orsini, P. G. Medaglia, G. Balestrino, *Disentangling strain effects in manganite heterostructures*, Appl. Phys. Lett. **94**, 242503 (2009);

[72] J. Nowotny and M. Rekas, *Defect Chemistry of (La,Sr)MnO_3*, J. Am. Ceram. Soc. **81**, 67 (1998);

[73] H. Heineke, V. Kirchner, H. Selke, R. Chierchia, R. Ebel, S. Einfeldt, D. Hommel, *X-ray scattering from GaN epitaxial layers - an example of highly anisotropic coherence*, J. Phys. D: Appl. Phys. **34**, A25 (2001);

[74] T.-B. Hur, Y.-H. Hwang, H.-K. Kim, H.-L. Park, *Study of the structural evolution in ZnO thin film by in situ synchrotron x-ray scattering*, J. Appl. Phys. **96**, 1740 (2004);

[75] M. J. Bentall, R. A. Cowley, R. C. C. Ward, M. R. Wells, A. Stunault, *The structure of rare earth thin films: holmium and gadolinium on yttrium*, J. Phys.: Condens Matter. **15**, 7155 (2003);

[76] A. Boulle, R. Guinebretière, A. Dauger, *Phenomenological analysis of heterogeneous strain fields in epitaxial thin films using x-ray scattering*, J. Phys. D: Appl. Phys. **38**, 3907 (2005);

[77] A. Boulle, R. Guinebretière, A. Dauger, *Highly localized strain fields due to planar defects in epitaxial $SrBi_2Nb_2O_9$ thin films*, J. Appl. Phys. **97**, 073503 (2005);

[78] M. Sirena, N. Haberkorn, M. Granada, L. B. Steren, J. Guimpel, *Oxygen and disorder effect in the magnetic properties of manganite films*, J. Magn. Mag. Mat. **272**, 1171 (2004);

[79] M. Martins, K. Godehusen, T. Richte, Ph. Wernet and P. Zimmermann, *Open shells and multi-electron interactions: core level photoionization of the 3d metal atoms*, J. Phys. B: At. Mol. Opt. Phys. **39**, R79(2006);

[80] A. J. Nelson, J. G. Reynolds, J. W. Roos , *Core-level satellites and outer core-level multiplet splitting in Mn model compounds*, J. Vac. Sci. Technol. A **18**, 1072 (2000);

[81] B. R. Strohmeier, D.M. Hercules, *Surface spectroscopic characterization of manganese/aluminum oxide catalysts*, J. Phys. Chem. **88**, 4922(1984);

[82] V. DiCastro, G. Polzonetti, *XPS study of MnO oxidation*, J. Electron Spectrosc. Relat. Phenom. **48**, 117 (1989);

[83] V. DiCastro, G. Polzonetti, G. Contini, C. Cozza, B. Paponetti, *XPS study of MnO_2 minerals treated by bioleaching*, Surf. Interface Anal. 16, 571(1990), Y. Umezawa, C.N. Reilley, *Effect of argon ion bombardment on metal complexes and oxides studied by x-ray photoelectron spectroscopy*, Anal. Chem. **50**, 1290(1978);

[84] J. A. Thorton, *Influence of apparatus geometry and deposition conditions on the structure and topography of thick sputtered coatings*, J. Vac. Sci. Technol. **11**, 666 (1974).

[85] P. F. Miceli and C. J. Palmstrøm, *X-ray scattering from rotational disorder in epitaxial films: An unconventional mosaic crystal*, Phys. Rev. B **51**, 5506 (1995)

Chapter 4

Magnetic structures with perpendicular magnetization

As seen in Chapter 1, in order to effectively influence the superconducting properties of a superconducting film in a superconducting/ferromagnetic thin film heterostructure, it is important that the ferromagnetic part, be it thin film or micro/nano structure, exhibits an out of plane component of its magnetization. In the last decades, due to the development of spintronics and the need for attaining ever increasing storage densities in magnetic recording media, there has been a wealth of literature regarding magnetic thin films and structures that display out-of-plane anisotropy. Among these, materials that exhibit a low out-of-plane anisotropy, such as Permalloy or textured Co thin films, represent an interesting class of magnetic materials for magnetic flux pinning in superconductors (SC), as they do not require special deposition conditions, such as elevated deposition temperatures, templates for epitaxial growth, etc. Besides their structural readiness for incorporation in SC/FM structures, these materials posses two remarkable magnetic properties that additionally recommend them in the afore mentioned applications. They are *weak stripe* domain structure and *rotatable magnetic anisotropy*, the latter being a direct consequence of the former. Weak stripe domains represent an important topic in the context of magnetic pinning in superconductors as they give rise to a periodic pinning potential of the SC vortices when aligned parallel to the current passing through a superconductor. In the perpendicular configuration the domain stripes constitute guides for the vortex motion and no pinning is expected.

In the present Chapter we analyze the physical conditions for which the stripe domain configuration is stabilized in Permalloy an Co thin films. Structural and magnetic measurements, both on a macroscopic and a microscopic scale, are used to characterize the stripe domain configuration in these systems. Epitaxial Co films are also studied as they represent the case for which a true out-of-plane anisotropy is present, unlike their textured counterpart for which the magnetization is not purely oriented perpendicularly to the film surface,

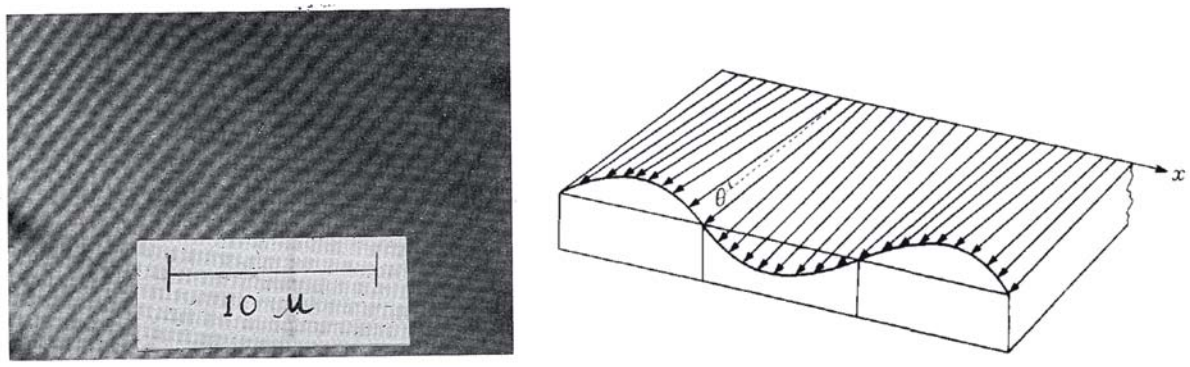

(a) (b)

Figure 4.1: (a) Weak stripe domain structure of Permalloy thin films. Taken from [1]. (b)Weak stripe spin configuration, as proposed by Chikazumi [2].

but at a certain angle. The fabrication of Permalloy and Co micro,- and nanostructures is also presented. Detailed account of their fabrication (optical lithography and ion beam etching) is given. An alternative lithographic method for the patterning of nanometric dot arrays is described. MFM characterization is used to analyze the different magnetic states (multi-domain, dipole, magnetic vortex) of the as obtained structures.

4.1 Permalloy ($Ni_{80}Fe_{20}$) thin films

The out-of-plane uniaxial anisotropy, K_U, can be induced in thin films, above a critical thickness, by growing the films at an angle with respect to the incidence of the evaporated or sputtered atoms [2]. This geometry allows for a columnar growth of the films which determines the out-of-plane orientation of the anisotropy. Perpendicular anisotropy can also originate, as for Permalloy ($Ni_xFe_{(1-x)}$, x=19-21 at.%) thin films, from a negative magnetostriction constant correlated with an in-plane tensile strain of the films. In this case the anisotropy constant is given by the expression [1]:

$$K_U = \frac{3}{2}\lambda_s\sigma, \tag{4.1}$$

where λ is the magnetostriction constant and σ represents the strain of the film.

As early as the mid 1960s, groups studying Permalloy thin films [1] found that above a certain film thickness, t_c, a stripe domain structure was stabilized, as shown in Figure 4.1a.

In order to describe the observed domain structure, Saito *etal.* [1] proposed a spin configuration in which adjacent spins are deflected by a constant angle θ, resulting in a triangular-like, *zig-zag*, distribution of the spins along an in-plane axis of the film. Chikazumi [2] proposed a sinusoidal deviation of the spins from the surface of the film, Figure 4.1b, de-

scribed by:

$$\theta = \theta_0 \sin\left(2\pi\frac{x}{\lambda}\right), \tag{4.2}$$

in which x lies in the plane of the film, perpendicular to the average spin axis and λ is the wavelength of the spin variation, *i.e.* width of the spin domain. Because of the fact that the spins are not oriented perpendicularly to the film surface the domain stripes are also referred to as *weak stripes*. Other spin distribution models include the one proposed by Murayama [3] in which the spin configuration is calculated using a variational method. In the following, an outline of the Chikazumi [2] derivation of the domain width λ is presented. Essentially, the derivation consists in expressing the relevant magnetic energy terms, anisotropy, exchange and magnetostatic, as a function of the maximum deflection angle θ_0 and minimizing the expression with respect to λ. All the energy terms were averaged over one wavelength. The magnetic uniaxial anisotropy energy term expressed in terms of θ is:

$$E_a = -K_U \cos^2\left(\frac{\pi}{2} - \theta\right) \tag{4.3}$$

Upon averaging, the anisotropy energy per unit area is found to be:

$$\varepsilon_a = -K_U\theta_0^2 \left\langle \sin^2\left(2\pi\frac{x}{\lambda}\right)\right\rangle h = -\frac{1}{2}K_U\theta_0^2 h, \tag{4.4}$$

h being the film thickness. The average exchange energy per unit area of the system is shown to be:

$$\varepsilon_{ex} = A\left\langle\left(\frac{\partial\theta}{\partial x}\right)^2\right\rangle h = \frac{2\pi^2}{\lambda}\theta_0^2 Ah, \tag{4.5}$$

where A is the exchange stiffness constant. Because the spins make an angle θ with the film plane, there is a finite density of magnetic charge, $\omega = M_s \sin\theta$ at the surface of the film, which in turn leads to a magnetostatic energy term expressed as:

$$\varepsilon_m = \frac{M_s^2\lambda\theta_0^2}{4\pi\mu_0}\left\langle \sin^2\left(2\pi\frac{x}{\lambda}\right)\right\rangle = \frac{M_s^2\lambda\theta_0^2}{8\pi\mu_0}. \tag{4.6}$$

Combining the three energy terms leads to the expression of the total energy

$$\varepsilon = \varepsilon_a + \varepsilon_{ex} + \varepsilon_m = \left(-\frac{1}{2}K_U h + \frac{2\pi^2}{\lambda}Ah + \frac{M_s^2\lambda}{8\pi\mu_0}\right)\theta_0^2. \tag{4.7}$$

Minimizing Equation 4.7 with respect to λ gives the expression for the domain width as:

$$\lambda = 4\pi\sqrt[3]{\frac{\mu_0 Ah}{2M_s^2}} \tag{4.8}$$

Similar dependence of the domain width on the film thickness was obtained by Saito *etal.*

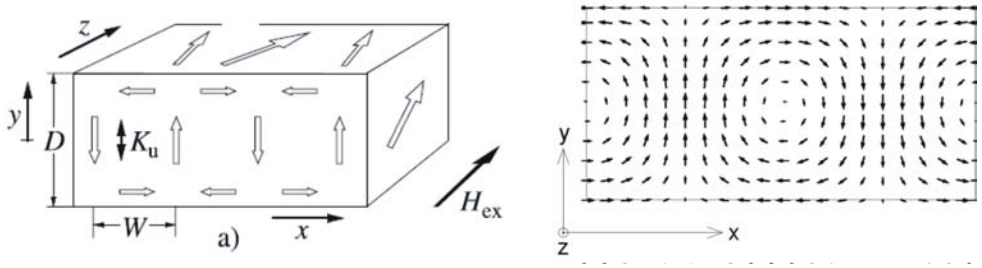

(a) (b)

Figure 4.2: (a) Flux-closed character of the stripe domains. (Taken from [4]), (b) Micromagnetic simulation of Py stripe domains. Taken from Ref. [6]

[1] using their triangular spin configuration:

$$\lambda = 2\left(\frac{\pi^2}{8}\right)^{2/3}\left(\frac{Ah}{M_s^2}\right)^{2/3} \tag{4.9}$$

In the model proposed by Murayama [3] additional degrees of freedom were added to the spin direction. It can be noticed that in the previous two models that were presented, the spin direction only varies in one in-plane direction, $\theta(x)$, perpendicular to the magnetic stripes. The authors allowed for a variation of the angle θ in the out-of-plane direction, $\theta(x, z)$, as well. Also, they introduced an new angle, denoted as $\varphi(x, z)$, which describes a deflection of the spins in the plane direction of the film. Their calculations led to a different expression for the stripe period:

$$\lambda = \sqrt{8h}\left(\pi^2\frac{A}{K2\pi M_s^2}(K + 2\pi M_s^2)\right)^{1/4} \tag{4.10}$$

Hubert and Schaefer [4] stress out the flux-closed character of the stripe domains in the case of thin films having a low out-of-plane anisotropy, summarized in Figure 4.2a. 2D numerical calculations of the spin configuration for Permalloy thin films exceeding the critical thickness have also been reported in literature [6]. These simulations confirm the existence of closure domains at the film surface and also a vortex-like character of the stripe domains in the plane perpendicular to that of the film surface. Figure 4.2b presents such a result.

Permalloy films exhibiting stripe domain structure posses a characteristic hysteresis cycle. In Figure 4.3 such a loop is presented, together with the corresponding domain patterns. The magnetization curve consists of a linear magnetization (rotation branch) decrease and a steep switching at small fields. The small hysteresis observed in the rotation branch is due to the slight difference in stripe period, which is dependent on the magnetic history of the film.

A direct consequence of the stripe domain pattern is the phenomena referred to as *ro-*

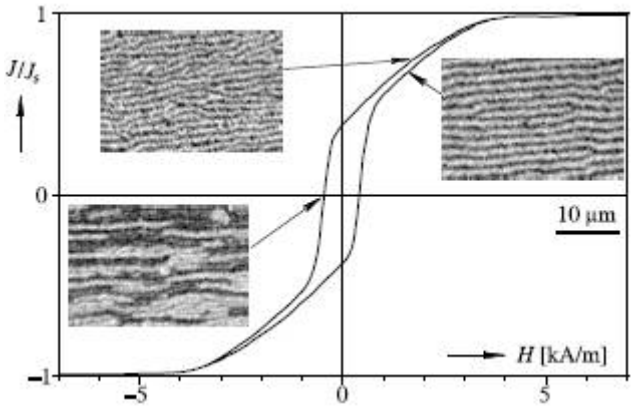

Figure 4.3: Hysteresis curve of a 1.6μm thick Permalloy film with corresponding domain patterns (Taken from [4]).

tatable magnetic anisotropy. It consists of a reorientation of the magnetic stripes along the direction of an externally applied field. This effect leaves the hysteresis cycle unchanged with respect to the direction of the applied magnetic field. This phenomenon may be understood as follows. When applying a relatively small field parallel to the film surface in a different direction than that of the stripes, the magnetization rotates. However, this rotation creates additional magnetostatic energy, as magnetic charge appears at the domain boundaries. If the field is strong enough, in order to avoid magnetostatic energy build-up at domain boundaries, the stripe domains align themselves along the direction of the external field.

4.1.1 Magnetic force microscopy of stripe domain patterns

This paragraph discusses briefly the principles of the magnetic signal detection in magnetic force microscopy experiments. We focus on the explanation of the magnetic contrast in case of a perpendicular stripe domain structure. In our explanation, we use the detection method which is sensitive to the force gradient by the resonance frequency shift of an oscillating cantilever [8]. The force gradient between the tip and the sample modifies the spring constant of the cantilever and consequently its resonant frequency: an attractive force softens the cantilever spring constant inducing a lower resonant frequency. Because to its scalar nature, we refer to $F' = dF_z/dz$ as the force derivative rather than the force gradient. Different models are used in the literature to model the interaction between a magnetized tip and a magnetic structure. In the particular approach where the tip consists of a point dipole $\mathbf{m} = (m_x, m_y, m_z)$, one can demonstrate that the derivative of the force between the tip and a stray field $\mathbf{H}(H_x, H_y, H_z)$ generated by the spatial distribution of the sample

magnetization is given by the following equation [9]:

$$F'_{mag} = m_x \frac{\partial^2 H_d^x}{\partial z^2} + m_y \frac{\partial^2 H_d^y}{\partial z^2} + m_z \frac{\partial^2 H_d^z}{\partial z^2} \tag{4.11}$$

Therefore, one can immediately see that if the tip magnetization has only a z perpendicular component $\mathbf{m} = (0, 0, mz)$, the force derivative will be proportional only with the second derivative of the z component of the stray field generated by the non-uniform distribution of magnetization:

$$F'_{mag} = m_z \frac{\partial^2 H_d^z}{\partial z^2} \tag{4.12}$$

The response of a perpendicular magnetization media constituted by adjacent up and down domains can be obtained using a simplified model in which the tip is treated as dipole and the transitions between the domains are considered to have a finite width w. For a single transition centered at $x = 0$ in a magnetic layer of thickness h, we assume that within the film the magnetization profile is given by [10]:

$$\begin{pmatrix} M_x \\ M_y \\ M_z \end{pmatrix} = \begin{pmatrix} 0 \\ 0 \\ -\frac{2}{\pi} M_s \arctan\left(\frac{x}{w}\right) H(z), \end{pmatrix} \tag{4.13}$$

where $H(z)$ is the Heaviside function,

$$H(z) = \begin{cases} 1 & \text{if} \quad 0 < z < h \\ 0 & elsewhere \end{cases} \tag{4.14}$$

The magnetization current density is calculated as the divergence of the magnetization:

$$\rho(x, y, z) = -\nabla \cdot \vec{M}(x, y, z) \tag{4.15}$$

The magnetic potential verifies the Poisson equation from electrostatics:

$$\Delta\Phi = -4\pi\rho(x, y, z) \tag{4.16}$$

Once solving the Poisson equation, we can immediately deduce the stray field vector as:

$$\overrightarrow{H_d}(x, y, z) = -\nabla\Phi(\mathrm{x}, \mathrm{y}, \mathrm{z}) \tag{4.17}$$

It can be seen that the stray field comes only from the zones where the divergence of the magnetization is nonzero (basically the domain wall region, because in a domain the magnetization is constant and therefore, $\rho(x, y, z) = 0$).

If we follow the strategy defined by the equations 4.15-4.17 starting from the magnetiza-

tion profile defined by 4.11, we get the vector stray-field:

$$\begin{pmatrix} H_d^x \\ H_d^y \\ H_d^z \end{pmatrix} = \begin{pmatrix} 2M_s \ln\left(\frac{(z+h+w)^2+x^2}{(z+w)^2+x^2}\right); \\ 0 \\ -4\pi M_s \tan^{-1}\left(\frac{xh}{(z+w)(z+w+h)+x^2}\right) \end{pmatrix}; \text{with} \quad z>0 \tag{4.18}$$

In this equation, the origin of z is taken at the surface of the film (shifted by h with respect to the initial figure). Therefore, $z>0$ represents the vertical distance above the surface of the sample. From the stray field vector, the z component of the second derivative of the stray field $\frac{\partial^2 H}{\partial z^2}$ can be derived as being:

$$\begin{pmatrix} \frac{\partial^2 H_d^x}{\partial z^2} \\ \frac{\partial^2 H_d^y}{\partial z^2} \\ \frac{\partial^2 H_d^z}{\partial z^2} \end{pmatrix} = \begin{pmatrix} -4M_s\left[\frac{x^2-(z+w)^2}{\left(x^2+(z+w)^2\right)^2} - \frac{x^2-(z+h+w)^2}{\left(x^2+(z+h+w)^2\right)^2}\right] \\ 0 \\ -8M_s x\left(\frac{z+w}{\left(x^2+(z+w)^2\right)^2} - \frac{z+w+h}{\left(x^2+(z+w+h)^2\right)^2}\right) \end{pmatrix} \tag{4.19}$$

with $z>0$. Now, we would like to model a series of transitions as the superposition of individual periodical (period p) transitions according to:

$$\vec{H}_{TOTAL}(x,y,z) = \sum_{n=-\infty}^{+\infty} (-1)^n \overrightarrow{H_d}(x-np,y,z) \tag{4.20}$$

The expressions 4.12, 4.19 and 4.20 can be used to calculate the force between the tip and the periodical perpendicular magnetization domain wall structure.

Following the above described formalism we have performed numerical calculations, for different values of material parameters. We present here the results corresponding to M_s=1420 emu/cm^3 (corresponding to Co), the transition width w=100 and 150 nm (reasonable values corresponding to [9], the film thickness h=200 nm and the periods of the stripe structure p=100, 150 nm. The following Figures illustrate the numerical results. From the results presented, Figures 4.4, 4.5, one can see that the magnetic signal comes from the transition region (domain wall) where the divergence of the magnetization is nonzero. However, in the center of the wall, M_z, H_z, $\partial^2 H_z/\partial z^2$ cross the zero value and the stray field detected by the MFM tip is spread over the adjacent domains. Therefore, the white/dark contrast measured by the MFM tip will localize adjacent up/down domains. It is important to note that the MFM tip is not probing the stray field of a domain where the magnetization is constant but stray fields of domain walls whose maxima and minima are localized on adjacent domains. An interesting situation appears when p/h ratio increases (the domain period is larger than the film thickness). The result is illustrated in the Figure 4.6. Here one see that for $p/h<1$ the signal has a sinusoid form, where the zero always locates the position of the

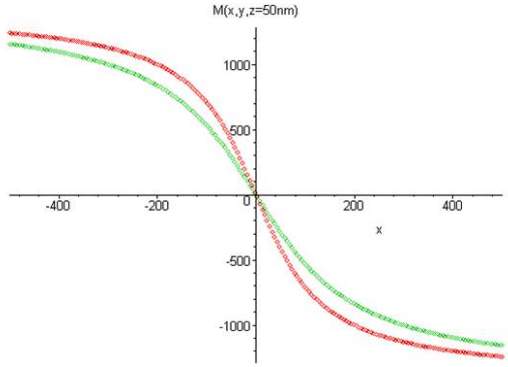

(a) Arctangent magnetization profile $M_z(x)$ defined by eq. 4.11 for a perpendicular magnetization media. The red curve correspond to a transition width w=150 nm and the red one to w=100 nm.

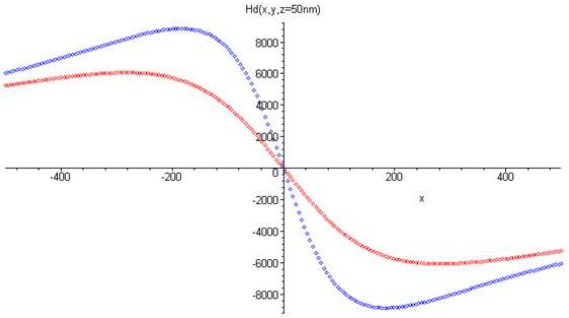

(b) The z component of the stray field corresponding to the magnetization profile $M_z(x,y,z=10$ nm)(blue curve) and $M_z(x,y,z=100$ nm)(red curve).

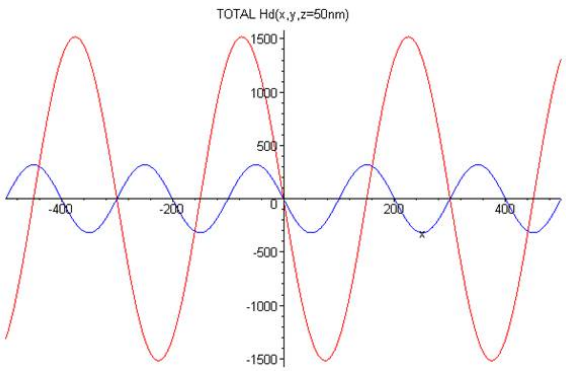

(c) The z component of H_d obtained from the superposition of periodical field profiles given by eq. 4.20. The blue curve corresponds to a period of 100 nm and the red one to p=150 nm

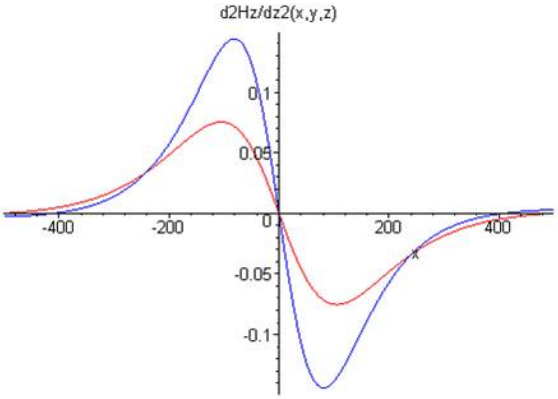

(d) The z component of the second derivative of the stray field corresponding to a sign transition up-down perpendicular domain structure. The blue (red) curves correspond to z=50 nm (100 nm).

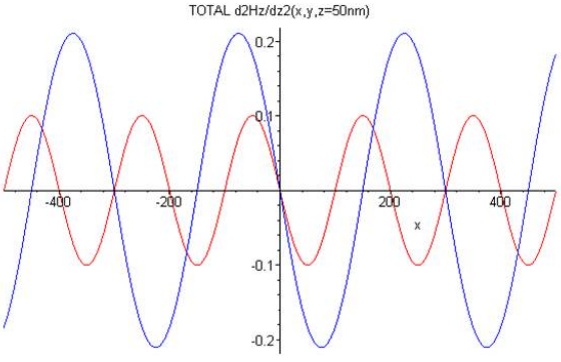

(e) z component of the second derivative of a total stray field corresponding to a periodical perpendicular stripe domain wall structure. The blue (red) curves correspond to a period of 100 nm (150 nm).

Figure 4.4

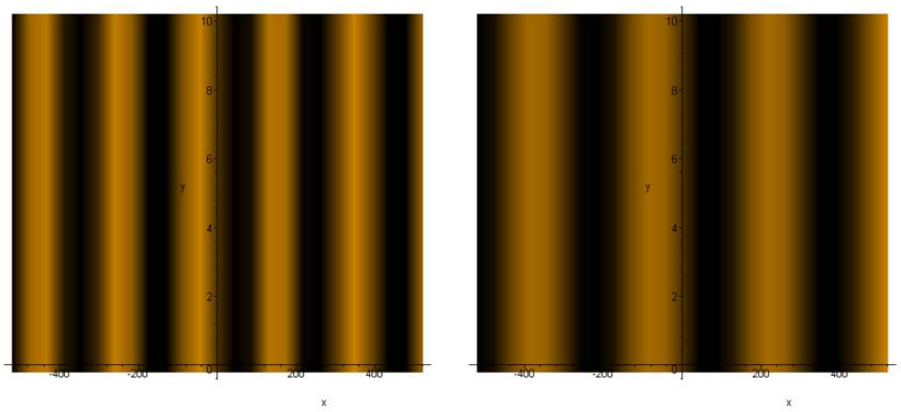

(a) **(b)**

Figure 4.5: Density plot representation of the $\partial^2 H_d^{z,total}$ (a) for p=100 nm, (b) p=150 nm. Following the equation 4.12, the force between a magnetized MFM tip and the magnetic distribution will be proportional to this quantity. This result will roughly qualitatively simulate the MFM contrast of a perpendicular magnetization stripe structure.

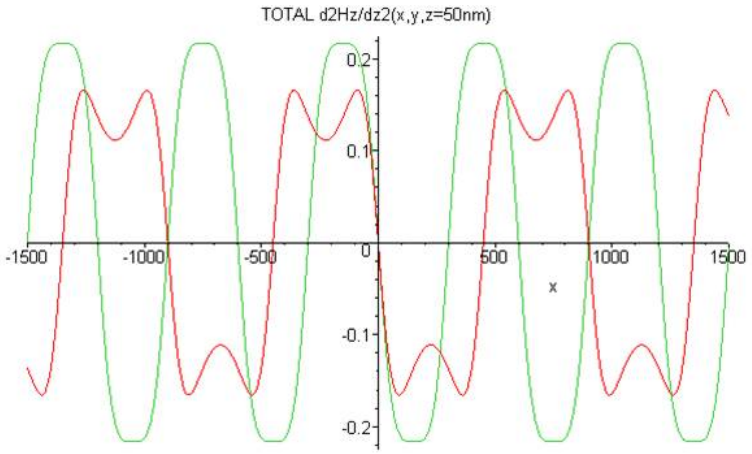

Figure 4.6: z component of the second derivative of a total stray field corresponding to a periodical perpendicular stripe domain wall structure. The green curve correspond to a period of 300 nm for a film thickness of 300 nm (p/h=1) and the red curve to p=450nm, h=300nm (p/h=1.5).

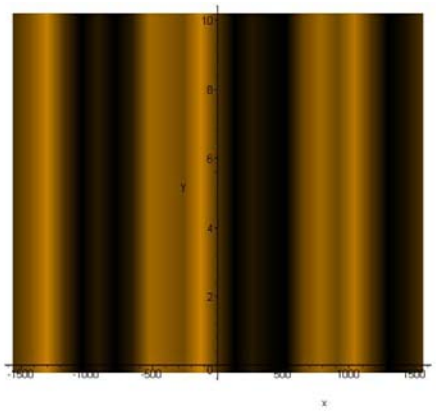

Figure 4.7: z component of the second derivative of a total stray field corresponding to a periodical perpendicular stripe domain wall structure. The green curve correspond to a period of 300 nm for a film thickness of 300 nm (p/h=1) and the red curve to p=450nm, h=300 nm (p/h=1.5).

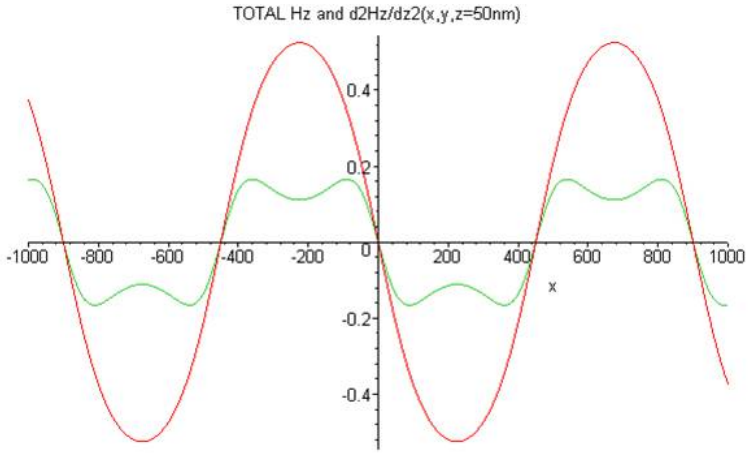

Figure 4.8: Normalized total stray field (red curve) and corresponding $\partial^2 H_d^{z,total}$ for h=300 nm, p=450 nm (green curve).

domain walls. For p/h>1, from the superposition of signals local minima appear which adds supplemental amplitude modulation on the measured signal $\partial^2 H_z/\partial z^2$.

However, even in this case, the position of zeros always localizes the position of the domain walls. Aside the p/h dependence, the results illustrated above depend on the film thickness value h. By reducing the h value, the critical p/h where additional modulation appears is pushed forward. The above analysis is meant to demonstrate that the second derivative of the z component of the stray field may have a complex spatial modulation. An accurate quantitative analysis of the periodical domain wall structure width represents a quite difficult task.

We focus now on the signal dependence on the z value (defining the tip lift distance above the sample when measuring the MFM signal). To do this, we performed calculations of the

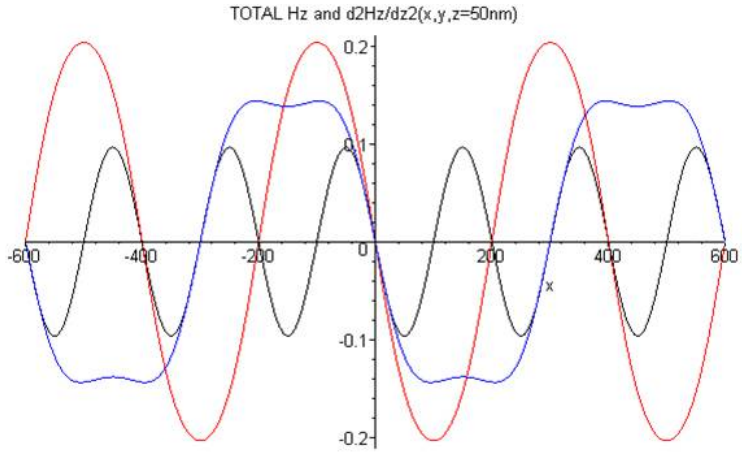

Figure 4.9: $\partial^2 H_d^{z,total}$ for h=100 nm and p=100 nm (p/h=1) black curve, p/h=2 red curve, p/h=3 blue curve.

second derivative of the field in two distinct cases: isolated DW separating two domains with opposite perpendicular magnetization (single transition) and periodical structure of DW (perpendicular stripe structure). In the case of the single transition, one can see that the width of the dark/white contrast depends on the z value. The larger is z (scan lift value), the larger would be the bright/dark contrast width. One could naively extrapolate these results and anticipate that the analysis of the domain wall width in a periodical stripe structure will be influenced by the scan lift value used for the MFM analysis. This would be a very bad thing for the experimental analysis of the MFM images because different scan lift values in different scan (often varied to optimize the amplitude/quality ratio of the measured signal) would influence the measured DW width. However, we demonstrate from our simulation that when periodical signals coming from periodical transitions superimpose, the width of the bright/dark contrast does not depend on the scan lift z value. For the periodical stripe DW structure, as expected, even if the amplitude of the measured signal (stray field) decreases with increasing the tip lift (z position) the x position of zeros (locating the DW) remains unchanged. This invariance of the DW width on the lift distance is very important when estimating the DW width from MFM images taken at different lift values. However, despite of this invariance an accurate quantitative analysis still remains a difficult task. As shown by Rugar *et al.* [9] by changing the angular orientation of the MFM tip from perpendicular (the case modeled here) to highly tilted position, the character of images changes significantly. Moreover, the imaging resolution depends on the tip quality (size, shape, etc.). One always convolutes the shape of the measured object with the shape of the tip (in MFM analysis the stray field of the magnetic object with the one of the tip). It is important to underline the distinction between the resolving power of the MFM probe and the sharpness of the stray field distribution. Even in case of a point-dipole tip (Delta Dirac

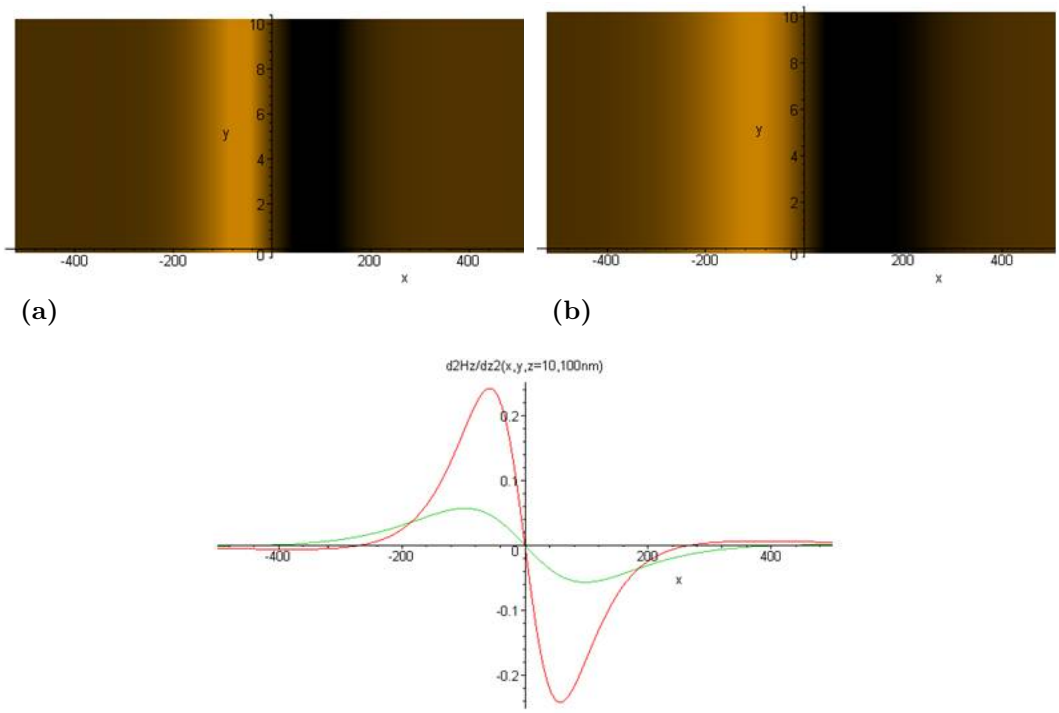

Figure 4.10: $\partial^2 H_d^{z,total}$ for a single transition corresponding to a scan lift value z=10 nm (red curve and (a)) and z=100 nm (green curve and (b)).

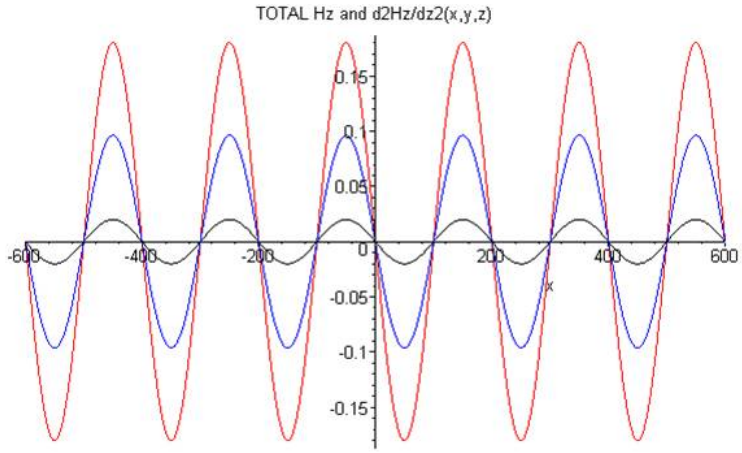

Figure 4.11: $\partial^2 H_d^{z,total}$ for h=100 nm at different z values above the surface z =30, 50, 100 nm (red, blue, black curves). One can see that by increasing z the amplitude of the signal decreases but the position of zeros remains unchanged.

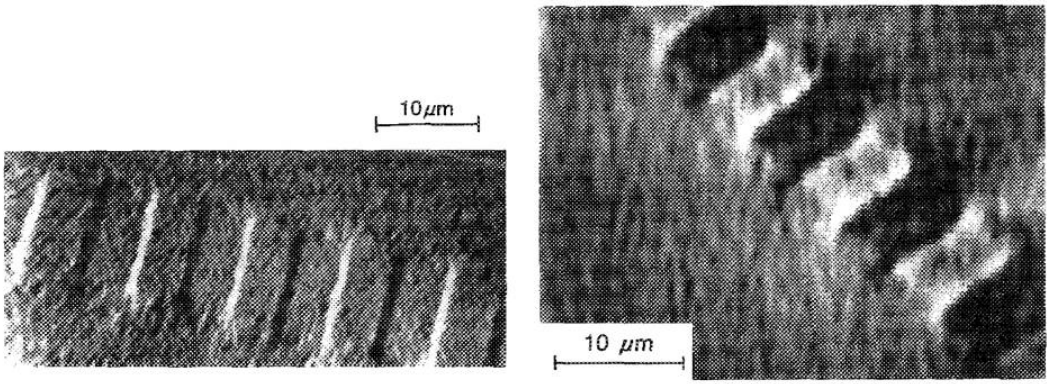

(a) (b)

Figure 4.12: MFM image taken on longitudinal magnetic storage media with a straight tip oriented perpendicular (a) and at an oblique angle of about 20° (b) with respect to the sample (taken from Rugar *et al* [9]).

probe function), the width of the measured field distribution will be finite and on the order of the spacing between the probe and the sample. Therefore, for a maximum resolution the scan lift distance should be minimized as much as possible. Moreover, as demonstrated by Rugar *et al.* [9], the resolution depends strongly on the tip size In applications where very close, adjacent domains have to be resolved, special tips are designed in the called cantilever geometry, Figure 4.13b.

4.1.2 Permalloy thin film growth

Permalloy films were grown on Si(111) single crystal substrates by dc magnetron sputtering. The deposition was performed at room temperature in 0.9 mTorr of flowing Ar atmosphere. A 2 inch sputtering target was prepared in house by plasma arc melting, having the $Ni_{80}Fe_{20}$ nominal composition. The base pressure in the chamber was $\sim 2\times10^{-8}$ Torr. In order to avoid oxidation of the films during growth, prior to the deposition the vacuum chamber underwent baking routines in order to degas the chamber walls, with temperatures reaching values higher than 100 °C. The film thicknesses considered for our studies varied from 6 nm to 720 nm determined from X-ray reflectometry (XRR). The structural properties were determined by X-ray diffraction in a grazing incidence (GIXRD) configuration. Magnetic properties were characterized by VSM and MFM imaging.

4.1.3 Structural Properties of Permalloy thin films

The structural properties of thick Permalloy films, *i.e.* with thicknesses exceeding the critical thickness for stripe domain formation, are very important because they determine the out-of-plane anisotropy, as seen from Eq. 4.1. Because of the high resolution configuration of

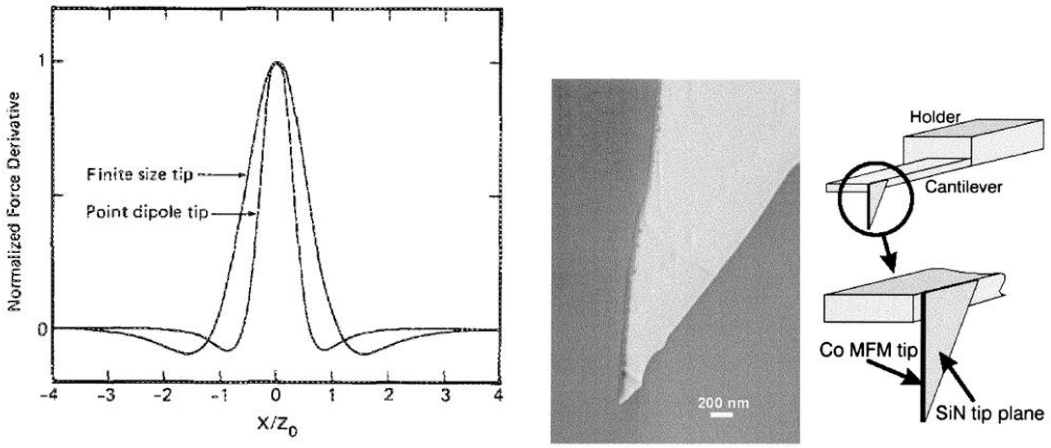

(a) **(b)**

Figure 4.13: (a) Force derivative point responses calculated for a point dipole measured object and two MFM tip geometries: point dipole and realistic finite size geometry (taken from [9]), z_0 is the tip to sample spacing. (b) SEM image and schematic picture of a cantilever used for high resolution MFM images (taken from [11]).

the X-ray diffractometer, and in particular due to the triple-bounce Ge (220) monochromator, the incident radiation intensity is strongly attenuated. Therefore, higher angle peaks were not recorded, as their intensity was too low for any practical purposes. Only the (111) $Ni_{80}Fe_{20}$ peaks were recorded for different film thicknesses in the range in which stripe domain configuration is expected (270, 460 and 720 nm). For example, in Figure 4.14a the (111) peak is shown for the 270 nm thick Py film. In order to accurately determine the peak positions, the peaks were fitted with pseudo-Voigt functions. The pseudo-Voigt function is a linear combination of a Gauss and a Lorentz function. It represents a good approximation of the Voigt function, which is a convolution of the two peak functions. The expression of the pseudo-Voigt function is written as:

$$pV(x) = \eta L(x) + (1-\eta)G(x), \tag{4.21}$$

where $L(x)$ and $G(x)$ represent the Lorentz and Gauss functions:

$$L(x) = \frac{1}{1+\left(\frac{x-x_0}{w}\right)^2} \text{ and } G(x) = \exp\left[-\ln(2)\left(\frac{x-x_0}{w}\right)^2\right]. \tag{4.22}$$

As it can be seen from Figure 4.14b that there is little variation in the position of the peak position for the different thicknesses. Magnetic measurements indicate that the films are under a tensile strain, so that the crystal lattice of the films suffers a tetragonal distortion. Since we do not have access but to one diffraction peak, no quantitative determination of the film lattice parameters can be performed. However, the invariance of the (111) peak position

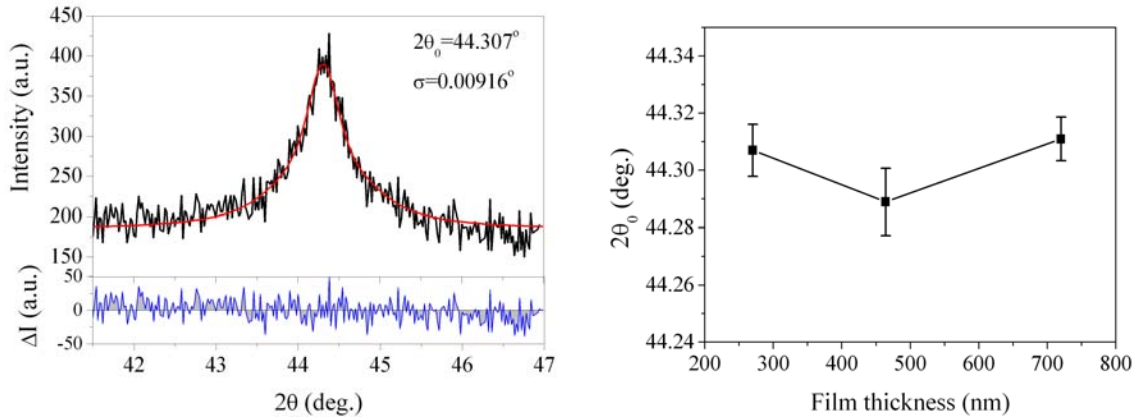

Figure 4.14: (a) Recorded (111) peak for the 270 nm thick film (black) and the corresponding pesudo-Voigt fit (red), ΔI represents the difference between the pseudo-Voigt fit and the experimental data; (b) Position of the (111) peaks as a function of film thickness.

is an indication that no variation of the magnetic anisotropy is to be expected, since in this thickness range there is no variation of the magnetostriction coefficient, λ_s[5].

4.1.4 Magnetic Properties of Permalloy thin films

The normalized magnetization cycles for the 6 nm, 62 nm and 125 nm thick films are shown in Figure 4.15. The magnetic field is applied in the in-plane direction of the film. The magnetization along the easy axis has a square shape as a function of the applied field, while the loops along the hard axis of magnetization are more tilted resulting in a lower value of the remanent magnetization. The shapes of the cycles are typical for films possessing in-plane anisotropy. Also, from the above loops we can draw the conclusion that in this thickness regime we are well below the critical thickness for weak stripe domain pattern stabilization. This conclusion is also supported by the MFM measurements, not shown here, which do not display any magnetic contrast. This is to be expected for Py films in this thickness range, which have domains of the order of ∼1mm [6].

As the thickness of the films is increased beyond 270 nm, the hysteresis curves change dramatically, Figure 4.16. The magnetization dependence on the externally applied field has the characteristic shape of the films that exhibit weak stripe domains, as the one presented in Figure 4.3. The magnetic field was applied parallel to the film surface plane. The linear decrease of the magnetization from saturation is observed with a small hysteresis, together with the steep switch of magnetization. In order to test the expected rotatable magnetic anisotropy, the cycles were performed applying the magnetic field in two different perpendicular directions. No modification of the loops were observed, proving thus the existence of rotatable anisotropy. Figure 4.16d presents the thickness dependence of two characteristic magnetic quantities, the magnetization at remanence, M_r, and the in-plane saturation field,

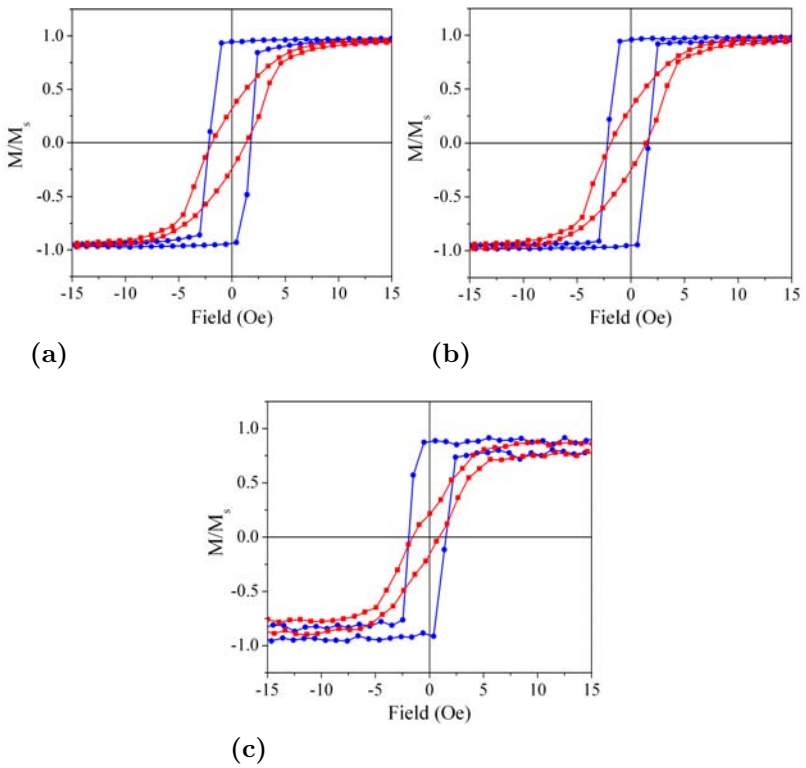

Figure 4.15: Hysteresis curves along the easy (blue) and hard (red) axes of the (a) 6 nm, (b) 62 nm and (c) 125 nm thick Py thin films.

$H_{sat}^{||}$. As the film thickness increases, the magnetostatic energy of surface charges decreases, allowing for the perpendicular anisotropy to manifest by an increase of the deviation angle of the spins, θ, with respect to the film surface plane. This increased deviation leads to a decrease of the in-plane magnetization remanence. Consequently, the larger magnetization perpendicular to the film plane leads to a higher in-plane saturation field. With respect to our goal to fabricate/study hybrid interface SC/FM systems for vortex pinning, higher θ values are expected to have a more pronounced influence on the superconducting properties of the bottom SC layer. Concomitantly, as it has been calculated in Eq. 4.8, an increase of film thickness also leads to an increase of stripe periodicity, *i.e.* domain width. In the following we present the results of MFM measurements on the films' domain structure and how it is affected by the film thickness.

The domain structure of the films having thicknesses of 270 nm, 460 nm and 720 nm are shown in Figure 4.17. As it can be seen the expected stripe domain configuration is present. Extracting a profile from the above images allows for an evaluation of the stripe wavelength, λ, and accordingly, of the domain width, $d = \lambda/2$, Figure 4.18. The domain width variation as a function of thickness has also been calculated according to the three models presented in the preceding paragraphs. For the calculation, the physical parameters entering the domain width expression were taken from Ref. [6], so that $M_s = 826$ emu/cm^3,

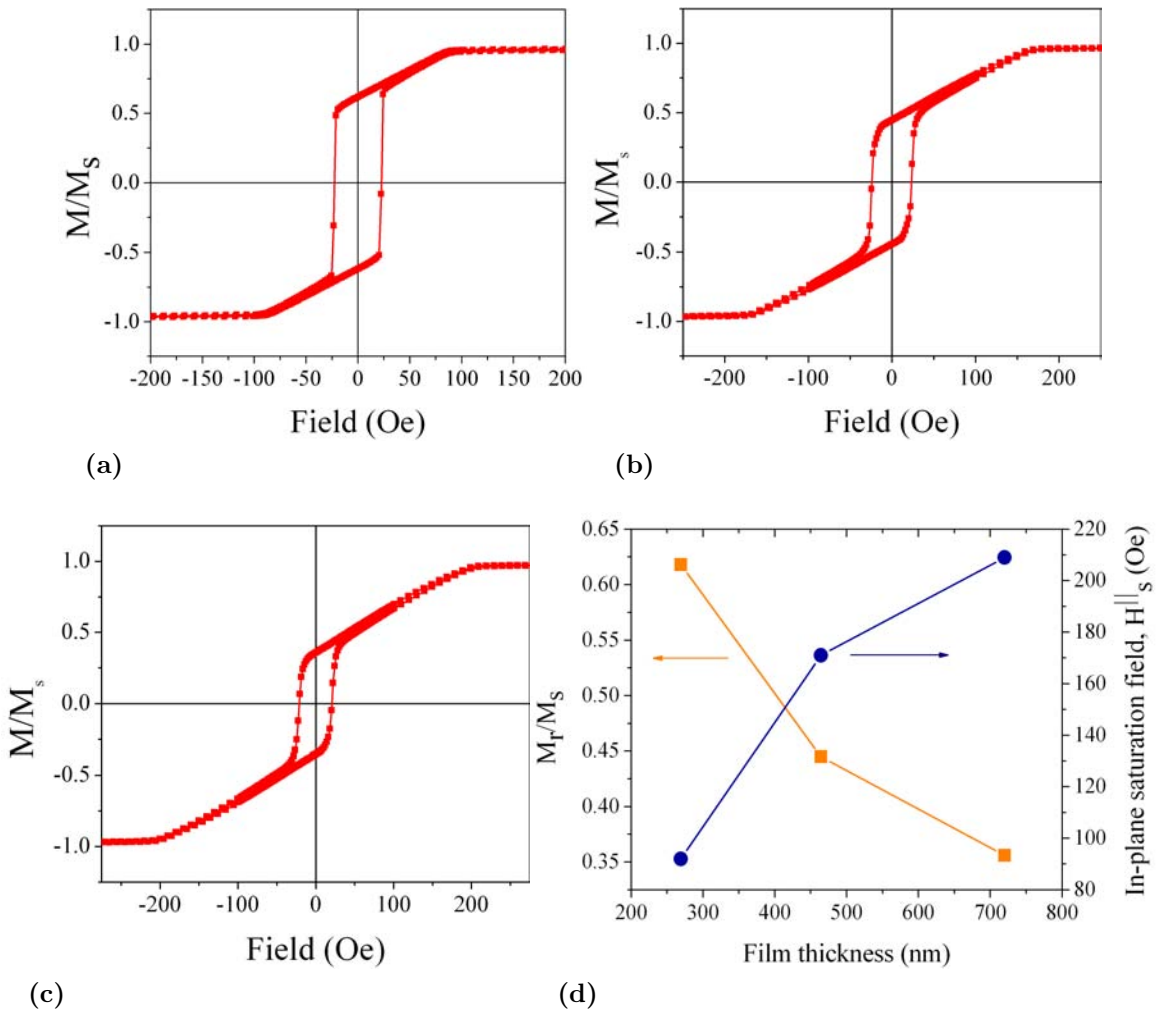

Figure 4.16: Hysteresis loops of the (a) 270 nm, (b) 6460 nm and (c) 730 nm thick Py thin films. The shape of the loop is typical for films having weak stripe domain configuration; (d) Variation of the normalized remanent magnetization, M_r/M_s, and of the in-plane saturation field, $H_s^{||}$ as a function of Py film thickness.

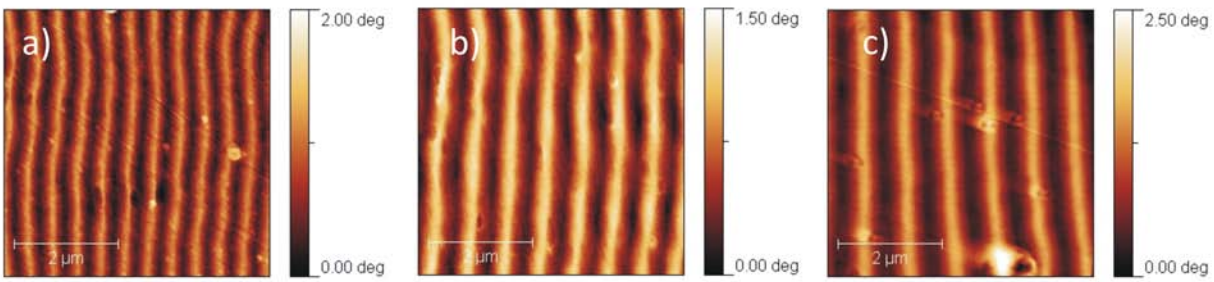

Figure 4.17: ($5\mu m \times 5\mu m$) MFM images of the (a) 270 nm, (b) 460 nm and (c) 720 nm thick Py films.

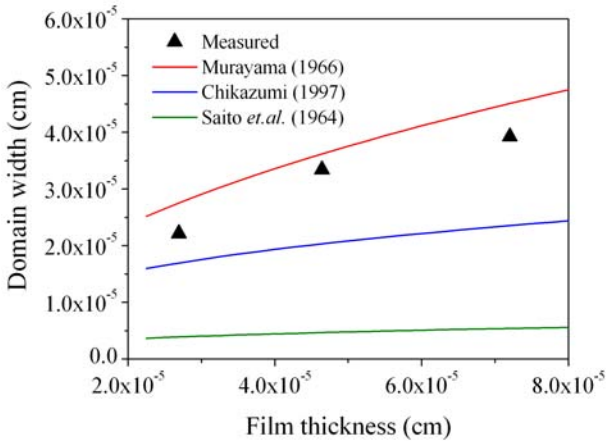

Figure 4.18: Domain width of the 270 nm, 460 nm and 720 nm thick Permalloy films. Domain width variation as a function of film thickness, calculated according to the three different models presented in the text.

the out-of-plane anisotropy constant, $K_U = 5 \times 10^4$ erg/cm^3, while the exchange stiffness constant was taken to be $A = 1 \times 10^{-6}$ erg/cm. Comparing the measured results with the three models, it is noted that the initial model of stripe domains, proposed by Saito *et al.* [1], in which the spin direction varies perpendicularly to the stripes in a $zig - zag$ as a function of position, is the worst approximation to the domain width value. A sine variation of the spin direction yields a better approximation of the domain width. Yet, the best results are found using the model proposed by Murayama [3]. Because of the fact that their model allows for the highest freedom in spin ordering, allowing for a variation of the spins with respect to all the coordinate axes, they are able to take into account the presence of closure domains at film surface. As it could be seen from the numerical simulations run on low out-of-plane anisotropy thin films, the model proposed by Murayama is the closest in describing the actual physical picture in these systems, and thus yields the most satisfactory result in predicting the domain width dependence on the film thickness.

As far as rotatable magnetic anisotropy is concerned, Figure 4.19 shows the orientation of the domain stripes in a remanent state after the application of an in-plane field along different directions. The value of the applied field was set at 650 Oe in order to ensure saturation of all the studied films. As it can be observed, the stripe domains align themselves along the direction of the applied magnetic field and do not change their orientation after the field is removed. The rotatable anisotropy feature of low out-of-plane anisotropy magnetic thin films is essential for the study of the influence of a periodic magnetic field on the superconducting properties of SC thin films, as it allows for a systematic modulation of the stray magnetic field produced by the FM layer [7].

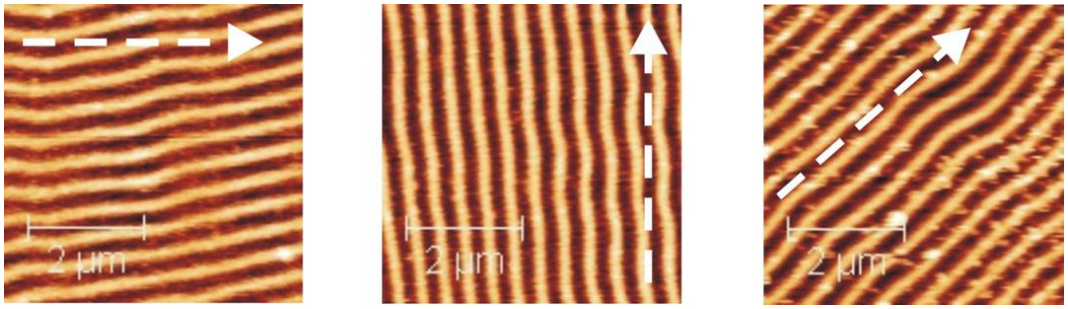

Figure 4.19: Rotatable anisotropy. Different magnetic stripe orientations correspond to the direction of the applied magnetic field (white dotted arrow) for a 464nm thick Py film.

4.2 Cobalt thin films

Over the last decades, cobalt thin films have been the subject of intensive studies, as they exhibit a wealth of magnetic properties suitable both for technological applications, as well as for fundamental studies regarding the magnetism of thin films. These properties are dependent on internal factors, such as crystal structure, film thickness, etc., or external factors, as the nature of the substrate the thin films were grown upon, the morphology of the substrate, capping layer, etc.

As we have mentioned in the beginning of this chapter, in order to create an effective flux pinning it is important to locally create a magnetic field that is perpendicular to the superconducting layer surface. This local field will interact with the magnetic vortices within the SC film exerting a pinning force on the latter, preventing them to move and thus, produce energy loss. The requirement for a perpendicular magnetic field can be met by depositing a magnetic layer or magnetic structures (micro-, or nano-,) having perpendicular anisotropy on top of the SC layer. The stray field thus produced by the magnetization lying perpendicular to the film surface, will then represent the magnetic *pinning field*. The effective uniaxial anisotropy constant, $K_{U,eff}$, responsible for the out-of-plane orientation of the magnetization, can be written as [12]:

$$K_{U,eff} = 2\pi D_m M_s^2 + K_U + B_{me}\epsilon + 2K_s/t, \tag{4.23}$$

where the first term represents the magnetic dipolar energy contribution, the second represents the magnetocrystalline anisotropy constant, $B_{me}\epsilon$ represents the film strain contribution to the overall anisotropy constant, while the last term is the surface anisotropy term. Thus, one can alter the anisotropy of a thin film in a wide variety of ways, acting on the structural properties of the film and the strain of the film which in turn is determined by the substrate, buffer/capping layers and the thickness of the film. In the following, we will briefly touch upon the above parameters and how they influence the magnetic state of Co

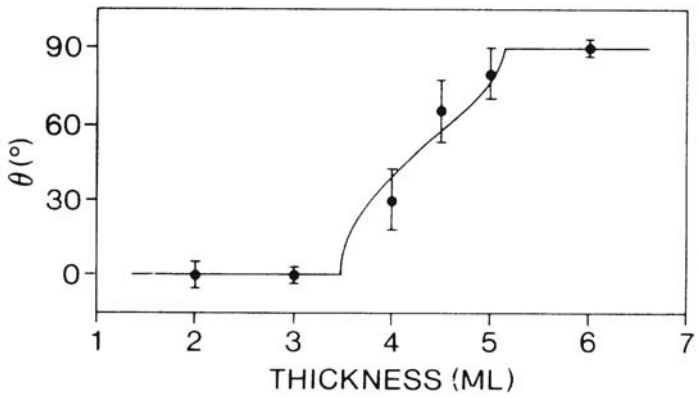

Figure 4.20: Angular dependence of the magnetization direction vs. thickness of Co(0001) thin films deposited on Au(111) single crystal substrates. Taken from [15].

thin films. A thorough review of the issues presented above is given by Vaz *et al.* [12].

Kowalewski *et al.* [13] studied the magnetic anisotropies of fcc Co(001) thin films, in the atomic mono-layer (ML) thickness range, deposited on Cu(001) single crystal substrates. They found that the epitaxial Co thin films were subjected to a in-plane tensile strain, which resulted in a compression of the lattice along the surface normal. The resulting face centered tetragonal lattice had a profound influence on the magnetic properties of the Co(001) films, namely it led to the stabilization of an out-of-plane magnetic anisotropy, which would not have been physically possible in the undistorted cubic lattice. The thickness dependence of the effective uniaxial anisotropy constant was found to consist of a constant term and an additional $\sim 1/t$ term, where t represents the film thickness. LEED studies revealed that above 4 ML the strain present in the Co films is constant with film thickness so that no thickness dependence was to be expected for the magnetoelastic term of the anisotropy. The $1/t$ dependence was thus attributed solely to the surface contribution term, Eq. 4.23. In order to assess the relative contributions to the effective perpendicular anisotropy constant, of the magnetocrystalline constant and of the strain induced magnetoelastic term, Vaz *et. al.* [14], studied Co/Ni/Cu(001) structures. Their option for these systems was determined by the fact that the Ni film lattice relaxes to its bulk lattice parameters above a certain thickness, while Co grows pseudomorphically on Ni. Thus, by varying the thickness of the Ni film one can modify the strain state of the Co film. This permits a coherent study of the influence of strain on the perpendicular anisotropy of Co thin films. Results show the existence of a large second order magnetocrystalline term that is not dependent on the film thickness and that the perpendicular magnetic anisotropy was not influenced by strain.

An important phenomena observed in a variety of thin films is the so-called *spin reorientation transition*, SRT, in which the magnetization easy axis switches from out-of-plane to in-plane direction with respect to the film surface. This transition occurs above a critical

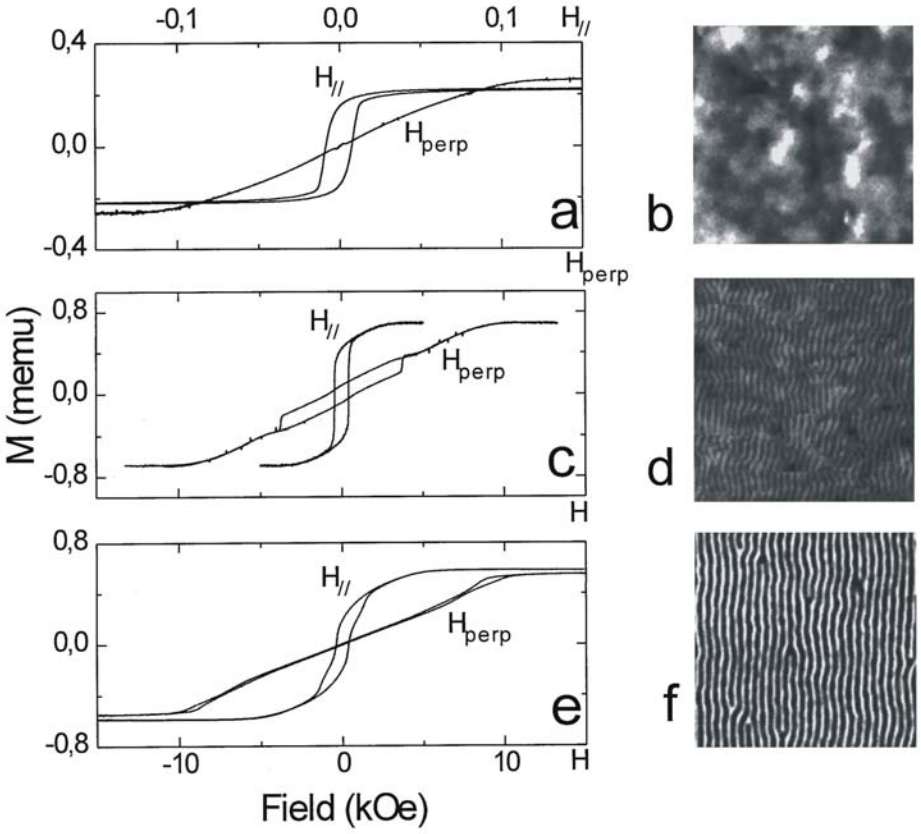

Figure 4.21: *M-H* curves with the magnetic field applied parallel and perpendicular with respect to the film surface for the (a) 10nm, (c) 25nm and (e) 50nm thick films. Corresponding 3μm$\times 3\mu$m MFM images of the demagnetized (b) 10 nm, (d) 25 nm and (c) 50 nm thick films. Taken from [18].

thickness, t_{SRT}, and can be understood as being the result of the competition between the surface and volume contributions to anisotropy. If we neglect the strain term in the expression of the effective anisotropy constant Eq. 4.23, the expression of the critical thickness, t_{SRT}, is given by

$$t_{SRT} = -2K_s/(2\pi M_s^2 + K_U), \tag{4.24}$$

where we have considered that in the case of thin films the out-of-plane demagnetizing factor, D_m, is approximately unity. Allenspach *et. al.* [15] studied the evolution of the magnetization direction vs. film thickness , on epitaxial hexagonal Co(0001) thin films deposited on Au(111) single crystal substrates. As can be seen from Figure 4.20, the transition from the out-of-plane direction, $\theta = 0°$, to the in-plane direction, $\theta = 90°$, of the magnetization takes place within a less than 2 ML interval.

As the film thickness is further increased, Kittel [16] predicted, based on energetic arguments, that for magnetic thin films having strong perpendicular magnetocrystalline anisotropy, K_U, the magnetization may switch from the in-plane direction, as we have seen

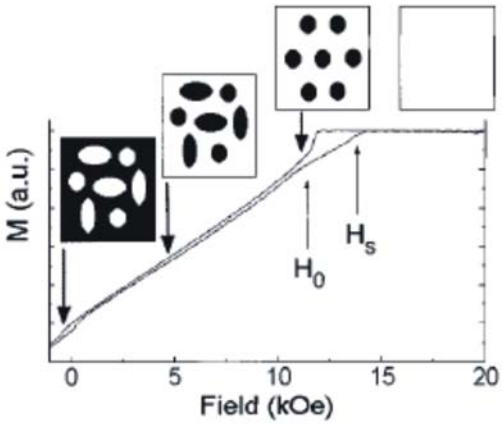

Figure 4.22: Positive field branch of the perpendicular $M-H$ characteristics of a 150nm thick Co film.Taken from [18].

in the case of Co(0001)/Au(111) thin films, back to the out-of-plane direction. For hexagonal Co thin films the critical thickness for the above transition was estimated to be around 30 nm. Donnet *et.al.* [17] conducted a study of epitaxial hcp Co thin films deposited on Ru buffered mica substrates, around the critical thickness predicted above. Indeed, they found that for a thickness of 40 nm, a *weak stripe* domain pattern is observed. This pattern was found to be similar to the pattern described in the previous Section, for Py films, as first proposed by Saito *et. al.* [1], in which the magnetization describes an out-of-plane oscillation around an in-plane direction. For 60 nm thick films, the stripe configuration persisted, but in this case, the observed domain structure consisted of "true" *up* and *down* orientations of the magnetization vector with respect to the film surface. Hehn *et.al.* [18] also conducted an experiment in which the thickness of epitaxial Co layers was varied from 10 nm to 500 nm. Their structures consisted of $Al_2O_3(11\bar{2}0)$//Ru(20 nm)/Co(t≥1 0nm)/Ru(5 nm) layers. Figure 4.21 shows the evolution of the hysteresis loops and corresponding domain structure, analyzed by MFM, for 10, 25 and 50 nm thick Co films.

As it can be seen from Figure 4.21(a) the magnetization lies in the in-plane direction of the film, as no hysteresis is observed in the perpendicular *M-H* loop in the case of the 10 nm film. As far as the domain structure is concerned, large domains, ∼1 μm, can be observed, Fig.4.21(b). The transition towards a perpendicular magnetization occurs at 25 nm as alternating dark and bright stripes can be observed, Fig.4.21(d), corresponding to a weak stripe configuration of the magnetization. For the 50 nm Co film, Fig.4.21(e), the perpendicular hysteresis loop exhibits a typical shape for thin films having alternatively up and down stripe domains, in which the magnetization in the middle of the stripe is perpendicular to the film. The same shape of the cycles was found to persist for the rest of the thickness range, up to 500 nm. Figure 4.22 presents the positive field part of the

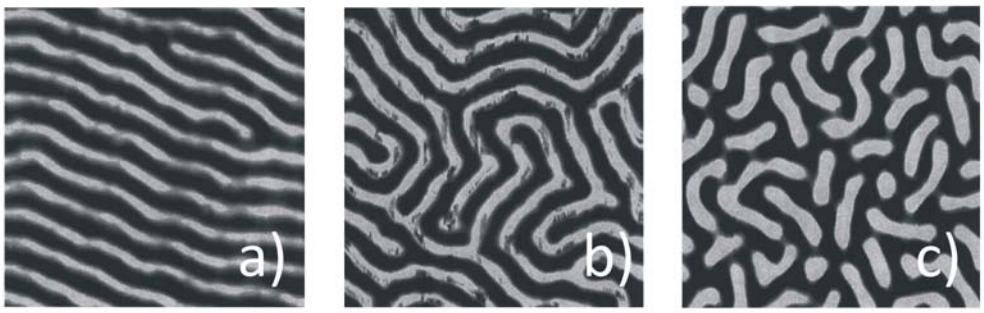

Figure 4.23: (a) Parallel demagnetized, (b) perpendicularly demagnetized and (c)perpendicularly magnetized states of a 500 nm thick, epitaxial Co thin film. Taken from [18].

perpendicular *M-H* loop for a 150 nm thick film, for which the perpendicular direction of the magnetization is expected. Hehn *et. al.* [18] correlate the different parts of the loop with the magnetic domain configuration of the films. At saturation, as it is to be expected, all the spins are oriented in the filed direction, so that no magnetic contrast is illustrated in the corresponding figure. As the magnetic field is decreased, a sharp drop in the magnetization can be observed. This singularity at H_0 marks the nucleation of magnetic bubble domains having the magnetization within them point in the opposite direction. H_0 is consequently named the *nucleation field*. Further decreasing the applied magnetic field, results in an increase of the bubble radius, *i.e.* a shrinkage of the bubble lattice parameter. The authors argue, citing on of the references included in the text [19], that above a certain bubble radius, the domains start to elongate assuming an elliptical shape. Elliptical domains represent the intermediate stage towards stripe domain configuration, even though in some cases the repulsive interaction between bubbles impede stripe formation [18]. As the last step in their description, the authors point out the reversal of the magnetization upon the applying a negative perpendicular magnetic field.

For the MFM analyses several magnetic states of the samples were prepared. In Figure 4.23 three of these states are presented. Figures 4.23 (a) and (b) represent the demagnetized states of the films. The demagnetization procedure consisted of sweeping the external applied magnetic field from positive to negative values, while simultaneously reducing its value. Figure 4.23(a) represents the *parallel demagnetized state*, in which the field was applied parallel to the sample surface. The result is a magnetic stripe domain pattern, having the stripes aligned to the direction of the field. The stripe orientation is a consequence of the magnetization parallel component minimizing Zeeman energy in the initial stages of the demagnetization process, when there is a field-induced parallel component of the magnetization. As far as the *perpendicular demagnetized state* is concerned, the domain structure is still characterized, by locally parallel stripe domains, but because the field was applied

perpendicularly, there is a new degree of freedom in the orientation of the magnetization, so that the magnetic stripes form a *labyrinth*-type structure. The last image, Fig. 4.23(c) correspond to a *perpendicular magnetized state*, in which the sample was saturated perpendicularly and the analyzed at remanence. The result is the observation of elongated domains that stem from the bubble domains formed initially at high fields.

4.2.1 Co thin film growth

As in the case of the Permalloy films reported in the previous section, Co films were deposited by means of dc magnetron sputtering technique at room temperature on Si(111) substrates, covered by a native SiO_2 layer. The sputtering gas was argon which was maintained at a pressure of 0.9 mTorr throughout the deposition process. The same chamber degas routine has been employed in order to ensure a low contamination of the films during growth. The deposition rate was estimated to be of ∼0.1 nm/s, from XRR measurements. XRD analysis show that within the studied thickness range, the films posses a hexagonal structure with a [0001] out-of-plane texture. Also, an epitaxial 150 nm thick Co film was deposited onto a $Al_2O_3(0001)$, *c*-cut sapphire, single crystal substrate. In order to avoid the oxidation of the Co film an approximately 5nm thick Ru film was deposited on top of the Co film as a capping layer. Both the Co and Ru layers were deposited at 400 °C. Prior to the deposition the substrate underwent a degassing procedure which consisted of an annealing step at 550 °C for half an hour.

4.2.2 Magnetic properties of Cobalt thin films

M-H loops for the thicker, 246 nm, 340 nm and 493 nm Co films are presented in Figure 4.24. It can be observed from the parallel cycles that all the three films exhibit a behavior that is quite similar to the thick Permalloy films presented in Section 4.1.4. Reducing the field from saturation there is an almost linear decrease of the magnetization, while in a negative field a sharp switch of the magnetization occurs. A stronger hysteresis is observed in the linear part of the magnetization in the case of the Co films than in the case of the Py ones. We may conclude that the relatively thick textured Co thin films posses a weak stripe domain structure, most likely due to the out-of-plane anisotropy induced by the film (001) texture. The existence of an out-of-plane magnetization in these films is confirmed by the perpendicular *M-H* loops, in which, for all the films a hysteresis is present, indicating the existence of a domain pattern with a perpendicular component of the magnetization. As in the case of Py films, the maximum deflection angle of the spins, θ_0, with respect to the surface plane of the film, increases. This increase leads to a reduction of the in-plane component of the magnetization, so that the parallel remanent magnetization decreases. As a consequence, saturating the magnetization in-plane becomes energetically more costly, so

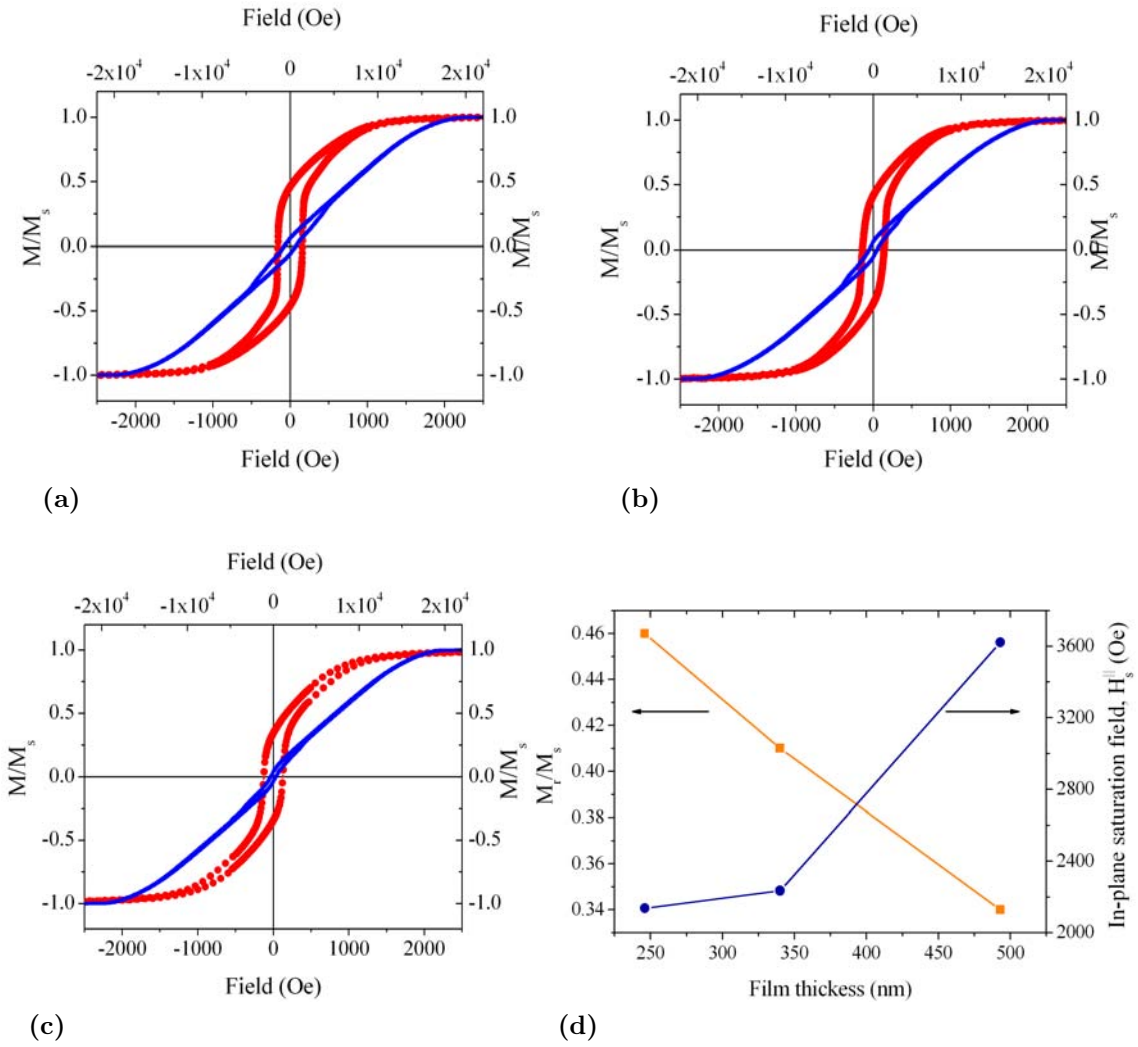

Figure 4.24: Parallel (red, left and lower axes) and perpendicular (blue, right and upper axes) hysteresis cycles of textured Co films having the indicated thicknesses, (a) 246 nm, (b) 340 nm and (c) 493 nm; (d) Variation of the normalized remanent magnetization, M_r/M_s, and of the in-plane saturation field, $H_s^{||}$ as a function of Co thickness.

the in-plane saturation field increases accordingly. The variation of the two parameters as a function of thickness is shown in Figure 4.24d.

As far as the epitaxial Co thin film grown on $Al_2O_3(0001)$ substrate is concerned, the hysteresis cycles, both parallel and perpendicular, are shown in Figure 4.25. The two loops are typical for epitaxial Co thin films having stripe domains with the magnetization within the domains laying in the perpendicular direction with respect to the film surface. In the in-plane magnetization cycle, at saturation all the spins lie in the plane of the film. As the external field is decreased, stripe domains are formed, with spins being deflected at a certain angle away from the in-plane direction. At remanence, the spins are perpendicular to the surface, the remanent magnetization originating solely within the domain walls. After the switch of the stripe orientation, the magnetization process proceeds symmetrically. The

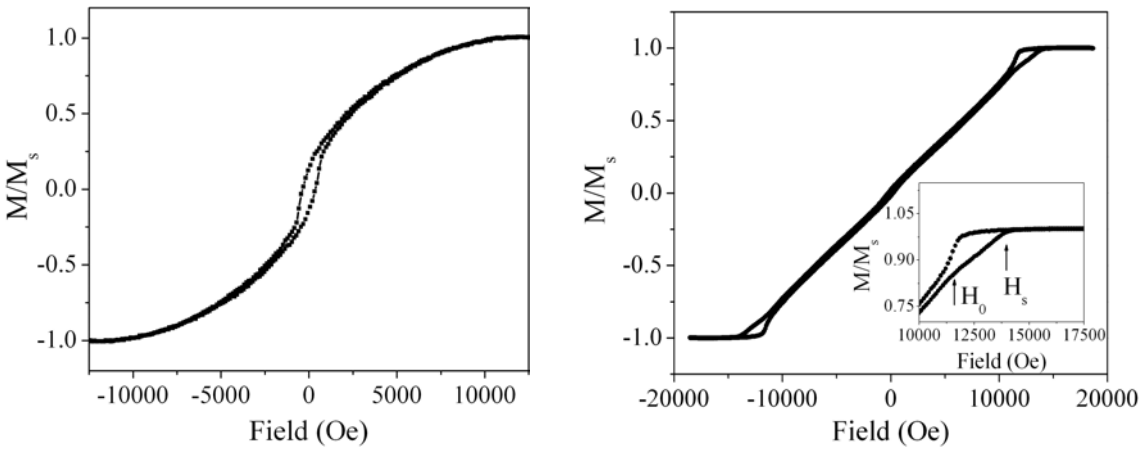

Figure 4.25: Parallel (a) and perpendicular (b) hysteresis cycles of the 150 nm thick Co film, (inset) saturation field and bubble nucleation filed are indicated.

perpendicular cycle has been described in detail in the introduction of the present Section. In summary, referring only to the high field end of the *M-H* loop, there are two characteristic fields, describing the magnetization phenomena. The saturation field, H_s, is defined on the branch of the loop coming from low fields, as the field at which all the bubble domains are annihilated. The other field quantity is defined as the bubble nucleation field, H_0, where spontaneous bubble domains appear. The decrease of the applied field leads to an elongation of the domains.

The domain structure of the thick textured Co films is presented in Figure 4.26. As it was expected from the shape of the corresponding hysteresis curves, the films exhibit stripe domain patterns. Similarly to the thick Py films, the stripe period increases with increasing film thickness. The weak stripe domain configuration of the Co films suggests that rotatable anisotropy should be present in these systems. Indeed, all the films exhibited this property. In Figure 4.27 we present the MFM images obtained on the 246 nm thick film after being subjected to three different orientations of a magnetic field of about 650 Oe. It can readily be seen that the magnetic stripes orient themselves along the field direction. However, slight branching of the domains can be observed. This may be due to the fact that the value of the applied field is lower than the saturation field, ∼2000 Oe.

The parallel demagnetized state of the epitaxial Co thin film, Fig. 4.28a does not differ significantly, from the MFM analysis point of view, from the textured films. Alternating bright and dark parallel stripes form the microscopy images in both cases. In the perpendicular demagnetized state, however, the perpendicular field allows for an arbitrary arrangement of the magnetic stripes. This fact leads to the formation of *chevron*-like stripes, and an overall labyrinth domain structure, typical for perpendicular magnetization Co thin films, Figure 4.28b.

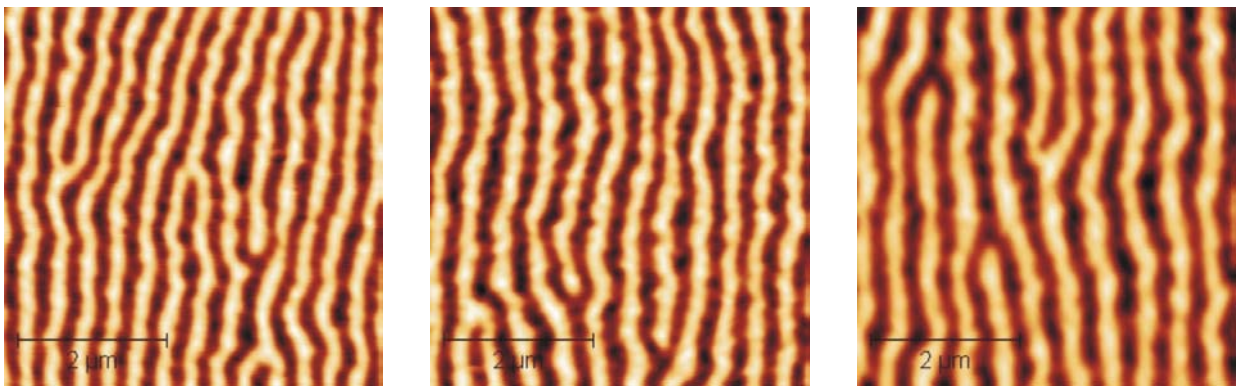

(a) **(b)** **(c)**

Figure 4.26: (5μm×5μm) MFM images of the (a) 246 nm, (b) 340 nm and (c) 493 nm thick Co films.

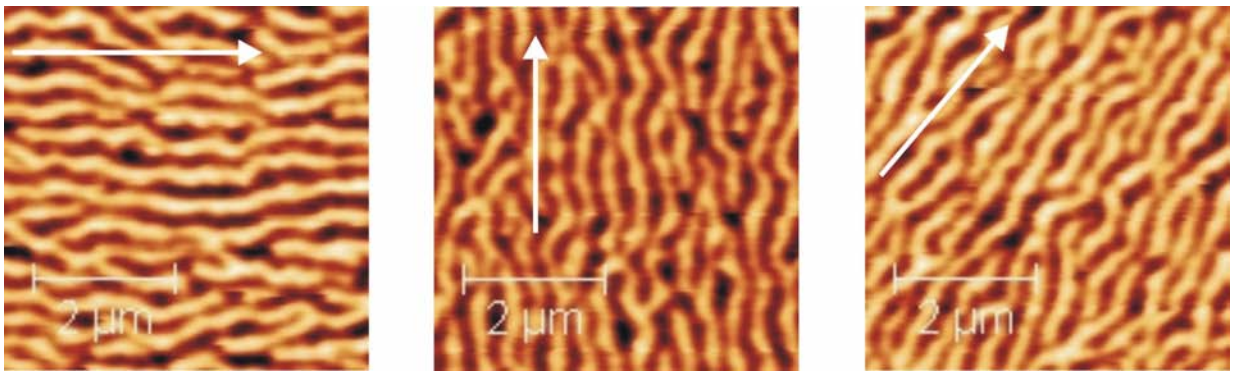

Figure 4.27: Rotatable anisotropy. Different magnetic stripe orientations correspond to the direction of the applied magnetic field (white arrow) for the 246 nm thick Co film.

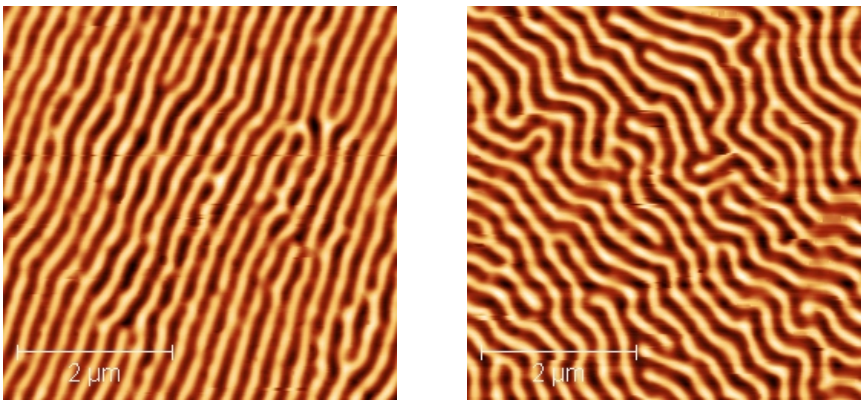

(a) **(b)**

Figure 4.28: (5 μm×5 μm) MFM imagnes of the (a) parallel and (b) perpendicular demagnetized states of the 150 nm thick epitaxial Co(0001) thin film.

4.3 Magnetic micro,- and nanostructures

In the previous Sections of the present Chapter we have shown that continuous magnetic thin films can be prepared in such a way so as to obtain a strong modulation of the magnetization, through the stabilization of the stripe domain configuration. Periodic stripes of alternating "up" and "down" orientation of the magnetization with respect to the film surface plane are expected to provide a strong pinning of the SC vortices, as shown in Chapter 1, when these alternations are oriented perpendicularly to the direction of the vortex motion. Magnetic micro,- and nanostructures, such as regular dot arrays, provide an additional degree of freedom to the modulation, as they are subject also to a topographic periodicity, given by the specific pattern of the arrays defined by lithographic techniques. In these sense, even the sole presence of such structures in the vicinity of SC films may give rise to a pinning potential of the vortices, as demonstrated by Hoffmann *et al.* [23] in their study of a Nb film deposited on top of a regular array of non-magnetic Ag dots. The flexibility in defining different configurations of dot lattices coupled with their respective magnetic configurations produce *commensurability effects*. These effects consist in resonant changes of the magnetoresistance of the SC layer, $\rho(H_{ext})$, with the appearence of equidistant minima having a period in H determined by lattice constant of the magnetic dot arrays. Also, these minima are visible in the field dependence of the critical current density, $J_c(H_{ext})$, or in the magnetization curves, $M(H_{ext})$. These effects are explained considering a strong magnetic pinning potential exerted by magnetic dots on the SC vortices and coupled with a structural match between the dot and vortex lattices. Thus, when the condition that an integer number of vortices per magnetic unit cell is fulfilled, a maximum number of vortices are pinned, producing resistivity minima or J_c maxima of the SC film. The field dependence of these effects is explained by the fact that the vortex lattice parameter is field-dependent. Because of the fact that the vortex lattice is triangular strong commensurability effects are produced by triangular dot lattice.

Lateral structuring of the magnetic films into micro or nanostrucutres also influences their magnetic configuration, so that the magnetic state of the film will be altered when it is patterned into dot structures. Jubert and Allenspach [24] constructed a phase diagram of the magnetic states of circular nanometric dots as a function of their thickness and diameter, based on micromagnetic simulations. The results are shown in Figure 4.29. The disk diameter and film thickness are given in terms of the exchange length, $\lambda_{exch} = \sqrt{2A_{exch}/\mu_0 M_s^2}$, with A_{exch} being the exchange constant and M_s the saturation magnetization. As it can be seen by varying the lateral size an thickness of the dots one is able to stabilize different magnetic states: in-plane single domain (IPSD), vortex (V) and out-of-plane single domain (OPSD). Carneiro [28] calculated the interaction energy between a SC vortex and an in-plane and out-of-plane magnetized dipole showing that different attraction interaction profiles ex-

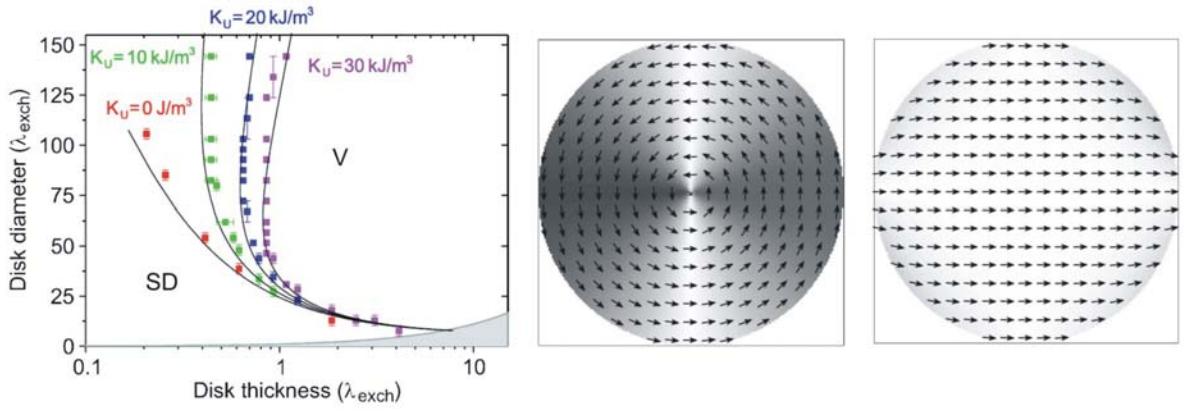

Figure 4.29: Single domain-vortex boundary for disks of different diameters and thicknesses with varying uniaxial anisotropy, K_U. Lines correspond to a proposed analytical model, while dots to micromagnetic simulations. Taken from [24]

ist between the dipole and the vortices in the two cases. Larger, micronic, dots that may be able to accommodate a multi-domain magnetic configuration are also interesting in the study of FM/SC structures as their net magnetic moment may be tuned by magnetizing the sample in a filed lower than the saturation field [25]. Also larger dots may be able to stabilize "giant" vortices that are able to carry more than one flux quantum [25].

In view of the above arguments, it can be seen that within the context of FM/SC heterostructures, magnetic micro,- and nanostructures present a special importance as they can produce effective magnetic pinning that can be modulated both by the dot lattice as well as their magnetic state.

4.3.1 Micro,- and nanostructures elaboration techniques

In the Experimental Methods chapter of the present thesis a brief overview of the microstructuration techniques was given. The main focus of the overview was to introduce the reader to the general principles behind the techniques used in the fabrication of microstructures, by means of optical lithography and ion beam etching. In the following paragraphs we will be addressing specific issues of the two methods, that have risen during the elaboration of the magnetic objects presented in the present Section. An account is also given of the elaboration of magnetic nanostructures using self-assembled polystyrene nanospheres.

Optical lithography was used in order to transfer the different motifs defined on a mask to the photoresist covered films. A variety of modes are used for photolithography process that are determined by the resolution that one wants to obtain. Because the smallest features on the masks were circles that measured 1 μm in diameter, which is a dimension close to the specified resolution limit of the mask aligner, <0.8 μm, for a ultraviolet wavelength of 400 nm, the *hard contact* lithography mode was chosen. In the hard contact mode, the mask

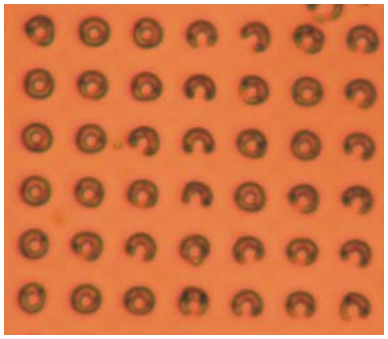

Figure 4.30: Image of the 2μm dot array after the exposure and developing of the photoresist. Holes are visible in the center of all the dots.

and the substrate are brought into contact and an additional N_2 flow inserted below the substrate so as to further press substrate onto the mask. The substrate was covered by a layer of about 1200 nm thick Microposit Shipley 1813 photoresist. The exposure time was set at 4 s in order to ensure a 160 mJ/cm^2 exposure dose.

In order to test the lithographic process various motifs were selected for lithography. These consist of circles (dots) having 20, 10, 5, 2 and 1 μm in diameter, squares with the same dimensions, as well as 2.5 μm wide stripes. For the large 20 and 10 μm circles and squares no particular feature could be noticed after the lithography. However, for the 5 and 2 μm diameter circles a hole in the center of the circles could be observed after the resist development, as shown in Figure 4.30. The holes in the middle of the dots arise from that specific region being illuminated by the radiation. This fact is due to the phenomenon known as *Poisson's spot*. A monochromatic plane wave $E(\vec{r},t) = E_0 \exp(ikz)\exp(-i\omega t)$ incident on a disk of radius a, as illustrated in Figure 4.31a, gives rise to an intensity in the point P,

$$I(z) = E_0^2 \frac{z^2}{a^2 + z^2}. \tag{4.25}$$

The variation of the relative intensity as a function of the distance z from the circle to the point P is represented in Figure 4.31b, for different circle diameters. It can clearly be seen that for diameters less than 5 μm the intensity of Poisson's spot is not negligible at distances of $\sim$1 μm, the photoresist thickness, leading thus to an exposure of the photoresist in the center of the circle and consequently the removal of photoresist in that particular area upon development. Minimizing or complete elimination of this effect is crucial in obtaining uniform circular magnetic dots of micrometric dimensions, and several approaches are used for solving this problem. The first, which is the most straightforward, is based on the expression of the intensity, $I(z)$, Eq.4.25, and consists of minimizing the mask/substrate distance, z. For this, the uniformity of the photoresist thickness is very important, as any thickness inhomogeneity results in a greater overall mask/substrate distance. This issue is especially sensitive when dealing with small area substrates, as the ones used in the current

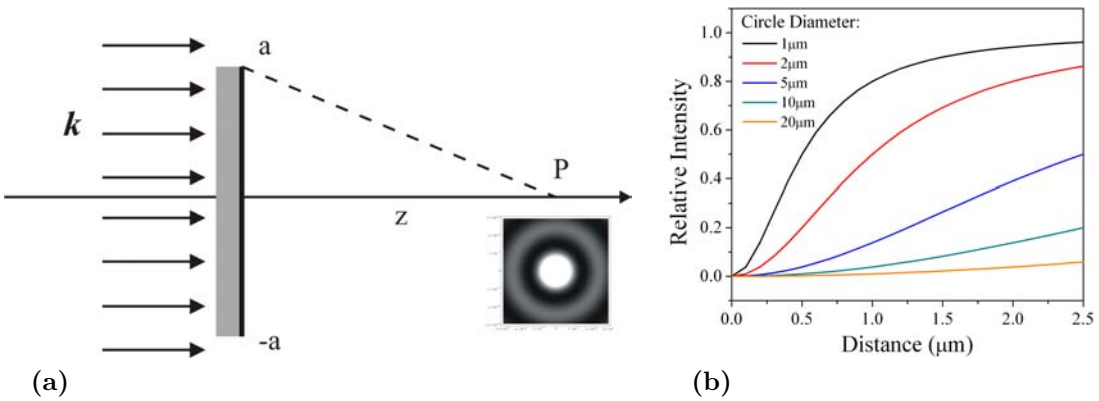

Figure 4.31: (a)Schematic representation of the Poisson's spot formation. The results of a numerical simulation of this phenomenon is also given. Taken from [20]. (b) Representation of the relative intensity of the Poisson's spot as a function of distance from the mask, for several dot diameters.

work, in which photoresist spinning leads to the creation of a thickness difference between the border and the center of the substrate. The thickness homogeneity was improved in our case by a high spinning rate of the photoresist, 5000 RPM. Reducing z can also be attained by the particular lithography mode that is used. It is evident that it is best to operate in the contact modes, that include the soft contact, hard contact and vacuum contact. In the soft contact mode the substrate is brought into contact with the mask, without any additional forces being exerted. In the hard contact mode, an additional push is exerted by a flow of N_2 on the substrate towards the mask. The vacuum contact mode gives the best results in terms of resolution, as it creates vacuum in the space between the mask and the substrate in addition to the N_2 flow. However, this mode was not employed for the lithography process as it posses additional difficulty in the mask/substrate alignment. Another technique to circumvent the formation of Poisson's spot is in the initial design of the mask, in the sense that the circle figures are replaced by polygons so as to impede the formation of constructive interference at the center of the projected image. As this approach meant the redesign of the mask, it was not adopted. Future developments using this approach are envisaged.

Ion beam etching was employed as a final step in defining the desired magnetic microstructures. As mentioned in the Experimental Methods chapter, IBE is a technique that consists in bombarding the film parts that are not covered/protected by the photoresist, while the covered areas remain unaltered. A high quality patterning requires an uniform ion beam over a large area. A Kauffman-type ion source was used. To avoid sample surface charge build-up, especially on insulating samples, a tungsten filament is placed at the outer side of the gun, for thermal emission of electrons that ensures *overall* charge neutrality of the beam.

Proper operation of the gun requires the determination of a few key process parameters. Here we present the determination of the optimum Ar gas flow and of the accelerator voltage.

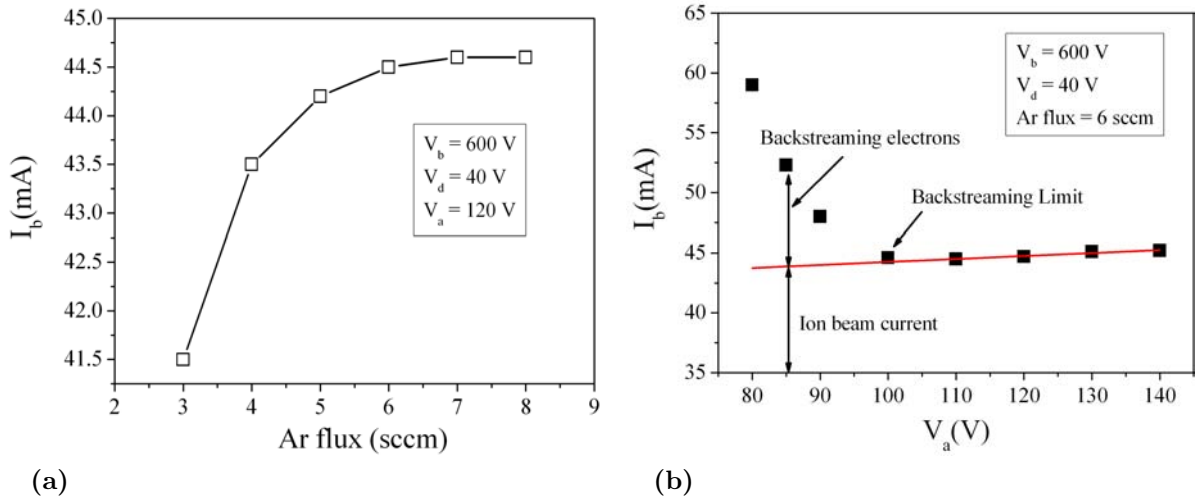

Figure 4.32: (a) Ion beam current, I_b as a function of the Ar flux. (b) Ion beam current, I_b variation as a function of the accelerating voltage, V_a. The electron backstreaming limit is also indicated.

Figure 4.32a presents the beam current variation as a function of the Ar flow. It can be observed that for high values of the gas flow the beam current increases slowly, while for lower values of the flow it decreases rapidly. The optimum gas flow is the approximate value where the rapid decrease of the beam current starts [21]. A gas flow below this value would result in an excess of the discharge power needed to maintain the plasma, while a higher value, as seen in the graph, brings only little change in the ion beam current intensity. As a consequence a value of 6 sccm Ar flow was used in all the etching experiments. The accelerator grid of the ion gun, besides accelerating the Ar^+ ions also prevents the inverse flow of the neutralizing electrons into the ion gun. The gun is positively biased and its walls are the anode for the plasma discharge, thus attracting the emitted electrons. This phenomena is know as *electron backstreaming*. In order to eliminate this effect the accelerator voltage must be kept above a certain value, the *backstreaming limit*. The backward flow of electrons is equivalent to an additional flow of Ar^+ ions, and thus the critical voltage for which an increase of the ion beam current is observed represents the limit for the backward flow of electrons, *i.e.* the backstreaming limit. For a true readout of the ion beam current the accelerator voltage must be kept above this limit. In the present work the accelerator voltage was taken to be 110 V, Figure 4.32b.

In Figure 4.33 we present the results of lithography and IBE in the structuration of dots having 1, 5 and 10 μm. The topography images were obtained in tapping mode using a magnetized MFM tip. The topography and magnetic signals were acquired within the same scan run. The relative poor definition of 1 μm dots is not a consequence of the imaging mode, even though the slight smearing of the dots is due to the magnetic interaction between the

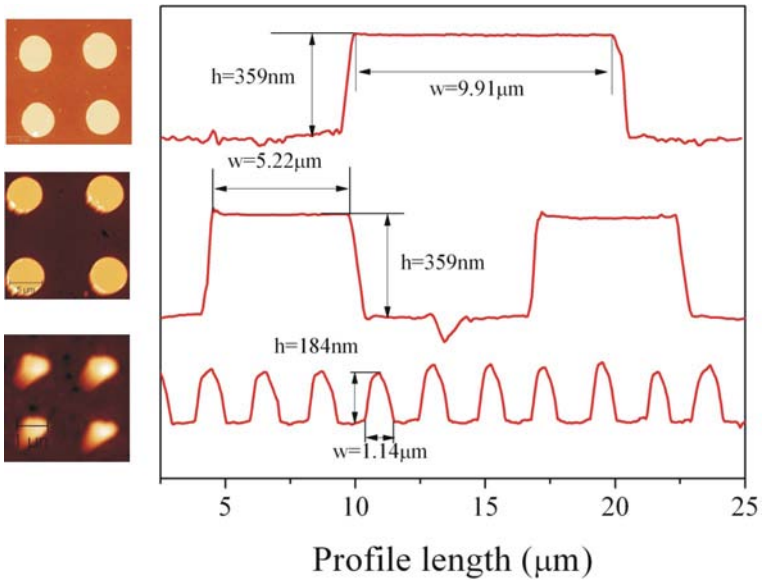

Figure 4.33: AFM images and corresonding profiles of th 1, 5 and 10μm diameter Py dots.

tip and the dot's magnetization. Upon a more careful analysis of the mask that was used to define the dots it can be seen that on the mask itself the dots have irregular shapes that deviate from the circular shape. The irregularity of the dot shape may be due to the chemical nature of the mask's substrate, which is soda lime. It is known that the best resolution for masks features of micron and sub-micron size are obtained on quartz substrates. Quartz has a low thermal expansion coefficient, 0.5 ppm/°C, as opposed to soda lime, 9.3 ppm/°C, so that in the process of mask manufacturing, in which e-beam or laser processing is involved the defined features are not subjected to thermal deformation. This permits defining sub-micronic patterns. In the case of the 5 μm and 10 μm dots the circular shape is very well preserved after lithography and etching. The profile analysis of the dots reveals well-defined sharp-edged features with widths close to the specified values 5.22(5) μm and 9.91(10) μm in the case of the higher diameter circles. The height of the dots is close to the predicted film thickness of 350 nm, indicating a good control of the etching process. In the case of the 1 μm dots their profile indicate a trapezoidal shape with the bottom base having 1.14 μm. The surprising feature of these structures is the low height value of 184 nm.

The self-assembly of colloidal polystyrene nanoparticles serves as a "lithographic" mask for producing sub-micronic features. The basic steps in producing nanometric structures using this technique is schematically illustrated in Figure 4.34. A monolayer of self-assembled nano-beads is deposited onto a substrate. The assembly of the polystyrene colloidal particles is achieved by depositing a thin layer of spheres by passing a so-called *deposition plate* above the substrate at a certain angle. At the intersection of the deposition plate and the substrate resides the colloidal solution, which is spread on the substrate by moving the deposition plate across the substrate at a certain velocity. The evaporation of the dispersion medium provides

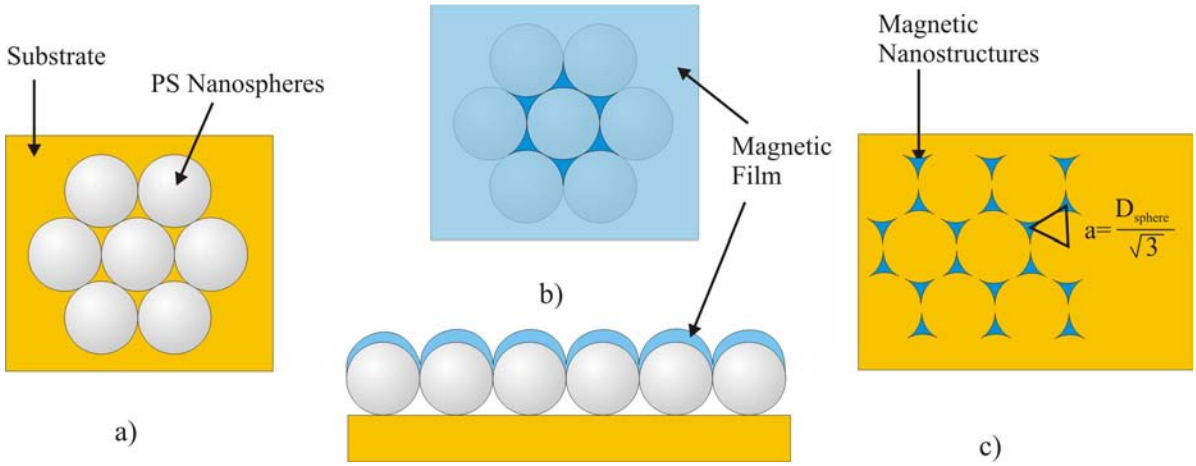

Figure 4.34: Schematic representation of the nanostructure formation using self-assembled PS nanospheres as a lithographic mask. (a) Self-assembly of spheres on a substrate, (b) Thin film deposition, (c) Sphere removal.

the drive force of the assembly process. This particular assembly mechanism is known as "convective assembly". Additional information regarding this process and the particularities of the experiments that were used in the present thesis can be found elsewhere [22]. A film, in our case Co, is deposited on top of the spheres. Part of the film will be deposited directly on top of the spheres while part of the film will fill the interstices formed by the bead assembly. The final step consists in removing the spheres and thus the film that has been deposited on top, by means of sonication in toluene. After this step the nanostructures are defined on the substrate, Figure 4.34c.

Figure 4.35a illustrates the SEM picture of 450 nm self-assembled polystyrene spheres. The picture reveals the single layer structure of the "film" and also some typical packing faults that appear as dark lines on the image. These faults represent a frequently encountered defect in these type of structures and it translates, after the film deposition, in the existence of metallic stripes besides the nanostructures. The stripes can be observed in both the inset in Figure 4.35a, as well as in Figure 4.35b, where a thin film of Co was deposited and then removed. As far as the remaining nanostructures are concerned, the inset in Figure 4.35b, reveals uniform structures having thicknesses of about 13 nm. The AFM images do not show clear triangular shaped dots, therefore a mean lateral dot size was estimated to be ∼200 nm. A problem that has been encountered in the lithographic process using nanospheres is related to a difference between the deposited film thickness and the actual height of the as obtained nano-dots. Because the fact that the flux of the sputtered atoms is not parallel but has a certain degree of divergence, shadowing effects due to the highly irregular surface of the self-assembled spheres, lead to a diminished height of the dots. Differences of several tens of nanometers have been observed between the expected height, corresponding to the equivalent film thickness, and the actual measured height of the nanostructures. This problem may be

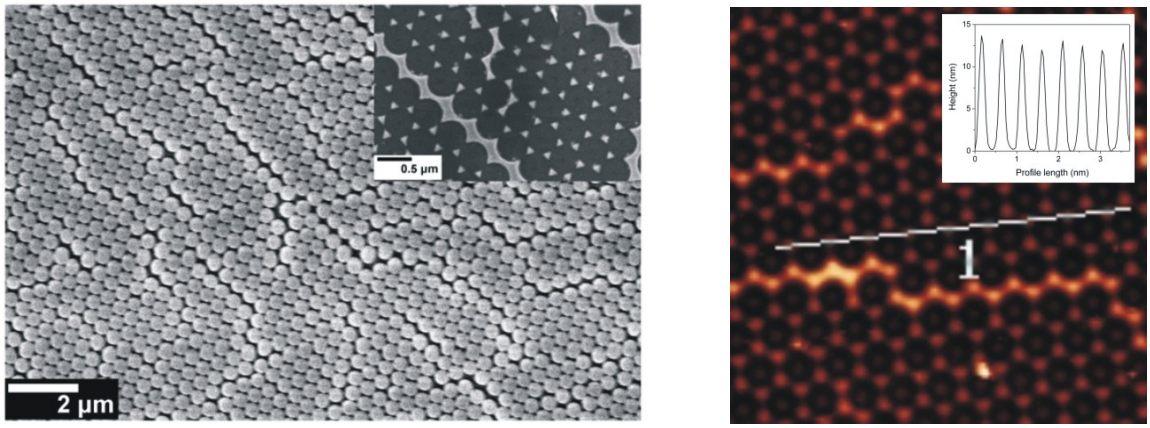

(a) **(b)**

Figure 4.35: (a) SEM image of 450nm in diameter PS spheres, (inset) gold nanaostructures. (b) Co nanostructures obtained using self-assembled PS sphere lithography, (inset) nanosturcture profile shows uniform structures.

overcome by reducing target-substrate distance during the film growth process. It can be observed that as a consequence of the particular packing of the PS spheres, the resulting hexagonal-like magnetic nanostructure lattice is similar to the triangular vortex lattice in SC films. Moreover, from geometrical considerations the lattice parameter of the magnetic structure may be modified by using PS spheres of different diameters, as $a = D_{sphere}/\sqrt{3}$, where a was taken to be the dot lattice parameter, while D_{sphere} is the diameter of the nanospheres. In view of these facts, the use of this alternative lithographic method may prove to be very useful for performing studies on the commensurablity effects between a magnetic dot and vortex lattices. Canpean *et al.* [26] have shown that if a reactive ion beam etching, in a mixture of Ar and O_2, is performed on the PS spheres, the result is a reduction of the sphere diameter. The reduction of the sphere size results in a physical decoupling of the spheres. If after this procedure a film is then deposited on top and then the spheres are removed, the result will be a continuous film having an ordered array of holes in it, referred to as anti-dots. Arrays of CoPt anti-dots have been proven to produce significant magnetic vortex pinning in Pb films, part of CoPt/Pb structures [27]. Also commensurability effects were observed between the anti-dot and vortex lattice visible in $M(H)$ loops. As a conclusion PS sphere lithography represents a versatile alternative in defining different arrays of sub-micronic magnetic structures that can be used in elaboration of FM/SC hybrid structures.

4.3.2 Magnetic properties of the micro,- and nanostructures

In this section we will address the magnetic properties characterization of the Py microstructure and Co nanostructure, whose elaboration has been described in the previous

Section. The characterization was performed by means of MFM. Figure 4.36 presents the magnetic images of circular, 350 nm thick Py dots having a diameter of (a)10, (b)5 and (c)1 μm. For the 10 μm dots, the diameter is well above the stripe domain width, estimated to be around 300 nm, according to the model proposed by Murayama [3]. As a consequence, the disks exhibit a well defined striped domain pattern. The stripes that are situated at the center of the disk have the same orientation and are very much similar to the case of a continuous film. As the stripes are closer to the edge of the microstrucutres, they tend to curve along the side of the dots, so as to prevent any magnetic charge build-up at the edges, and so to reduce the magnetostatic energy of the system. These *closure domain*-type structures have a limited spatial extension with respect to the overall area of the dots. As the diameter of the dots is reduced to 5 μm, even though this dimension is still considerably higher than the domain width, the stripe pattern is almost entirely pertaining to the closure domains. As a consequence the MFM images of the 5 μm dots is composed of alternating bright and dark concentric circles. Again, locally the parallel stripe order is maintained. However, this is not the only domain configuration that can be observed. Another domain pattern that is observed, resembles the one present in the 10 μm structures. It consists of straight magnetic stripes in the center and elongated circles at the edges as closure domains. It can be noted that the surface "covered" by the closure domains is much larger than in the 10 μm case, reaching 100% for the circular stripe pattern. In view of the evolution that was observed so far, the domain pattern for 1 μm dots is not surprising. As the diameter of the microstructures is reduced towards the limiting value of the stripe width, the competition between the anisotropy and magnetostatic energies results in the formation of stripe domains in the form of concentric rings, corresponding to two magnetic domains, Figure 4.36c (inset).

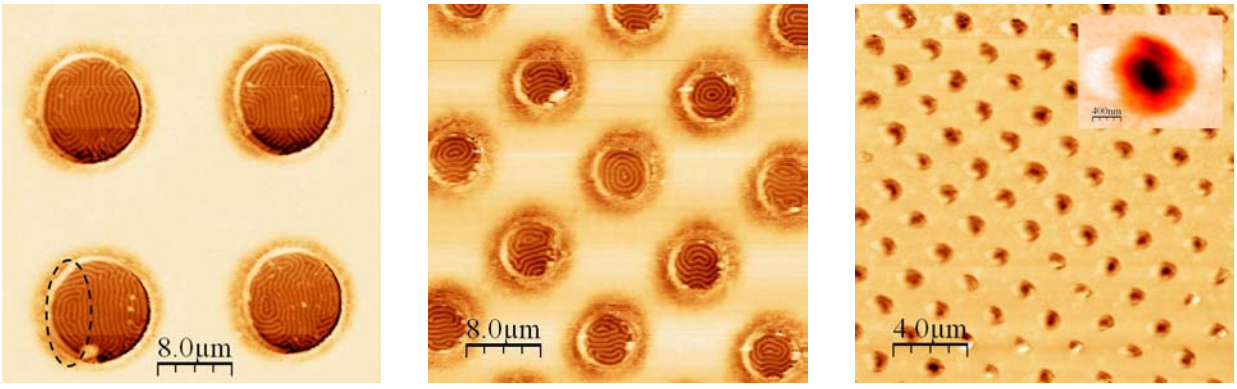

(a) **(b)** **(c)**

Figure 4.36: MFM images of (a)10 μm (40 μm×40 μm), (b) 5μm (40 μm×40 μm), (c) 1μ m (20 μm×40μm), Py dots.

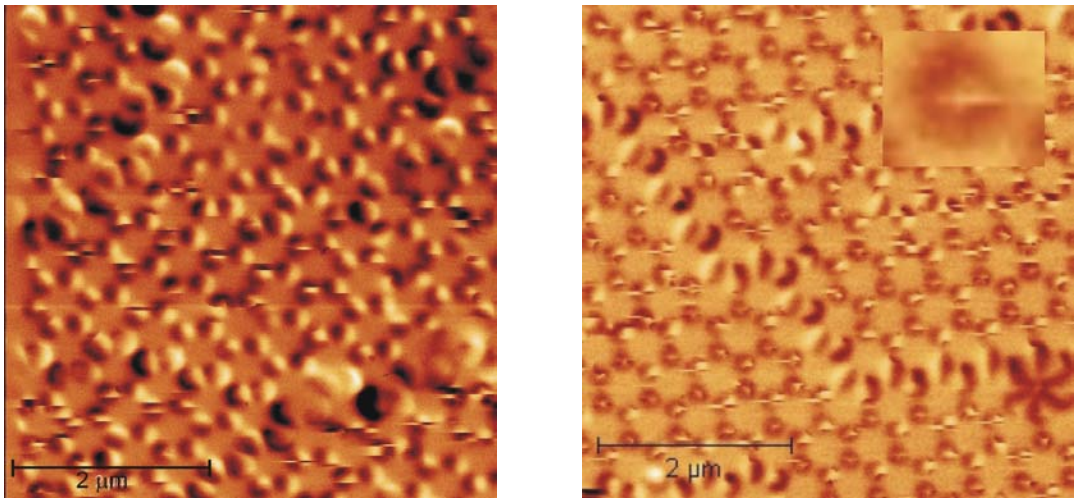

(a) **(b)**

Figure 4.37: MFM images of Co nanostructures having different thicknesses: (a) 20 nm (magnetic dipoles) and (b) 12 nm (magnetic vortices).

Co nanostructures were obtained using the polystyrene nanosphere lithography described previously. A 170 nm and 40 nm thick films were deposited on a nanoshpere patterned Si substrate. After lift-off, triangular Co structures remain on the substrate. Even though a large difference in the deposited film thickness was prepared, the height of the nanostructures in the case of the two films did not differ significantly. In the case of the 40 nm thick film, the mean height of the magnetic structures was of 12 nm, while for the thicker 170 nm film, the resulting dots were of only 25 nm high. The large difference in the expected value of the height of the dots and the actual one is due, as mentioned in the previous paragraph, to the shadowing effect produced by a divergent beam of sputtered atoms and also by the large height of the spheres (450 nm), which accentuates these effects. The MFM analysis performed on the two films are shown in Figure 4.37. For the 25 nm high structures, the dots are in a mono-domain state, Figure 4.37a. The MFM contrast is typical for such a structure which is essentially corresponding to a magnetic dipole. If the initial film thickness is decreased, the magnetic configuration of the nanostructures changes, as can be seen in Figure 4.37b, into a vortex-like spin configuration. The MFM contrast is typical dots in this configuration, haying a bright center and the rest of the dot exhibiting a darker shade. Of course, upon reversing the out-of -plane direction of the magnetization of the magnetic vortices, the resulting image would be the negative of the image presented in Figure 4.37b. As shown in the introductory remarks of the tis Section, Jubert *et al.* [24], based on micromagnetic simulations constructed a phase diagram for ferromagnetic dots, Figure 4.29. Their diagram took into consideration the diameter and thickness of the dots as a function of the exchange length $\lambda_{exch} = \sqrt{2A_{exch}/\mu_0 M_s^2}$. In the case of Co, the saturation

magnetization is M_s=1.424×10^6 A/, while the exchange constant is A_{exch}=30×10^{-12} J/m, yielding an exchange length λ=4.85 nm. In units of λ_{exch} the dots thickness was 2.5, in the case of the 12 nm thick dots, and 5 in the case of the 20 nm dots. The mean lateral extension of the dots, 200 nm, corresponds to 41 λ_{exch}. According to the diameter-thickness phase diagram, Figure 4.29, both dots should have been in the magnetic vortex state, and moreover the behavior predicted by the phase diagram is that for thicker dots the vortex state becomes more stable for a larger range of dot diameters. Our findings point out a different behavior, in the sense that thicker structures are found to be in the single domain state. Although no concrete explanation was found for this trend, we suspect that the particular shape of the dots, in our case triangular, may play an important role in modifying the magnetic phase diagram. The results presented in Figure 4.29 were calculated for circular magnetic dots.

4.4 Résumé de chapitre en français

Dans ce chapitre nous présentons l'élaboration et la caractérisation des couches minces magnétiques à aimantation perpendiculaire. Pour les applications aux systèmes hybrides d'interface avec un supraconducteur il est important que la couche ferromagnétique continue ou structurée présente une composante perpendiculaire de l'aimantation.

Dans la première partie du chapitre une introduction fait un rappel des propriétés micromagnétiques des films de permalloy ($Ni_{80}Fe_{20}$) qui présentent une configuration magnétique de type *weak-stripe* et des propriétés d'anisotropie rotatoire. Nous présentons une analyse de la configuration de l'aimantation weak-stripe selon quelques modèles analytiques utilisés dans la littérature. Par la suite, nous montrons les résultats expérimentaux obtenus sur les films de $Ni_{80}Fe_{20}$ élaborés au laboratoire. Ces films ont étés déposés sur des substrats de Si(111) couverts par une couche amorphe d'oxyde de Si native par la technique de pulvérisation cathodique. Les dépôts sont faits à la température ambiante dans un vide de base de 2×10^{-8} Torr. L'épaisseur des films a été variée entre 6 et 720nm. Les propriétés magnétiques ont été caractérisées par la magnétométrie VSM (à l'échelle macroscopique) et la microscopie à force magnétique (à l'échelle microscopique). Avant la caractérisation magnétique, de manière systématique les films ont été caractérisés d'un point de vue structural par les techniques de diffraction X (réflectométrie X pour l'épaisseur et XRD pour la cristallinité, paramètres de maille). La morphologie (rugosité) a été déterminée par les mesures de microscopie à force atomique (AFM).

L'analyse magnétique par VSM montre l'évolution progressive des propriétés magnétiques macroscopiques avec l'augmentation de l'épaisseur du film. Au-delà d'une épaisseur critique, les cycles d'aimantation mesurés correspondent à des configurations magnétiques de type *weak-stripe*, qui représentent une modulation périodique de l'aimantation avec une com-

posante perpendiculaire orientée alternativement vers le haut et vers le bas par rapport à la surface du film. Par ailleurs, dans ce régime d'épaisseur nous démontrons l'apparition de l'anisotropie rotatoire. L'analyse micro magnétique par MFM confirme l'apparition de la configuration weak-stripe. Les images MFM montrent des bandes de contraste noir et blanc dont l'analyse permet d'extraire des informations sur la largeur de domaines magnétiques adjacents et l'évolution de ce paramètre avec l'épaisseur du film magnétique. Les résultats de notre analyse sont bien décrits dans le cadre d'un modèle analytique caractéristique aux structures de type weak-stripe.

Un paragraphe suivant est dédié à l'étude de propriétés structurales, magnétiques et micro-magnétiques des films minces de cobalt. Ces films constituent une autre alternative pour des structures magnétiques à aimantation perpendiculaire, toujours dans l'idée de les interfacer avec un supraconducteur à haute température, pour envisager le pinning extrinsèque des vortex supraconducteurs via le champ magnétique perpendiculaire. Comme pour les films de permalloy, nous avons tout d'abord effectué une analyse de l'évolution des propriétés magnétiques avec l'épaisseur du film de Co. En utilisant une analyse basée sur la littérature nous expliquons l'origine et la stabilisation du régime à aimantation perpendiculaire et de la structure micromagnétique de type perpendicular-stripe et ses propriétés magnétiques caractéristiques à l'échelle macroscopique et microscopiques. Par la suite, nous introduisons les résultats obtenus sur les films de cobalt élaborés dans le cadre de cette thèse. En fonction du type de substrat utilisé, deux types des films de Co on été élaborés. La première classe de films, déposés sur du Si(111) oxydé naturellement est texturé. En revanche, lorsque le Co est déposé sur des substrats de Al2O3(0001) et après un traitement thermique de recuit, le film obtenu est monocristallin. Au delà d'une épaisseur critique, ces films présentent une anisotropie perpendiculaire qui conduira à une structure micromagnétique sous forme de bandes périodiques constitués des domaines à aimantation perpendiculaire up/down. Comme pour les couches de permalloy, la période des bandes et la largeur des domaines sont modulées par l'épaisseur du film magnétique. Ce chapitre contient également un paragraphe dédié à la modélisation analytique du contraste magnétique spécifique aux structures de type bande à aimantation perpendiculaire. Cette modélisation permet de mieux comprendre l'origine du contraste de parois qui séparent les domaines perpendiculaires dans une structure de type périodique et d'identifier les paramètres critiques qui influencent la largeur des bandes du contraste noir et blanc mesurés expérimentalement par MFM.

La dernière partie du chapitre présente les propriétés micromagnétiques des structures de taille latérale réduite, réalisées par des techniques de lithographie. La réduction de la taille latérale de l'objet magnétique ouvre une voie supplémentaire pour le contrôle des ses propriétés micromagnétiques. Par les techniques de la lithographie optique et la gravure ionique sèche, nous avons élaboré des structures magnétiques de formes circulaire avec des

dimensions caractéristiques dans la gamme 20, 10, 5, 2, 1 microns. Les analyses par la microscopie à force atomique fournissent les informations sur la forme et les dimensions exactes des objets lithographies, alors que l'analyse simultanée par MFM nous donne leurs structure micro-magnétique. Afin d'obtenir des objets magnétiques de dimensions sub-micronique, une technique de lithographie à base des billes nanométriques de polystyrène a été utilisé. L'analyse micromagnétique détaillée sur l'ensemble des structures de taille latérale réduite montre la possibilité du contrôle de la configuration de l'aimantation par l'effet de la forme et de la taille de l'objet magnétique. L'une des configurations micromagnétique particulièrement importante pour les systèmes d'interface avec le supraconducteur est celle des vortex magnétiques. Nous discutons, sur la base d'un diagramme de phase, la possibilité de stabiliser cette configuration et par la suite nous démontrons sa réalisation expérimentale dans des nanostructures de Co de taille nanométrique.

Le chapitre s'achève avec une discussion sur le potentiel d'intégration des structures magnétiques à aimantation perpendiculaire à base de Py et Co, dont les propriétés magnétiques sont modulées par l'effet de la dimensionnalité, dans les systèmes d'interface avec un supraconducteur. Un tout dernier paragraphe présente les conclusions et les perspectives.

Bibliography

[1] N. Saito, H. Fujiwara and Y. Sugita, *A new type of magnetic domain structure in negative magnetostriction Ni-Fe films*, J. Phy. Soc. Jap. **19**, 1116 (1964);

[2] S. Chikazumi, *Physics of Ferromagnetism*, Oxford Science Publications (1997);

[3] Y. Murayama, *Micromagnetics on stripe domain films. I. Critical cases*, J. Phy. Soc. Jap. **21**, 2253 (1966);

[4] A. Hubert and R. Schäfer *Magnetic Domains - The Analysis of Magnetic Microstructures*, Springer (1998);

[5] Y. K. Kim, T. J. Silva, *Magnetostriction characteristics of ultrathin permalloy films*, Appl. Phys. Lett. **68**, 2885 (1996);

[6] J. Ben Youssef, N. Vukadinovic, D. Billet and M. Labrune *Thickness-dependent magnetic excitations in Permalloy films with nonuniform magnetization*, Phys. Rev. B **69**, 174402 (2004);

[7] A. Belkin, V. Novosad, M. Iavarone, J. Pearson, and G. Karapetrov *Superconductor/ferromagnet bilayers: Influence of magnetic domain structure on vortex dynamics*, Phys. Rev. B **77**, 180506(R) (2008);

[8] G. Binning, C.F. Quate, Ch. Gerber, *Atomic Force Microscope* Phys. Rev. Lett. **56**, 930 (1986);

[9] D. Rugar, H.J. Mamin, P. Guethner, S.E. Lambert, J.E.Stern, I.McFadyen, T.Yogi, *Magnetic force microscopy: General principles and application to longitudinal recording media* J. Appl. Phys. **68**, 1169 (1990);

[10] R. I. Potter, *Analysis of Saturation Magnetic Recording Based on Arctangent Magnetization Transitions*, J.Appl.Phys. **41**, 1648 (1970);

[11] H. Saito, A. van den Bos, Leon Abelmann, and J. Cock Lodder, *Magnetic printing technique for perpendicular thin-film media with coercivity of up to 10 000 Oe*, IEEE Trans. Magn. **39**, 2234 (2003);

[12] C. A. F. Vaz, J. A. C. Bland and G. Lauhoff *Magnetism in ultrathin film structures*, Rep. Prog. Phys. **71**, 056501 (2008);

[13] M. Kowalewski, C. M. Schneider and B. Heinrich *Thickness and temperature dependence of magnetic anisotropies in ultrathin fcc Co(001) structures*, Phys. Rev. B **47**, 8748 (1993);

[14] C. A. F. Vaz and J. A. C. Bland *Strain-induced magnetic anisotropy in Cu/Co/Ni/Cu/Si(001) epitaxial structures*, Phys. Rev. B **61**, 3098 (2000);

[15] R. Allenspach, M. Stampanoni and A. Bischof *Magnetic domains in thin epitaxial Co/Au(111) films* Phys. Rev. Lett. **65**, 3344 (1990);

[16] C. Kittel *Theory of the structure of ferromagnetic domains in films and small particles*, Phys. Rev. **70**, 965 (1946);

[17] D. M. Donnet, K. M. Krishnan and Y. Yajima *Domain structure in epitaxially grown cobalt thin films* J. Phys. D: Appl. Phys. **28**, 1942 (1995);

[18] M. Hehn, S. Padovani, K. Ounadjela and J. P. Bucher *Nanoscale magnetic domain structures in epitaxial cobalt films* Phys. Rev. B **54**, 3428 (1996);

[19] A. A. Thiele *Device implications of the theory of cylindrical magnetic domains* Bell Syst. Tech. J. **50**, 725 (1971);

[20] http://demonstrations.wolfram.com/PoissonSpot

[21] *Manual for 4-cm DC Ion Source - Model KDC 40*, Kauffman&Robinson Inc. (2008);

[22] V. Canpean, S. Astilean, T. Petrisor Jr., M. Gabor, I. Ciascai *Convective assembly of two-dimensional nanosphere lithographic masks*, Mat. Lett. **63**, 1834 (2009);

[23] A. Hoffmann, P. Prieto and I. K. Schuller, *Periodic vortex pinning with magnetic and nonmagnetic dots: the influence of size*, Phys. Rev. B **61**, 6958 (2000);

[24] P.-O. Jubert and R. Allenspach, *Analytical approach to the single-domain-to-vortex transition in small magnetic disks*, Phys. Rev. B **70**, 144402 (2004);

[25] A. Yu. Aladyshkin, A. V. Silhanek, W. Gillijns and V. V. Moshchalkov, *Nucleation of superconductivity and vortex matter in superconductorferromagnet hybrids*, Supercond. Sci. Technol. **22**, 053001 (2009);

[26] V. Canpean and S. Astilean, *Extending nanosphere lithography for the fabrication of periodic arrays of subwavelength metallic nanoholes*, Materials Letters **68**, 2520 (2009);

[27] M. Lange, M. J. Van Bael, V. V. Moshchalkov and Y. Bruynseraede, textitAsymmetric flux pinning by magnetic antidots, J. Magn. Magn. Mater. **240**, 595 (2002);

[28] G. Carneiro, *Pinning and creation of vortices in superconducting films by a magnetic dipole*, Phys. Rev. B **69**, 214504 (2004).

Chapter 5

Ferromagnetic/high temperature superconductor hybrid structures

In the present Chapter we set out to investigate the influence of the FM layers on the pinning properties of YBCO thin films. From the systems suitable for this purpose that were considered in the previous chapters, we have chosen two systems. The first is represented by LSMO thin films with strongly modulated surface morphology. The LSMO thin films were prepared so that, due to the intrinsic growth mechanism, they are formed of highly ordered arrays of grains. A two component pinning mechanism is expected to affect the vortex motion in the YBCO layer. A normal pinning mechanism due to the defects induced in the YBCO thin film by the LSMO grains and a magnetic pinning mechanism, given by the ferromagnetic nature of LSMO at low temperatures. Detailed morphological, structural and magnetic studies are employed to assess the different pinning mechanisms. The second FM system considered is represented by Py thin films exhibiting a stripe domain structure. Rotatable magnetic anisotropy allows for the orientation of the magnetic stripes in different configurations with respect to the current flowing in the YBCO film. Two orthogonal configurations were studied. Electrical measurements were employed to confirm the magnetic pinning mechanism originating from the magnetic modulation of Py thin films.

5.1 LSMO/YBCO hybrid structures

As it was shown in the overview of LSMO studies, this material is ferromagnetic, has a half-metallic character, and thus a high degree of spin polarization, exhibiting at the same time a metallic behavior in the temperature range where ferromagnetism exists. The Curie temperature of LSMO is also the highest among doped rare-earth manganites, exceeding room-temperature. Also, there is a good structural compatibility between the lattices of LSMO and YBCO. These facts recommend LSMO as a suitable candidate in the realization

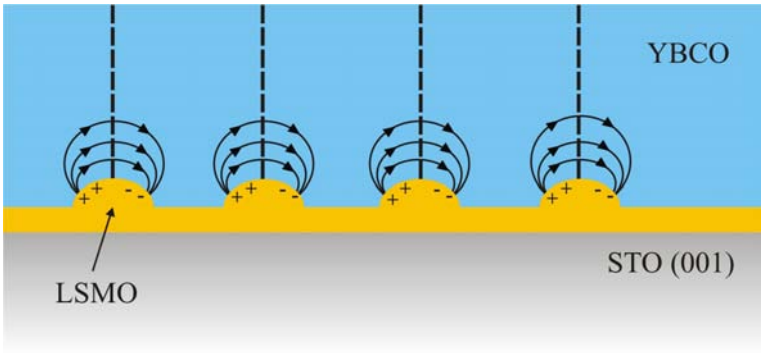

Figure 5.1: Schematic representation of the LSMO/YBCO hybrid structures. Pinning is expected to arise from columnar defects (dotted lines) induced by LSMO nano-islands, and from the magnetic moment and stray field created by the particles.

of FM/SC structures having YBCO as the superconducting layer. LSMO/YBCO bi-layers have been elaborated in order to study FM/SC proximity effects, spin polarized current injection in YBCO films and also magnetic pinning of the ferromagnetic LSMO on the SC YBCO vortices. From more practical point of view, LSMO layers have been considered to be used as a single buffer layer for YBCO deposited on metallic substrates (NiW) in superconducting tape fabrication. As opposed to the usual buffer layer architecture, which consists of several insulating oxidic materials, LSMO has metallic conduction at the working temperature of YBCO. A good electric contact between YBCO and the metallic substrate would ensure a current relieve in the case that regions in the YBCO layers transit to the normal state, preventing the quench development in the superconducting tapes. For all the above reasons we have decided to tackle the subject of LSMO/YBCO in order to enhance the pinning characteristics of the YBCO film making use of the modulated morphology of the LSMO films and of the fact that LSMO is ferromagnetic.

In the Chapter 3 we have shown that when a LSMO film is grown on a terraced STO substrate, highly ordered nanoislands are formed. These islands are aligned along the step edges, resulting in a periodically modulated surface. The idea behind our study is to make use of these modulations, *i.e.* surface decoration, in order to induce dislocations at the respective island sites in the top YBCO layer that is deposited afterwards. Hence, the modulated LSMO surface would induce an ordered array of columnar defects, *i.e.* dislocations, in the YBCO film. These defects will act as pinning centers for the normal core of vortices within the superconducting film. Because the fact that LSMO is also ferromagagnetic, magnetic charge will build up on the sides of the nanoislands, producing thus a periodic stray field structure. This stray field will interact with the magnetic moment of vortices within the YBCO film producing thus an additional, magnetic, pinning. The hybrid LSMO/YBCO structure is expected to show strong pinning characteristics, resulting in high critical current density, J_c, and high irreversibility fields. Figure 5.1 illustrates the driving principle behind our study.

This Section is structured as follows: in the beginning a brief review of the surface decoration techniques used to enhance vortex pinning is given. The experimental procedure of the fabrication of LSMO/YBCO structures is presented. A detailed account of the morphological and structural properties of the YBCO thin films epitaxially grown on LSMO buffered STO (001) substrates is also addressed. A particular emphasis is placed on the morphology properties of the terraced STO substrates and the deposited LSMO nano-islands. Structural characterization is also discussed, with attention being placed on the influence of the particles on the (00l) YBCO ω-scans, interpreted with the aid of the model described in Chapter 3. The Section ends with the evaluation of the YBCO pinning characteristics as derived from magnetic measurements.

5.1.1 Surface decoration and vortex pinning

In the quest for increasing the pinning force exerted on the superconducting vortices several paths have been followed throughout the years. Some of them have been briefly reviewed in the introductory section of the first Chapter. Surface decoration has been employed quite recently, in the last decade, as an alternative method for vortex normal core pinning. In principle it consists of growing nanometric islands on a substrate prior to the superconducting thin film deposition. Upon growing the superconducting film on the as prepared template, one dimensional, columnar defects are expected to form in the SC film at the sites of the nano-islands. Studies have been performed in order to quantify the effect of the islands on the pinning characteristics of the SC layer, as a function of the material used for decoration (Ir, Ag, Y_2O_3, CeO_2) and as a function of the morphologic properties, such as grain lateral size distribution, grain height and areal density. To better understand and interpret our results we will briefly touch upon some of the main results found in literature.

Mele *et al.* [9] have used PLD in order to grow Y_2O_3 nanoislands on TiO_2 terminated STO(001) substrates. Varying the number of laser pulses that hit the Y_2O_3 target, the authors were able to modify the size and density of the dots. In order to find a causality relation between the islands and the amount of defects the chemical etching method proposed by Huijbregtse *et al.* [20] was used. This procedure consists in immersing the YBCO films in a Br/ethanol solution for a brief period of time, ∼10 s, and then analyzing the YBCO surface. The solution acts mainly to etch the areas around the dislocations present in the films, and thus create the so-called *etch pits*. A good agreement was found between the areal density of nanoislands and the etch pit density. Therefore, nanoislands act effectively to produce columnar defects in the YBCO films and thus enhance flux pinning. J_c evaluation demonstrated that for the surface decorated samples a stronger pinning is present, which lead to higher critical current densities than in the case of the bare YBCO films. Sparing *et al.* [10] used an alternative method for Y_2O_3 nanoparticle surface decoration. The method, inert

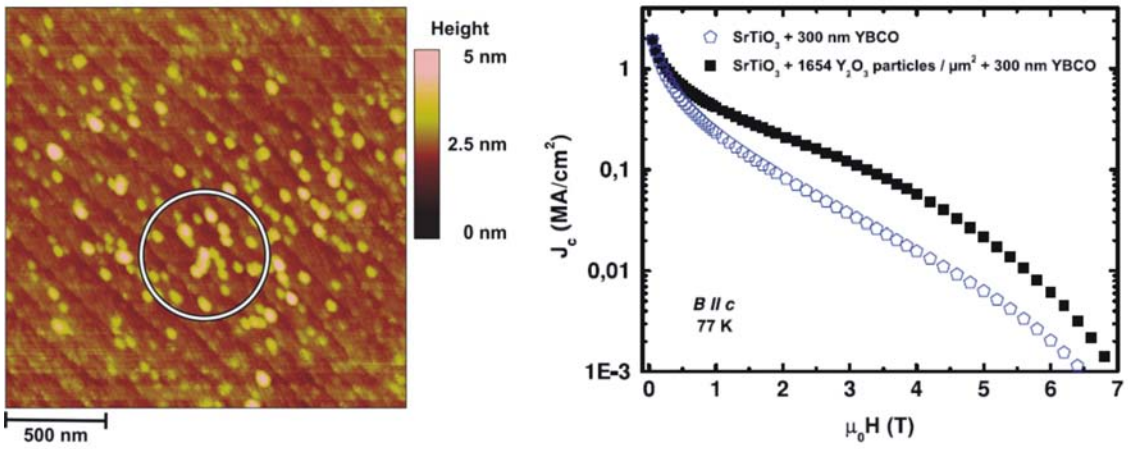

Figure 5.2: (left) TiO_2 terminated $SrTiO_3$ substrate with Y2O3 nanoparticles after heat treatment in 0.7 mbar O2 at 750°C; (right) $J_c(B)$ dependence for a standard off-axis YBCO film and a YBCO film on a substrate decorated with 1654 particles/μm^2 for $B||c$ at 77 K. Taken from [10].

gas phase condensation process, allows for the independent control of the particle size and density, a feature which is not achievable by the common deposition methods, such as PLD or sputtering. Also, the proposed method allows for a much narrower grain size distribution than in the case of the afore mentioned deposition processes. Areal densities varying from 120 to 4200 particles/μm^2 of Y_2O_3 nanoparticles were prepared on TiO_2 terminated STO (001) substrates. The particle diameter was reported to be of 8 nm. As far as the island height, in the initial deposition process, performed at room temperature, a value of about 9 nm was recorded. However, upon annealing in oxygen at a temperature equal to the YBCO deposition temperature, 750 °C, the height was reduced to about 1 nm. The J_c values revealed the fact that there exists a critical particle density for which pinning becomes more efficient than in the case of a single YBCO film. Substrates with island densities exceeding ~1500 particles/μm^2 show significant improvement of J_c and a shift of the maximum pinning force to higher field values, 3 T. No change, however, in the flux pinning characteristics were observed for the samples of lower island densities. A typical AFM image of a Y_2O_3 decorated STO substrate is presented in Figure 5.2, together with a $J_c(B)$ measurement for a YBCO film grown on an un-decorated substrate and for a YBCO film grown upon a 1654 particles/μm^2 decorated substrate. Stronger flux pinning is observed in the case of the decorated substrate.

Other studies include decoration with particles of different materials. Metal particles are especially suited for these kind of experiments, since the difference between the surface energies of metals and the oxide substrates lead to a three-dimensional growth of the former, yielding uniform, disordered arrays of nanoislands on the substrates. Aytug *et al.* [11] reported STO substrate decoration with Ir particles. TEM studies did not reveal the presence

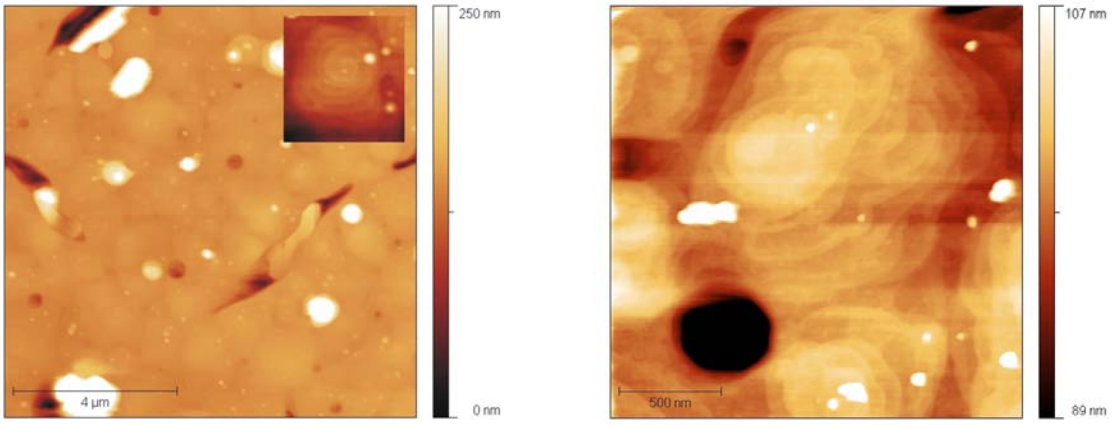

(a) **(b)**

Figure 5.3: 10μm×10μm AFM image of the YBCO film deposited directly on the STO (001) (inset) detail of a grain grown around a screw dislocation, (b) 2μm×2μm image of YBCO crystallites, the scale was modified in order to distinguish the stepped characteristic of the grains.

of any columnar defects, however planar defects were observed together with a secondary, $BaIrO_3$, phase at the interface between the Ir crystallites and the YBCO film. This phase is most likely the consequence of a chemical reaction between Ir and YBCO. A strong pinning enhancement was observed for the SC films deposited on decorated substrates. This is an indication that the induced normal, non-superconducting, secondary phase zones acted as pinning centers for the SC vortices.

As a conclusion, the studies above reveal the possibility of using surface decoration as an effective method of enhancing the pinning force in SC films. The studies also show that in order to produce additional pinning, the morphology of the nano-islands have to meet some morphological criteria in order to act as effective pinning centers.

5.1.2 Experimental procedure

The LSMO/YBCO bi-layers were deposited on STO (001) single crystal substrates. Prior to the deposition the substrates were etched in a NH_4 buffered HF solution, in order to ensure a uniform TiO_2 termination layer. Subsequently, a thermal treatment was performed on the substrates in 15 l/h flowing O_2, in order to stabilize the terraced surface of the substrates. This procedure has already described in Chapter 3 of the present thesis. Different temperatures were used for substrate annealing varying from 950 °C to 1200 °C. This variation was due to poor reproducibility of the annealing effects on the substrate surface terrace structure. More details are given in the paragraph dedicated to STO substrate morphology. Subsequently the LSMO film was deposited by DC sputtering. The film growth was performed at a substrate temperature of 800 °C in a mixture of Ar and O_2 in a 3:1

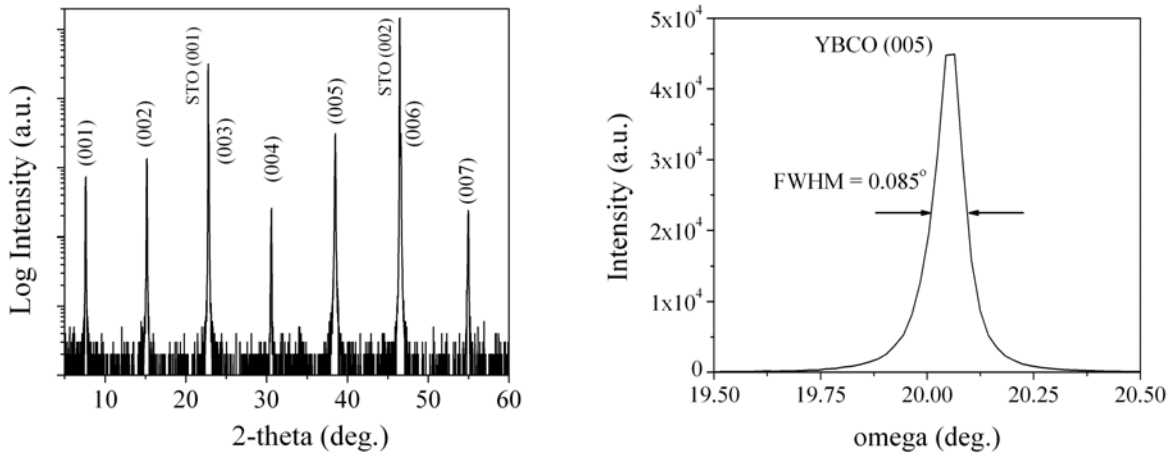

Figure 5.4: (a) $2\theta/\omega$-scan on the YBCO film and (b) ω-scan around the (005) reflection of the film.

ratio at an overall gas pressure of 40 mTorr. After the deposition the samples were cooled at room temperature in 3/4 atm of O_2, with a dwell at 550 °C for 1/2 hour. The LSMO film thicknesses as determined from XRR measurements were approximately 1.5, 3, 7 and 35 nm. The top YBCO layer was deposited using PLD, from a stoichiometric $YBa_2Cu_3O_7$ target. The laser used on the deposition equipment was a XeCl excimer laser (λ=308 nm) at a repetition rate of 10 Hz and a laser fluence of 120 mJ/cm^2. The deposition was carried out at a substrate temperature of 850 °C in 290 mTorr of O_2. As in the case of LSMO films, cooling was performed in 3/4 atm of O_2 with a 15 min. dwell at 450 °C. Under these deposition conditions, the YBCO film thickness was of 70 nm.

5.1.3 Single YBCO film

In order to better evaluate the influence of the LSMO layers on the top YBCO films, a single test YBCO film was deposited directly on a STO(001) substrate. No additional thermal treatment was applied to the substrate prior to the film deposition. AFM was used in order to characterize the film surface. The results are shown in Figure 5.3. Results show a uniform surface with the presence of few defects, Figure 5.3a, such as cracks and large particulates, *i.e.* droplets, the latter being inherent to the ablation process used for the film deposition. A typical feature of YBCO films is the presence of crystallites that grow around screw dislocations, Figure 5.3a (inset) and 5.3b. The crystallites show a stepped structure, with a step height of ∼1 nm, close to the ideal out-of-plane lattice parameter, c=11.6804 Å.

The XRD structural characterization reveals that the YBCO film has grown epitaxially on the STO(001) substrate, as only the (00l) peaks are present in the diffraction pattern shown in Figure 5.4a. No other secondary phases or grains oriented with the a-axis oriented

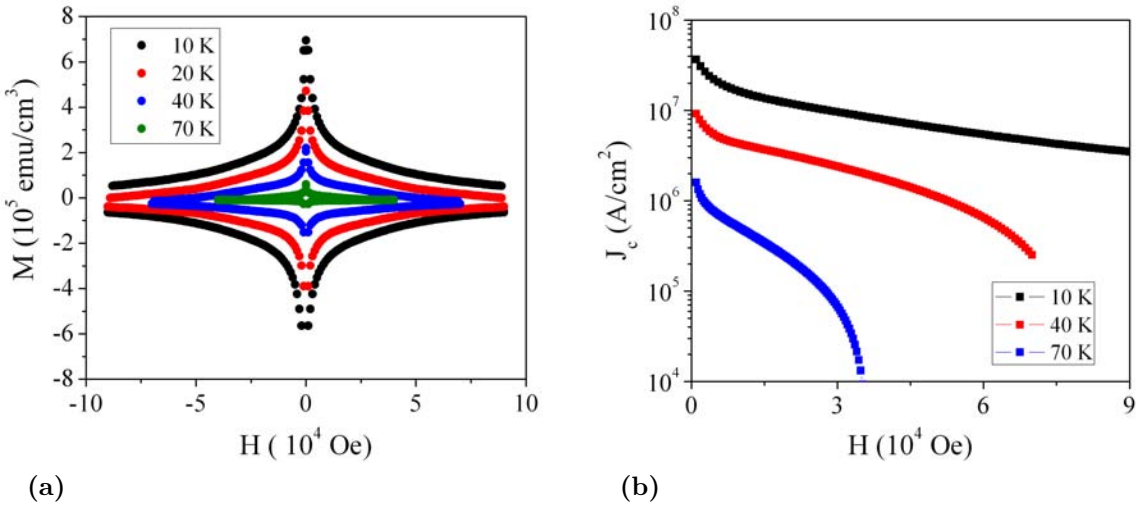

Figure 5.5: (a) $M(H)$ cycles of the YBCO film measured at different temperatures, (b) $J_c(H)$ dependence for 10, 40 and 70 K calculated using 5.2 from $M(H)$.

perpendicular to the substrate were detected in the $2\theta/\omega$-scan. One of the parameters used in the evaluation of the quality of the epitaxial growth is the FWHM of the out-of-plane grain distribution, *i.e.* ω-scans (rocking curves). The FWHM of the ω-scan, performed around the YBCO (005) peak, Figure 5.4b, was of 0.085°. The low FWHM value indicates minimal out-of-plane grain dispersion a sign of the high epitaxial quality of the films.

The magnetic field dependence of the critical current density, $J_c(H)$, at different temperatures was derived from $M(H)$ measurements, Figure 5.5a. Magnetic measurements represent an alternative to the electrical measurements used for J_c determination, that require no patterning or contacting of the sample [12]. Because a superconducting sample shields itself from the external magnetic field, H, a compensating magnetization, M, is produced by the ring currents in the sample. Bean [13] suggested that it is energetically more favorable for a SC to shield itself with the highest current density, which is the critical current density, J_c. Therefore, since M is produced by J_c, one can evaluate the critical current density from a magnetization cycle. However, to do so, the evaluation of the irreversible part of the magnetization, M_{irr} is needed. M_{irr} is given by:

$$M_{irr} = \frac{M_+ - M_-}{2}, \tag{5.1}$$

where M_+ and M_- represent the magnetizations recorded from $0 \rightarrow H_{max}$, M_+, and from $H_{max} \rightarrow 0$, M_-, respectively. The relationship between the magnetization M and J_c was calculated, using an approximation to the Bean model, in the case of rectangular SC samples

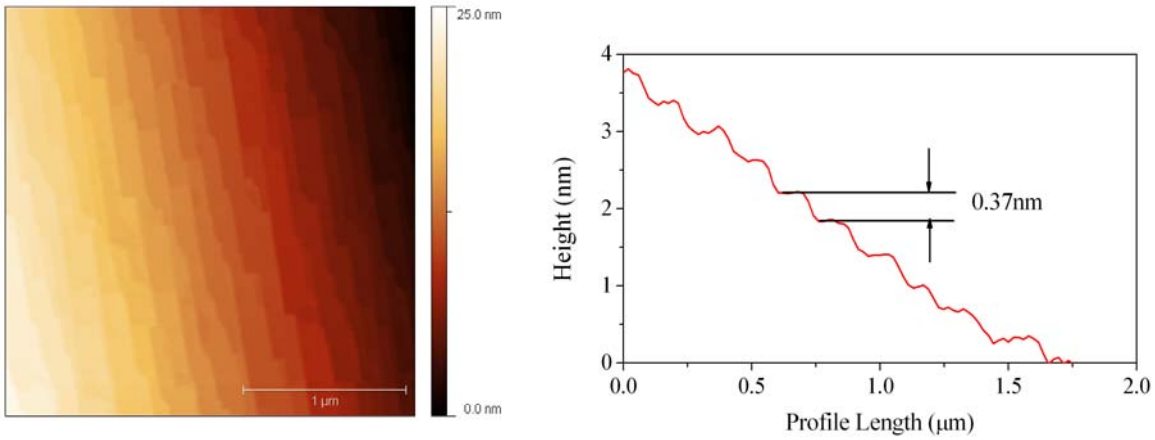

(a) **(b)**

Figure 5.6: (a) 2.5μm×2.5μm AFM image of the terraced STO substrate used for the deposition of the 1.5 nm LSMO film, (b) Profile extracted from a STO terraced substrate with uniform TiO_2 termination, good agreement is observed between the STO lattice parameter 3.905 Åand the step height, 3.7 Å

as:

$$J_c = 20\frac{\frac{M_+ - M_-}{2}}{w\left(1 - \frac{w}{3l}\right)}, \tag{5.2}$$

where w and l are the width and length of the sample. The calculated critical current density variation as a function of H for the YBCO film are given in Figure 5.5b for three different temperatures. As a point of reference, the calculated critical density, in a 0.1T field at 70 K, was of 1.57 MA/cm^2. This figure is typical value for YBCO films deposited on single crystal substrates under the above field and temperature conditions.

5.1.4 Morphology of the LSMO/YBCO structures

The morphologic properties of the LSMO/YBCO bi-layers have been studied by means of AFM in the Contact mode and SEM. In the following paragraphs we give a detailed account of the surface properties starting from the bare STO substrate, LSMO films and finally the top YBCO film in the hybrid structure. As it was seen in the above literature overview, morphology plays an important role in determining the flux pinning response caused by surface decoration.

STO substrates

In order to obtain STO (001) terraced substrates, having a single lattice plane termination, TiO_2, the substrates underwent a thermal and chemical treatment described in the "Experimental procedure" Section of the present Chapter. The presence of atomic steps

Table 5.1: Annealing temperatures, time and step height for each STO (001) substrate upon which a specific LSMO layer was deposited.

LSMO thickness (nm)	Temperature (°C)	Annealing time (hours)	Step height (Å)
1.5	1000	1	10.7
3	950	0.2	4.1
7	1000	1	3.6
35	1200	1	3.8

in the substrate ensures that LSMO grains are distributed in an orderly fashion along the surface steps, since step corners constitute preferential grain nucleation sites. On the other hand, a uniform chemical composition of the substrate surface yields a uniform LSMO grain growth. A uniform grain size is desired as we would like to ensure the creation of uniformly distributed sites, in order to attain efficient vortex pinning. In defining the optimum thermal treatment for the STO substrates prior to film deposition, difficulties have been encountered related to a poor reproducibility of different annealing procedures. As a consequence a dispersion of the annealing parameters (annealing temperature and annealing time) exists for the STO substrates prepared for LSMO deposition. The different parameters do not produce dramatic changes in the substrate surface landscape, however, the substrates are not identical. Therefore, in order to be able to interpret morphology data on the deposited films, a good characterization of the substrates is necessary.

Figure 5.6a presents the surface of the STO (001) substrate annealed at 1000 °C for 1 hour used to deposit the 1.5 nm thick LSMO film. The surface steps are clearly defined. As opposed to the other prepared substrates, the steps are discontinuous and also the mean step height was estimated to be of 10.7 Å. This fact is surprising since the STO lattice parameter is a=3.905 Å. Therefore, the step height includes 2 and a half lattice parameters, which means that the termination layer may not be always consisting of TiO_2 planes, but also SrO layers [9]. For the other substrates the STO terrace edges are continuous while the step height is around the expected value. Figure 5.6b shows a profile for one of the substrates, for which the mean step height, 3.84 Å, close to the STO lattice parameter. Table 5.1 summarizes the annealing temperatures and times, together with the step height values. It can be observed that, except the 1.5 nm sample, all the other substrates have almost the same step height. Differences between samples arise in the shape of step edges and terrace width, not shown here.

LSMO films

Figure 5.7 shows the AFM images obtained on LSMO thin films deposited on terraced STO substrates together with a distribution of the grain size for each individual film. The

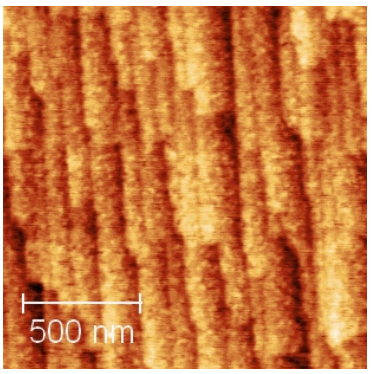

(a) 1.5 nm

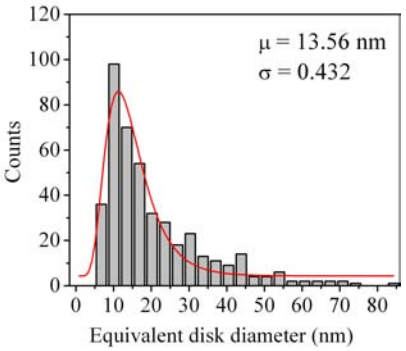

(b) 1.5 nm

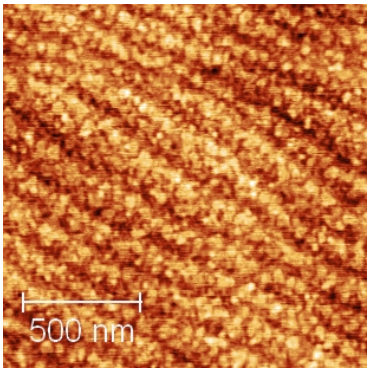

(c) 3 nm

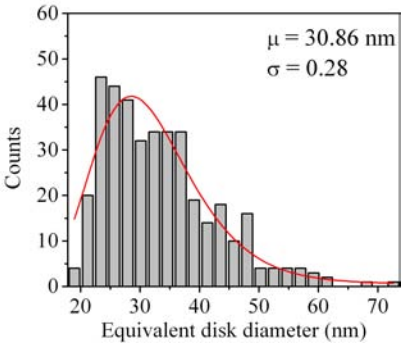

(d) 3 nm

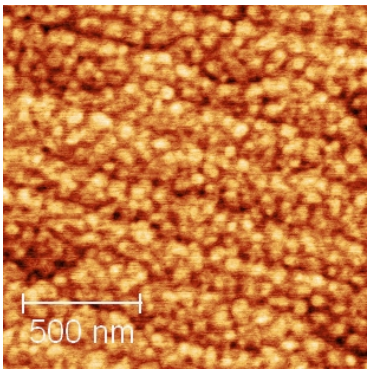

(e) 7 nm

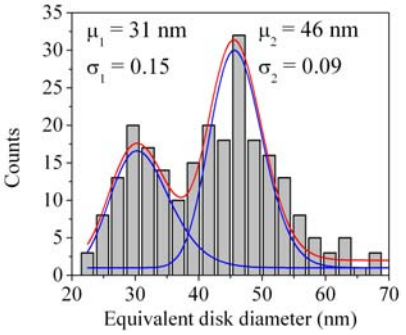

(f) 7 nm

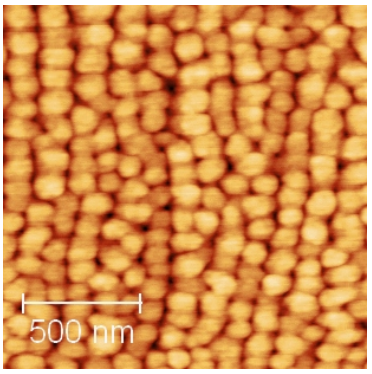

(g) 35 nm

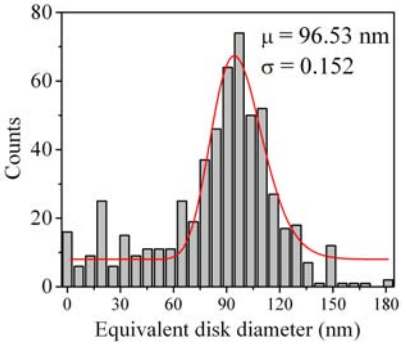

(h) 35 nm

Figure 5.7: 1.5 μm× 1.5 μm AFM images of the LSMO films grown on STO(001) terraced substrates (a), (c), (e), (g), and grain size distributions of the LSMO surface grains (b), (d), (f), (h).

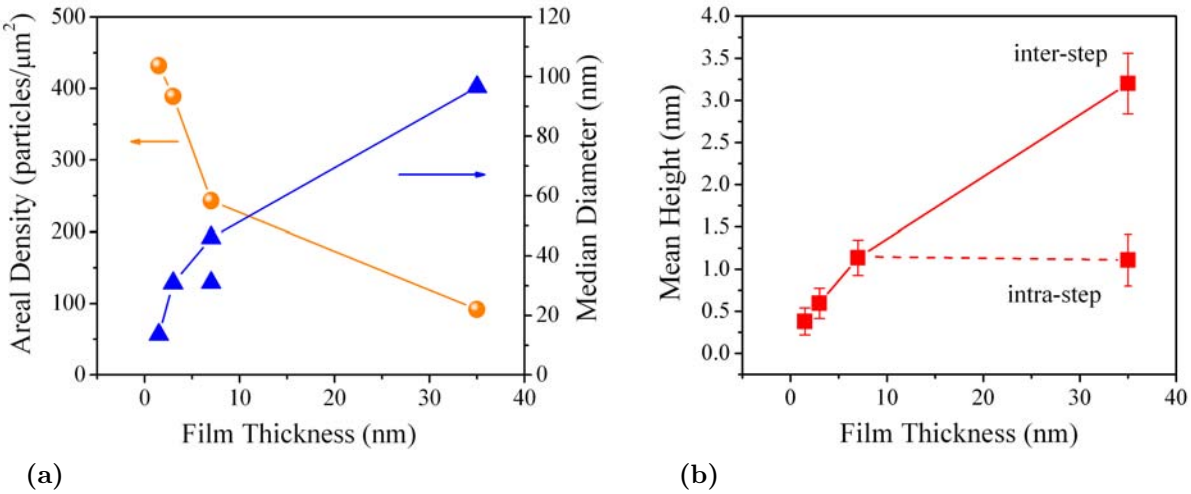

Figure 5.8: (a) Areal density and equivalent diameter evolution of the LSMO grains as a function of film thickness, (b) Mean height distribution of the grains as a function of LSMO film thickness.

grain size distribution was evaluated using the Gwyddion software in which the watershed grain identification routine was implemented. As mentioned before, the watershed algorithm finds local minima in an inverted (negative) AFM image in order to find the grain location and size. As a parameter of the grain size we have used the diameter of a circle having the same projected surface as that of the grains. A log-normal distribution function was employed to fit the various grain size distributions, for which a median value, μ, of the equivalent diameter was calculated. While most of the grain distributions obey well the log-normal law, in the case of the 7 nm film, the distribution seems to be comprising of two different contributions. This may be explained by the larger step widths of the substrate the 7 nm LSMO film was grown upon. It is known that step corners are energetically favorable for grain nucleation, however, due to the increased terrace width, a non-negligible number of grains begin to form on the terraces, away from the corner sites. Even though the corner grains are more developed than the rest of the grains, for this film thickness, grain coalescence has not yet set into place, so that two distinct categories of grains exist, yielding two different grain size distributions.

Grain coalescence prevents one from being able to control independently the particle size and density when using traditional physical vapor deposition techniques for surface decoration. As it can be seen in Figure 5.8a as the film thickness increases, as expected, the size of the grain increases. At the same time the particle, *i.e.* grain, density decreases from 432 particles/μm^2 for the 1.5 nm film to 92 particles/μm^2 for the 35 nm film. This means that no new grains nucleate with increasing film thickness, but rather the grains originating from the initial stages of film growth coalesce, reducing thus the number of particles per unit area.

Table 5.2: Morphology parameters of the YBCO thin films deposited on LSMO.

LSMO thickness (nm)	Areal Density (particles/μm^2)	Median grain size (μm)	RMS roughness (nm)
1.5	557	0.256	24.7
3	227	0.284	43.4
7	361	0.315	28.2
35	575	0.091	12

As far as the particle height is concerned, its mean value as a function of the film thickness is given in Figure 5.8b. The value was estimated from height profiles extracted from AFM images. The mean height value is lower than the estimated film thickness for all of the four samples. This fact is an indication that the growth mode of the LSMO films on the STO substrates, is a mixed 2D and 3D mode. A continuous film layer grows on top of the STO substrate, after which independent grains nucleate. The grain height increases as the thickness increases up to the point when the grains touch each other. This situation corresponds to the 35 nm LSMO film. The evaluation of the grain height, from profiles taken along a substrate step leads to an under estimation of the grain height, as the AFM tip does not touch the substrate, because of the grain size. Therefore, we have evaluated the mean grain height taking inter-step profiles.

LSMO/YBCO bi-layers

The AFM images of the 70 nm YBCO films grown on top of the LSMO layers presented in the above paragraph are given in Figure 5.9. It can be noticed that, contrary to the single YBCO film, all the YBCO layers pertaining to the FM/SC structure, show the presence of outgrowths on their surface. Since all the YBCO films were deposited under the same conditions, a study of the grain features was performed in order to see if there is a correlation between the morphology of the LSMO bottom layer and the YBCO surface morphology. As in the previous paragraph the grains were identified and their size distribution fitted with a log-normal function. The areal grain density and RMS roughness was also evaluated. The results are given in Table 5.2. No correlation whatsoever could be identified between the evolution of the morphology parameters of the two films. Taking into consideration that for all the LSMO films, the grain height is lower than the film thickness so that a continuous film covers the entire STO substrate surface, we may conclude that the presence of YBCO particles are an effect of YBCO growing on LSMO, irrespective of the morphology of the latter. This conclusion is supported by the morphology of the YBCO surface deposited directly on STO, for which, no surface grains were observed, except for large particles inherent to the deposition method, PLD. Aytung *et al.* [15] have reported a similar finding on YBCO

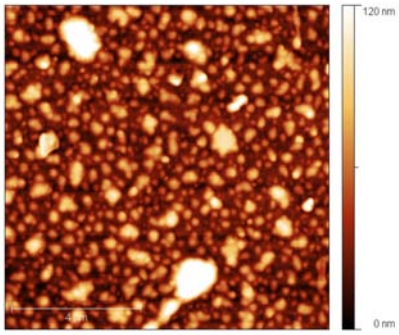

(a) 1.5 nm

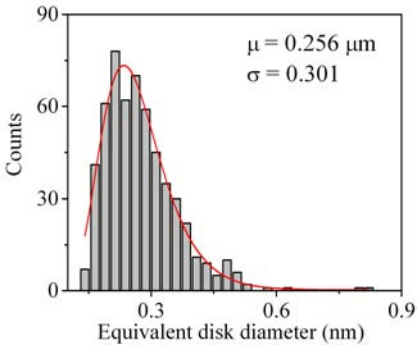

(b) 1.5 nm

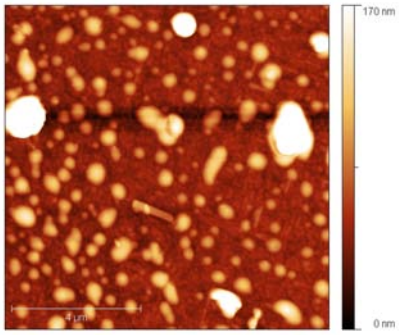

(c) 3 nm

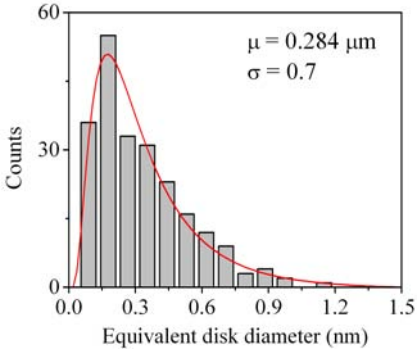

(d) 3 nm

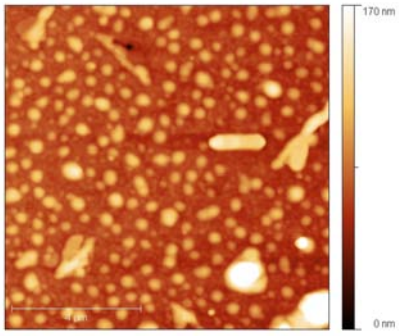

(e) 7 nm

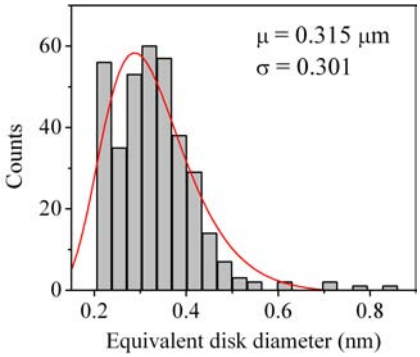

(f) 7 nm

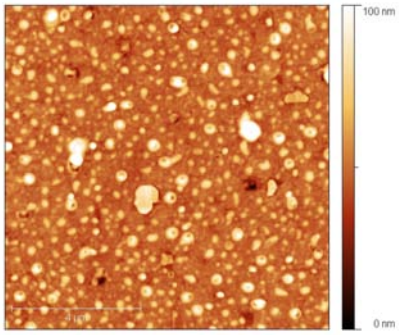

(g) 35 nm

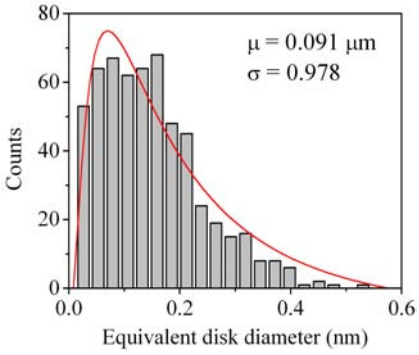

(h) 35 nm

Figure 5.9: 10μm× 10μm AFM images of the YBCO films (a), (c), (e), (g), and grain size distributions of the YBCO surface grains (b), (d), (f), (h).

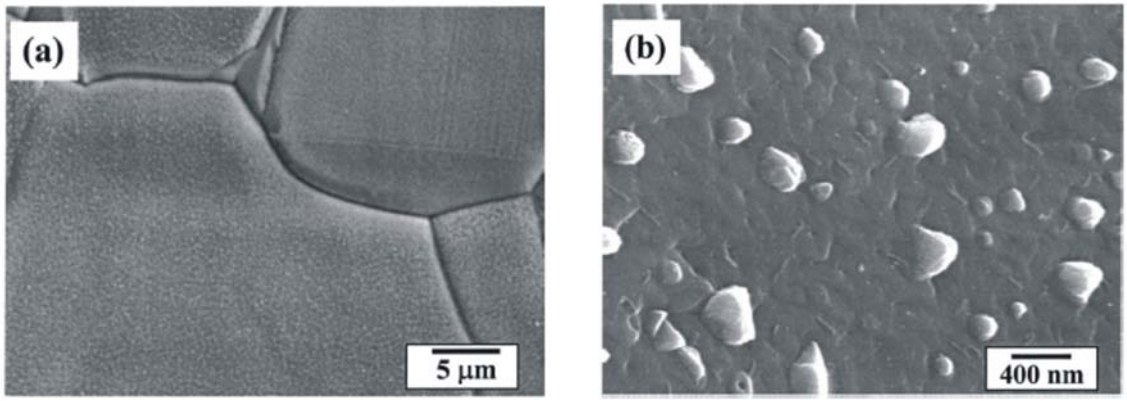

(a) (b)

Figure 5.10: SEM images of a (a) LSMO layer deposited on a Ni substrate and (b) YBCO layer deposited on the LSMO/Ni structure. Taken from [15].

grown on LSMO films initially deposited on Ni metallic substrates. As can be seen in Figure 5.10. The LSMO surface deposited on the metallic Ni substrates, Figure 5.10a, reveal a smooth surface, with an additional influence from the grain boundaries of the Ni substrate. Even if the LSMO surface does not show any particular height modulation, the YBCO surface, Figure 5.10b, taken within the perimeter of a substrate grain, show the formation of outgrowths similar in size as the ones shown in the previous Section. Therefore, we may indeed attribute the surface characteristics of YBCO films to the LSMO buffer and not to it's particular morphology.

5.1.5 Structural properties of the LSMO/YBCO structures

YBCO/LSMO bi-layers

The $2\theta/\omega$ scans for the YBCO films grown on top of LSMO layers of different thicknesses are presented in Figure 5.11a. XRD patterns indicate that all of the YBCO films have grown epitaxially on the STO//LSMO template, as only the $(00l)$ peaks corresponding to the YBCO layers are visible. From the measurements presented, a $[001]_{YBCO}\|[001]_{LSMO}\|[001]_{STO}$ out-of-plane epitaxial relationship was deduced. No presence of any YBCO crystallites having the a axis oriented perpendicularly on the LSMO layer was observed from the diffraction data. The out-of-plane lattice parameter, c, of the YBCO films was determined from the angular position of the (005) peak. The results are shown in Figure 5.11b.

In order to quantify the influence of the LSMO decorated substrate surface on the subsequent structural properties of YBCO, the (002) and (005) ω-scans were fitted using the model described in Chapter 3. The model developed by Boulle *et al.* [14] is used to model the two component rocking curves, in order to determine the correlation length and mosaicity of the defects present within a thin film. In the present case we assume that the LSMO grains

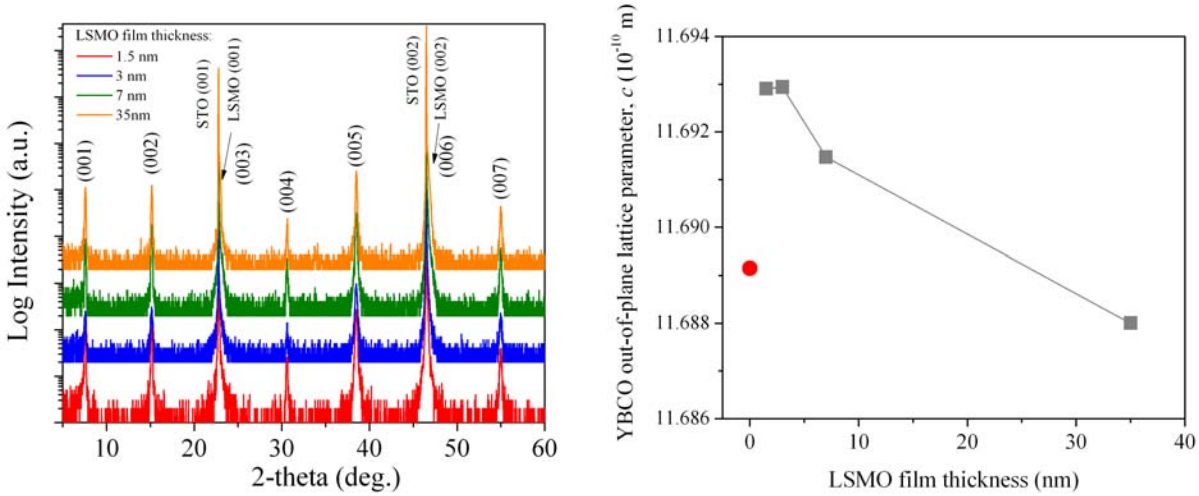

(a) **(b)**

Figure 5.11: (a) Diffraction patterns of the LSMO/YBCO bi-layers; (b) Evolution of the out-of-plane lattice parameter, c, of the YBCO films as a function of the LSMO film thickness. The red point indicates the value of c for the YBCO film deposited directly on an STO (001) substrate.

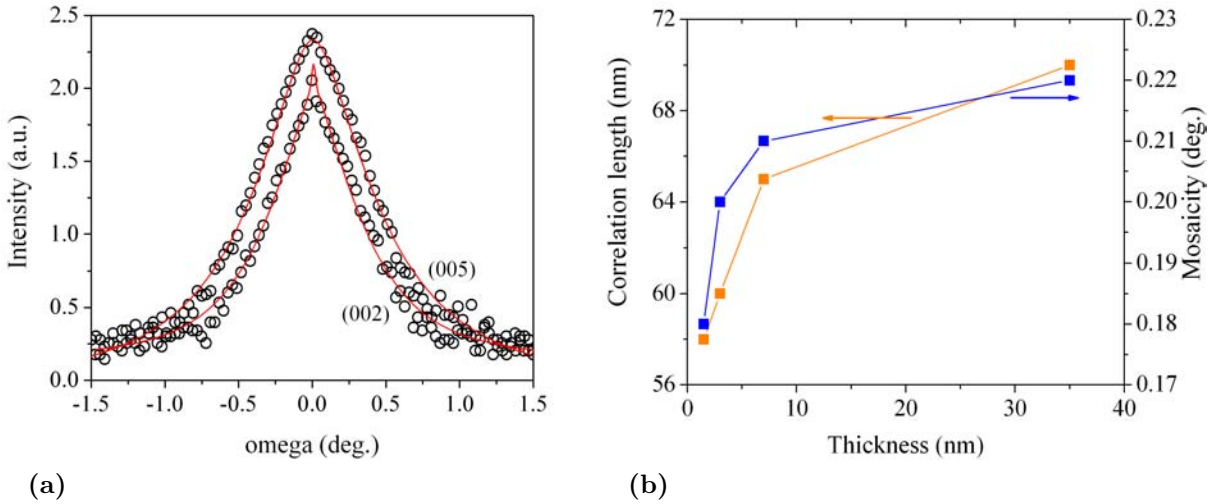

(a) **(b)**

Figure 5.12: (a) ω-scans around the (002) and (005) peaks of the YBCO layer deposited on the 35 nm thick LSMO film, together with the corresponding simulations (data points were removed for clarity); (b) The correlation length and mosaicity of the defects within the YBCO film, extracted from the ω-scan simulations.

lead to formation of defects in the YBCO layers. These defects act as pinning centers for the SC vortices, so that their structural characterization is important for the further interpretation of the superconducting transport properties of the YBCO films. The ω-scans around the YBCO (002) and (005) peaks were fitted well by the used model. For exemplification, Figure 5.12a shows the recorded rocking curve and the corresponding simulations. From the simulations the correlation length and mosaicity of the defects were determined and are presented as a function of LSMO film thickness in Figure 5.12b. It can be seen that as the thickness of the LSMO layer increases the correlation length of the defects increases. The correlation length of a defect represents its spatial extent in the crystal lattice. Short correlation length are an indication of the presence of a large number of defects in the lattice as the spatial extent of the defects is limited by the presence of adjacent defects. On the contrary, when fewer defects are present in the lattice, each defect is able to extend more within the crystal. Hence the correlation length may be regarded as being inversely proportional to the defect density present within a film. The values of the correlation length in the YBCO films indicates that for the film deposited on a 1.5 nm thick LSMO layer has the lowest value, and thus the highest number of defects is present within the SC lattice. As the thickness of the LSMO layer increases, the correlation length increases indicating a decrease in the number of defects. If we consider the areal density of the LSMO grains, a direct influence of the surface grains is observed on the defects present in the YBCO films. For a high density of grains, as is the case of the 1.5 nm LSMO film the highest defect density in the YBCO layer is recorded. As the LSMO layer thickness increases, the areal grain density decreases and so does the number of YBCO defects, corresponding to an increase of the correlation length. As far as the mosaicity is concerned, it may be interpreted as the root mean square strain of the defects. The evolution of mosaicity as a function of the LSMO film thickness indicates that as the LSMO grains grow, the mosaicity of the defects within the YBCO layer increases. It may be observed also that the height of the LSMO grains correlates well with the evolution of the mosaicity. Even though the areal density of grains is higher in the case of thinner LSMO films, the corresponding mosaicity of the YBCO defects is lower, due to the reduced LSMO grain height. An interesting case is that of the YBCO film deposited on top of the 35 nm LSMO film. In its case, the high mosaicity is related to the height of the grains determined from inter-step profiles, as the intra-step grain height is lower than that of the grains pertaining to 7 nm film. We may thus conclude that the mosicity is related to the holes in the LSMO film, which is otherwise almost continuous. We will address again this issue in the discussion paragraph of this Section.

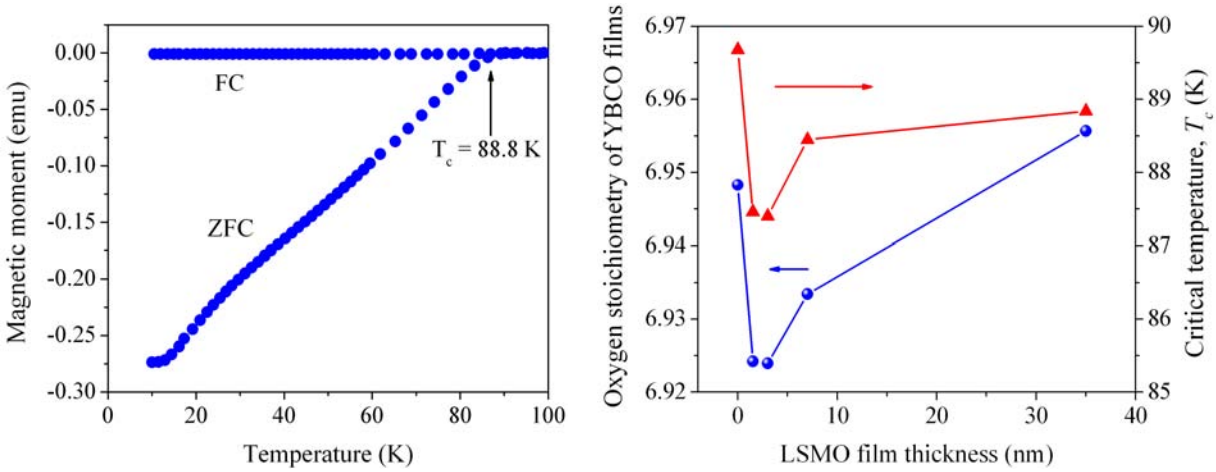

Figure 5.13: (a) Field cooled (FC), zero field cooled (ZFC) $M(T)$ curves for the YBCO film deposited on the 35 nm LSMO film; (b) Oxygen stoichiometry of the YBCO thin films and critical temperature, T_c, as function of the LSMO thickness.

5.1.6 Superconducting properties of LSMO/YBCO structures

Superconducting transition and critical temperature

From the FC and ZFC $M(T)$ measurements the critical transition temperature of the YBCO films was determined. Figure 5.13 shows a typical $M(T)$ curve measured on the YBCO film deposited on the 35 nm LSMO film, together with the evolution of T_c as a function of the thickness of the LSMO template. As a first remark it can be seen that all of the T_c values are situated below the recorded value for the single YBCO film, 89.68 K. It is well known that the critical temperature is correlated with the out-of-plane lattice parameter, c, through the oxygen concentration. Cava *et al.* [16] deduced a relation between the oxygen content in YBCO and c. There expression is:

$$c = 12.771 - 0.1557x, \tag{5.3}$$

where x is the YBCO oxygen stoichiometry, 7 in the ideal case. Using 5.3 we have calculated the oxygen content in the YBCO films. The results are given in Figure 5.13b. For comparison, results on the single YBCO film are also given. A remarkable feature of the oxygen content evolution is the very good correlation with the T_c, in the sense that the two exhibit almost identical behavior as a function of the LSMO thickness. This strong correlation supports the hypothesis that the c lattice parameter varies due to the oxygen content in the films and not due to different in-plain strain states induced by the LSMO buffer. Cava *et al.* [17] have shown that indeed T_c increases as the oxygen content reaches its ideal value, 7. In the case of the single YBCO film, even though its oxygen content is similar, even a bit lower,

than that of the YBCO film deposited on the 35 nm thick LSMO layer, its T_c is almost 1K higher than that of the latter. This may be explained by a higher structural quality of the single SC film, demonstrated by a lower value of the FWHM of the ω-scan around YBCO (005) peak reflection. In the case of the bi-layer the FWHM was 0.3°, while for the single film it was only of 0.08°. The origin of the different oxygen content in the films is still unclear. Some authors [18] suggest that different film morphologies influence the oxygen loading of the CuO_x chains during cool-down and result in a change of the superconducting properties of the YBCO. The morphology parameters of the YBCO films, given in Table 5.2, do not show any correlation with the calculated oxygen content in the YBCO films.

Critical current density and irreversibility fields

The $J_c(H)$ dependencies, as derived from $M(H)$ cycles, are shown in Figure 5.14. The J_c curves for the bare YBCO film were also included for comparison with the buffered films. It can be seen that all of the J_c values for the YBCO layer within the hybrid structures lie below the values of the corresponding single YBCO film. Aytug *et al.* [15, 19] using secondary ion mass spectrometry (SIMS) analyzed the composition profiles of Ni/LSMO/YBCO structures. The result is shown in Figure 5.15. The measurements reveal that there exists a Sr contamination of the YBCO layer at the YBCO/LSMO interface, as signal coming from Sr is still present in the YBCO layer. As in our case the authors did not observe any significant modification of the transition temperature, but instead a decrease of J_c was observed. As being the case, it is impossible to evaluate the vortex pinning characteristics of the LSMO template on YBCO by comparison to the YBCO single film, based solely on the current density values, since the two systems are not equivalent from a chemical point of view. For a more relevant analysis on the pinning characteristics of the two systems, the irreversibility field temperature dependencies and pinning forces are determined.

Comparing the different J_c results obtained on the YBCO films deposited on LSMO, it can be seen that the highest values were measured for the LSMO(35 nm)/YBCO bi-layer at all temperatures for all the magnetic fields. In the case of the other films, J_c values vary so as we cannot form a strict hierarchy in order classify these samples according to their respective flux pinning strengths. From a morphological point of view, the separation of the LSMO(35 nm) from the others is supported by the fact that while for the thinner films the surface is composed by independent grains, in the case of the thickest film, the grains are fully developed so that they occupy the entire step width. This fact leads to the formation of holes between the grains pertaining to different steps. Along the same step because adjacent grains touch each other, the surface modulation is not as pronounced, the intra-step "height" was evaluated as 1.11 nm, even lower than the mean grain height in the case of the 7 nm LSMO film, which was of 1.14 nm, Figure 5.8b. The situation is different across steps, as

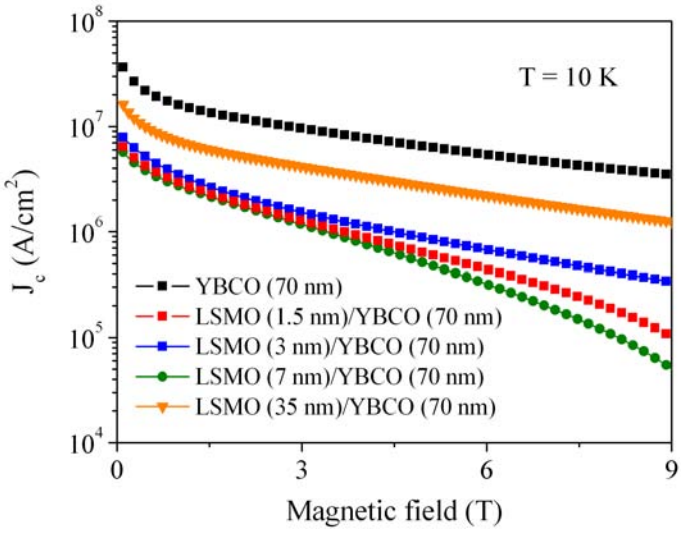

(a)

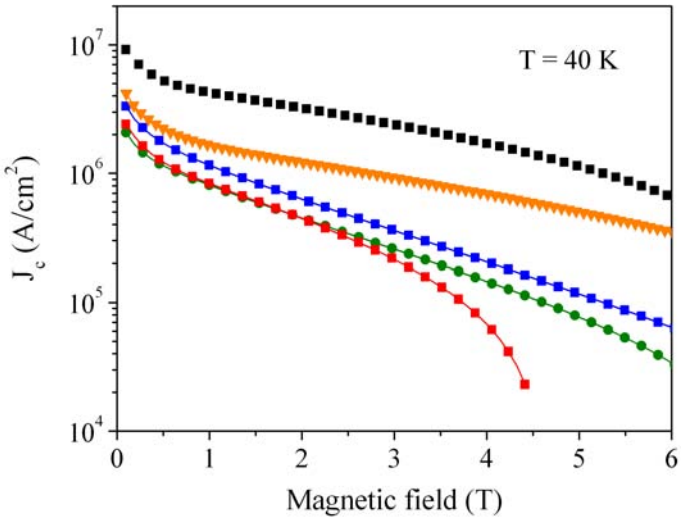

(b)

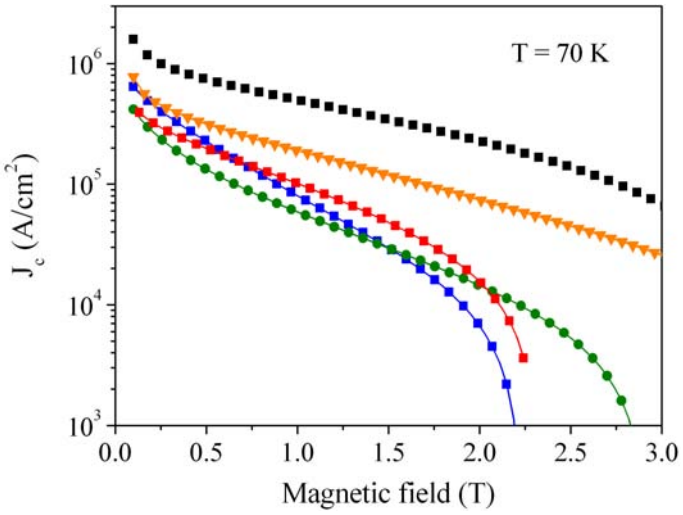

(c)

Figure 5.14: $J_c(H)$ dependence of the YBCO films at (a) 10 K, (b) 40 K and (c) 70 K calculated from the respective $M(H)$ loops.

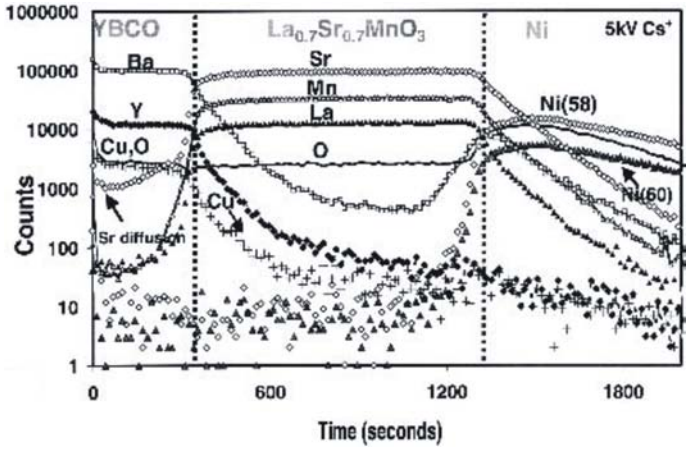

Figure 5.15: SIMS measurements on Ni/LSMO/YBCO structures. The arrow indicated Sr contamination of the YBCO layer. Taken from [19].

the surface modulation is stronger because of the hole formations. The mean grain height evaluated from profiles taken across the steps, inter-step, was considerably higher, 3.2 nm. The large difference suggests that the high J_c value for the YBCO film deposited on top of the 35 nm LSMO layer is due to defects generated by the holes in LSMO. This assumption is backed by the mosaicity around the defects in the YBCO film grown on LSMO (35 nm). The mosaicity is equivalent to the strain around the defect, so that higher mosaicity means higher strain and "stronger" defects, that produce the highest YBCO lattice alteration. One would naturally expect strong flux pinning from defects having the highest mosaicity, which is the case for the LSMO(35 nm)/YBCO structure. Moreover, the low RMS roughness value of YBCO in this case suggests that YBCO grows smoothly on the large LSMO grains, so that defects are indeed formed at the hole sites.

The irreversibility field, H_{irr} was estimated by linear extrapolation of the $J_c^{1/2}H^{1/4}$ versus H curve to the horizontal axis [21]. The results are presented for the single YBCO film and the YBCO grown on the 35 nm thick LSMO film, Figure 5.17. Although the critical current density of the single YBCO layer is higher than for YBCO/LSMO structure, H_{irr} is higher for the latter in the high temperature range. The observed H_{irr} temperature dependencies for the two samples can be explained taking into account the presence of two contributions to the pinning mechanism in bi-layer structure: a classic temperature dependent pinning mechanism on normal defects and an additional temperature independent magnetic pining. In the low temperature range, where the contribution of the classic pinning is dominant, the two irreversibility fields have practically the same value. This suggests that the classical pinning is the same in both samples. On the contrary, as the temperature is increased the irreversibility field of the single YBCO layer has a steeper decrease with respect to the YBCO film grown on the 35 nm LSMO layer. The higher values of H_{irr} of the YBCO/LSMO superconducting structure confirms the existence of the magnetic pinning contribution, relevant

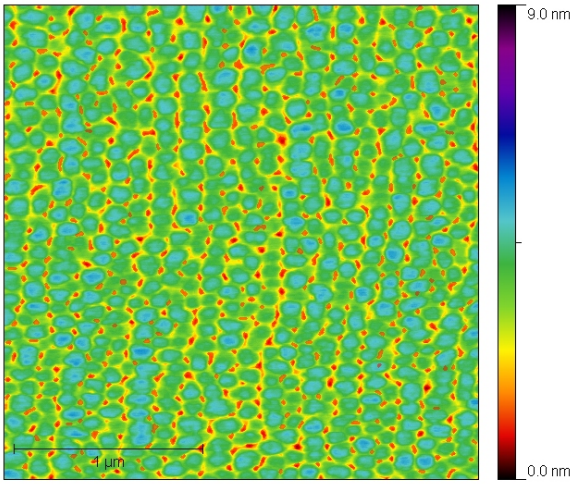

Figure 5.16: AFM image of the 35 nm thick LSMO film. Color scale and inverse watershed hole determination results mark the holes in red to emphasize the location of the holes.

in the high temperature range, where classic pinning energy, $(\Phi_0/8\pi\lambda_L)^2$, tends towards zero as $T \to T_c$. The origin of the magnetic pinning can be understood taking into account the morphology of the 35 nm thick LSMO film, as shown in Figure 5.16. The LSMO surface may be described as consisting of a continuous film having regular hole arrays along the STO substrate steps. This situation corresponds to the magnetic antidot arrays studied by Raedts *et al.* [23] in connection to the pinning properties of a Pb film. The presence of antidots in the LSMO film produces a magnetic field gradient around the hole regions, which in turn results in a magnetic vortex pinning force. This mechanism is valid in the high applied magnetic field range, $H > H_{sat}$. This explains the high J_c values of the YBCO/LSMO superconducting structure, with respect to the single YBCO film in the high field range. Another effect of the hole presence is the formation of structural defects in the YBCO film, as supported by X-ray data simulations. However, the low, 90 holes/μm^2, density, which is approximately equal to the induced structural defect density, cannot be responsible for the high irreversibility line observed in this sample. As it was shown by Sparing *et al.* [10] effective pinning enhancement is produced by a density of defects one order o magnitude higher than the one present in our case.

The magnetic field dependence of the density of pinning force ($F_p = J_cB$) contains information about the pinning mechanism, as shown by [22]. The normalized pinning force, $f = F_p/F_{p,max}$, versus the reduced field, $h = H/H_{irr}$, dependence typically overlap at different temperatures when a single pinning mechanism is present. In Figure 5.18 the $f(h)$ curves are shown for both the YBCO film and the YBCO grown on the LSMO (35 nm) layer. With respect to the YBCO film, Figure 5.18a, the $f(h)$ curves for different temperatures are significantly more separated in the case of the YBCO/LSMO bi-layer, Figure 5.18b. This

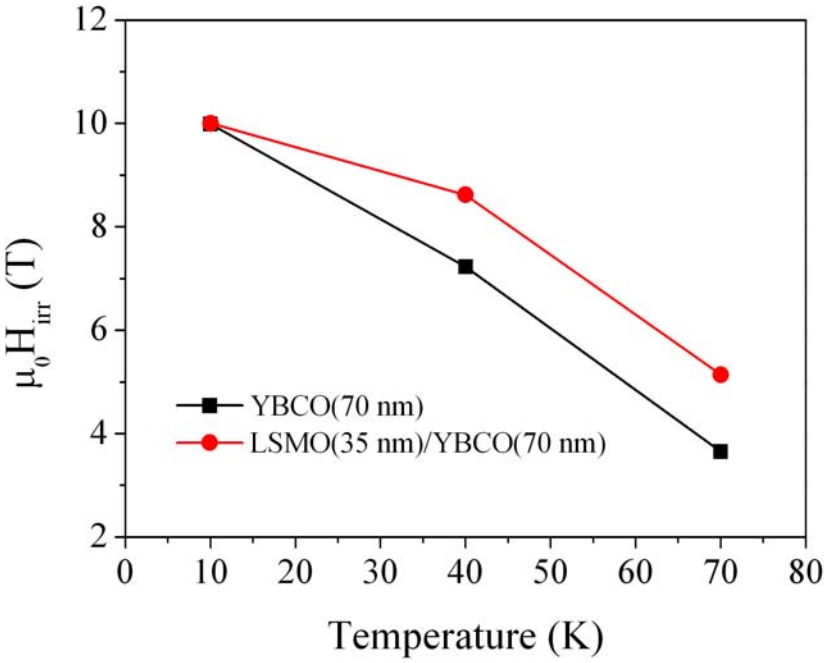

Figure 5.17: Irreversibility field, H_{irr}, temperature dependencies for the single YBCO film and the YBCO film deposited on the 35 nm thick LSMO thin film.

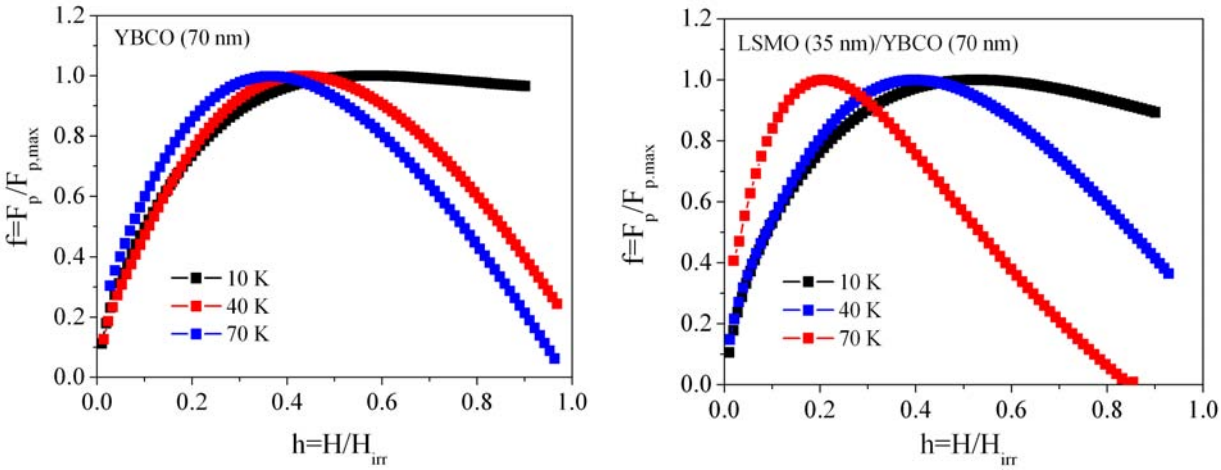

(a) **(b)**

Figure 5.18: Normalized pinning force, $f = F_p/F_{p,max}$ versus the reduced magnetic field $h = H/H_{irr}$ for the single YBCO film and the YBCO film deposited on the 35 nm thick LSMO thin film, at different temperatures.

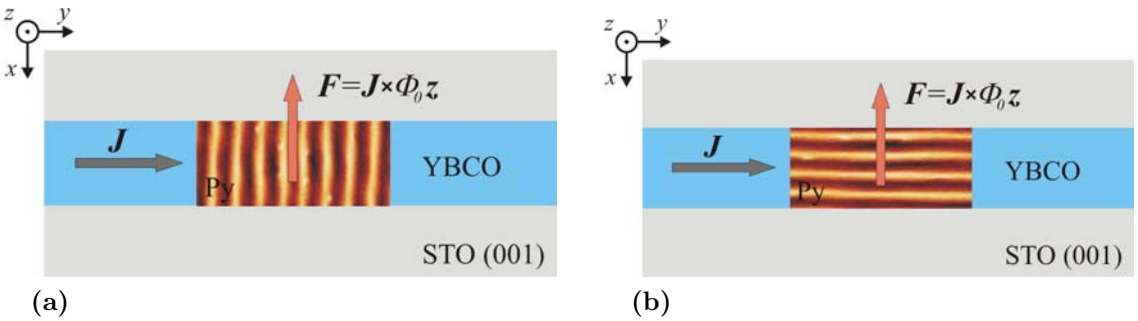

(a) (b)

Figure 5.19: Schematic view of the principle behind the magnetic pinning using stripe domains.

indicates the presence of an additional pinning mechanism. This result confirms the existence of the magnetic pinning mechanism, as suggested by the irreversibility field temperature dependence.

5.2 YBCO/Permalloy Structures

In the introductory chapter of the present thesis it has been shown that the stripped magnetic domain configuration of a FM film can produce an effective vortex pinning in a SC film, integrated in a FM/SC hybrid bi-layer structure [24]. Vlasko Vlasov *et al.* [8] studied the entrance and exit patterns of vortices in a SC/FM structure, with the FM Py layer exhibiting a stripped magnetic structure. Their study revealed that vortices move preferentially along the magnetic stripe. This situation arises due to the fact that no variation of the magnetization occurs along a domain stripe, and therefore there is no magnetic force acting on the SC vortices. Belkin *et al.* [7] have shown that by controlling the orientation of the magnetic stripes with respect to the current passing through the SC layer an anisotropy in the flux pinning characteristics is present. A higher critical current density of the SC layer is measured when the current passing through the SC layer is parallel to the magnetic stripes of the FM. The Lorentz-type force acting on the vortices tends to displace them in a direction perpendicular to the stripes. The periodic modulation of the magnetization will act on the vortices so as to pin them, resulting in a higher depinning critical current density, J_c. The situation is presented schematically in Figure 5.19. It is to be noted that so far, most of the of the studies regarding the vortex pinning effect of the stripe magnetic domain of the FM layer in a FM/SC structure were performed on low temperature superconductors. Similar experiments on high temperature based FM/SC bi-layers are of interest both from a theoretical and practical point of view. Such experiments open the possibility to investigate the role of magnetic pinning on the thermally activated flux flow and related phenomena. On the other hand, the magnetic field control of the superconducting current by means of the relative orientation of the magnetic stripes, could open up the way towards hybrid

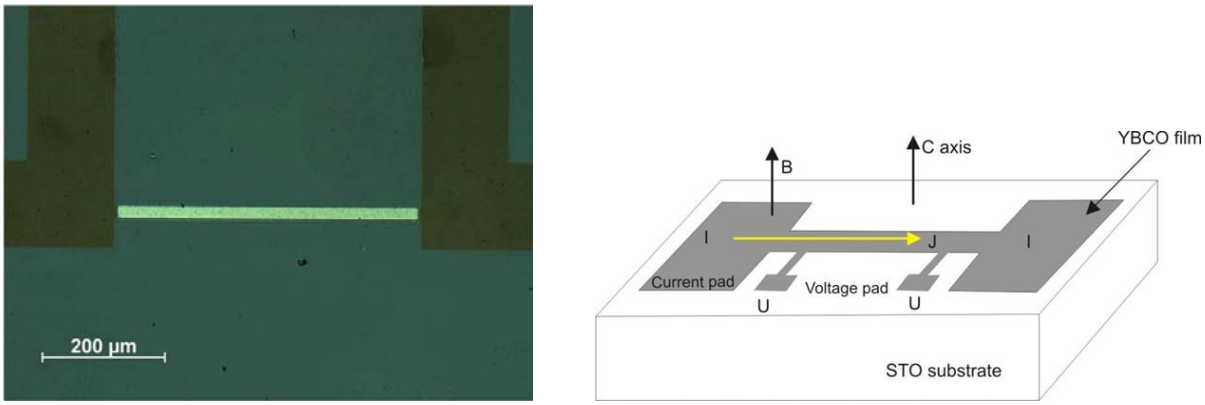

(a) (b)

Figure 5.20: (a)Optical image of a Py stripe (bright) deposited on top of a YBCO stripe (not visible) for electrical measurements; (b) Schematic diagram of the four-probe method used for J_c determination.

magnetic/superconducting devices, operating at liquid nitrogen temperature.

5.2.1 Experimental procedure

In order to study the influence of the the modulated domain structure on vortex pinning in high temperature FM/SC structures we have developed YBCO/Py bi-layer structures. Because of *rotatable anisotropy*, which permits the rotation of the magnetic domain stripes with a relative weak magnetic field, together with the possibility of modulating the stripe periodicity by the film thickness, highly recommend the use of Py thin films in studies of the influence of periodic magnetic structures on the magnetic pinning of SC vortices.

The deposition of the YBCO film was performed by means of PLD in the same conditions as were reported in the previous Section. As far as the Py film is concerned it was deposited by dc sputtering at room temperature in a 1 mTorr Ar pressure. The film thickness was evaluated at 300 nm by extrapolation from XRR measurements performed on thinner samples.

After the whole stack was deposited, in order to perform electrical measurements and J_c evaluation, patterning of the bi-layers was needed to define a precise geometry. Optical lithography and etching processes were used in patterning the sample. A first mask was used to define a Py stripe after which a Ar ion beam etching was used to remove the Py film leaving just 40 μm wide Py stripe on the YBCO film. A second mask was used to define the YBCO stripe and contact pads. The excess YBCO film was removed by chemical etching (a nitric acid-deionized water solution in a volume concentration of 3/1000). A gold thin films was deposited on the contact pads in order to ensure good electrical contact with the measurement leads. The result of the patterning process is shown in Figure 5.20a

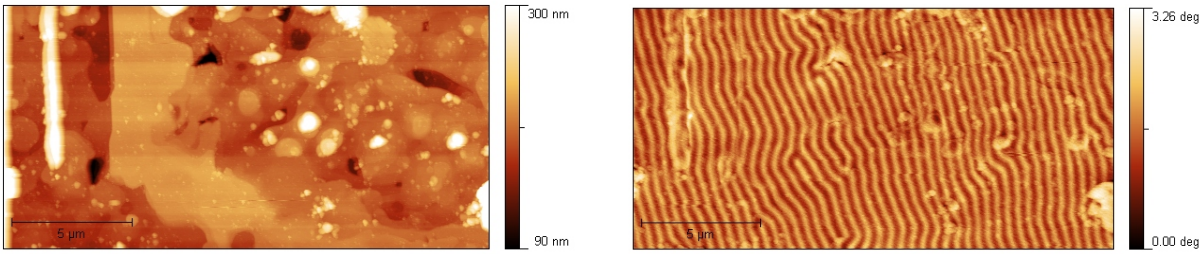

(a) **(b)**

Figure 5.21: (a) AFM image of a 300 nm thick Py thin film deposited on a YBCO film, the characteristic YBCO features are still visible after the Py deposition; (b) MFM image on the Py (300 nm), weak-stripe domains are clearly visible.

5.2.2 MFM on the Py film

After the deposition of the Py film, MFM images were acquired in order to characterize the magnetic stripe domains. The topography image of the FM film, Figure 5.21a, shows that the Py film copies the surface features of the YBCO layer. As a consequence droplets and the *a*-axis crystallites that were present on the YBCO film are visible in the topography of the Py film. As far as the magnetic image is concerned, after applying an external field in a desired direction, parallel stripes are visible, characteristic of thick Py films, as discussed in Chapter 4. The stripe domain width was evaluated from the stripe periodicity to be of ∼230 nm. We have used a 600 Oe magnetic field produced by a permanent magnet to orient the stripes in an in-plane direction.

5.2.3 Superconducting properties of the YBCO/Py structure

The critical current density of the YBCO layer was determined by electric measurements, recording the *I*-*V* curves. The critical current density was derived from *I*-*V* characteristics using a 1 μV/cm criterion. The electrical measurements were performed using the four-probe technique. A critical point in these type of measurements is the contact resistance which may generate excessive heat from the bias current. In turn the thermal energy may shift the temperature of the sample and cause temperature gradients at the contacts and in the superconductor. To avoid these unwanted effects, a Au film was deposited on the patterned YBCO contact pads.

In order to evaluate J_c for different orientations of the magnetic stripes, the domains were aligned with a 600 Oe field generated by a permanent magnet in the two direction, parallel and perpendicular to the bias current. The results of the $J_c(T)$ measurements for the two configurations are given in Figure 5.22a. As it can be seen, in the high temperature range, $T > 60$ K, the critical current density is higher for the parallel oriented stripes. As

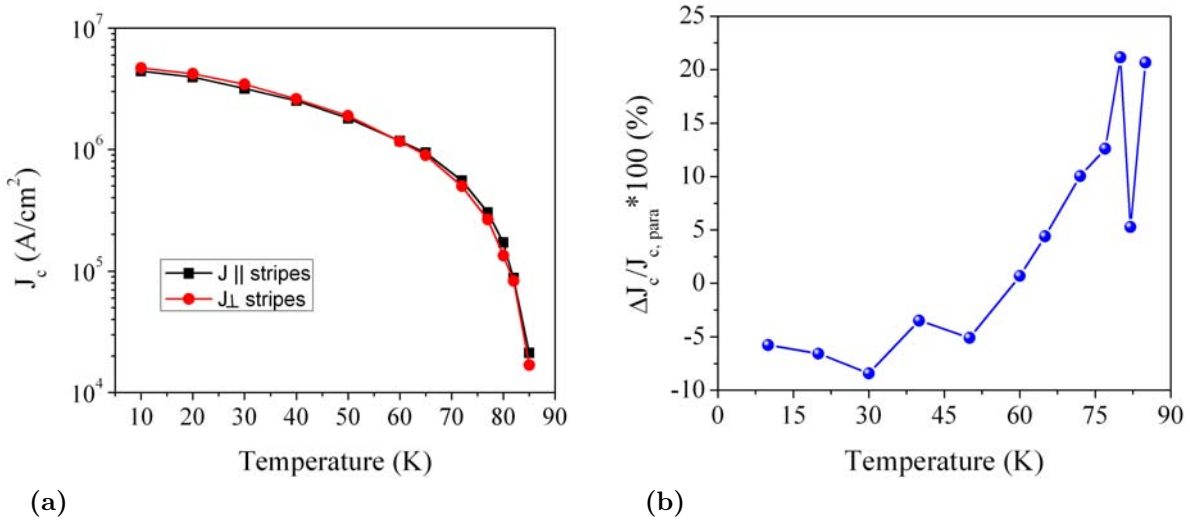

(a) (b)

Figure 5.22: (a) $J_c(T)$ dependence for the two magnetic stripe configurations, parallel and perpendicular to the measuring current; (b) The relative variation of J_c in the two configurations.

argued above, this is to be expected as the vortex motion is hindered by the presence of a modulation of the magnetization along the direction of the vortex motion, which gives rise to a magnetic force which causes the magnetic pinning of vortices. On the contrary, in the perpendicular case, the vortex motion takes place along the magnetic stripes, where no variation of the magnetization occurs. For a better quantification of the effects of the magnetic modulation on the pinning of the vortices, in Figure 5.22b we have calculated the variation of the critical current densities in the two cases, as

$$\Delta J_c(\%) = \frac{J_{c,para} - J_{c,perp}}{J_{c,para}} \times 100. \tag{5.4}$$

It can be seen that as the temperature increases so does $\Delta J_c\%$, reaching a maximum value of 20% at 80 K, corresponding to J_c=0.17 MA/cm^2. The increase of the difference between the two configurations with increasing temperature is due to the fact that magnetic pinning is temperature independent, while conventional pinning strength decreases with temperature, see Chapter 1. As the temperature increases, the difference between the two configuration increases, suggesting that at low temperatures pinning is mostly due to the intrinsinc mechanisms, grain boundaries, dislocations or secondary phases, while at high temperatures, magnetic pinning becomes dominant, giving rise to the observed increase.

5.3 Résumé de chapitre en français

Le dernier chapitre de cette thèse présente des concepts, des bases théoriques ainsi que des résultats expérimentaux préliminaires concernant les effets de pinning magnétique ex-

trinsèque et de proximité réciproque à l'interface supraconducteur - film magnétique. Une attention toute particulière est consacrée à la spécificité des vortex et leur dynamique dans les supraconducteurs à haute température (HTCSC), par rapport aux supraconducteurs classiques. Nous discutons les effets d'un champ magnétique d'ancrage sur les vortex de type Abrikosov et Josephson, les effets de la température finie dans les expériences de pinning des vortex dans les HTCSC.

Dans une deuxième étape, nous exposons la problématique expérimentale. Après la réalisation et l'étude des systèmes magnétiques qui présentent des propriétés micromagnétiques modulables par l'effet de la dimensionnalité, nous avons réalisé des structures hybrides d'interface avec le supraconducteur de haute température YBaCuO. L'accent a été mis sur des structures de type LSMO/YBaCuO et $Ni_{80}Fe_{20}$/YBaCuO, structurés sous forme de linges bicouche pour pouvoir effectuer des mesures de transport électriques en température variable. L'objectif était de démontrer l'influence directe de la couche magnétique, via les champs de fuites associés aux nanostructures magnétiques, sur les propriétés électriques de la couche supraconductrice (température et champ critique) et de démontrer les effets de pinning magnétique sur les vortex dans la couche supraconductrice. Dans les systèmes hybrides d'interface LSMO/YBaCuO les deux types de pinning, intrinsèque (par les défauts structuraux) et extrinsèque (magnétique), on été étudiés. Cette partie de la thèse comporte une problématique très complexe, entre la réalisation et la caractérisation des structures bicouche d'interface, les mesures magnétiques et électriques en température variable et l'interprétation des résultats. A la fin de cette thèse, elle ouvre une large palette de perspectives expérimentales et théoriques.

Bibliography

[1] J. Y. Gu, C.-Y. You, J. S. Jiang, J. Pearson, Ya. B. Bazaliy, and S. D. Bader, *Magnetization-Orientation Dependence of the Superconducting Transition Temperature in the Ferromagnet-Superconductor-Ferromagnet System: CuNi/Nb/CuNi*, Phys. Rev. Lett. **89**, 267001 (2002);

[2] T. W. Clinton and M. Johnson, *Mesoscopic magnetoquenched superconducting valve*, Appl. Phys. Lett. **70**, 1170 (1997);

[3] D. Stamopoulos, E. Manios, and M. Pissas, *Stray-fields-based magnetoresistance mechanism in $Ni_{80}Fe_{20}$-Nb-$Ni_{80}Fe_{20}$ trilayered hybrids*, Phys. Rev. B **75**, 184504 (2007);

[4] G. Carapella, F. Russo, and G. Costabile, *Low-field transport measurements in superconducting Co/Nb/Co trilayers*, Phys. Rev. B **78**, 104529 (2008);

[5] D. Y. Vodolazov, B. A. Gribkov, S. A. Gusev, A. Yu. Klimov, Yu. N. Nozdrin, V. V. Rogov and S. N. Vdovichev, *Considerable enhancement of the critical current in a superconducting film by a magnetized magnetic strip*, Phys. Rev. B **72**, 064509 (2005);

[6] N. Touitou, P. Bernstein, J. F. Hamet, Ch. Simon, L. Mechin, J. P. Contour and E. Jacquet, *Nonsymmetric currentvoltage characteristics in ferromagnet/superconductor thin film structures*, Appl. Phys. Lett. **85**, 1742 (2004);

[7] A. Belkin, V. Novosad, M. Iavarone, J. Fedor, J. E. Pearson, A. Petrean-Troncalli and G. Karapetrov, *Tunable transport in magnetically coupled MoGe/Permalloy hybrids*, Appl. Phys. Lett. **93**, 072510 (2008);

[8] V. V. Vlasko-Vlasov, U. Welp, G. Karapetrov, V. Novosad, D. Rosenmann, M. Iavarone, A. Belkin and W.-K. Kwok, *Guiding superconducting vortices with magnetic domain walls*, Phys. Rev. B **77**, 134518 (2008);

[9] P. Mele, K. Matsumoto, T. Horide, O. Miura, A. Ichinos, M. Mukaida, Y. Yoshida and S. Horii, *Tuning of the critical current in $YBa_2Cu_3O_{7-x}$ thin films by controlling the size and density of Y_2O_3 nanoislands on annealed $SrTiO_3$ substrates*, Supercond. Sci. Technol. **19**, 44 (2006);

[10] M. Sparing, E. Backen, T. Freudenberg, R. Hühne, B. Rellinghaus, L. Schultz and B. Holzapfel, *Artificial pinning centres in YBCO thin films induced by substrate decoration with gas-phase-prepared Y_2O_3 nanoparticles*, Supercond. Sci. Technol. **20**, S239 (2007);

[11] T. Aytug, M. Paranthaman, A. A. Gapud, S. Kang, H. M. Christen, K. J. Leonard, P. M. Martin, J. R. Thompson, D. K. Christen, R. Meng, I. Rusakova, C. W. Chu and T. H. Johansen, *Enhancement of flux pinning and critical currents in $YBa_2Cu_3O_{7-\delta}$ films by nanoscale iridium pretreatment of substrate surfaces*, J. Appl. Phys **98**, 114309 (2005);

[12] J. Mannhart, *Critical Currents in High-T_c Superconductors* in *Physics of High-Temperature Superconductors*, S. Maekawa and M. Sato (Eds.), Springer-Verlag (1991);

[13] C. P. Bean, *Magnetization of Hard Superconductors*, Phys. Rev. Lett. **8**, 250 (1962); C. P. Bean, *Magnetization of High-Field Superconductors*, Rev. Mod. Phys. **36**, 31 (1964);

[14] A. Boulle, R. Guinebretière, A. Dauger, J. Phys. D: Appl. Phys. **38**, 3907 (2005);

[15] T. Aytug, M. Paranthaman, B. W. Kang, S. Sathyamurthy, A. Goyal and D. K. Christen, *$La_{0.7}Sr_{0.3}MnO_3$: A single, conductive-oxide buffer layer for the development of $YBa_2Cu_3O_{7-\delta}$ coated conductors*, Appl. Phys. Lett. **79**, 2205 (2001);

[16] R.J. Cava, A.W. Hewat, E.A. Hewat, B. Batlogg, M. Marezio, K.M. Rabe, J.J. Krajewski, W.F. Peck Jr. and L.W. Rupp Jr., *Structural anomalies, oxygen ordering and superconductivity in oxygen deficient $Ba_2YCu_3O_x$*, Physica C **165**, 419 (1990);

[17] R. J. Cava, B. Batlogg, C. H. Chen, E. A. Rietman, S. M. Zahurak, and D. Werder, *Single-phase 60-K bulk superconductor in annealed $Ba_2YCu_30_{7-\delta}$ ($0.3< \delta <0.4$) with correlated oxygen vacancies in the Cu-O chains*, Phys. Rev. B **36**, 5719 (1987);

[18] J. M. Tranquada, A. H. Moudden, A. I. Goldman, P. Zolliker, D. E. Cox, G. Shirane, S. K. Sinha, D. Vaknin, t D. C. Johnston, M. S. Alvarez, A. J. Jacobson, J. T. Lewandowski, and J. M. Newsam, *Antiferromagnetism in $YBa_2Cu_30_{6+x}$*, Phys. Rev. B **38**, 2477 (1988);

[19] T. Aytug, M. Paranthaman, H.Y. Zhai, H.M. Christen, S. Sathyamurthy, D.K. Christen and R.E. Ericson, *Single buffer layers of LaMnO3 or $La_{0.7}Sr_{0.3}MnO_3$ for the development of $YBa_2Cu_3O_{7-\delta}$-coated conductors: A comparative study*, J. Mater. Res. **17**, 2193 (2002);

[20] J. M. Huijbregtse, B. Dam, R. C. F. van der Geest, F. C. Klaassen, R. Elberse, J. H. Rector, and R. Griessen, *Natural strong pinning sites in laser-ablated $YBa_2Cu_3O_{7-\delta}$ thin films*, Phys. Rev. B **62**, 1338 (2000);

[21] E. J. Kramer, *Scaling laws for flux pinning in hard superconductors*, J. Appl. Phys. **44**, 1360 (1973);

[22] W. A. Fietz and W. W. Webb, *Hysteresis in Superconducting AlloysTemperature and Field Dependence of Dislocation Pinning in Niobium Alloys*, Phys. Rev. B **178**, 657 (1969);

[23] S. Raedts, J. M. Van Bael, K. Temst, M. Lange, L. Van Look, J.Swerts, V. V. Moshchalkov and Y. Bruynseraede, *Pinning of domain walls and flux lines in a nanostructured ferromagnet/superconductor bilayer*, Physica C **369**, 258 (2002);

[24] L. N. Bulaevskii, E. M. Chudnovsky and P. M. Maley, *Magnetic pinning in superconductorferromagnet multilayers* Appl. Phys. Lett. **76**, 2594 (2000);

Chapter 6

Conclusions and Perspectives

In the present Chapter we give a brief summary of the main results obtained throughout the thesis together with a description of future work that will be pursued. The present thesis is concerned with the elaboration and study of magnetic thin film structures that are suitable for magnetic pinning applications in superconducting $YBa_2Cu_3O_7$ (YBCO) layers. For this purpose several magnetic thin films systems were fabricated, including $La_{0.66}Sr_{0.33}MnO_3$ (LSMO), $Ni_{80}Fe_{20}$ (Py) and Co. Also magnetic, Co and Py, micro,- and nanostructures have been studied with respect to their magnetic pinning potential.

Our studies of epitaxial LSMO thin films consist in the optimization of the growth process and a detailed study of oxygen incorporation effects in epitaxial LSMO layers. With respect to the overall goal of the thesis, we have shown that by controlling the growth mode of LSMO, highly regulated LSMO nano-islands on terraced $SrTiO_3$ (STO) substrates may be produced. Thermal treatment in oxygen atmosphere of the STO substrates induces the formation of atomic terraces. The steps represent nucleation centers for the LSMO grains, so that after deposition, the LSMO film consists of highly regular nano-islands arranged along the substrate step edges. Upon the deposition of the superconducting YBCO on top, two effects were sought after with respect to flux pinning: the first consists in the creation of dislocations in the YBCO film at the sites were the LSMO nano-islands are present, while the second is the creation of a modulated stray magnetic field having the same spatial periodicity as that of the islands.

Divalent ion doped rare earth manganites are known for the strong connection between their structural, magnetic and electric properties. Behind this relation lies the *double exchange* interaction between Mn ions in the Mn^{3+}-O-Mn^{4+} bond, mediated by the simultaneous transfer of an e_g electron from Mn^{3+} to an O^{2-} ion and from O^{2-} to Mn^{4+}. In this picture oxygen plays an important role, as it is directly involved in the double exchange mechanism. Also, it has been show, that if oxygen in found in excess in the LSMO lattice, it produces additional hole doping, *i.e.* produces additional Mn^{4+} valence ions, as well as cationic (La, Sr, Mn) vacancies. From the above considerations it can be seen that oxygen

content plays a crucial role in determining the physical properties of LSMO thin films. In order to evaluate these effects we have performed a systematic study by annealing LSMO thin films in different mixtures of Ar:O_2 flowing gas. High resolution x-ray diffraction measurements were used to quantify the effects of oxygen incorporation on the structure of the films. Using a numerical model we have simulated the ω-scan diffraction data in order to describe the effect of vacancies on the structure of the LSMO films. This last point represents an original approach in the study of excess oxygen incorporation effects. In order to support our assumptions based on the diffraction data, as well as to depict a more accurate physical picture of the processes involved, we have also performed the magnetic characterization of the samples, by means of SQUID measurements. From the chemical composition point of view, XPS analyses were employed to trace the evolution of the Mn and O ion concentration in the different annealing gas mixtures. Electrical measurements were performed using the four probe method and the results were interpreted using the variable range hopping regime. The study regarding oxygen incorporation in LSMO thin films with an emphasis on the effects produced by oxygen excess on the lattice structure, represents an original approach to the subject. Even though oxygenation studies have been performed by other groups, our approach using numerical simulations of ω-scans to determine the structural parameters of the defects, correlation length and mosaicity, has allowed the publication of our work, T. Petrisor, *et al.*, *Oxygen incorporation effects in annealed epitaxial* $La_{1-x}Sr_xMnO_3$ *thin films*, J. Appl. Phys. **109**, 123913 (2011).

Because of the strong correlation between the structural and magnetic properties of LSMO films, as shown in the literature overview presented at the beginning of Chapter 3, these type of films are highly recommended for the study of magnetic pinning experiments in YBCO thin films. For future work, studies regarding the stabilization of several domain configurations (stripe, bubble, check-board) in LSMO thin films are envisioned in a close relationship to the study of the influence of such domains on the magnetic pinning characteristics in YBCO. In order to avoid mixing the effects of classic pinning, due to a surface modulation of LSMO thin films and magnetic pinning, strategies of obtaining flat LSMO film surfaces will be considered. One of the approaches is suggested by the evolution of the LSMO thin film surface at high annealing temperatures. As it could be seen, flat atomic terraces are formed upon annealing at high temperatures. Our studies have shown that terrace formation is independent on the gas mixture used for annealing. Therefore a high temperature, post deposition, *in-situ*, annealing sequence of the LSMO films before the subsequent YBCO deposition will be addressed in a future study.

Magnetic thin films of Co and Permalloy ($Ni_{80}Fe_{20}$) exhibiting parallel stripe domain configuration for magnetic vortex pinning applications have been prepared. The films were deposited on Si (111) single crystal substrates at room temperature. In order to stabilize the stripe domain pattern, we have performed a study of the films with varying thickness.

It is known that perpendicular magnetic anisotropy, the cause behind the stripe domain formation, stabilizes only for thicknesses exceeding a critical value. An interesting aspect of the films is that as the thickness increases so does the periodicity of the magnetic stripes. This is an important aspect, as it allows for the study of the influence of the superconducting properties on the YBCO layer as a function of the stray field modulation periodicity. Films with weak stripe domain structures also present the so-called *rotatable anisotropy*. This type of anisotropy refers to the fact that if an external field is applied in any in-plane direction, the in-plane component of the magnetization will align itself in the direction of the applied field, and will remain as such even after the field is removed. This phenomenon allows for the study of the magnetic flux pinning as a function of the stray magnetic field having different orientation with respect to the current direction in the superconducting layers. The magnetic studies on the films were performed by magnetic force microscopy, MFM and vibrating sample magnetometry, VSM. An interesting case of ferromagnetic film with true perpendicular anisotropy is the case of epitaxial Co thin film grown on $Al_2O_3(0001)$ substrates. A short study was dedicated to this structure, but due to the challenges related to the epitaxial Co film growth on YBCO layers, this subject was analyzed only as a proof of concept. However, demagnetization routines performed in directions parallel and perpendicular to the surface plane have indicated yet another possibility of magnetic modulation. While the parallel demagnetization procedure resulted in a stripe domain configuration having a highly anisotropic orientation, the perpendicular routine produced a more isotropic stripe configuration. The two resulting domain structures are expected to have significantly different effects in terms of magnetic vortex pinning, as the isotropic configuration allows for a greater superconducting flux mobility. A further step in magnetic modulation consists in the micro and nanostructuration of magnetic dots. Optical lithography and ion beam etching were used in the fabrication of magnetic objects at the micron scale. An important part of the work in this field was devoted to the technical aspects of the above techniques and to the optimization of the overall microfabrication process (UV lithography and ion beam etching). As the dimensionality of the magnetic objects is decreased border effects, *i.e.* closure domains, begin to play the leading role in determining the domain configuration. We studied the evolution of the domain structure with decreasing the objects' lateral size. As far as nanostructuturation process is concerned, we have employed an alternative lithographic process, with respect to the "classic" techniques such as e-beam lithography. This consisted in the use of self-assembled polystyrene beads, with diameters on hundreds of nanometers, as a lithographic mask for nanofabrication. After the deposition of the magnetic film and removal of the spheres, triangular magnetic features of a few hundreds of nanometers were defined on the substrate. Depending on their thickness we were able to stabilize a magnetic dipole type structure of these objects, as well as vortex-like configuration of the magnetization.

Even though the subject of metallic magnetic thin films has been the subject of intense scientific research over the last decades, perspectives for future studies arise when one considers using the films for new applications, such as magnetic pinning in high temperature superconductors. In order to produce effective magnetic pinning, magnetic films having strong out-of-plane uniaxial anisotropy represent a viable solution for attaining this goal. Epitaxial Co thin films, produced in the present thesis, have been demonstrated to have the desired out-of-plane anisotropy axis. However, the need of epitaxy in order to stabilize the desired anisotropy makes Co films difficult to incorporate directly in a Co/YBCO bi-layer structure. An additional Al_2O_3 layer grown epitaxially on YBCO is under consideration for future work, in order to promote the epitaxial growth of Co. Other systems such as TbFe or TbCo are also being considered for this purpose, as they show a strong out-of-plane anisotropy, even in the polycrystalline phase, making them suitable candidates for direct integration in FM/YBCO structures.

As concluded in the previous paragraphs, magnetic Py and Co micro-, and nanostructures have been fabricated using the UV lithography, ion beam etching and the self-assembly of polystyrene nanospheres. With respect to the Py microstructures, MFM characterization has shown that upon reducing the lateral size of the dots, effects related to the minimization of the magnetostatic energy, *i.e.* formation of closure domains, become predominant. Circular stripe domains have been demonstrated to form in dots having the diameter below 5 μm. A more detailed magnetic characterization of these system is envisioned for future work, in which we plan to control the specific magnetic remanent configuration of the dots by inducing different magnetic histories. The different magnetic states of the microstructures are expected to produce different magnetic pinning behaviors in the YBCO layers, such as pinning of giant vortices, a sum of individual vortices, at each microstructure site. The effects of the double periodicity (spatial and magnetic) will also constitute the subject of further research. As far as magnetic nanostructures are concerned micromagnetic simulations will be employed in order to construct a magnetic phase diagram in order to foresee the magnetic configuration, vortex or single domain, of the as-obtained triangular structures with respect to their physical dimensions, lateral size and height. This would enable us to prepare the desired magnetic configuration and to integrate it in FM/SC structures for magnetic pinning studies. Because of the specific hexagonal structure of the nanosphere assembly, hexagonal arrays of magnetic structures were produced. This fortunate physical picture enables the use of the nanostructured hexagonal arrays to study commensurability effects between the dot lattice and the vortex lattice, since the latter also stabilizes in a hexagonal lattice. Another very important aspect for future research will consist in the fabrication of anitidot (hole) structures in the magnetic film and the use of the produced arrays for pinning studies. The antidot structures will be prepared using an additional intermediate reactive ion etching process. Reactive ion etching will act as to reduce the diameter of the nanospheres, so that

after the subsequent film deposition and removal of the spheres, a regular array of holes will exist within the film. From the magnetic pinning of SC vortices perspective, the presence of holes in a magnetic film is more advantageous than a continuous film. This is so because the at large magnetic fields, the magnetization of the film saturates, which leads to the disappearance of any field gradients in the film that could act magnetic pinning sites. On the other hand, the presence of holes in the film, ensures the existence of magnetic field gradients around the hole edges even at saturation. Therefore, creation of hole arrays in magnetic films with strong perpendicular anisotropy, TbFe, TbCo, represent in our opinion the research path to follow for viable magnetic pinning applications.

The last chapter of the thesis is concerned with the actual integration of the FM structures presented in the previous chapters in bi-layered structures with YBCO superconducting films. A brief account is given on the preparation of epitaxial YBCO films deposited by pulsed layer deposition on STO(001) substrates. Two categories of structures are analyzed. First, we present the LSMO/YBCO structures, were the ferromagnetic film represents the bottom layer while YBCO is epitaxially grown on top of it. High resolution x-ray diffraction measurements were performed in order to establish the influence of the modulated LSMO surface on the structural properties of the superconducting films. The morphological evaluation of the samples was performed by means of AFM. The superconducting properties of the structures were analyzed using VSM measurements at low temperatures. Our studies reveal that a two component pinning mechanism is present in the YBCO films: a classic mechanism, due to the defects created in the superconducting film by the particular morphology of the LSMO layers, and a magnetic pinning component arising from the stray field gradients produced by the LSMO nano-islands. To our knowledge the use of LSMO surface decoration in ordered to produce both classic and magnetic pinning in superconducting YBCO films, represents an original approach that will constitute the subject of a future publication. As far as the metallic films are concerned, Py layers having stripe domain configuration were deposited on top of the YBCO films. Because of the fact that the electric transport properties were determined performing $I-V$ measurements at different temperatures, lithography was employed in order to define structures having a precise geometry. The results of the $I-V$ characteristics and critical current density, J_c , measurements for different orientation of the stripes are given. A 20% increase in J_c was recorded for the parallel configuration of the magnetic stripes to the current in the superconductor, with respect to the perpendicular configuration, confirming thus the pinning potential of weak stripe domains for magnetic SC vortex pinning. Even though the use of Py thin films exhibiting magnetic stripe domains for magnetic pinning has been already reported for low temperature superconductors, no paper exists, to our knowledge, on the pinning effects exerted on YBCO films.

Acknowledgments

Although a Ph. D. thesis is by definition a subjective endeavor, a great number of people have brought their contribution to its completion. The present Section is dedicated to acknowledging their support.

First, I would like to start by thanking my supervisors. To Prof. Dr. Ionel Chicinaş I am grateful for accepting me as his student and for the valuable support throughout the thesis. I would also like to thank Dr. Coriolan Tiuşan for his help, discussions and scientific optimism. I am deeply grateful for giving me the opportunity of elaborating a thesis in "cotutelle" between the Technical University of Cluj-Napoca and "Henri Poincaré" University of Nancy, France.

This thesis could not have been possible without the support of my father, Prof. Dr. Traian Petrisor, who has founded the Materials Science Laboratory. I would like to express my gratitude towards him for both his scientific and personal support.

I would also like to express my gratitude towards the jury members who have read and helped improve the quality of the manuscript: Prof. Dr. Nathalie Viart, Prof. Dr. Michel Hehn, Dr. Viorel Sandu, Prof. Dr. Adelina Carmen Ianculescu and Dr. Gilles Gaudin.

The work presented in the thesis has been performed in several laboratories. First and fore most I would like to thank the members of the Materials Science Laboratory of the Technical University of Cluj-Napoca. My thoughts of deep appreciation are directed towards Prof. Dr. Lelia Ciontea, to whom I would also like to thank for her scientific enthusiasm. Also, I would like to thank Conf. Dr. Tania Ristoiu and my colleagues at MSL: Bianca, Amalia, Mircea and Robert, to whom I am grateful for creating a wonderful working environment, in which the hardships of the thesis were overcome more easily. Also I am thankful to Razvan for his constant technical support and for his friendship. I am indebted to the members of the Laboratoire de Physique des Matériaux /Institut "Jean Lamour", Nancy, for welcoming me. In particular I would like to thank Dr. Christine Bellouard for her unconditional help and to Prof. Dr. Michel Hehn for the helpful discussions.

I am very grateful for the wonderful experiences at the ENEA Laboratories, Frascati, Italy to the members of the Superconductivity group. A very special thank you is dedicated to their great "family": Giuseppe, Angelo, Alessandro, Valentina, Antonella, Andrea, Achille and Fabio. For his support and for teaching me a lesson on the meaning of scientific

collaboration, I would like to thank Dr. Alexandre Boulle at the "Université de Limoges", France. The support with the magnetic measurements of the superconductivity group of the INFM, Bucuresti, was very valuable within the context of the thesis. For this I am grateful to: Dr. L. Miu, Dr. V. Sandu, Dr. S. Popa and I. Ivan. The collaboration with the group of Prof. Dr.S. Astilean at the "Babes-Bolyai" University was a very fruitful one. For this I would like to thank Dr. V. Canpean. For helpful discussions I am also grateful to Prof. Dr. M. Coldea and Dr. I. G. Deac, to whom I would also like to thank for the collaboration on the electrical and magnetic characterization of some of the samples. The XPS measurements were performed at the INCD-TIM institute of Cluj-Napoca for which I would like to thank, Dr. O. Pana. I would also like to thank the group of Dr. L. Giurgiu, Dr. A. Popa, Dr. O. Raita and Dr. D. Toloman for the FMR measurements performed.

A special thank you is dedicated to my friend and colleague Mihai for all the good times that we have spent in our professional and personal "coming of age".

For their constant support and patience, I would like to thank my family, my mother, my wife, Cristina, and my little daughter, Maria.

Appendix A

Vortex state and dynamics

Since the present thesis is mainly dedicated to the phenomena at the superconductor-ferromagnet interface namely magnetic pinning of the superconducting vortices and related phenomena, the aim of the present chapter is to introduce the basic concepts of type II superconductivity and of the vortex state and dynamics in high temperature superconductors. The concepts introduced in this chapter represent the theoretical basis for the understanding and interpretation of the magnetic pinning phenomenon in hybrid interface systems between high temperature superconductors and ferromagnetic structures.

A.1 Vortex state

A.1.1 Ginzburg-Landau equations

The phenomenological description of superconductivity is given by the Ginzburg-Landau free-energy functional:

$$g_s = g_n + \int_V \left[\alpha(T) |\Psi|^2 + \frac{1}{2}\beta(T) |\Psi|^4 + \sum_{j=1}^{3} \frac{1}{2m_j} |(-i\hbar\nabla - 2e\mathbf{A})\Psi|^2 \right] dv + \int_V \frac{1}{2\mu_0}\mathbf{B}^2 dv, \tag{A.1}$$

where $\Psi(\mathbf{r})$ is the order parameter, $\mathbf{A}$ is the vector potential, $\mathbf{B} = \nabla \times \mathbf{A}$ is the magnetic field and g_n is the Gibbs free energy of the normal state. The Ginzburg-Landau parameter $\alpha(T) = -\alpha(0)(1 - T/T_c)$ is temperature dependent and changes sign at the transition temperature, while β is taken to be constant in temperature. The m_j, j=1,2,3, terms are the effective masses along the main axes of the crystal. In the absence of a magnetic field the solution of equation A.1 is $|\Psi|^2 = |\alpha|/\beta$. For $T < T_c$ the difference between the energy of the superconducting and normal states is given by the condensation energy $-B_c^2/2\mu_0 = -\alpha^2/2\beta$, where B_c is the thermodynamic critical field. B_c is the smallest

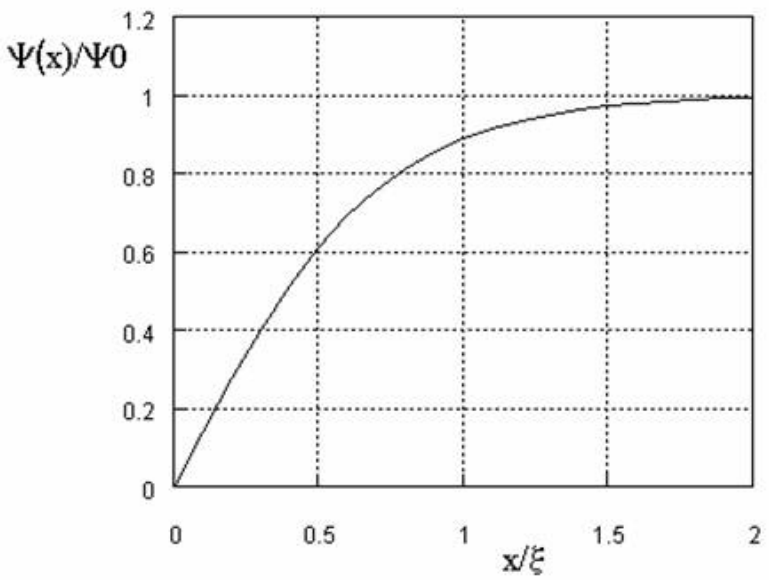

Figure A.1: Superconducting order parameter, Ψ, dependence on the distance x from the superconductor surface, in a superficial layer of width ξ.

magnetic field necessary to destroy the superconducting state. From the minimum condition of the functional A.1, with respect to the order parameter $\Psi(\mathbf{r}) = |\Psi| \exp(i\phi)$ and the vector potential $\mathbf{A}$, result the equations:

$$\xi^2 \left(\nabla + \frac{2\pi i}{\Phi_0} \mathbf{A} \right)^2 \Psi + \Psi - \frac{|\Psi|^2}{|\Psi_0|^2} \Psi = 0 \tag{A.2}$$

$$\lambda^2 \frac{|\Psi_0|^2}{|\Psi|^2} \nabla \times \nabla \times \mathbf{A} + \mathbf{A} = -\frac{\hbar}{2e} \nabla \phi, \tag{A.3}$$

The relation A.2 and A.3 are known as the Ginsburg-Landau (GL) equations and determine the spatial variation of $\Psi(\mathbf{r})$ and $\mathbf{A}$. In the absence of the magnetic field, the solution of the first GL equation is

$$\Psi = \Psi_0 \tanh \frac{x}{\sqrt{2}\xi}. \tag{A.4}$$

The solution of A.4 is presented in Figure A.1. As it can be seen, for $x > \xi$ the order parameter is Ψ_0, while at the normal-superconducting interface ($x = 0$) $\Psi(0) = 0$. Thus, the length $\xi(T)$ from the first GL equation determines the distance over which the order parameter can vary and is called the coherence length. In the terms of BCS microscopic theory ξ can be interpreted as the distance between two electrons of the Cooper pair within the highly correlated superconducting electrons system.

As it will be shown in the Section A.1.3, the length $\lambda(T)$ form the second GL equation

determines the scale of variation of the magnetic field inside the superconductor. This length is known as London penetration depth or penetration depth. In terms of GL parameters these lengths are given by

$$\xi^2(T) = \frac{\hbar^2}{2m\left|\alpha\left(T\right)\right|} = \xi^2\left(0\right)\frac{1}{1-T/T_c}, \tag{A.5}$$

and

$$\lambda^2\left(T\right) = \frac{m}{2\mu_0 e^2|\Psi_0|^2} = \frac{m}{2\mu_0 e^2}\frac{\beta}{|\alpha|} = \lambda^2\left(0\right)\frac{1}{1-T/T_c}$$

.

A.1.2 Fluxoid quantization

One of the most important result of the GL theory is the explanation of the magnetic flux quantization inside the superconductor. The integration of the second GL equation A.3 around a closed contour gives

$$\frac{m}{e^2}\oint\frac{\mu_0\mathbf{J}}{|\Psi|^2}d\mathbf{l} + \oint\mathbf{A}d\mathbf{l} = \frac{\hbar}{2e}\oint\nabla\varphi\, d\mathbf{l} \tag{A.6}$$

For the order parameter to be single valued the line integral of the phase φ around a closed contour must be a multiple of 2π so that equation A.6 becomes

$$\frac{m}{e^2}\oint\frac{\mu_0\mathbf{J}}{|\Psi|^2}d\mathbf{l} + \Phi = n\Phi_0, \tag{A.7}$$

where $\Phi_0 = h/2e$ and $\Phi = \oint\mathbf{A}d\mathbf{l}$ is the magnetic flux through the closed contour. The first member of the left part of A.7 represents the magnetic flux created by the superconducting current. Thus, according to A.7 the total magnetic flux within a superconductor is quantized and is a multiple of the flux quanta $\Phi_0 = h/2e \ = 2.07\times10^{-15}\,Wb$.

A.1.3 London equations

From the electrodynamics point of view the superconducting state is described by the London equations:

$$\mathbf{E} = \mu_0\lambda^2\frac{d\mathbf{J}}{dT}, \tag{A.8}$$

$$\mathbf{B} = -\mu_0\lambda^2\nabla\times\mathbf{J}, \tag{A.9}$$

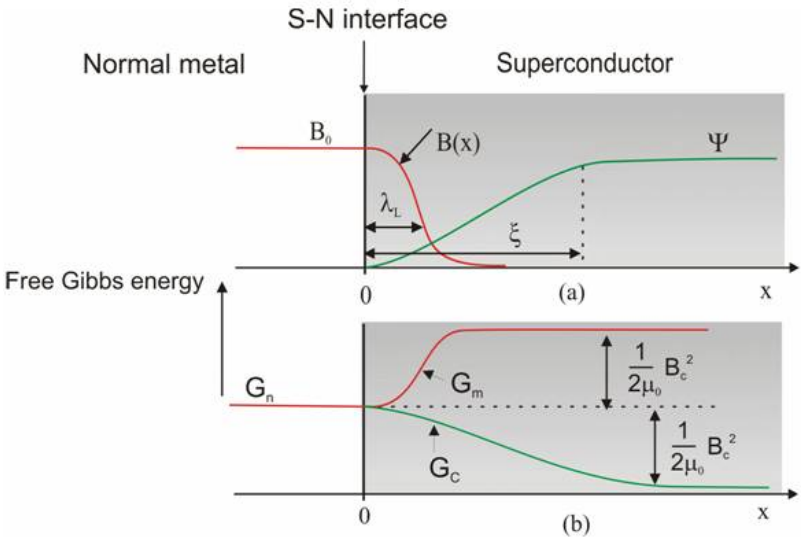

Figure A.2: The variation of the magnetic field and coherence length at the $N-S$ interface (a) and the contributions to the Gibbs free energy of the superconducting region (b).

where $\mathbf{J}$ is the superconducting current density. The first London equation describes the infinite electric conductivity, $\sigma \to \infty$, of a superconductor and is similar to Ohm's law for an ideal conductor, where drag force acting on electron is zero. The second equation describes the Meissner effect and is a consequence of the second GL equation for the case of a weak magnetic field for which the spatial gradient of the order parameter can be neglected and, as a result, $\nabla\varphi = 0$. Considering Ampère's law, $\nabla \times \mathbf{B} = \mu_0\mathbf{J}$, the Equation A.8 and A.9 can be written as

$$\nabla^2\mathbf{B} = \frac{\mathbf{B}}{\lambda_L^2}, \tag{A.10}$$

and

$$\nabla^2\mathbf{J} = \frac{\mathbf{J}}{\lambda_L^2}. \tag{A.11}$$

In Cartesian coordinates these two equations correspond to the Helmholtz equations. According to the equation A.10 the magnetic field decays exponentially inside the superconductor, $B = B_0 \exp(-x/\lambda)$. The magnetic field penetrates the superconducting only in a layer closed to the surface of thickness λ, and therefore λ is also called London penetration depth. Inside the superconductor ($x >> \lambda$) the magnetic field is zero, $B = 0$, in agreement with the Meissner effect. The variation of the coherence length ξ and the exponential decay of the magnetic field are presented in Figure A.2 for a normal-superconductor interface. The energy of the normal-superconducting interface has two contributions: the magnetic and the condensation energy, as it is shown in Fig.A.2b. The excess of free energy of the superconducting region with respect to normal one, is the difference between the condensation

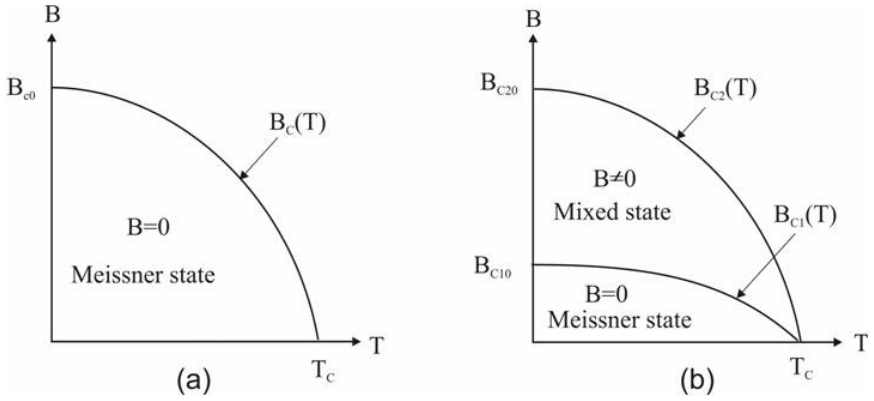

Figure A.3: The B-T phase diagram for (a) Type I and (b) Type II superconductors.

energy and the magnetic energy. In the case of a rectangular shape approximation for ξ and λ (dashed curves in the Fig.A.2b) the interface energy is

$$\sigma \approx \frac{1}{2}\mu_0 H_c^2 \left(\xi - \lambda\right), \tag{A.12}$$

in a thick layer closed to the surface and is zero inside superconductors.

A.1.4 Type I and Type II superconductors

If $\xi > \lambda$ the surface energy is positive, $\sigma > 0$, so that normal-superconductor (N-S) interface is not in equilibrium. In this case, the whole superconductor will be either in the superconducting or in the normal state. Such a material is called a type I superconductor. For applied fields less than $H_c\left(T\right)$ a type I superconductor will completely expel the magnetic flux and hence will find itself in the Meisner state, $B = 0$, exhibiting the properties of perfect diamagnetism, $\chi = -1$. The B-T phase diagram of Type I superconductors is shown in Fig. A.3a. On the contrary, when $\xi < \lambda$ the surface energy is negative, $\sigma < 0$, and hence, the N-S interface is in equilibrium. Moreover, in order to minimize its energy, within the superconductor a great number of S-N interfaces will form, and as a result, the superconductor will have a domain structure. In this case the materials are known as Type II superconductors. As illustrated by the phase diagram (Fig. A.3b) for a Type II superconductor there are two critical fields H_{c1} and H_{c2}. For applied field strengths less than H_{c1} the superconductor exhibits the Meissner effect, while for the applied fields higher than H_{c2} the superconductivity is destroyed and the material becomes normal. For intermediate field values, $H_{c1} < H < H_{c2}$, the superconductor is in a mixed or, vortex, state. In the mixed state, the superconductor no longer exhibits the properties of perfect diamagnetism, so that a finite amount of flux penetrates the volume of the superconductor. It was experimentally demonstrated that in the mixed state the flux penetrates the type II superconductor in a

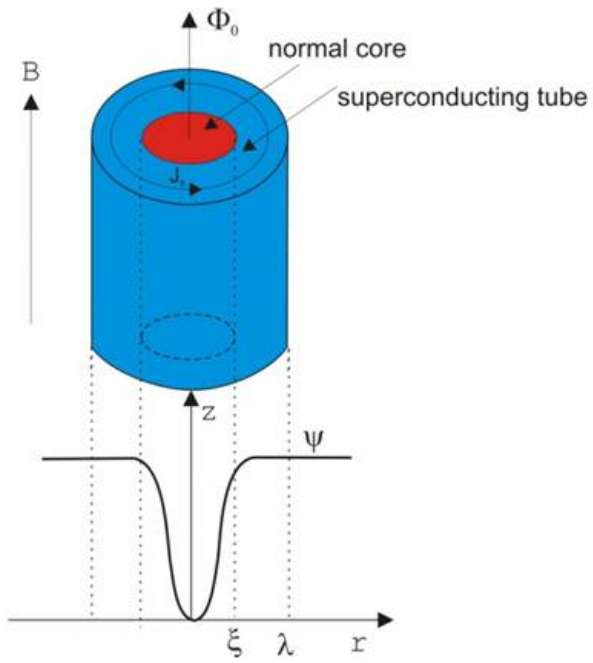

Figure A.4: The model of an Abrikosov vortex.

discrete array of entities known as *vortices*. The vortices are a direct consequence of the fluxoid quantization in the superconducting state, each vortex carrying a single flux quanta $\Phi_0 = h/2e$.

A.1.5 The Abrikosov vortex

The true explanation of the partial flux penetration in type II superconductors was given by Abrikosov [1], who demonstrated that the GL equation has a periodic solution for $\kappa = \xi/\lambda \ > 1/\sqrt{2}$. Abrikosov interpreted this solution as a lattice of parallel flux line, now also called flux tube, fluxons or Abrikosov vortex line, each vortex line carrying a quantum of magnetic flux $\Phi_0 = h/2e = 2,07 \times 10^{-15}\ Wb$. At the center of a flux line the superconducting order parameter $\Psi(r)$ vanishes. The line $\Psi(r) = 0$ is surrounded by abnormal tube of radius called the normal vortex core. In the closed superconducting region of the vortex core a superconducting current, $\mathbf{J}(\mathbf{r})$, circulates, which generates the magnetic field of the flux line. Actually, the superconducting currents circulate only in a superconducting tube of radius λ. The model of an Abrikosov vortex is presented in Figure A.4. The distribution of the magnetic field in the superconducting region of the vortex line is given by the Helmholtz equation A.10. Taking into account the cylindrical symmetry of the vortex line and the boundary condition $B(r) = 0$ when $r \to \infty$, the flux density is given by

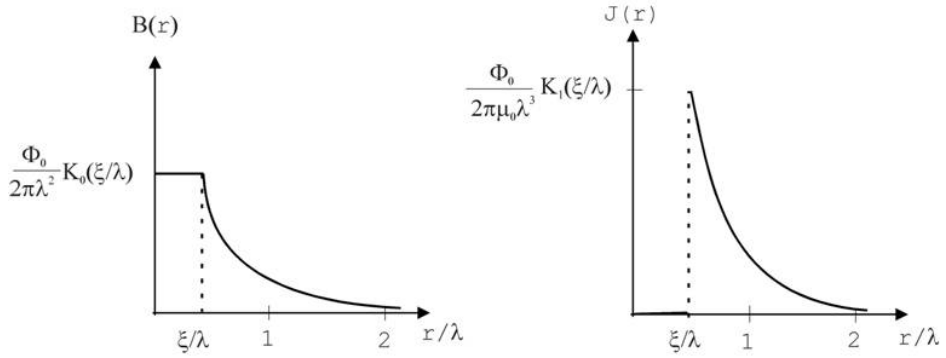

Figure A.5: The magnetic flux and the superconducting current density for a single vortex as a function of radius from the center of the vortex core.

$$B_z(r) = \begin{cases} \frac{\Phi_0}{2\pi\lambda^2} K_0\left(\frac{r}{\lambda}\right) & r \geq \xi \\ \frac{\Phi_0}{2\pi\lambda^2} K_0\left(\frac{\xi}{\lambda}\right) & r < \xi \end{cases} \tag{A.13}$$

where the K_m is the m^{th} order modified Bessel function. The superconducting current density associated with this flux density can be deduced from Ampère's law ($\nabla \times \mathbf{B} = \mu_0 \mathbf{J}_s$):

$$J_z(r) = \begin{cases} \frac{\Phi_0}{2\pi\mu_0\lambda^3} K_1\left(\frac{r}{\lambda}\right) & r \geq \xi \\ 0 & r < \xi; \end{cases} \tag{A.14}$$

Figure A.5 shows the exponential decay of both the flux and the current density in the superconducting region of the vortex tube. In the normal region of the vortex line the flux is constant, $B\,(r < \xi) = (\Phi_0/2\pi\lambda^2)K\,(\xi/\lambda\,)$ and the current density is zero, $J\,(r < \xi) = 0$.

A.1.6 The vortex energy

The total electromagnetic energy associated with the flux line has two contributions: the energy of the normal core, W_n, and the energy of the superconducting region, W_s,

$$W_n = \frac{1}{2\mu_0} \int_{V_n} \mathbf{B}^2 \, dv \tag{A.15}$$

and

$$W_s = \frac{1}{2\mu_0} \int_{V_s} \mathbf{B}^2 \, dv + \frac{1}{2} \int_{V_s} \mu_0 \lambda^2 \mathbf{J}_s^2 dv, \tag{A.16}$$

where V_n and V_s is the volume of the normal core and of the superconducting part of the vortex, respectively. For a type II superconductor, $\lambda >> \xi$, so the contribution of the normal core can be neglected. The integration of relation A.16 leads directly to evaluating the energy

per unit length of vortex as

$$w = \frac{\Phi_0^2}{4\pi\mu_0\lambda^2} K_0\left(\frac{\xi}{\lambda}\right), \tag{A.17}$$

where K_0 is zeroth order Bessel function.

A.1.7 The critical fields

For a type I superconductor, at a given temperature below T_c, the transition from superconducting to normal state at B_c is a first order one, contrary to the type II superconductor which undergoes a second order phase transition at B_{c2}. For a second order phase transition close to B_{c2}, the order parameter is small and the first GL equation becomes:

$$\frac{1}{2m}(i\hbar\nabla + 2e\mathbf{A})^2\Psi = -\alpha\Psi, \tag{A.18}$$

where the second order term in Ψ was neglected. This equation describes the motion of a charged particle ($q = 2e$) in a magnetic field. The eigenvalues of the Schrödinger equation above are

$$E_n = -\alpha_n = \frac{m{v_z}^2}{2} + \left(n + \frac{1}{2}\right)\hbar\omega \tag{A.19}$$

where v_z is the velocity of the particle along the direction of the magnetic field and $\omega = 2eB/m$ is the cyclotron frequency. The lowest energy level ($v_z = 0$ and $n = 0$) is

$$E_0 = \frac{1}{2}\hbar\omega = -\alpha, \tag{A.20}$$

which corresponds to the maximum magnetic field,

$$B_{c2} = \frac{m\alpha}{e\hbar} = \frac{\Phi_0}{2\pi\xi^2} \tag{A.21}$$

Thus, the GL Equation A.18 has a nonzero solution for Ψ and hence the appearance of the superconducting state is possible only for $B < B_{c2}$.

The lower critical field B_{c1} corresponds to the thermodynamic limit above which it is energetically favorable for vortices to penetrate the superconductor. The Gibbs free energy which corresponds to the entry on n vortices per unit volume is

$$\Delta g = nw - \mathbf{BH} = B\left(\frac{w}{\Phi_0} - H\right), \tag{A.22}$$

where w is the vortex energy per unit length and $n = B/\Phi_0$. The vortex state is stable if $\Delta g \leq 0$. This condition is satisfied if the applied field $H > H_{c1} = \frac{w}{\Phi_0}$. Using A.17 for the

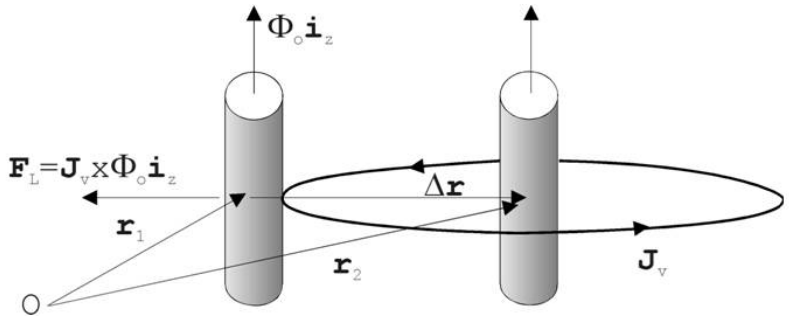

Figure A.6: Two vortices placed in r_1 and r_2, respectively. The magnetic field is along z-axis.

vortex energy per unit length, one obtains

$$B_{c1} = \frac{\Phi_0}{4\pi\lambda^2} \ln \frac{\lambda}{\xi}. \tag{A.23}$$

A.2 Vortex interaction and dynamics

A.2.1 Vortex interaction

The total energy of a two vortices, Figure A.6, separated by the distance $\Delta r = r_2 - r_1$, is a sum of the individual energies of the vortices plus an interaction term:

$$w' = 2\frac{\Phi_0^2}{4\pi\mu_0\lambda^2} K_0\left(\frac{\xi}{\lambda}\right) + \frac{\Phi_0^2}{2\pi\mu_0\lambda^2} K_0\left(\frac{r_2 - r_1}{\lambda}\right) \tag{A.24}$$

where the last term is the interaction energy between the vortices and is equal to Φ_0 multiplied by the field $B(r_2 - r_1)$ created by the vortex placed at r_2 and "felt" by the vortex located at r_1. Because $K_0(x) > 0$, this energy is positive and, as a consequence, the vortices repeal each other. The force of the vortex 1 on the vortex 2 is:

$$\mathbf{f}_{12} = -\frac{\partial w'}{\partial l} = \frac{\Phi_0^2}{2\pi\mu_0\lambda^3} K_1\left(\frac{l}{\lambda}\right) \mathbf{i}_l,$$

where $l = r_2 - r_1$ and $i_l = l/|l|$ is the unit vector of direction l . Considering that the current of the vortex 1 at a distance $l = r_2 - r_1$ is given by A.14,

$$\mathbf{J}_{12} = \frac{\Phi_0}{2\pi\mu_0\lambda^3} K_1\left(\frac{l}{\lambda}\right) \mathbf{i}_\Phi \tag{A.25}$$

the force between two vortices may be written as:

$$\mathbf{f}_{12} = \mathbf{J}_{12} \times \Phi_0 \mathbf{i}_z, \tag{A.26}$$

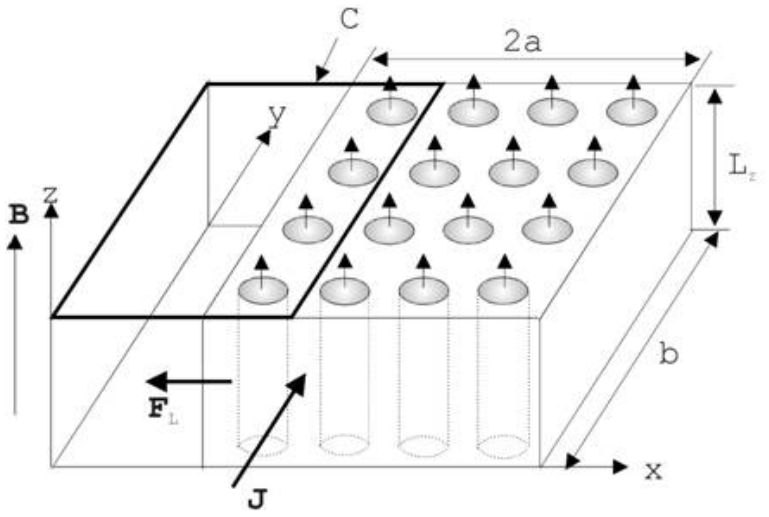

Figure A.7: The contour (C) of integration used for Fraday's law.

where $\mathbf{i}_z = \mathbf{i}_r \times \mathbf{i}_\Phi$ is the unit vector of the z-axis. This force is a Lorentz like force. It is important to note that expression A.26 is a general one and is valid for any current flowing in the superconductor. If the vortices have opposite vorticity , for example vortex 1 has the vorticity 1, while the vortex 2 has -1, the interaction force is

$$f_{12} = -\frac{\Phi_0^2}{2\pi\mu_0\lambda^3} K_1\left(\frac{l}{\lambda}\right) i_l \tag{A.27}$$

Thus, the vortex-antivortex interaction is an attractive one.

A.2.2 Flux flow

The vortex lattice is in equilibrium until the only circulating currents in the superconductor are the vortex currents. If in the superconductor a current, $\mathbf{J}$, is injected by external sources, each vortex is subjected to a Lorentz force per unit length $\mathbf{f}_L = \mathbf{J} \times \Phi_0 \mathbf{i}_z$, as it is shown Figure A.7. The Lorentz force due to the current $\mathbf{J}$ will cause the vortices to move with a velocity u_x in the x-direction (perpendicular to the current). The variation of the flux in the contour C is the total number of vortices which enter in the contour in a time Δt multiplied by Φ_0:

$$\Delta\Phi = \Phi_0 n_v u_x b \Delta t \tag{A.28}$$

where n_v is the vortex density. Faraday's law states that the voltage across the contour is:

$$U = \frac{d\Phi}{dt} = \Phi_0 n_v u_x b. \tag{A.29}$$

It is important to be noted that the electric field $\mathbf{E} = \mathbf{B} \times \mathbf{v}$ is parallel with the current density $\mathbf{J}$. Because the current has the same direction as the voltage difference, there must be power dissipated equal to UI,

$$P = UI = I\Phi_0 n_v u_x b \tag{A.30}$$

Since the flux line motion dissipates energy, it can be described in terms of viscosity. The vortex motion is assumed to be damped by a force proportional to the velocity, $f_\eta = \eta u_x$, where η is the viscosity. The drift velocity of the vortex line can be obtained by equating the Lorentz force to the friction force, $f_L = f_\eta$, resulting

$$u_x = \frac{J\varphi_0}{\eta}. \tag{A.31}$$

Combining equations A.29, A.31 and taking into account that $E = U/b$, results a linear relation between the electric field and the current density, similar to the Ohm's law:

$$E = \rho_{ff} J, \tag{A.32}$$

where,

$$\rho_{ff} = \frac{B\Phi_0}{\eta} \tag{A.33}$$

is called *flux flow* resistivity. The microscopic calculation of the viscosity gives the value [3]

$$\eta = \frac{\Phi_0^2 \sigma_n}{2\pi\xi^2}, \tag{A.34}$$

σ_n is the electrical conductivity in the normal state. Using this relation, the flux flow resistivity can be written as

$$\rho_{ff} = \frac{B}{B_{c2}}\rho_0 \tag{A.35}$$

A.2.3 Vortex pinning and critical currents

Externally driven current causes the vortices to move and, as a result, energy dissipation in the superconductor. From a practical point of view, in order to transport high current densities without any dissipation, it is necessary to prevent vortex motion. The prevention of the vortex motion is known as *pinning* the vortices. The conventional way to pin a vortex is to take advantage of the force exerted on the vortex at the boundary between a superconductor and normal region Figure A.8. The presence of the vortex core in the normal

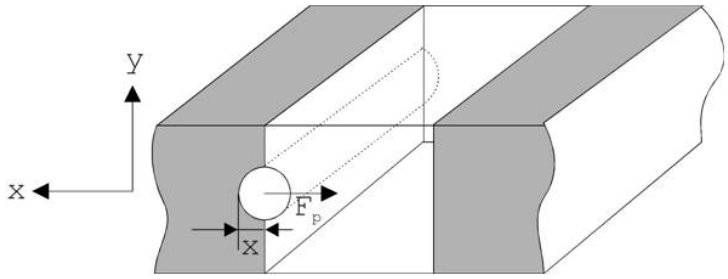

Figure A.8: The vortex partially in the normal region.

region raises the free energy of the superconductor with

$$\Delta G = \frac{1}{4\mu_0} B_c^2 \pi \xi L_z x, \tag{A.36}$$

where L_z is the length of the vortex and B_c is the thermodynamic critical field, $B_c = \Phi_0/2\sqrt{2}\pi\xi\lambda$. The force on the core due to the normal boundaries is

$$F_p = -\frac{\partial G}{\partial x} = -\frac{1}{4\mu_0} B_c^2 \pi \xi L_z \tag{A.37}$$

This force is in the negative x-direction, so as it acts to pull the vortex into the normal region. In an energetic picture Figure A.9, the system tends to lower its energy by having the vortex core in the normal region, rather than creating a normal core in the superconducting region. The pinning force on the unit length of the vortex can be written as

$$|f_p| = \frac{\Phi_0^2}{32\pi\mu_0\lambda^2\xi} \tag{A.38}$$

Usually, in a superconductor normal regions, having a low order parameter, are created around defects such as: grain boundaries, dislocations, twins, off-stoichiometric regions, etc. If the lateral extent of the defects is of order of coherence length ξ they represent effective *pinning centers* for the vortices. Since the Abrikosov lattice is rigid, if one vortex is pinned, it tends to pin other vortices from its close vicinity. When an externally current passes through the vortex lattice, the total force per unit length, acting on a vortex, is

$$\mathbf{f}_{tot} = \mathbf{f}_p + \mathbf{f}_L + \mathbf{f}_\eta \tag{A.39}$$

In the case presented in Figure A.8 the forces and the vortex velocity are in the x-direction, so that

$$f_{tot} = J\Phi_0 - f_p - \eta u_x \tag{A.40}$$

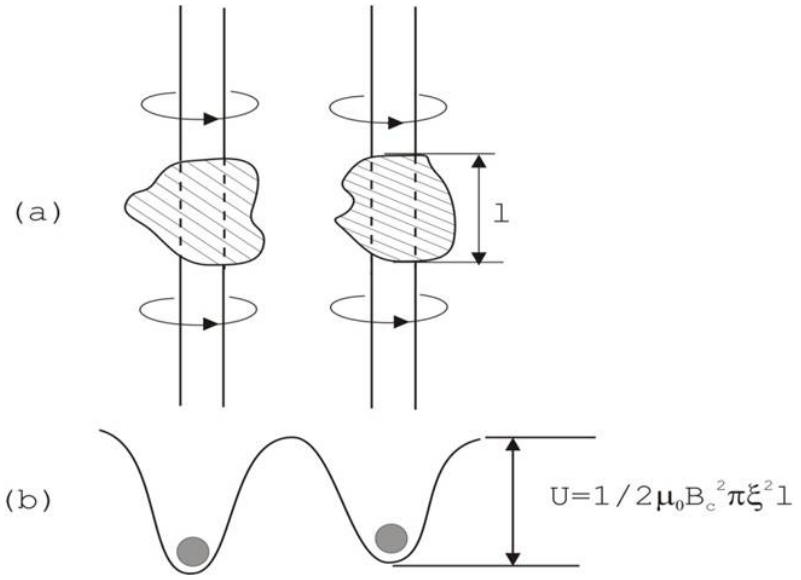

Figure A.9: From energetic point of view the vortex in vortex-normal system (a) can be assimilated with a vortex in the potential well of finite height $1/2\mu_0\, B_c^2 \pi \xi^2 l$ (b).

In the steady state, $f_{tot} = 0$, so that the steady-state velocity is given by

$$u_x = \frac{1}{\eta}\left(J\Phi_0 - f_p\right) \tag{A.41}$$

The velocity is zero for $f_L = f_p$. The current density J_c for which $f_L = f_p$ is called critical current density and is given by the expression

$$J_c\left(T\right) = \frac{f_p}{\Phi_0} \tag{A.42}$$

For $J < J_c$, the vortex velocity and the voltage drop are zero. On the other hand, for $J > J_c$ the Lorentz force becomes greater than the pinning force, $f_L > f_p$ and the vortex moves with a steady-state velocity given by A.41 creating a voltage,

$$U = \rho_{ff}\left(J - J_{c0}\right) l \tag{A.43}$$

where l is the length of the sample in the direction of the current flow. Thus, for $J < J_c$, the transportation of the current takes place without energy dissipation, while for $J > J_c$ there is dissipation. In other words J_c is the maximum critical current density which can be injected trough the supraconductor without dissipation. For practical applications it is important to have a type II superconductor with a high critical current density, J_c. To reach this goal the only way is to engineer the pinning center density. However, the maximum

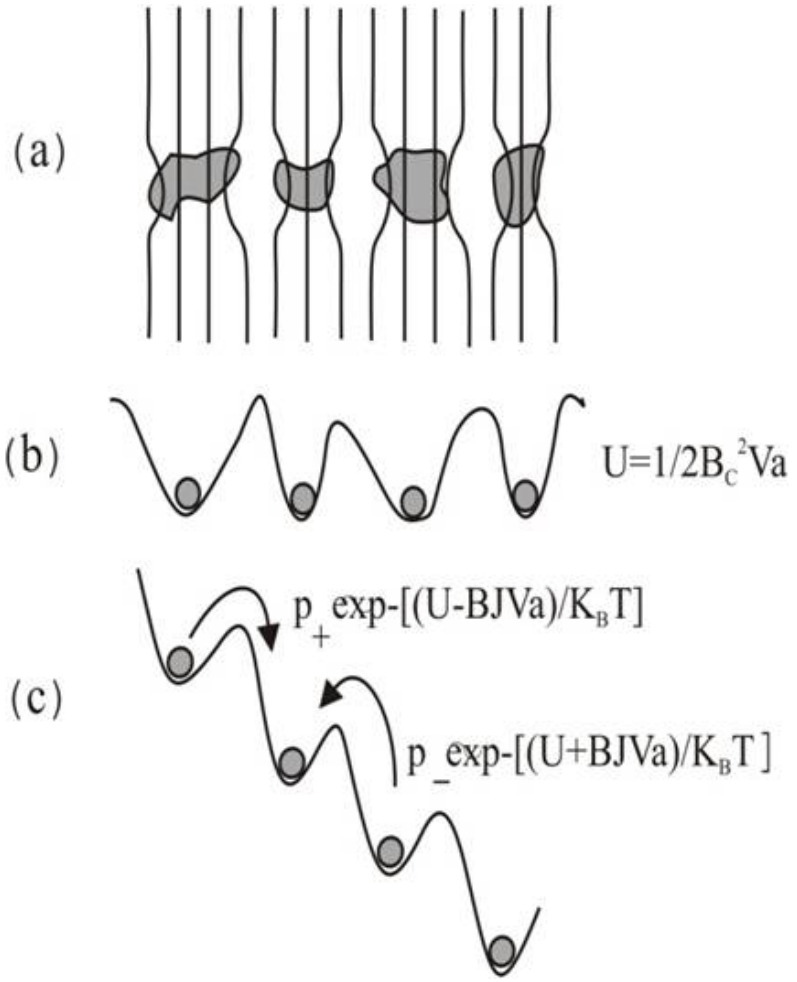

Figure A.10: Schematic representation of the vortex bundle jumping over barriers between to adjacent pinning centers. (a) Zero driving force. (b) Driving force due to the external current favoring the jumps a "downhill" direction.

critical current density can not be greater than the GL depairing critical current

$$J_c^{dep} = \frac{\Phi_0}{3\sqrt{3}\pi\mu_0\lambda^2\xi} \tag{A.44}$$

which is an intrinsic characteristic of a superconductor related to the energy of the Cooper pair. For $J > J_c^{dep}$, the kinetic energy is higher than the interaction energy between electrons from the Cooper pair, so that the pair is broken.

A.2.4 Thermally activated flux flow. Flux creep

At finite temperatures, due to the thermal energy, the vortex line can move even for $f_L < f_p$, because there is a finite probability that the flux lines overcome the pinning energy barriers. Thus, even for $J < J_c(0) = J_{c0}$ the vortex motion takes place and a resistive voltage will be detected in the sample. This behavior is known as *thermal flux creep*, or

simply *flux creep*. For the first time this behavior was measured experimentally for the first time by Kim *et al.* [4]. They investigated the persistent currents induced in a tubular sample by measuring the magnetic field created by these currents and they observed a logarithmic decay of the magnetic field.

In order to explain the logarithmic decay of the superconducting currents, Anderson [5] developed a flux flow model based on the thermal activation of vortices, Figure A.10. As it was shown by Beasley *et al.* [6], due to the electromagnetic interaction between the flux lines, any pinning center contains more than one vortex. Therefore, this model assumes that flux creep occurs by bundles of flux lines, jumping between adjacent pinning centers. In the presence of an external current J, the barrier is reduced by a quantity $BJVa$, where V is the volume of the vortex bundle and a is the distance over which the vortex bundle moves. The "wash-board" model (Fig.A.10c) for the potential barrier leads to a net jump rate in the direction of the Lorentz force given by the equation

$$\nu = \nu_+ - \nu_- = \nu_0 \exp\left(-\frac{\mathrm{U}}{\mathrm{k_B}T}\right) \sinh\left(\frac{JU}{J_{c0}k_BT}\right), \tag{A.45}$$

where ν_0 is the frequency of the flux line jumps, which is in the range 10^5-10^{11} sec^{-1}. The flux bundle will move with the velocity

$$u = \nu d = \nu_0 d \exp\left(-\frac{U}{k_BT}\right) \sinh\left(\frac{JU}{J_{c0}k_BT}\right) \tag{A.46}$$

where d is the distance between two pinning centers. The flux creep velocity will create an electric field, $E = Bu$, given by

$$E = B\nu_0 \mathrm{d} \exp\left(-\frac{\mathrm{U}}{\mathrm{k_B}T}\right) \sinh\left(\frac{JU}{J_{c0}k_BT}\right) \tag{A.47}$$

The current voltage characteristic A.47 has three different regimes. For $J > J_{c0}$ we have a nearly ohmic dissipation regime, $E = \rho_{ff}\,(J - J_{co})$. For $J << J_{c0}$, $\sinh JU/J_{c0}k_BT \approx JU/J_{c0}k_BT$ and the expression A.47 becomes

$$E = \left(\frac{2\rho_c U}{k_BT}\right) \exp\left(-\frac{U}{k_BT}\right) J = \rho_{TAFF} J, \tag{A.48}$$

where

$$\rho_{TAFF} = \left(\frac{2\rho_c U}{k_BT}\right) \exp\left(-\frac{U}{k_BT}\right), \tag{A.49}$$

is called *thermally assisted flux flow resistivity* (TAFF). This Ohmic regime appears only in high temperature superconductors. The TAFF regime was evidenced by several authors [7, 8].

For external currents close to the critical current, $J \approx J_{c0}$, the current-voltage character-

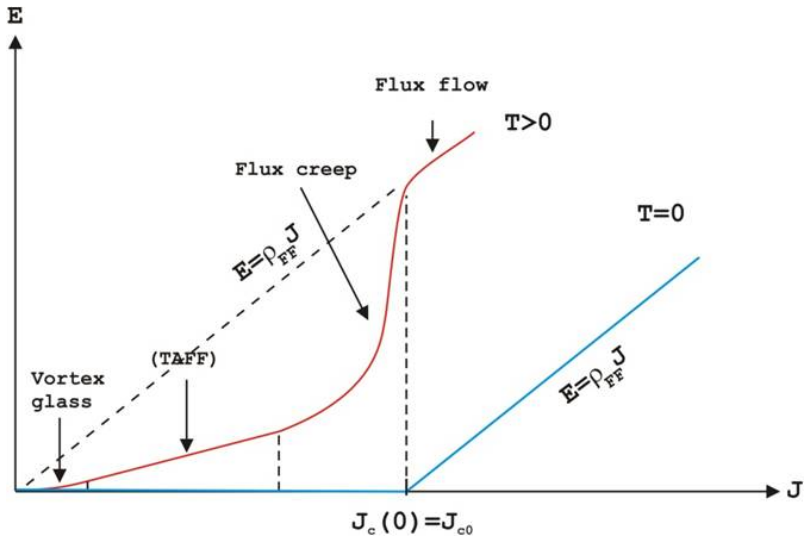

Figure A.11: Schematic presentation of the current-voltage characteristics for $T = 0$ (blue line) and at finite temperature (red line).

istic A.47 can be approximated as

$$E = \rho_c J \exp\left[\left(\frac{J}{J_{c0}} - 1\right)\frac{U}{k_B T}\right]. \tag{A.50}$$

Fisher *et al.* [9, 10] have experimentally determined that in the range of low temperatures and magnetic fields the TAFF Ohmic regime is not valid for currents below a certain characteristic value, J_g. For $J < J_g$ the voltage depends exponentially on the current,

$$E(J) \approx \exp\left[-(J_g/J\,)^{\mu}\right] \tag{A.51}$$

where $0 \leq \mu \leq 1$. To explain this nonlinear $E - J$ characteristic which appears in the range of small current densities, where linear TAFF regime should be valid, Fischer [9, 10] proposed the existence of a "vortex-glass" phase below a characteristic temperature, T_g. The vortex glass state was for the first time predicted by Larkin and Ovchinnikov [11] which shows that in the presence of a density of pinning centers the long range order of the flux lattice is destroyed beyond a volume V_c, within which there is short-range order. The aforementioned regimes are illustrated in Figure A.11.

A.2.5 Irreversibility line

Sometimes, it is more intuitive to represent the flux flow regimes in a magnetic field-temperature ($B - T$) diagram, as it is shown in Fig. A.12a. At a given temperature, the vortex flow regime depends only on the magnetic field. Thus, in the limit of low fields the vortex glass phase is stable, in which the flux line are completely pinned. If the field is

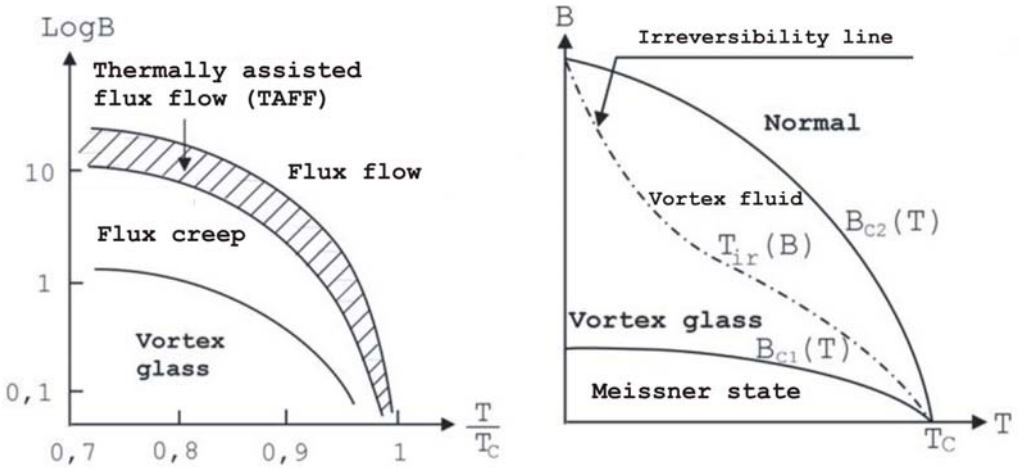

Figure A.12: The $B-T$ diagram (a) and the equilibrium phase diagram for the vortex system (b).

high enough, we have the flux flow regime. In a narrow range of magnetic fields, below flux flow regime, the thermally assisted flux flow regime (TAFF) is stable. Both the flux flow and the TAFF regimes have an Ohmic type $E-J$ characteristics. Between TAFF and vortex glass regimes there is a flux creep regime with an exponential $E-J$ characteristic. It is to be noted that, contrary to conventional superconductors, for high-temperature superconductors, thermally activated flux flow regimes (flux creep and TAFF) are observed in a large temperature and magnetic field range. This fact can be qualitatively explained as follows: in spite of their low coherence length, high-temperature superconductors have a higher condensation energy $B_c^2/2\mu_0$, therefore, the activation energy $U \approx B_C^2\xi^3/2\mu_0$ of the high-temperature superconductors has the same order of magnitude with that of a conventional superconductor. Because the critical temperature of HTS is one order of magnitude higher than that of conventional superconductors, it is clear that the thermally activated process with rates proportional to e^{-U/K_BT} will be exponentially more important in HTS.

The $B-T$ diagram from Fig. A.12a leads to an equilibrium phase diagram for the vortex system presented in Fig.A.12b. For $B < B_{c1}$ the sample is in the Meissner state with $B = 0$. If the magnetic field is greater the B_{c1} the sample is in a vortex state. Due to the presence of disordered pinning centers, the Abrikosov lattice is transformed into a vortex glass phase with $\rho = 0$. Another characteristic of the vortex state is the irreversibility of the magnetic and electrical properties. With the temperature increase, the short range order will be destroyed, and above a certain temperature T_M(B), called the melting temperature, the vortex glass is transformed into a liquid phase. Close to the melting temperature the liquid is still viscous and can be pinned (TAFF regime with $\rho_{TAFF} = (2\rho_c U/k_BT\,)\exp(-U/k_BT\,)$. For fields close to B_{c2} the vortex fluid has very low viscosity and the vortex can move freely with $\rho = \rho_{ff}$(flux flow regime). In the liquid phase the vortex motion is reversible, but with

energy dissipation. Therefore, the melting line is also named the irreversibility line, $T_{irr}(B)$. In conventional superconductors, were the thermally activated processes are very weak, the irreversibility line coincides with B_{c2}. The magnetic field dependence of the irreversibility line can be approximated [12] as

$$B \approx \left[1 - \frac{T_{ir}(B)}{T_C}\right]^n, \tag{A.52}$$

where n=1.2 for thin films and n=2 for bulk materials.

From a practical point of view, the irreversibility line is a very important parameter, because it separates the dissipative from the non-dissipative regime in the $B-T$ phase diagram. For high field applications of HTS, the $T_{irr}(B)$ has the same role as J_c for conventional superconductors. Therefore, the increase of the irreversibility line by means of artificial enhancement of pinning, *i.e.* magnetic extrinsic pinning represents a very important issue in the field of HTS materials.

Bibliography

[1] A. A. Abrikosov, *On the Magnetic Properties of Superconductors of the Second Group*, Sov. Phys. JTEP **5**, 1174 (1957);

[2] B.I.Chakravarty, B.I. Ivlev and Y.N. Ovchinnikov, *Thermally activated flux creep in strongly layered high-temperature superconductors*, Phys. Rev. B **42**, 2143 (1990);

[3] T. P. Orlando and K. A Delin, *Foundations of Applied Superconductivity*, Addison-Wesley (1991);

[4] Y. B. Kim, C. F. Hempstead, A. R. Strand, *Critical Persistent Currents in Hard Superconductors*, Phys. Rev. Lett. **9**, 306 (1962);

[5] P. W. Anderson, *Theory of Flux Creep in Hard Superconductors*, Phys. Rev. Lett. **9**, 309, (1962);

[6] M. R. Beasley, R. Labusch and W. W. Webb, *Flux Creep in Type-II Superconductors*, Phys. Rev. **181**, 682 (1969);

[7] T. K. Worthington, M. P. A. Fisher, D. A. Huse, J. Toner, A. D. Marwick, T. Zabel, C. A. Feild, F. Holtzberg, *Observation of separate vortex-melting and vortex-glass transitions in defect-enhanced $YBa_2Cu_3O_7$ single crystals*, Phys. Rev. B **46**, 11854 (1992);

[8] T. T. M Palstra, B. Battlogg, R. B. van Dover, L. F. Schneemeyer, J. V. Waszczak, *Dissipative flux motion in high-temperature superconductors*, Phys. Rev. B **41**, 6621 (1990);

[9] M. P. A. Fisher, *Vortex-glass superconductivity: A possible new phase in bulk high-T_c oxides*, Phys. Rev. Lett. **62**, 1415 (1989);

[10] D. S. Fisher, M. P. A. Fisher, D. A. Huse, *Thermal fluctuations, quenched disorder, phase transitions, and transport in type-II superconductors*, Phys. Rev. B 43, 130 (1991);

[11] A.I. Larkin, Yu. N. Ovcinikov, *Pinning in type II superconductors*, J. Low. Temp. Phys. 34, 409 (1979);

[12] M. Xu, D. Shi, R. F. Fox, *Generalized critical-state model for hard superconductors*, Phys. Rev. B **42**, 10773 (1990).

Modulated magnetic structures for vortex pinning in high temperature superconductors

The present thesis deals with the fabrication and study of hybrid, ferromagnetic/superconducting, interface systems. Magnetic mezoscopic systems, whose magnetic properties were modulated by the dimensionality (thickness and lateral size) of the systems was studied. Two types of structures were considered. The first consisted of perovskite-like epitaxial LaSrMnO thin films. We have demonstrated the direct correlation between oxygen incorporation in the LaSrMnO lattice and the evolution of its structural, magnetic and electric properties. A second class of magnetic materials that has been studied consisted of transition metals (Co) and alloys ($Ni_{80}Fe_{20}$). We have defined micronic objects from the as-deposited films, by means of optical lithography and ion beam etching. These structures were then integrated to form an interface with thin epitaxial high T_c superconducting films: YBaCuO. The ultimate goal of the above studies was the control of vortex dynamics within the superconducting layer by two mechanisms: the first, intrinsic, in which flux pinning is achieved by structural defects within the superconducting film, and a second one, extrinsic, correlated with influence of the magnetic field modulations created by the adjacent mezoscopic magnetic structure.

Keywords: *supeconductivity, nanomagnetism, mezoscopic magnetism, lithography, superconducting vortex, micromagnetism, vortex dynamics*

Structures magnétiques modulées pour le pinning dans les supraconducteurs à haute température

Cette thèse porte sur la réalisation et l'étude de systèmes hybrides d'interface entre une couche magnétique et un supraconducteur. Tout d'abord, nous avons réalisé et étudié des structures magnétiques mésoscopiques dont les propriétés magnétiques ont été modulées par l'effet de la dimensionnalité du système (épaisseur et taille latérale). Deux types des structures ont été considérés. La première est constituée par des couches minces de pérovskite LaSrMnO. Par une étude complexe nous avons réussi à démontrer la corrélation directe entre l'incorporation de l'oxygène dans le LaSrMnO et l'évolution de ses propriétés structurales, magnétiques et électriques. Une deuxième classe de matériaux magnétiques étudiés est constituée des métaux de transition (Co) et des alliages ($Ni_{80}Fe_{20}$). Les couches ont étés structurées par lithographie optique et gravure ionique sous forme d'objets de taille micronique. Par la suite, ces structures ferromagnétiques ont été interfacées avec des films minces constitués d'un supraconducteur à haute température : YBaCuO. L'objectif ultime de cette étude a été le contrôle de la dynamique des vortex dans le supraconducteur par deux types de mécanismes: intrinsèque ou les centres de pinning sont les défauts structuraux dans le film supraconducteur et un mécanisme extrinsèque lié à l'influence des modulations du champ magnétique généré par la structure magnétique mésoscopique adjacente.

Mots clés: *supraconductibilité, nanomagnétisme, magnétisme mésoscopique, lithographie, vortex supraconducteur, micromagnétisme, dynamique des vortex, supraconducteur à haute température.*